UNIVERSITY OF SOUTHAMPTON

FACULTY OF ENGINEERING, SCIENCE & MATHEMATICS

OPTOELECTRONICS RESEARCH CENTRE

Direct UV Writing of Structures In Lithium Niobate and Lithium Tantalate

by

Iain Wellington

Thesis for the degree of Doctor of Philosophy

October 2007

UNIVERSITY OF SOUTHAMPTON

ABSTRACT

FACULTY OF ENGINEERING, SCIENCE AND MATHEMATICS
OPTOELECTRONICS RESEARCH CENTRE

Doctor of Philosophy

Direct UV Writing of Structures in Lithium Niobate and Lithium Tantalate

By Iain Wellington

This thesis presents results from fabrication of UV direct write structures in lithium niobate and lithium tantalate. Unassisted direct writing of surface channel waveguides using λ = 244 nm cw light resulted in polarisation specific waveguides fabricated on *z*- cut crystals. Waveguides were characterised using mode profiles, propagation losses, numerical aperture and refractive index measurements. In z-cut congruent lithium niobate, waveguides were written on the +*z* and -*z* faces producing structures that guided TM polarisation only with +*z* face waveguides exhibiting the lowest propagation loss of ~ 2 dB/cm, a maximum refractive index difference of ~ 8 x 10^{-4} and a mean lifetime of τ ~ 4.5 days. The waveguiding mechanism is believed to be due to a lithium out-diffusion enhanced by a transient photorefractive effect. Waveguides were also written in stoichiometric and doped samples to test improvements in waveguide lifetimes. Surface domain reversal was observed in congruent lithium niobate on both +*z* and –*z* faces. Channel waveguides written into lithium tantalate were characterised and compared with lithium niobate.

Surface ferroelectric domain reversal via illumination of single pulsed λ = 266 nm light through a phasemask on +*z* face congruent lithium niobate produced ordered alignment of domain lines along the crystallographic y-axes with minimum domain separation width of ~ 2 μm. Results from high temperature exposures and multi-pulse regimes are presented and a domain formation mechanism is proposed via an Nb anti-site model.

DECLARATION OF AUTHORSHIP

I, Iain Tristan Wellington declare that the thesis entitled *Direct UV Writing of Structures in Lithium Niobate and Lithium Tantalate* and the work presented in the thesis are both my own, and have been generated by me as the result of my own original research. I confirm that:

- this work was done wholly or mainly while in candidature for a research degree at this University;
- where any part of this thesis has previously been submitted for a degree or any other qualification at this University or any other institution, this has been clearly stated;
- where I have consulted the published work of others, this is always clearly attributed;
- where I have quoted from the work of others, the source is always given. With the exception of such quotations, this thesis is entirely my own work;
- I have acknowledged all main sources of help;
- where the thesis is based on work done by myself jointly with others, I have made clear exactly what was done by others and what I have contributed myself;
- parts of this work have been published as listed in Appendix A.

Signed: Iain Wellington……..

Date: 8/1/2008……

Contents

Chapter 1

Introduction

1.1 Integrated Optics

Integrated optics today dominates the telecommunications industry with light sources used to transmit signals, optical fibres used to carry these signals and other devices, such as amplifiers used to manipulate or boost these signals.

Miller first postulated in 1960 that field of optics could be transformed by reducing bulk optical apparatus down, to the equivalent of integrated circuits, to devices and waveguides all on the same substrate. Integrated optics takes many of the advances discovered in integrated circuits and adapts these methods to manipulate light instead of electrons. The ultimate aim of integrated optics is to fabricate all devices on a single chip thus being cheap to produce and small for convenience. With the advent of low loss optical fibres and connectors, together with new sub-micron

photolithography techniques and semiconductor devices, the integrated optics field grew tremendously.

Two major breakthroughs galvanised the optical telecommunications industry. The first was the invention of semiconductor light sources, whether lasers for long distance communication or light emitting diodes for short distance communications, allow compact, cheap devices to be used. The second, optical fibre with low propagation loss, currently around 0.2dB/km, was important for long distance transmission of signals without signal loss and for high bandwidth applications. Suitable connectors are needed to ensure the signal is delivered into and out of the fibre with little degradation to the quality of the signal. Optical fibres can be used to amplify the signal by doping a fibre with an optically active element such as erbium. Amplification is achieved by stimulating emission from photons from the dopant ions. Although amplification is a useful process, many other manipulations of the signal are needed for an optical network. Planar devices fit this category and can be used for splitters, switches, modulators, interferometers and polarisers.

The important improvement with integrated optics is the optical confinement nature of all devices, allowing manipulation of light while on the substrate. Planar waveguide devices confine light in one dimension and are used to manipulate light in ways that fibre cannot. A sub-section of planar waveguides are channel waveguides in which light is confined in two dimensions and more complex devices can be realised with channel waveguides are they designed to used the single-mode of the signal. Devices that change the waveguide direction (interconnects), divide the signal (splitters), change the signal intensity/phase (modulators) and frequency converters (optical parametric oscillators) are fabricated in planar substrates because the size of the device can be made much smaller or the properties of the materials used can be exploited.

Many different materials have been used to fabricate integrated optics devices and lithium niobate was identified early as a promising candidate due to its wide range of

properties as identified by Ashkin in the mid-1960s [1]. Glasses, due to their amorphous structure, can be used as passive waveguides and, when doped with an active ion, waveguide lasers[2]. The use of silicon leads to the considerable desire of exploiting current fabrication methods and processes already in use in the electronics industry for the optics industry – the sheer scale of reduction of production costs is hugely compelling.

Ultraviolet direct writing in lithium niobate was initiated by Mailis, who had observed an index change on the surface of lithium niobate after exposure to 244nm light [3]. The direct writing technique had already been used successfully to produce waveguides and more complex devices such as gratings in germanium-doped silica [4], waveguides and waveguide lasers in chalcogenide glasses [5] and waveguides in a variety of other glasses as expanded on in chapter 4.

1.2 Synopsis

The motivation for this thesis is to investigate the relatively simple UV direct writing technique to fabricate integrated optics using lithium niobate as a substrate material. The second chapter introduces lithium niobate as a material and outlines its various properties relevant to this thesis, ranging from electro-optic to thermal properties. The third chapter will begin with a brief summary of the theory of waveguiding and how light propagates in optical devices; the chapter will then describe how lithium niobate has been used to produce integrated optics and will present a brief summary of the current state of the art fabrication techniques and some devices that have been realised.

The fourth chapter outlines the main experimental work done on continuous-wave (cw) ultraviolet direct writing of waveguides in congruent lithium niobate, some attempts at fabricating devices and the possible waveguide mechanism behind it. In addition domain formation via cw UV exposure is summarised. The fifth chapter includes cw UV written waveguides in stoichiometric and various doped lithium

niobate crystals finishing with lithium tantalate. The sixth chapter focuses on ultraviolet direct writing of domain with a phasemask in lithium niobate using nanosecond pulse duration lasers, concentrating on the fabrication of ordered lines of domains. An estimation of thermal effects, such as the pyroelectric effect and thermo-optic effect, of direct writing on the properties of lithium niobate is demonstrated via computer modelling. Finally, a concluding chapter will summarise results in this thesis and will outline future work.

1.3 References

1. Ashkin, A., G.D. Boyd, J.M. Dziedzic, R.G. Smith, A.A. Ballman, J.J. Levinstein, and K. Nassau, *Optically-Induced Refractive Index Inhomogenities In $LiNbO_3$ AND $LiTaO_3$.* Applied Physics Letters, 1966. **9**(1): p. 72-74.

2. Guilhot, D.A., G.D. Emmerson, C.B.E. Gawith, S.P. Watts, D.P. Shepherd, R.B. Williams, and P.G.R. Smith, *Single-mode direct-ultraviolet-written channel waveguide laser in neodymium-doped silica on silicon.* Optics Letters, 2004. **29**(9): p. 947-949.

3. Mailis, S., C. Riziotis, P.G.R. Smith, J.G. Scott, and R.W. Eason, *Continuous wave ultraviolet radiation induced frustration of etching in lithium niobate single crystals.* Applied Surface Science, 2003. **206**(1-4): p. 46-52.

4. Emmerson, G.D., S.P. Watts, C.B.E. Gawith, V. Albanis, M. Ibsen, R.B. Williams, and P.G.R. Smith, *Fabrication of directly UV-written channel waveguides with simultaneously defined integral Bragg gratings.* Electronics Letters, 2002. **38**(24): p. 1531-1532.

5. Mairaj, A., A.M. Chardon, D.P. Shepherd, and D.W. Hewak, *Laser Performance and Spectroscopic Analysis of Optically Written Channel Waveguides in Neodymium-Doped Gallium Lanthanum Sulphide Glass.* IEEE Journal of Selected Topics in Quantum Electronics, 2002. **8**(6): p. 1381-1388.

Chapter 2

Lithium Niobate

This chapter summarises the physical and optical properties of lithium niobate and specifically addresses those optical effects that have been observed during either fabrication or characterisation of the optical waveguides produced later in this thesis.

2.1 Introduction

Lithium niobate (LN, $LiNbO_3$) is an artificial dielectric crystal, first fabricated in Bell Laboratories in the mid-sixties, and has various attractive properties which have been exploited in many applications. It is most commonly available in 3-inch diameter wafer and bulk crystal form and is inert at room temperature.

$LiNbO_3$ is referred to as a non-linear crystal, but due to its ferroelectric properties, it possesses a wide range of both linear and non-linear properties, which are mentioned later and include the electro-optic effect, acousto-optic effect, photovoltaic effect, photorefractive effect, piezoelectric and pyroelectric effects. It has large non-linear coefficients, which make the material attractive for photonic applications such as harmonic conversion.

In this introduction, only the properties and effects that affect the UV writing experiments are mentioned. Weis and Gaylord have summarised all properties in a comprehensive review [1]. Section 2.2 covers the growth and structure of the crystal, section 2.3 discusses various optical properties of lithium niobate and section 2.4 outlines the basic process and use of lithium niobate in second harmonic generation.

2.2 Crystal Structure & Properties

Lithium niobate is usually manufactured using the Czochralski growth method [1]. It is commercially available in two main crystal compositions: congruent and stoichiometric. The composition is usually represented by a lithium ion concentration as given by:

$$C = \frac{[Li]}{([Li]+[Nb])} \tag{2.1}$$

Where the [ ] symbols denote concentrations. Congruent crystals have a lithium ion content of less than 50 %mol Li_2O (typically ~48.5 mol% Li_2O) while stoichiometric crystals have a lithium ion content much nearer to the ideal 50 mol% Li_2O, and therefore congruent crystals are said to be lithium deficient compared to stoichiometric crystals. The exact composition of the crystal can also be estimated by measurements of the birefringence and the Curie temperature [2].

The Czochralski method uses a seed crystal which is dipped into a melt of congruent Li_2O-Nb_2O_5 just above the melting temperature and is subsequently slowly rotated and raised. The composition of the crystal can be variable if produced in a non-congruent melt due to thermal effects from melt convection and lack of melt depth. For these reasons, some stoichiometric crystals are grown via a double crucible Czochralski method [3] and this allows a constant melt source to be continuously added thus allowing stoichiometric crystals of uniform homogeneity to be produced. Single crystal stoichiometric LN can also be produced via the single Czochralski process with the addition of 8 mol% K_2O to the melt [4].

Figure 2.1 illustrates the nomenclature of the crystallographic directions used with ferroelectric-phase lithium niobate by depicting a hexagonal unit cell (without oxygen planes). Lithium niobate has three planes of symmetry which denotes the *c*-axis. The planes are represented as mp1, mp2 and mp3, all of which are perpendicular to the *c*-axis. The hexagonal cell allows use of Cartesian co-ordinates and the *c*-axis is equivalent to the *z* polar axis, the *x*-axis is one of the *a*-axes and the *y*-axis perpendicular to both the *z*- and *x*- axes. When the crystal is cooled from the melt, the face that becomes positively charged is defined as the +*c* face.

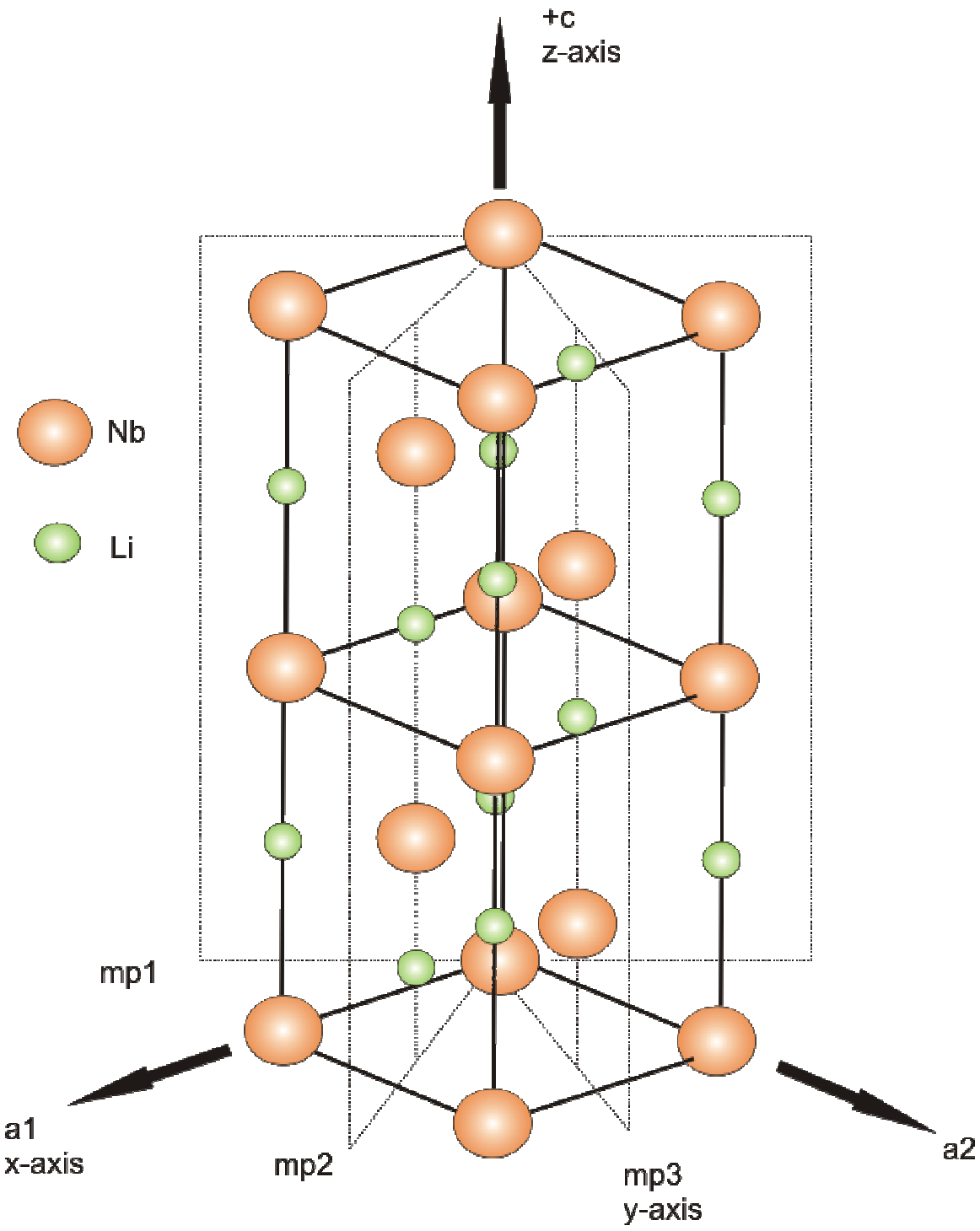

Figure 2.1: Crystallographic directions for ferroelectric lithium niobate [1].

At temperatures lower than the Curie temperature (<~1415 K), $LiNbO_3$ is a ferroelectric material which has a spontaneous electric polarisation caused by $LiNbO_3$ having no inversion symmetry of the unit cell (a non-centrosymmetric crystal). The spontaneous polarisation is induced by a movement of the lithium and niobium ions

as a result of elastic forces within the crystal lattice. The spontaneous polarisation is randomly aligned in one of two directions, either along the +*c* or – *c* direction. It can be made to align in a chosen direction along the *c* axis by the application of an external electric field while cooling through the Curie temperature. The Curie temperature of a material is a transition point above which the material exhibits no spontaneous polarisation as it has undergone a phase change, to the paraelectric phase and it has a different structure which is centrosymmetric – i.e. no spontaneous polarisation present.

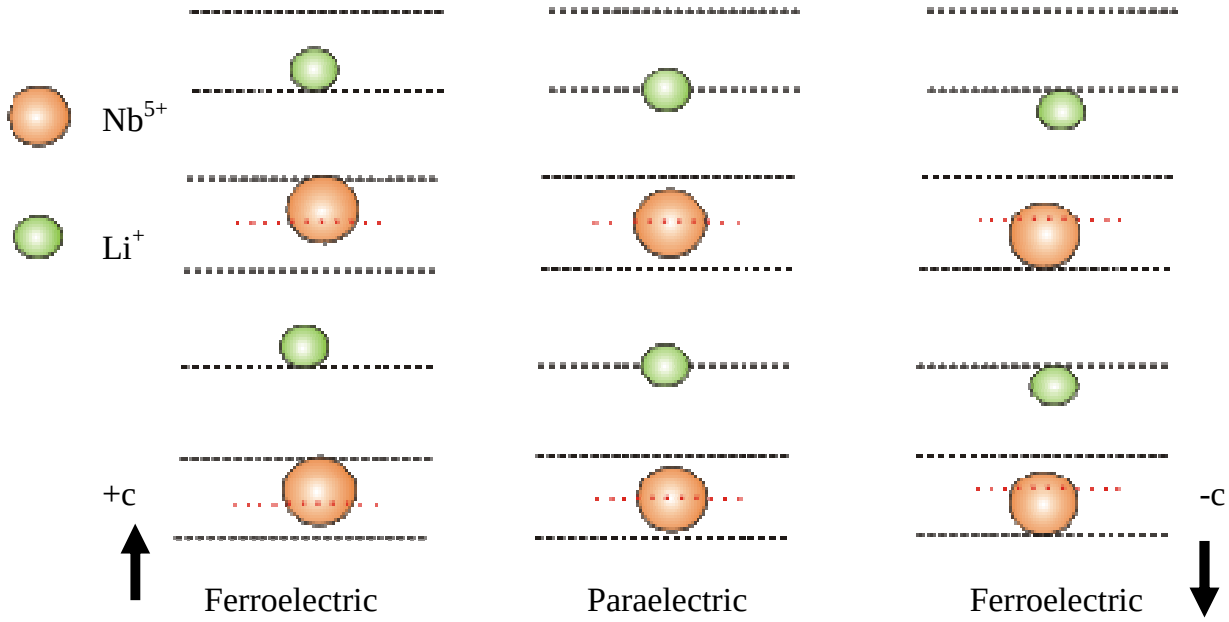

Figure 2.2: Structure of $LiNbO_3$ showing both paraelectric and ferroelectric phases [5].

The niobium and lithium ions are distributed between planes of oxygen atoms. Figure 2.2 illustrates the structure of the crystal in both the paraelectric and ferroelectric phases with the oxygen planes denoted as dashed lines for simplicity. The centre diagram is the paraelectric phase which has a net polarisation of zero due to the inversion symmetry of the crystal structure. Either side of the paraelectric phase is a diagram of the ferroelectric phase with the net polarisation aligned either along the +*c* or –*c* axis.

If we include the oxygen planes, the structure of $LiNbO_3$ at room temperature in the ferroelectric phase is shown in fig. 2.3. It is composed of layers of distorted octahedrons along the *c* axis.

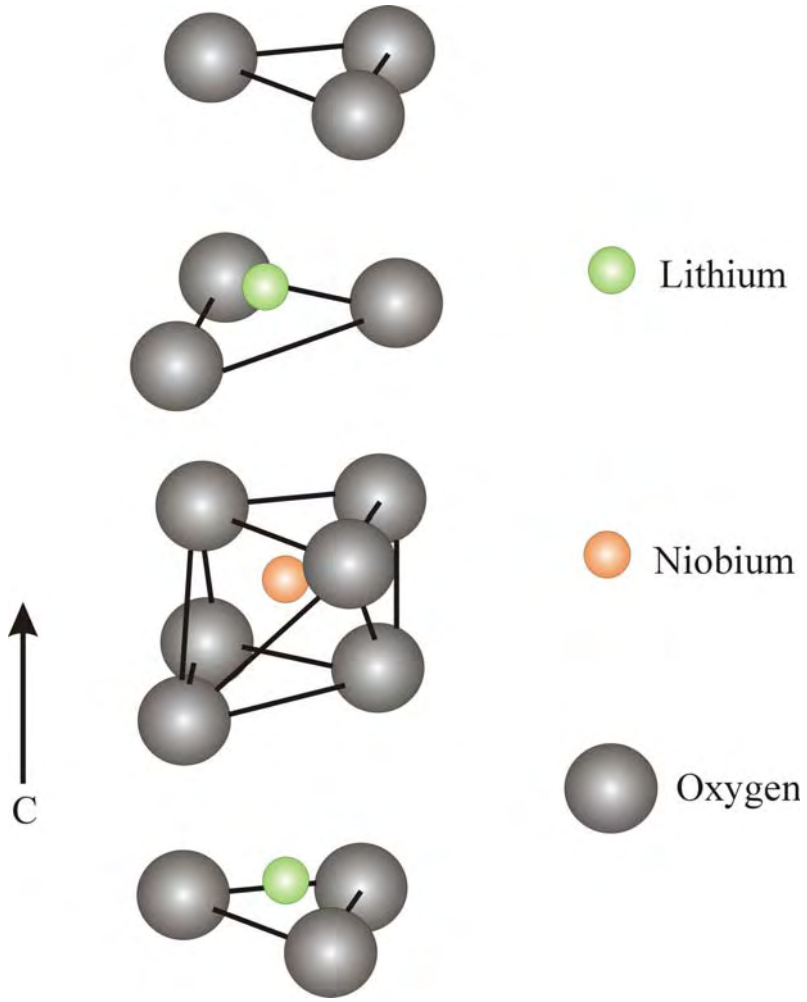

Figure 2.3: Structure of $LiNbO_3$ at room temperature [1].

Commercially-bought crystals today are sold as single domain, meaning the orientation of the crystal's polarisation is in one direction. A domain is defined as a region of uniform polarisation within the crystal. On application of an external field, the field value needed to reverse the direction of the spontaneous polarisation is referred to as the coercive field, E_c. The appliance of E_c is said to 'pole' the crystal and the field needed for this in congruent $LiNbO_3$ is ~ 22 kV/mm and stoichiometric $LiNbO_3$ ~ 4 kV/mm [6].

Several congruent crystal properties are listed in table 2.1:

Property	Value
Density	4648 kg/m^3
Crystal Structure	3m
Melting Point	1240ºC
Curie Point	1140ºC
Specific Heat	633 J/kg K
Thermal Diffusivity	1.36 x 10^{-5} m^2/s

Table 2.1: Properties of congruent $LiNbO_3$

2.3 Optical Properties

2.3.1 Optical Transmission

Lithium niobate has a wide spectral region for use in photonic applications; it is optically transparent in the region $\lambda \sim 0.4 - 5.0\mu m$ and the ultraviolet absorption edge, which occurs at ~ 320 nm is shown in figure 2.4.

2.3.2 Birefringence

$LiNbO_3$ is a negatively birefringent uniaxial crystal. A polarisation parallel to the optic axis sees an extraordinary refractive index (n_e) and a polarisation perpendicular to the optic axis sees an ordinary refractive index (n_o) and the optic axis for lithium niobate is situated along the *z*-axis. As the ordinary refractive index is larger than the extraordinary refractive index, $n_e < n_o$, the crystal is said to be negative uniaxial.

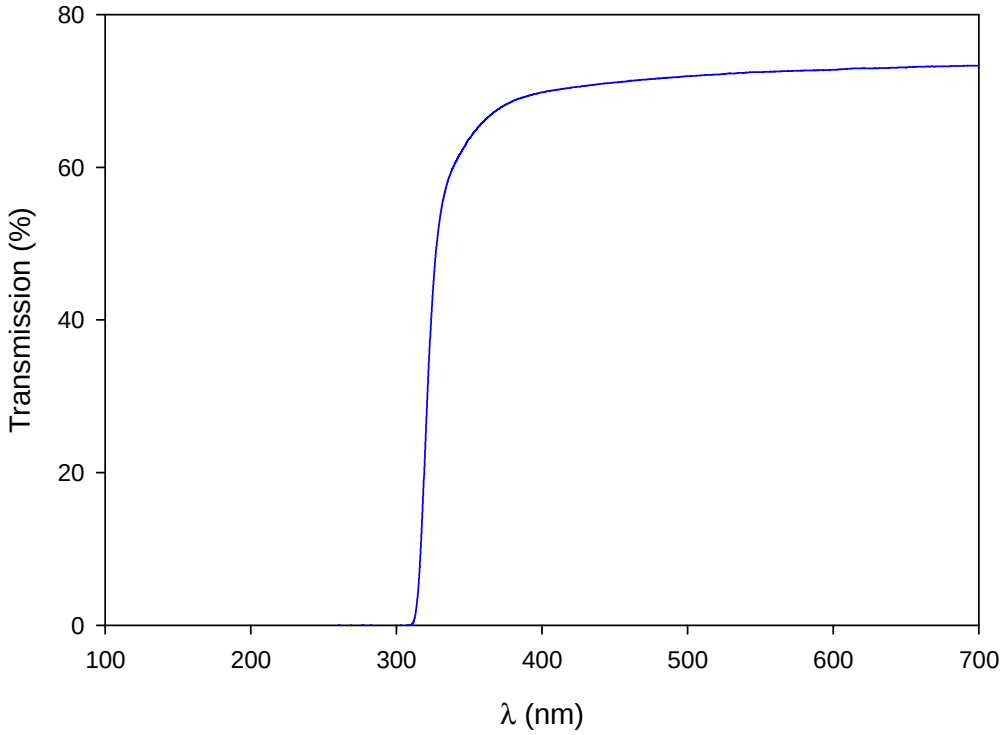

Figure 2.4: Transmission spectrum of congruent lithium niobate.

Through the Sellmeier equation in Eq. 2.2 it is possible to predict the refractive indices at different wavelengths and crystal compositions [7]. Table 2.2 gives the parameters needed for the Sellmeier equation and figure 2.5 illustrates the change in index over wavelength for congruent and stoichiometric lithium niobate.

$$n_i^2 = 1 + \frac{50 + C_{Li}}{100}\frac{A_{0,i}}{1 - \frac{\lambda_{0,i}^2}{\lambda^2}} + \frac{50 - C_{Li}}{100}\frac{A_{1,i}}{1 - \frac{\lambda_{1,i}^2}{\lambda^2}} \qquad (2.2)$$

Parameter	n_e	n_o
$A_{0,i}$	3.854	3.489
$\lambda_{0,i}$	186.535 nm	176.466 nm
$A_{1,i}$	3.552	6.004
$\lambda_{1,i}$	208.592 nm	223.479 nm

Table 2.2: Parameters for lithium niobate Sellmeier equation [7].

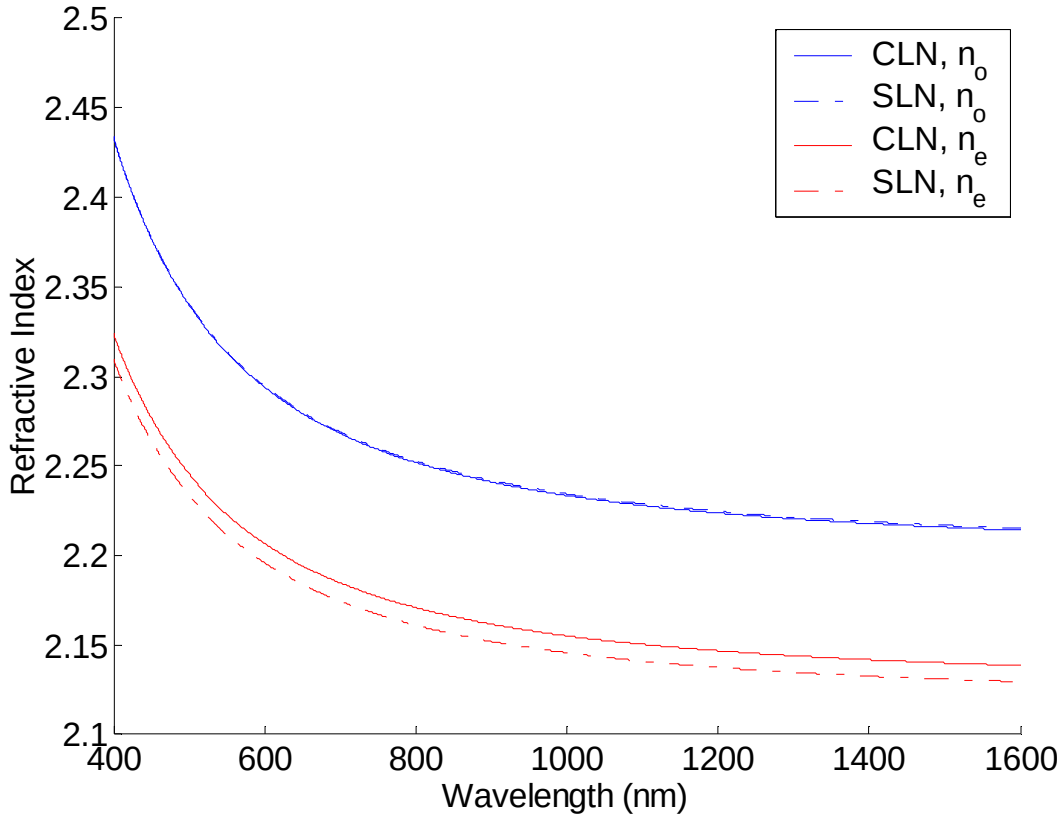

Figure 2.5: Extra-ordinary and ordinary refractive indices for congruent (full lines) and stoichiometric (dashed lines) lithium niobate [7].

2.3.3 Electro-optic Effect

The linear electro-optic effect (also called the Pockels effect) in $LiNbO_3$ occurs when the refractive index of the crystal is modified by the application of an electric field. The linear electro-optic effect has the relationship [8]:

$$\Delta n = -\frac{1}{2} n^3 r_{ijk} E \tag{2.3}$$

Where Δn is the change in refractive index, $\boldsymbol{r_{ijk}}$ the relevant electro-optic tensor coefficient, and E is the applied electric field. The electro-optic tensor $\boldsymbol{r_{ijk}}$ has coefficients which can be reduced from an initial 27 terms to 18 and then finally to 4

different values due the symmetry of the crystal. Equation (2.4) lists the r_{ijk} coefficients in lithium niobate.

$$r_{ijk} = \begin{pmatrix} 0 & -r_{22} & r_{13} \\ 0 & r_{22} & r_{13} \\ 0 & 0 & r_{33} \\ 0 & r_{42} & 0 \\ r_{42} & 0 & 0 \\ -r_{22} & 0 & 0 \end{pmatrix} \tag{2.4}$$

This effect is exploited for use in modulators, an example of which is a Pockels cell [9], [10]. The highest linear electro-optic coefficient for $LiNbO_3$ is the r_{33} coefficient, which has a value of 30.8pm/V. For comparison, quartz has an r_{41} coefficient of only 1.4 pm/V.

2.3.4 Pyroelectric Effect

The pyroelectric effect considers the change in spontaneous polarisation ΔP with a change in temperature ΔT with a tensor multiplication factor p_3 [11]:

$$\Delta P = \begin{bmatrix} 0 \\ 0 \\ p_3 \end{bmatrix} \Delta T \tag{2.5}$$

The constant p_3 is -4x 10^{-5} C K^{-1} m^2 and is due to movement of the *Li* and *Nb* ions in the *z*-direction only and so this effect is absent in the *x* and *y* directions and is negative indicating that on cooling, the +*z* face becomes more positively charged.

2.3.5 Photovoltaic Effect

The photovoltaic effect in $LiNbO_3$ is the dominant charge migration mechanism and is a photo-induced current which ionises impurities when the crystal is uniformly illuminated. A voltage can be observed between the *z* faces when the sample is illuminated. This effect is important when the crystal is used for photorefractive applications.

2.3.6 Photorefractive Effect

The photorefractive effect is found in $LiNbO_3$ crystals due to its electro-optic and photovoltaic properties. Exposure to optically intense inhomogeneous visible light induces a reversible change in the refractive index of the medium [12] and the crystal is more susceptible to wavelengths shorter than $\lambda \sim 1$ μm. This effect is generally agreed to be a combination of several mechanisms – incident high intensity light excites charge carriers (electrons for visible light) which are promoted from donor states to the conduction band and then become mobile and, through migration, get trapped at new sites such as an empty donor or acceptor. Regions of high intensity therefore lose electrons while regions of low intensity acquire surplus electrons. This alters local space-charge fields, modulating the refractive index via the linear electro-optic effect (Eq 2.3).

Figure 2.6 describes the process above. The first part is the initial stage of generation of charge carriers via illumination by a source of intensity *I*. The charges become mobile and move to regions of low intensity via the photovoltaic effect and diffusion, increasing the charge density ρ in these regions; by means of Poisson's equation, the charge density is related to a local charge-space field and this field consequently modulates the local refractive index Δn via Eq. 2.3.

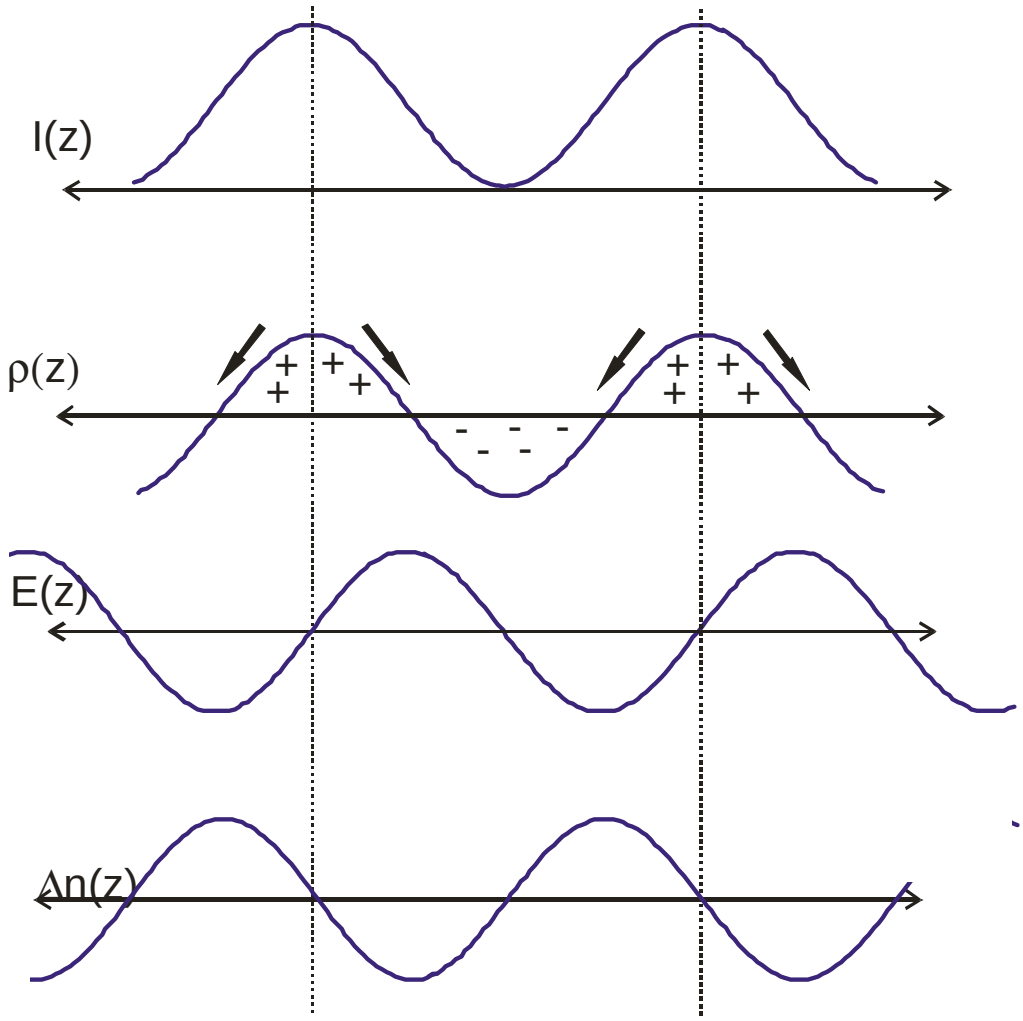

Figure 2.6: Photorefractive mechanism for lithium niobate with light intensity *I* top, the charge density *ρ* below, the resulting electric field via Poisson's equation and the change in refractive index *Δn* at the bottom.

Early on in the material's characterisation, this effect was deemed detrimental to waveguide fabrication [13] as power dissipates throughout propagation, limiting the use of waveguides in $LiNbO_3$ to low optical powers or operation at wavelengths beyond 1µm.

The effect is generally accepted to be due to iron impurities in the crystal [14] – iron exists in two oxidation states Fe^{2+} and Fe^{3+} which due to absorption of photons produce electrons and holes which get promoted to the conduction band:

$$Fe^{2+} + h\nu \rightarrow Fe^{3+} + e^{-} \quad (2.6)$$

$$Fe^{3+} + h\nu \rightarrow Fe^{2+} + h^{+} \quad (2.7)$$

Stoichiometric LN has been shown to have a reduction in optical damage compared to congruent LN [15]. The effect can persist for times that can vary from minutes to tens of years following exposure to illumination. Although unfavourable for optical waveguides, this can be an advantageous effect if these index changes are made permanent resulting in optical storage [16]. Doping the crystal with Fe ions increases the sensitivity of the material to light and becomes useful in applications such as holographic recording [17].

The crystals are often doped with magnesium oxide during the growth process for greater resistance to optical damage due to the photorefractive effect [18]. Zinc is also a useful dopant for reduced photorefractive sensitivity and it behaves in a similar way to magnesium. Approximately 4-6 mol% drastically changes the optical properties [19]. Recently, low Hf doping of ~0.5 %mol has also shown a resistance to optical damage [20].

2.4 Second Harmonic Generation

The demand for applications using shorter wavelengths is growing and the lack of suitable lasing devices in the UV to near-visible region of the spectrum means second harmonic generation from a fundamental frequency to a wave of double frequency is a suitable technique to achieve this. One of the main applications for lithium niobate crystals lies in second harmonic frequency conversion devices.

The types of frequency generation are sum frequency generation (SFG) sometimes called up conversion, difference frequency generation (DFG) or mixing, and optical parametric generation (OPG). SFG involves mixing two frequencies ω_1 and ω_2 together, to produce a higher frequency output at ω_3. DFG is mixing two frequencies

ω_3 and ω_2 and producing the difference frequency ω_1. OPG is a similar process to SFG but in reverse; the processes are governed by the frequency/energy conservation equations:

SFG: $$\omega_1 + \omega_2 = \omega_3 \quad (2.8)$$

DFG: $$\omega_3 - \omega_2 = \omega_1 \quad (2.9)$$

OPG: $$\omega_3 = \omega_1 + \omega_2 \quad (2.10)$$

Where $\omega_3 > \omega_2 > \omega_1$. Second harmonic generation (SHG) is a specific case of sum frequency generation when $\omega_1 = \omega_2$. To understand SHG, we look at the polarisation of a non-linear crystal while an electric field is propagating through it. The linear polarisation, ***P***, of a crystal is described by the vacuum permittivity ε_0, the susceptibility tensor χ and the incident electric field, ***E***:

$$P = \varepsilon_0\left(\chi^{(1)}E + \chi^{(2)}E^2 + \chi^{(3)}E^3 + ...\right) \quad (2.11)$$

The susceptibility tensor, $\chi^{(2)}_{ijk}$, is related to the non-linear tensor, $\mathbf{d_{ijk}}$, by:

$$d_{ijk} = \frac{1}{2}\chi^{(2)}_{ijk} \quad (2.12)$$

Where ***d*** can be reduced in the same manner as ***r*** via the crystal symmetry and is described by [21]:

$$d_{ij} = \begin{pmatrix} 0 & 0 & 0 & 0 & d_{15} & -d_{22} \\ -d_{22} & d_{22} & 0 & d_{15} & 0 & 0 \\ d_{31} & d_{31} & d_{33} & 0 & 0 & 0 \end{pmatrix} \quad (2.13)$$

The most commonly used coefficients of the non-linear tensor are the coefficients d_{22} = 3 pm/V and the largest coefficient, d_{33} = 31 pm/V. Due to the non-centrosymmetric

nature of lithium niobate, there is a non-zero $\chi_{ijk}^{(2)}$ present, and second order effects are possible. If we substitute an electric field of the form $E = E_0 \cos(\omega t)$ into (Eq. 2.11) the polarisation response becomes:

$$P = \varepsilon_0 \chi^{(1)} E + \varepsilon_0 \chi^{(2)} E^2$$
$$P = \varepsilon_0 \chi^{(1)} E_0 \cos(\omega t) + \frac{1}{2} \varepsilon_0 \chi^{(2)} E_0^2 \cos(2\omega t) + DC \qquad (2.14)$$

The first term is a response at the fundamental frequency, the second term is the response at the second harmonic frequency, at double the fundamental frequency, and the third term is a resulting DC electric field. The fundamental and second harmonic waves propagate throughout the crystal and the second harmonic term has an intensity proportional to the fundamental intensity squared:

$$I(2\omega) \propto I^2(\omega) \omega^2 L^2 \sin c^2 \left(\frac{\Delta k L}{2} \right) \qquad (2.15)$$

The second harmonic intensity thus increases quadratically over the interaction length L and is wavelength dependent with the term Δk the wave vector mismatch. If Δk is non-zero, the second harmonic intensity is modulated throughout the crystal, reducing the conversion efficiency hence phase matching (i.e. phase velocity matching) is needed. The SHG phase matching condition is $\Delta k = k_{2\omega} - 2k_{\omega} = 0$.

2.4.2 Phase Matching

In order to maximise non-linear conversion efficiencies and obtain useful output intensities, with the phase matching condition described in equation (2.16), the phase relationship between the two waves needs to be zero:

$$\Delta k = k_{2\omega} - 2k_{\omega} = 0 \qquad (2.16)$$

Where k_ω and $k_{2\omega}$ are the wavevectors of the fundamental and frequency doubled waves. As the waves propagate through the medium, they become more mismatched and out of phase due to dispersion so a solution is required to preserve $\Delta k = 0$. There are two main ways of achieving phase matching in lithium niobate for second harmonic generation: angle tuning with temperature tuning and quasi-phase matching.

Angle tuning uses the birefringence of the crystal to achieve the phase matching condition. The incident beam has a specific polarisation and the crystal axes are orientated in a certain direction. The change in refractive index is obtained via varying the angle θ by:

$$\frac{1}{n^2(\theta)} = \frac{\sin^2\theta}{n_e^2} + \frac{\cos^2\theta}{n_o^2} \tag{2.17}$$

There are a few constraints with this method due to factors such as the small range of angles available, the Poynting-vector walk-off due to the difference in phase velocity and power flow directions (which restricts the interaction length) and use of alternative non-linear coefficients due to wave polarisation. Temperature tuning with angle tuning can be achieved via birefringence; the refractive indices are, and hence birefringence is, temperature-dependent and heating a correctly orientated crystal with a specific polarised incident beam fulfils the phase-matching condition.

A less restrictive technique is quasi-phase matching (QPM) which involves inverting alternatively the domains in a crystal in a periodic fashion [22]. Dispersion from travelling through the crystal induces a phase shift between the fundamental and second harmonic waves which is a function of the interaction length. After travelling through one coherence length (L_c), the second harmonic power reaches a local maximum; inverting the domain over the next coherence length flips the sign of the non-linear coefficient, introducing a 180° phase shift, constructively interfering with

the wave and increasing the second harmonic power once again. If the phase matching condition is not satisfied the second harmonic power reverts to zero after two coherence lengths. The QPM phase-matching condition has an extra grating vector term to account for the phase correction and is given by:

$$\Delta k = k_1 - k_2 - \frac{2\pi}{\Lambda} = 0 \tag{2.18}$$

Where the factor Λ is the grating period and is $2L_c$. Fig. 2.7 illustrates the second harmonic intensity generated vs. interaction length for three conditions of phase matching: line ***a*** is perfect phase matching, line ***b*** quasi-phase matching with the inverted nonlinear coefficient every coherence length and line ***c*** the condition where no phase matching occurs.

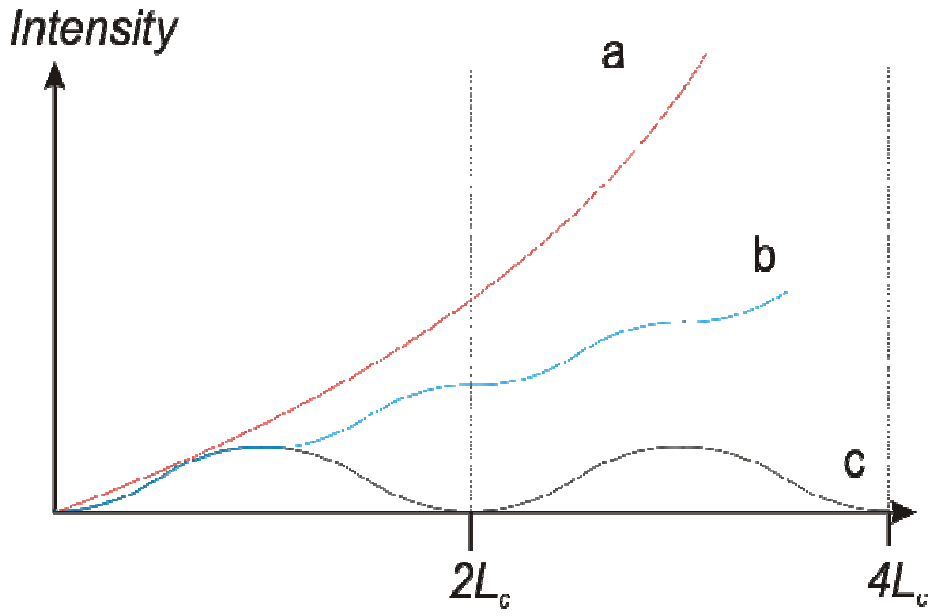

Figure 2.7: Second harmonic generation intensity with a) perfect phase matching, b) quasi-phase matching and c) non-phase matched conversion. The coherence length is denoted as L_c.

This technique allows a greater degree of flexibility, suffering none of the problems associated with the angle tuning technique and allows access to the d_{33} coefficient

that birefringent phase matching cannot [23]. Conversion efficiencies of 81% in zinc doped PPLN have been reported [24].

2.4.3 Periodically Poled Crystals

Originally, this process was envisaged by stacking thin sheets of material one coherence length in width in alternating directions, but practically this is extremely difficult as well as time-consuming. First realised in 1992, periodic domains were fabricated in lithium niobate via an external field at room temperature to produce devices for optical frequency generation [25]. The variety choice of period Λ from Eq. 2.18 with the fundamental frequency allows a range of possible doubled frequencies for many non-linear applications. A constraint of this method is the period is limited by fabrication conditions, with periods of below 3 μm difficult with usual photolithographic techniques. For an example of parameters needed for a periodically poled crystal, the fundamental wavelengths of λ = 915 nm and λ = 1130 nm with crystal periods of 5.2 μm and 8.3 μm produce second harmonic efficiencies of ~ 24% and ~ 20% respectively in different samples [26].

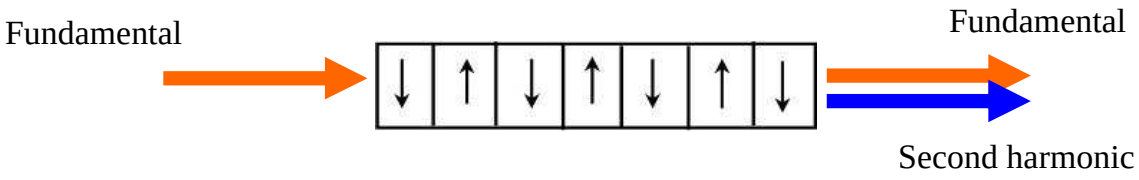

Figure 2.8: PPLN second harmonic process.

Poling the crystal is typically achieved by patterning metal electrodes using photolithography, such as aluminium, on the +*z* face of the sample and applying a high voltage that exceeds the coercive field at room temperature (~ 22 kV/mm) via electrodes as in figure 2.9 [27]. The external field is required to remain for a specific

duration in order for the domain reversal to be permanent, Myers reported a time of between 0.36 - 1.9 seconds [28].

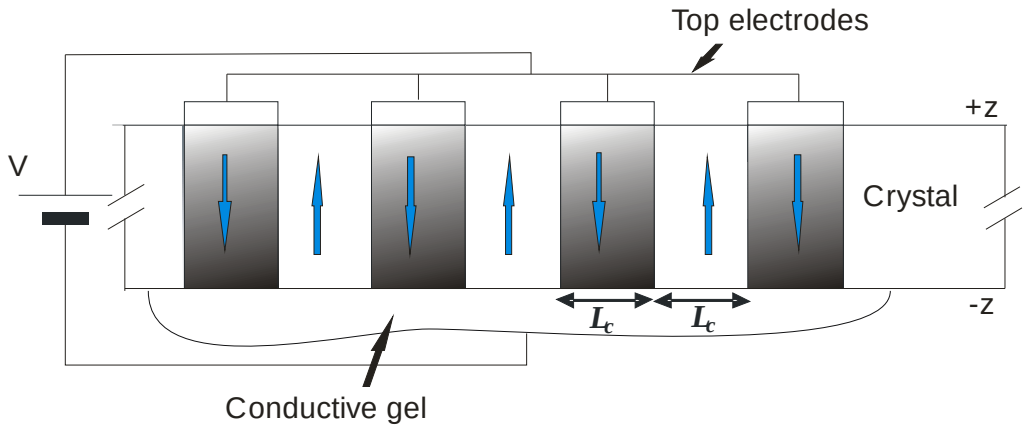

Figure 2.9: Apparatus used for periodic poling in +*z* cut lithium niobate. The spontaneous polarisation direction is denoted by blue arrows and reversed domains are dark grey.

Another method of electric field poling include spin coating a photoresist on the –*z* face instead of metal electrodes and patterning using a mask with photolithography. There are other techniques of poling without applying an external electric field which have been investigated such as heat treatment [29] but the methods generally lack the high degree of control over domain size and experimental practicality of electric field poling. More complex aperiodically poled lithium niobate can be used to produce several wavelengths at once via fabrication of a chirped grating [30].

2.5 Conclusion

Lithium niobate is a popular choice for integrated optics thanks to its high non-linear coefficients and ease of production. It is suitable for a wide range of applications including optical waveguiding, electro-optic modulators and frequency generation. As such, many commercial devices have been fabricated and lithium niobate is and will be the material of choice for the foreseeable future.

2.6 References

1. Weis, R.S. and T.K. Gaylord, *Lithium Niobate: Summary of Physical Properties and Crystal Structure.* Applied Physics A: Solids and Surfaces, 1985. **37**: p. 191-203.

2. Wohlecke, M., G. Corradi, and K. Betzler, *Optical methods to characterise the composition and homogeneity of lithium niobate single crystals.* Applied Physics B: Lasers and Optics, 1996. **63**(4): p. 323-330.

3. Kitamura, K., Y. Furukawa, and N. Iyi, *Progress in single crystal growth of $LiNbO_3$ using double crucible Czochralski method.* Ferroelectrics, 1997. **202**: p. 21-28.

4. Bermudez, V., P.S. Dutta, M.D. Serrano, and E. Dieguez, *On the single domain nature of stoichiometric $LiNbO_3$ grown from melts containing K_2O.* Applied Physics Letters, 1997. **70**(6): p. 729-731.

5. Rauber, A., *Chemistry and physics of lithium niobate,* in *Current Topics in Materials Science,* E. Kaldis, Editor. 1978, North-Holland Publishing Company. p. 481-601.

6. Kim, S. and V. Gopalan, *Coercive fields in ferroelectrics: A case study in lithium niobate and lithium tantalate.* Applied Physics Letters, 2002. **80**(15): p. 2740-2742.

7. Schlarb, U. and K. Betzier, *Refractive indices of lithium niobate as a function of wavelength and composition.* Journal of Applied Physics, 1993. **73**(7): p. 3472-3476.

8. Yariv, A., *Optical Electronics in Modern Communications*. Fifth ed. 1997, New York: Oxford University Press Inc. 744.

9. Noda, J., N. Uchida, S. Saito, T. Saku, and M. Minakata, *Electro-optic amplitude modulation using three-dimensional $LiNbO_3$ waveguide fabricated by TiO_2 diffusion.* Applied Physics Letters, 1975. **27**(11): p. 19-21.

10. Wooten, E.L., K.M. Kissa, A. Yi-Yan, E.J. Murphy, D.A. Lafaw, P.F. Hallemeier, D. Mack, D.V. Attanasio, D.J. Fritz, G.J. McBrien, and D.E. Bossi, *A Review of Lithium Niobate Modulators for Fiber-Optic Communications Systems.* IEEE Jounrnal of Selected Topics in Quantum Electronics, 2000. **60**(1): p. 69-82.

11. Lines, M.E. and A.M. Glass, *Principles and Applications of Ferroelectrics and Related Materials*. Oxford Classic Texts in the Physical Sciences 2001, Oxford: Oxford University Press.

12. Gunter, P. and J.-P. Huignard, eds. *Photorefractive Materials and Their Applications 1:Fundemental Phenomena*. Topics in Applied Physics. Vol. 61. 1988, Springer-Verlag: Berlin. 296.

13. Chen, F.S., *Optically Induced Change of Refractive Indices in $LiNbO_3$ and $LiTaO_3$.* Journal of Applied Physics, 1969. **40**(8): p. 3389-3396.

14. Buse, K., *Light-induced charge transport processes in photorefractive crystals I: Models and experimental methods.* Applied Physics B: Lasers and Optics, 1997. **64**(3): p. 273-291.

15. Yasunori, F., S. Masayoshi, K. Kenji, Y. Yoshiyuki, and M. Makoto, *Optical damage resistance and crystal quality of $LiNbO_3$ single crystals with various [Li]/[Nb] ratios.* Journal of Applied Physics, 1992. **72**(8): p. 3250-3254.

16. An, X., D. Psaltis, and G.W. Burr, *Thermal Fixing of 10,000 Holograms in $LiNbO_3$:Fe.* Applied Optics, 1999. **38**(2): p. 386-393.

17. Kip, D., *Photorefractive waveguides in oxide crystals: fabrication, properties and applications.* Applied Physics B: Lasers and Optics, 1998. **67**(2): p. 131-150.

18. Bryan, D.A., R. Gerson, and H.E. Tomaschke, *Increased optical damage resistance in lithium niobate.* Applied Physics Letters, 1984. **44**(9): p. 847-849.

19. Volk, T.R., V.I. Pryalkin, and N.M. Rubinina, *Optical-damage-resistant $LiNbO_3$:Zn crystal.* Optics Letters, 1990. **15**(18): p. 996-998.

20. Edvard, P.K., G.B. Vahan, G.D. Gagik, B.G. John, and E. Sandor, *Periodically poled structures in doped lithium niobate crystals.* Journal of Applied Physics, 2002. **92**(3): p. 1544-1547.

21. Yariv, A., *Optical Electronics in Modern Communications*. 5th ed. 1997, New York: Oxford University Press Inc.

22. Fejer, M.M., G.A. Magel, D.H. Jundt, and R.L. Byer, *Quasi-phase-matched second harmonic generation: tuning and tolerances.* Quantum Electronics, IEEE Journal of, 1992. **28**(11): p. 2631-2654.

23. Houe, M. and P.D. Townsend, *An introduction to methods of periodic poling for second-harmonic generation.* Journal of Physics D: Applied Physics, 1995. **28**(9): p. 1747-1763.

24. Ming, L., C.B.E. Gawith, K. Gallo, M.V.O. Connor, G.D. Emmerson, and P.G.R. Smith, *High conversion efficiency single-pass second harmonic generation in a zinc-diffused periodically poled lithium niobate waveguide.* Optics Express, 2005. **13**(13): p. 4862-4868.

25. Yamada, M., N. Nada, M. Saitoh, and K. Watanabe, *First-order quasi-phase matched $LiNbO_3$ waveguide periodically poled by applying an external field for efficient blue second-harmonic generation.* Applied Physics Letters, 1993. **62**(5): p. 435-436.

26. Ya-lin, L., L. Yan-qing, C. Xiang-fei, X. Cheng-cheng, and M. Nai-ben, *Growth of optical superlattice $LiNbO_3$ with different modulating periods and its applications in second-harmonic generation.* Applied Physics Letters, 1996. **68**(20): p. 2781-2783.

27. Shi-ning, Z., Z. Yong-yuan, S. Wen-zong, W. Hai-feng, Z. Zhi-yong, M. Nai-ben, C. Yong, and S. Xue-chu, *Field-induced periodic poled bulk using Al electrodes.* Journal of Physics D: Applied Physics, 1996(1): p. 76.

28. Myers, L.E., G.D. Miller, R.C. Eckardt, M.M. Fejer, R.L. Byer, and W.R. Bosenberg, *Quasi-phase-matched 1.064- μm -pumped optical parametric oscillator in bulk periodically poled $LiNbO_3$.* Opt. Lett., 1995. **20**(1): p. 52.

29. Koide, A., H. Shimizu, and T. Saito, *Main Cause of Surface Waveguides Formed under $LiNbO_3$ Crystal Surface during Thermal Treatment.* Japanese Journal of Applied Physics, 1997. **36**(Part 1, No. 1A): p. 239-242.

30. Capmany, J., *Simultaneous generation of red, green, and blue continuous-wave laser radiation in Nd^{3+}-doped aperiodically poled lithium niobate.* Applied Physics Letters, 2001. **78**(2): p. 144-146.

Chapter 3

Waveguide Theory and Fabrication in $LiNbO_3$

This chapter introduces the relevant waveguide theory needed to understand the processes in the later chapters. We begin with a look at the geometries of waveguide technology then a derivation of planar waveguiding parameters from Maxwell's equations to current fabrication techniques used with lithium niobate waveguides.

3.1 Waveguide Theory

3.1.1 Introduction

An optical waveguide is a device which can guide electromagnetic radiation via total internal reflection. In order to design and fabricate waveguides, an understanding of the theory behind how a waveguide propagates optical modes is required. The propagating distribution of the electric field of the wave will be affected by the structure and characteristics of the waveguide and therefore optical devices are designed for wave confinement over long distances.

A waveguide consists of a region of refractive index, or increased dielectric constant ε, surrounded by regions of lower refractive index. The most famous of these is the optical fibre which has a central core surrounded by a lower index cladding in a cylindrical geometry. There are various geometries for waveguides depending on the type of confinement and in how many dimensions. A simple waveguide with confinement in one dimension (1D) is known as a planar waveguide while confinement in 2D implies a channel waveguide. Confinement in 3D occurs in photonic crystals. For this thesis we are concerned with planar and channel waveguides fabricated in bulk crystals.

There are various types of waveguide structure available, some examples being ridge, buried and strip-loaded waveguides. Figure 3.1 illustrates some typical geometries with ridge a), planar b), buried c) and an optical fibre d). Ridge waveguides use the physical structure produced through fabrication to confine light while some waveguides change only the chemical composition of the substrate in certain regions to provide confinement. Many complex structures and devices, such as couplers and modulators, are based on channel waveguides.

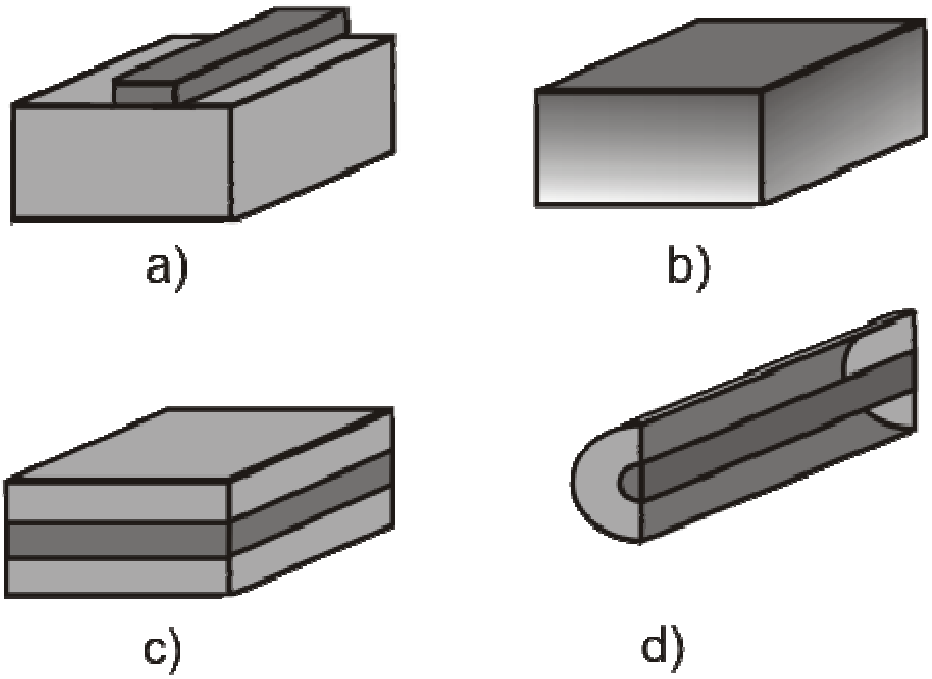

Figure 3.1: Waveguide geometries: a) ridge, b) planar, c) buried and d) optical fibre. Darker areas indicate regions of higher refractive index and hence optical mode confinement. The ridge waveguide uses physical structure for mode confinement while the planar, buried and fibre waveguide can confine the optical mode via chemical modification of the core or high index layer.

Parameters such as waveguide width and depth and dielectric constant can be adjusted to suit the incident wavelength of the light and the degree of confinement. Single mode operation offers low loss and low dispersion for easier operation of modulators and interferometers. This can be engineered by designing the diameter of the guide to operate at the required wavelength; if the guide is too small, a significant amount of power will be lost through the evanescent field crossing into the substrate. A large index change will ensure the electromagnetic fields are confined better by reducing the critical angle needed for total internal reflection and this will also reduce the guide dimensions. This summary of waveguide theory is based on several derivations that can be found in Yariv [1], Hunsperger [2] and Syms [3]. As these texts are so extensive, an abbreviated account only is given in this chapter. Section 3.2 briefly outlines the two current waveguide fabrication techniques, ion diffusion and ion exchange, that dominate waveguide production in lithium niobate.

3.1.2 Maxwell's Equations

Consider a light wave with the transverse-electric (TE) and transverse-magnetic (TM) modes transverse to the direction of propagation, which we will call the *z*-direction. TE modes have their electric field vectors, ***E***, parallel to the *y*-direction of propagation and TM modes have their magnetic field vectors, ***H***, parallel to the *y*-direction and both are normal to the *z*-direction of propagation. This section will use the geometry of an asymmetric slab waveguide as shown in figure 3.2. There are three regions designated *1*, *2* and *3*. Region *1* is usually air, region *2* the waveguide core of depth *d* (*–d/2* to *d/2*) and region *3* the substrate.

The boundary between regions 1 and 2 is at depth *d/2* and the boundary between regions 2 and 3 is at *–d/2*. The core region is defined as having $n_2 > n_3 , n_1$.

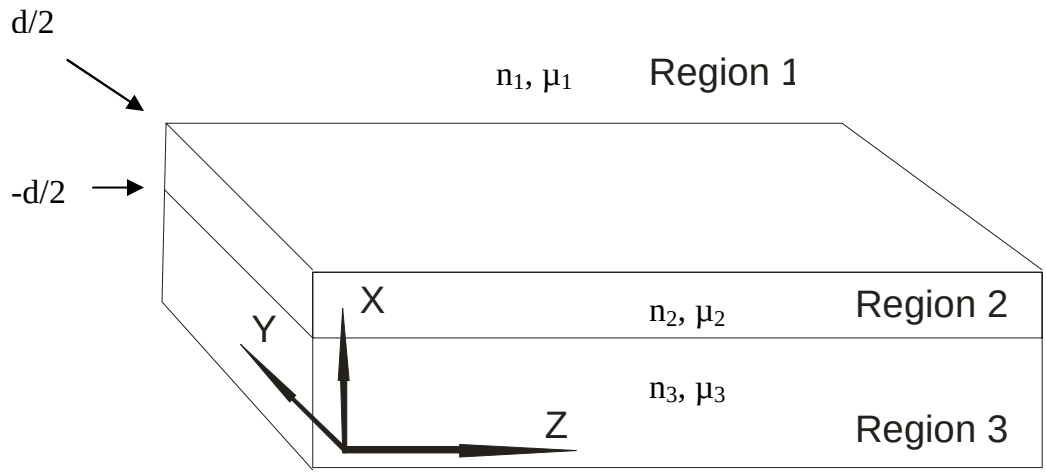

Figure 3.2: Waveguide geometry where *d* is the core depth, *n* the refractive index and *μ* the magnetic permeability of the medium.

Maxwell's equations describe the propagation characteristics of optical waves in a dielectric medium:

$$\nabla \times \underline{E} = -\mu_0 \frac{\partial \tilde{H}}{\partial t} \tag{3.1a}$$

$$\nabla \times \underline{H} = \varepsilon_0 n^2 \frac{\partial \tilde{E}}{\partial t} \tag{3.1b}$$

$$\nabla \cdot \underline{E} = 0 \tag{3.1c}$$

$$\nabla \cdot \underline{H} = 0 \tag{3.1d}$$

The other parameters are: μ_0 the permeability of free space, ε_0 the permittivity of free space and n the refractive index of the medium.

Separating the temporal and spatial variables from (Eqs. 3.1) allows simplification of the wave equation and assuming a field that is time harmonic, i.e. sinusoidal with time, travelling in the z-direction:

$$\tilde{E} = E(x, y)e^{j(\omega t - \beta z)} \tag{3.2}$$

$$\tilde{H} = H(x, y)e^{j(\omega t - \beta z)} \tag{3.3}$$

If we define $\varepsilon = \varepsilon_0 \varepsilon_r$ and $\mu = \mu_0 \mu_r$ where μ_r and ε_r are the relative permeability and permittivity for a medium and substituting (Eq. 3.2) into (Eq. 3.3) gives us the following components of the electromagnetic field:

$$\nabla \times \underline{E} = -i\omega\mu \underline{H} \tag{3.4}$$

$$\nabla \times \underline{H} = i\omega\varepsilon \underline{E} \tag{3.5}$$

$$\nabla \cdot \underline{E} = 0 \tag{3.6}$$

$$\nabla \cdot \underline{H} = 0 \tag{3.7}$$

Combining the relations (Eqs. 3.4 – 3.7) gives us the Helmholtz equation. For the TE wave (Eq. 3.8) and the TM wave (Eq. 3.9), we get the following wave equations:

$$\frac{d^2 E_y}{dx^2} + \left(k_0{}^2 n^2 - \beta^2\right) E_y = 0 \tag{3.8}$$

$$\frac{d^2 H_y}{dx^2} + \left(k_0{}^2 n^2 - \beta^2\right) H_y = 0 \tag{3.9}$$

Where $k_0 = \frac{2\pi}{\lambda_0}$ and the wave vector, or propagation constant, is $\beta = k_0 n \sin\theta$.

The values k_0 and the refractive index of medium m, n_m can also be defined as:

$$k_0 = \omega\sqrt{\mu_0\varepsilon_0} \text{ and } n_m = \sqrt{\frac{\varepsilon_m}{\varepsilon_0}} \tag{3.10}$$

3.1.3 Dispersion Equations

We will apply these wave equations to an asymmetric geometry as this structure is investigated later in the experimental work. In the direction of propagation, the z direction, the field solution is expressed (as previously) by:

$$\underline{E}(\underline{r},t) = \underline{E}(\underline{r})e^{i(\omega t - kz)} \tag{3.11}$$

The proposed TE spatial solutions are considered as a propagating solution in region *2* and evanescent solutions in regions *1* and *3*:

$$E_y(x,z) = \begin{Bmatrix} A_1 e^{-\alpha_1 x} & & x > \frac{d}{2} \\ A_2 \cos(k_x x + \Psi) & & \frac{d}{2} \geq x \geq \frac{-d}{2} \\ A_3 e^{-\alpha_3 x} & & x < \frac{-d}{2} \end{Bmatrix} e^{-ikz} \tag{3.12}$$

Where A_1 is an amplitude constant from region *1* (and correspondingly A_2 from region *2* and A_3 from region *3*) α_x is a decay coefficient for region x, k_x the transverse wave vector in the guided region, and Ψ is a phase constant describing the asymmetry of the waveguide. The coefficients k_x, α_1 and α_3 are defined as:

$$k_x = \sqrt{\omega^2\mu_2\varepsilon_2 - k_z^{\,2}} \tag{3.13}$$

$$\alpha_1 = \sqrt{k_z^2 - \omega^2 \mu_1 \varepsilon_1} \tag{3.14}$$

$$\alpha_3 = \sqrt{k_z^2 - \omega^2 \mu_3 \varepsilon_3} \tag{3.15}$$

As the boundary conditions require the ***E*** and ***H*** fields tangential to the interface to be continuous, we equate the ***H*** field with ***E*** field using (Eq. 3.16):

$$H_z(x,z) = \frac{i}{\mu_m \omega} \frac{\partial}{\partial x} E_y(x,z) \tag{3.16}$$

The *z*-component of the **H**-field within each region of the waveguide is now:

$$H_z(x,z) = \begin{Bmatrix} \dfrac{-i\alpha_1}{\mu_1 \omega} A_1 e^{-\alpha_1 x} & x > \dfrac{d}{2} \\ \dfrac{-ik_2}{\mu_2 \omega} A_2 \cos(k_x x + \Psi) & \dfrac{d}{2} \geq x \geq \dfrac{-d}{2} \\ \dfrac{-i\alpha_3}{\mu_3 \omega} A_3 e^{-\alpha_3 x} & x < \dfrac{-d}{2} \end{Bmatrix} e^{-ik_z z} \tag{3.17}$$

Again the mode is confined to the core and decays exponentially in the cladding.

To find the field amplitude coefficients, we need to solve these equations via application of the boundary conditions again. The boundary conditions state that $\boldsymbol{H}_z$ and $\boldsymbol{E}_y$ are continuous at the interfaces of the core-substrate and core-air ($x = \pm d/2$). Simplifying (Eq. 3.12) and (Eq. 3.17) via solving the field at the interfaces at $x = \pm d/2$ to state the coefficients in terms of A_2 the core coefficient, the TE solutions are:

$$E_y(x,z) = A_2 \begin{Bmatrix} \cos\left(\dfrac{k_x d}{2} + \Psi\right) e^{-\alpha_1 (x - d/2)} & x > \dfrac{d}{2} \\ \cos(k_x d + \Psi) & \dfrac{d}{2} \geq x \geq \dfrac{-d}{2} \\ \cos\left(\dfrac{k_x d}{2} - \Psi\right) e^{-\alpha_3 (x + d/2)} & x < \dfrac{-d}{2} \end{Bmatrix} e^{-ik_x z} \tag{3.18}$$

For TM solutions, with the phase constant Ψ' describing the asymmetry of the TM mode:

$$H_y(x,z) = A_2 \begin{cases} \cos\left(\frac{k_x d}{2} + \Psi'\right) e^{-\alpha_1 (x - d/2)} & x > \frac{d}{2} \\ \cos(k_x x + \Psi') & \frac{d}{2} \geq x \geq \frac{-d}{2} \\ \cos\left(\frac{k_x d}{2} - \Psi'\right) e^{-\alpha_3 (x + d/2)} & x < \frac{-d}{2} \end{cases} e^{-ik_z z} \tag{3.19}$$

Hence the guidance condition for TE solutions at $x = d/2$ is:

$$\frac{k_x d}{2} + \Psi = \tan^{-1}\left(\frac{\mu_2 \alpha_1}{\mu_1 k_x}\right) \tag{3.20}$$

And at $x = -d/2$:

$$\frac{k_x d}{2} - \Psi = \tan^{-1}\left(\frac{\mu_2 \alpha_3}{\mu_3 k_x}\right) \tag{3.21}$$

Combining the two conditions to produce the mode guidance condition for TE and TM modes:

$$2k_x d - \phi_1^{TE} - \phi_3^{TE} = 2p\pi \tag{3.22}$$

$$2k_x d - \phi_1^{TM} - \phi_3^{TM} = 2p\pi \tag{3.23}$$

Where $p = 0, 1, 2, \ldots$ is the mode number and:

$$\phi_m^{TE} = 2\tan^{-1}\left(\frac{\mu_2 \alpha_m}{\mu_m k_x}\right) \tag{3.24}$$

$$\phi_m^{TM} = 2\tan^{-1}\left(\frac{\varepsilon_2 \alpha_m}{\varepsilon_m k_x}\right) \tag{3.25}$$

Where *m* denotes either region *1* or *3*. The phase terms, ϕ_m^{TE} and ϕ_m^{TM}, are due to reflections at the core-substrate interfaces. Each value of *p* corresponds to a guided mode and from this the number of guided modes can be found for a particular guide. Figure 3.3 illustrates the electric field (Eq. 3.18) for a TE guided mode at three different wavelengths for a 3.5 µm wide arbitrary symmetric waveguide with substrate index n_s = 1.6 and guide index n_g = 1.615. Decreasing the wavelength increase the number of modes and increases the mode confinement.

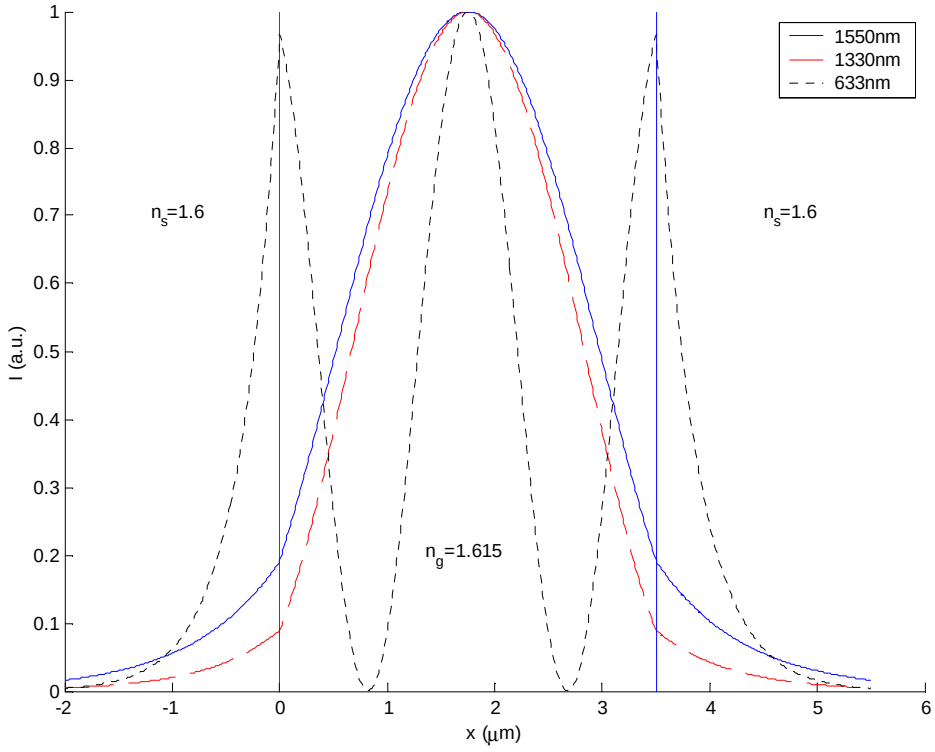

Figure 3.3: E-field profiles for TE mode arbitrary waveguide with different wavelengths.

The cut-off condition, the point at which the confinement of the electric field tends to zero, for a particular frequency can be found by:

$$\left(\frac{k_0 h}{2}\right)\sqrt{n_2^2 - n_1^2} = \frac{\nu\pi}{2} \tag{3.26}$$

Where h is the waveguide width and ν corresponds to the mode number. For the lowest order mode, $\nu = 1$. Via this relation, a waveguide can be designed to guide only a single mode by using the cut-off condition:

$$h < \frac{\lambda_0}{2\sqrt{n_2^2 - n_1^2}} \tag{3.27}$$

3.2 Waveguide Fabrication

3.2.1 Introduction

Fabrication of waveguides in $LiNbO_3$ owes much to technology developed for the semiconductor industry. Many processes used to create semiconductor devices, such as lithography and impurity doping, can be easily transferred to lithium niobate. The main process through which an index change can be achieved in lithium niobate is through doping the crystal with impurities. Many techniques exist with the two most common summarised in the next chapter, namely ion diffusion and ion exchange.

3.2.2 Ion diffusion

The diffusion of ions into a lithium niobate substrate requires depositing a thin layer (~100nm) of a dopant on the substrate, typically with a mask, and heating to temperatures of 850°C - 1000°C in an inert atmosphere for a time of the order of hours. Over this time, the dopant ions will diffuse into the substrate in a well understood manner [4]. For

long diffusion times in which the dopant is defined as depleted, the concentration profile becomes a Gaussian function:

$$C(x.t) = \frac{N_{tot}}{2\sqrt{\pi Dt}} e^{\left(-\frac{x^2}{4Dt}\right)} \tag{3.28}$$

For shorter diffusion times, where the dopant is defined as an unlimited source, the dopant profile has an *erfc* function:

$$C(x,t) = C_s erfc\left(\frac{x}{2\sqrt{Dt}}\right) \tag{3.29}$$

The adjustment of the diffusion time and temperature allows good control over the concentration profile and hence the resultant index profile.

Metal in-diffused lithium niobate substrates were first fabricated in 1974 by Schmidt and Kaminow [5]. The choice of transition metals, such as Ni, V, Ti and Cr, for the dopant has long been known to offer the best optical confinement due to the size of the refractive index change induced. Schmidt and Kaminow [5] identified early that titanium ions demonstrated the greatest refractive index change; an increase of 0.04 was observed when a 50nm Ti_2O layer was in-diffused at 960°C for six hours. Titanium increases both ordinary and extra-ordinary refractive indices, allowing guidance of both TE and TM modes within the guide and the electro-optic properties of the crystal are unaffected by the diffusion process. Increasing the diffusion temperature increases the speed of diffusion but the diffusion temperature should be kept below the Curie temperature (~1210°C) as beyond this, the crystal becomes de-poled.

The propagation losses of titanium in-diffused $LiNbO_3$ are amongst the lowest reported for all in-diffused waveguides, and losses of less than 0.1dB/cm have been detailed [6]. Drawbacks of this method are that the waveguides suffer from the photorefractive effect with visible light, but this can be reduced using thermal fixing [7] or using a doped

substrate, for example MgO:$LiNbO_3$ [8]. The high temperatures needed for Ti in-diffusion can induce out-diffusion of lithium ions from the substrate, causing unwanted surface guiding. This can be significantly reduced by diffusion in a water vapour atmosphere [9].

Zinc has been demonstrated to have a higher threshold for optical damage [10], than that of titanium in-diffused waveguides in congruent $LiNbO_3$. The temperature required for zinc in-diffusion is lower than for titanium at between 550°C - 950°C so the possibility of lithium out-diffusion is thereby reduced. The increase in quality of these guides is due to the technique of diffusion using a zinc-vapour atmosphere. Losses of ~<1dB/cm have been reported for single-mode zinc in-diffused TE/TM waveguides at 1550nm [11].

Nickel in-diffusion allows the choice of TM or TE polarization subject to fabrication conditions. It has been demonstrated that low diffusion temperatures (~650°C) guide TM polarizations only, while higher diffusion temperatures (~900°C) guide TE polarizations only [12]. Nickel in-diffusion temperatures are lower than titanium so it does not suffer from out-diffusion of lithium and the electro-optic coefficients are maintained. The limitation of nickel is that the losses are higher than for titanium in-diffused waveguides at 0.7dB/cm for the ordinary mode and 1.4dB/cm for the extra-ordinary mode.

Active waveguide devices have been fabricated by in-diffusing active ions such as erbium, and neodymium. Hempstead et al. demonstrated Nd lasing in Ti:$LiNbO_3$ with an efficiency of 55% [13] and a cw Er diffused $LiNbO_3$ waveguide laser was first fabricated by Brinkmann [14].

Despite some drawbacks, titanium in-diffusion remains the commercial choice for $LiNbO_3$ waveguides due to its low propagation losses for each mode and the fact that electro-optic properties of the crystal are unaffected by the diffusion process.

3.2.3 Ion Exchange

Ion exchange involves submerging a $LiNbO_3$ substrate into an ampoule with a bath of an ion donator with a gradual replacement of host ions in the crystal with external ions. The change in composition of the substrate causes an increase in refractive index, allowing guiding. To obtain channel waveguides, a mask is usually placed on the surface beforehand to spatially confine the exchange. The thickness and depth of the guide can be determined by the exchange time and the temperature while the index change can be controlled by the concentration of the donator.

In 1975 Shah initially used silver ions to exchange [15] but although a high index difference was produced, TM modes were guided only and had high propagation losses of 6dB/cm. It was later realised that acids were ideal proton donators, offering high ion exchanges at low exchange temperatures and a large increase in refractive index.

First synthesised by Jackel *et al*. in 1982, proton exchange replaces lithium ions in the crystal with hydrogen ions [16]. The result is an increase in the extraordinary refractive index and a slight decrease in the ordinary refractive index, forming a step-like guiding region for TM polarised beams only in x and z cut crystals. There is an increase in resistance to optical damage compared to titanium diffusion.

Benzoic acid was realised to be one of the best donors in the early stages of this technique. The chemical reaction for the exchange is given as:

$$C_6H_5COOH \leftrightarrow C_6H_5COO^- + H^+ \tag{3.30}$$

This first step generates the protons needed for the exchange which occurs when the protons dissociate from the benzoic acid at a temperature near the boiling point of the acid, around 300°C. The number of protons available is only dependent on temperature. The actual exchange is an equilibrium reaction:

$$LiNbO_3 + xH^+ \leftrightarrow Li_{1-x}H_xNbO_3 + xLi^+ \quad (3.31)$$

It has been found that by adding traces of lithium (in the form of a salt, lithium benzoate for example) into the acid melt to buffer it, the strength of the acid can be reduced allowing a softer exchange. Previously up to 70% of lithium ions were replaced by hydrogen ions, causing damage to the crystal [17]. Another salt that can be used is lithium nitrate; the lithium ions dissociate in the melt, reducing the concentration of protons.

A simple proton exchange reduces the electro-optic properties of the crystal. A post-exchange anneal (APE) has the effect of graduating the refractive index profile and repairing some of the damaged electro-optic properties of the crystal incurred from the exchange [18].

Magnesium-oxide-doped proton-exchanged $LiNbO_3$ shows similar characteristics to undoped PE samples with the addition of double the optical damage threshold [19]. Neodymium-doped $LiNbO_3$ has also been PE and shown to allow good fabrication of waveguides, for use as amplifiers or lasers, with losses <1 dB/cm [20]. Both of these doped substrates have little effect on the PE mechanism but have significant optical damage resistance.

Several other exchange techniques are available and include Reverse Proton Exchange (RPE) [21], which involves burying the waveguide via a second exchange to reintroduce lithium to the surface and Vapour-Phase Proton Exchange (VPE) [22, 23] which uses the proton donator in its vapour phase.

The VPE method is similar to the original PE process except the sample is just exposed to the acid vapour at ~300°C for 24 hours. The advantages of this method are that it offers a less aggressive exchange and the sample doesn't require annealing afterwards to repair the crystal's properties. VPE looks as if it will become the leading PE process as the crystal has increased resistance to photorefractive damage, one stage of fabrication is

removed, a high step index profile and non-linear coefficients that are almost unaffected. The propagation losses are reported as <0.35 dB/cm [23] and an index change of 0.11 has also been reported [24].

3.3 Conclusion

The advantages and disadvantages of the main fabrication methods are listed in table 3.1. Titanium in-diffusion and annealed proton exchange are both methods used commercially in the optoelectronics industry, depending on the application required. Polarisation specific devices may use proton exchange while for other applications titanium in-diffusion may be the more attractive process. All methods discussed above have limitations that will affect the choice of fabrication process.

Method	Advantages	Disadvantages
Ti^+ In-Diffusion	Guides both TE & TM modes. Low losses.	High temperatures required. High sensitivity to photorefractive damage. Low index change. Multi-step process.
Proton Exchange	High index change. Cheap process. Less sensitive to optical damage.	One mode guided only. Multi-step process. Post exchange annealing may be required.

Table 3.1: Advantages and disadvantages of waveguide fabrication methods

3.4 References

1. Yariv, A., *Optical Electronics in Modern Communications*. 5th ed. 1997, New York: Oxford University Press Inc.

2. Hunsperger, R.G., *Integrated Optics: Theory and Technology*. 5th ed. 2002, Berlin: Springer-Verlag. 446.

3. Syms, R. and J. Cozens, *Optical Guided Waves and Devices*. First ed. 1992, London: McGraw-Hill Book Company. 498.

4. Griffiths, G.J. and R.J. Esdaile, *Analysis of Titanium Diffused Planar Optical Waveguides in Lithium Niobate.* IEEE Journal of Quantum Electronics, 1984. **QE-20**(2): p. 149-159.

5. Schmidt, R.V. and I.P. Kaminow, *Metal-diffused optical waveguides in $LiNbO_3$.* Applied Physics Letters, 1974. **25**(8): p. 458-460.

6. Burns, W.K., P.H. Klein, E.J. West, and L.E. Plew, *Ti diffusion in Ti:$LiNbO_3$ planar and channel optical waveguides.* Journal of Applied Physics, 1979. **50**(10): p. 6175-6182.

7. Becker, R.A., *"Thermal fixing" of Ti-indiffused $LiNbO_3$ channel waveguides for reduced photorefractive susceptibility.* Applied Physics Letters, 1984. **45**(2): p. 121-123.

8. Sjoberg, A., G. Arvidsson, and A.A. Lipovskii, *Characterization of waveguides fabricated by titanium diffusion in magnesium-doped lithium niobate.* Journal of the Optical Society of America B, 1988. **5**(2): p. 285-291.

9. Jackel, J.L., V. Ramaswarmy, and S.P. Lyman, *Elimination of out-diffused surface guiding in titanium-diffused $LiNbO_3$.* Applied Physics Letters, 1981. **38**(7): p. 509-511.

10. Nevado, R. and G. Lifante, *Low-loss, damage-resistant optical waveguides in Zn-diffused $LiNbO_3$ by a two-step procedure.* Applied Physics A, 2001. **72**: p. 725-728.

11. Shigematsu, T.Y., M. Fujimura, and T. Suhara, *Fabrication of $LiNbO_3$ TE/TM Waveguides for 1.5 micron Wavelength Band by Zn/Ni Diffusion in Low-Pressure Atmosphere.* Japanese Journal of Applied Physics, 2002. **41, Part 1**(7B): p. 4825-4827.

12. Liao, Y.-P., D.-J. Chen, R.-C. Lu, and W.-S. Wang, *Nickel-Diffused Lithium Niobate Optical Waveguide with Process-Dependent Polarization.* IEEE Photonics Technology Letters, 1996. **8**(4): p. 548-550.

13. Hempstead, M., J.S. Wilkinson, and L. Reekie, *Waveguide lasers operating at 1084nm in N diffused $LiNbO_3$.* IEEE Photonics Technology Letters, 1992. **4**: p. 852-855.

14. Brinkmann, R., W. Sohler, and H. Suche, *Continuous-wave Er-diffused $LiNbO_3$ waveguide laser.* Electronic Letters, 1993. **27**: p. 415.

15. Shah, M.L., *Optical waveguides in $LiNbO_3$ by ion exchange technique.* Applied Physics Letters, 1975. **26**(11): p. 652-653.

16. Jackel, J.L., C.E. Rice, and J.J. Veselka, *Proton exchange for high-index waveguide in $LiNbO_3$.* Applied Physics Letters, 1982. **41**(7): p. 607-608.

17. Canali, C., A. Carnera, G.D. Mea, P. Mazzoldi, S.M.A. Shukri, A.C.G. Nutt, and R.M.D.L. Rue, *Structural characterization of proton exchanged $LiNbO_3$ optical waveguides.* Journal of Applied Physics, 1986. **59**(8): p. 2643-2649.

18. Suchoski, P.G., T.K. Findakly, and F.J. Leonberger, *Stable low-loss proton-exchanged $LiNbO_3$ waveguide devices with no electro-optic degradation.* Optics Letters, 1988. **13**(11): p. 1050-1053.

19. Digonnet, M., M. Fejer, and R. Byer, *Characterization of proton-exchanged waveguides in MgO:$LiNbO_3$.* Optics Letters, 1985. **10**(5): p. 235-237.

20. Li, M.J., M.P.D. Micheli, D.B. Ostrowsky, E. Lallier, J.M. Breteau, M. Papuchon, and J.P. Pocholle, *Optical Waveguide fabrication in Neodymium-doped lithium niobate.* Electronics Letters, 1988. **24**(15): p. 914-915.

21. Jackel, J.L. and J.J. Johnson, *Reverse exchange method for burying proton exchanged waveguides.* Electronics Letters, 1991. **27**(15): p. 1360-1361.

22. Masalkar, P.J., M. Fujimura, T. Suhara, and H. Nishihara, *Vapour phase proton-exchange: Technique for waveguide fabrication in $LiNbO_3$.* Electronics Letters, 1997. **33**(6): p. 519-520.

23. Rams, J., J. Olivares, and J.M. Cabrera, *High-index proton-exchanged waveguides in Z-cut $LiNbO_3$ with undegraded nonlinear optical coefficients.* Applied Physics Letters, 1997. **70**(16): p. 2076-2078.

24. Tsou, D.H., M.H. Chou, P. Santhanaraghvan, Y.H. Chen, and Y.C. Huang, *Structural and optical characterization for vapor-phase proton exchanged lithium niobate waveguides.* Materials Chemistry and Physics, 2002. **9610**: p. 1-6.

25. Destefanis, G.L., J.P. Gailliard, E.L. Ligeon, S. Valette, B.W. Farmery, P.D. Townsend, and A. Perez, *The formation of waveguides and modulators in $LiNbO_3$ by ion implantation.* Journal of Applied Physics, 1979. **50**(12): p. 7898-7905.

26. Hu, H., F. Lu, F. Chen, F.-X. Wang, J.-H. Zhang, X.-D. Liu, K.-M. Wang, and B.-R. Shi, *Optical waveguide formation by MeV H^+ implanted into $LiNbO_3$ crystal.* Optics Communications, 2000. **177**: p. 189-193.

Chapter 4

Ultraviolet CW Direct Writing in Congruent $LiNbO_3$

This chapter aims to outline previous knowledge of cw UV direct write techniques in other materials and the steps taken to apply these techniques to lithium niobate. Waveguides were fabricated in congruent lithium niobate using a variety of exposure conditions and were subsequently characterised via propagation losses, mode sizes, numerical apertures and therefore refractive index changes. More complex structures, such as s-bends and y-junctions have also been fabricated with a discussion of the waveguiding mechanism concluding the chapter.

4.1 Introduction

This brief summary of previous work is restricted to cw UV writing on planar materials as numerous papers exist on writing in optical fibres [1] and pulsed waveguide writing [2-4] which are outside the scope of this chapter; pulsed UV writing will be considered in chapter 6.

UV writing offers several advantages over conventional waveguide fabrication techniques, previously mentioned in chapter 3; it is a single-step process that does not require a clean-room environment, high temperatures or hazardous chemicals. Structures can be produced quickly, reliably and with a good degree of reproducibility with minimal human input needed as the process can be computer-controlled. Disadvantages include the serial nature of the process, which make it ideal for rapid prototyping but less desirable for large scale production.

The majority of interest in this process has been focussed on photosensitive glasses as these display the large index changes necessary for producing channel optical waveguides and more advanced structures. Direct writing of low loss optical waveguides has been demonstrated in a wide range of materials such as germanium doped silica, chalcogenide glasses, telluride glasses and polymer materials (such as PMMA) being identified as suitable waveguide substrates for use at the 244 nm wavelength. The next section will briefly outline UV writing used in other materials followed by the reasons behind selection of lithium niobate for this fabrication method.

Section 4.2 summarises the writing system used in this chapter and results of waveguides written for use at λ = 633 nm and λ = 1549 nm are presented in sections 4.3 and 4.4. Sections 4.5 and 4.6 include brief experiments on more complex waveguide structures, s-bends and y-junctions. The possible mechanisms behind waveguide formation are discussed in section 4.7; domain formation is discussed in section 4.8 with the chapter summary presented in section 4.9.

4.1.1 Ge:Doped Silica

The UV wavelength sensitivity of germanium doped silica ($Ge:SiO_2$) was discovered in optical fibre nearly thirty years ago by Hill [5]. Incident $\lambda = 244$ nm light was measured to induced a local refractive index change of $\Delta n = 5 \times 10^{-3}$ [6]. The $\lambda = 244$ nm wavelength was chosen as it lies in the absorption band of germania-oxygen defects; UV exposure creates dissociation of electrons, modifying the crystal properties and hence the refractive index [7].

The first application of this technique to planar samples used a pulsed KrF excimer laser ($\lambda = 248$ nm) to write channels into the photosensitive layer via a phasemask [8]. The photosensitive layer was composed of a SiO_2-GeO_2 core surrounded by SiO_2 cladding layers. Svalgaard simplified this method by using a cw 244 nm argon ion laser without the phasemask [9]. The silica was doped with ~ 11 mol% germanium to increase the photosensitivity of the glass and waveguides had propagation losses of ~1 dB/cm. Pre-treating the doped samples with hydrogen by means of high pressure loading [10] significantly increased the index change after irradiation. The combination of high Ge doping (~ 13 mol%) and hydrogen loading (~ 2 mol%) has led to low loss < 0.2 dB/cm waveguides with a high index change $\Delta n \sim 10^{-3}$ [11]. Other devices produced by this group include directional couplers, power splitters [12] and variable optical attenuators [13].

UV written devices in active materials have also been fabricated; writing on neodymium-doped silica has produced low threshold channel waveguide lasers [14]. Bragg gratings have also been extensively investigated in silica with a single step technique of producing gratings via two beam interference being reported [15].

4.1.2 Other Materials

Glasses have been an active area in direct writing with many different compositions having been tested. Lead silicate glass waveguides [16] which,

although they exhibit large index changes ($\Delta n \sim 3 \times 10^{-2}$), have high propagation losses of ~ 4.8 dB/cm. Chalcogenide glass waveguides display large index changes ($\Delta n \sim 10^{-3}$) and have a low propagation loss of ~ 0.2 dB/cm [17] with neodymium-doped waveguide lasers also fabricated [18]. Fluoride glasses also display a large index change ($\Delta n \sim 10^{-3}$) for guiding [19]. Apart from glasses, polymers such as PMMA [20] show promising results for UV written waveguides with high index changes ($\Delta n \sim 10^{-3}$) and propagation losses of ~ 1 dB/cm.

4.1.3 Lithium Niobate

Lithium niobate was identified as a possible candidate suitable for UV writing due to its high absorption at wavelengths shorter than the absorption edge. Mailis [21] observed that using a frequency-doubled Ar^+ laser at λ = 244 nm, surface structures could be directly fabricated on lithium niobate that resisted chemical etching and offered the potential to write waveguides on the material due to a small change in the extraordinary refractive index (n_e) on +z face congruent crystals.

Due to the high optical absorption of lithium niobate at ultraviolet wavelengths, as shown in the transmission vs. wavelength curve in figure 2.4, it is only possible to fabricate surface structures. Mamedov has studied the absorption coefficient in the VUV region [22] and the optical penetration depth at λ = 244 nm is 14.9 nm, severely limiting the depth of structures.

4.2 The Writing System

Direct writing in lithium niobate was achieved using a *Coherent Innova FreD* argon ion laser which used the technique of intra-cavity frequency doubling through a barium borate (BBO) crystal to produce continuous wave light of λ = 244 nm with a maximum output power of 120 mW. A schematic of the system is shown in fig. 4.1.

The 0.5 mm beam radius output was initially expanded by a concave lens, L1 (f = -100 mm), and then collimated by a convex lens L2 (f = 200 mm), to achieve a beam width of 8 mm; the beam was spatially filtered with the pinhole P to obtain an approximately Gaussian intensity profile. The final lens, L3 (f = 30 mm) focuses the beam to a radius of approximately 4 μm. With a direct writing set up, it is often difficult to see where an incident beam is at focus and for this reason, an interferometric system was added via a wedge to observe the focal point [23]. When the writing beam is at focus straight lines are observed on the screen while off focus, curved fringes are observed.

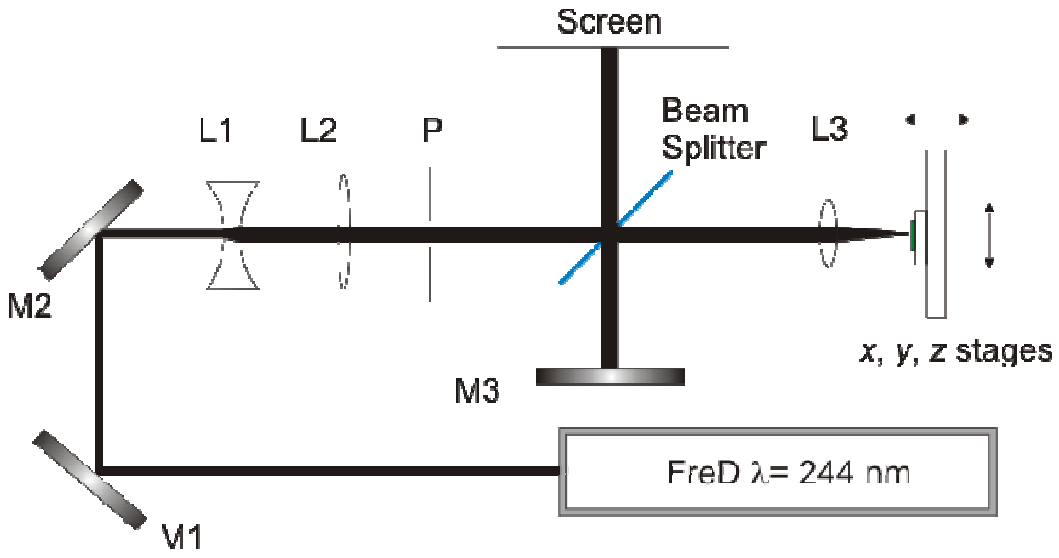

Figure 4.1: Writing system setup, including 244 nm cw FreD laser, components (M = mirror, L = lens, P = pinhole) and the *x, y, z* computer controlled translation stages on which the sample is held in place by a vacuum mount. The interferometric system consists of mirror 3, the beam splitter and the observation screen.

The sample was held in place by a vacuum mount on the *x*, *y* and *z* stages. Optical power was adjusted by changing the laser current and was measured before the lens L3. The two other main writing parameters of the system, spot size and velocity, were computer controlled by using a set of moving *x*-*y*-*z* precision stages (Aerotech Inc). The stages were controlled by a user-programmed set of commands written in the Unidex 600II programming language.

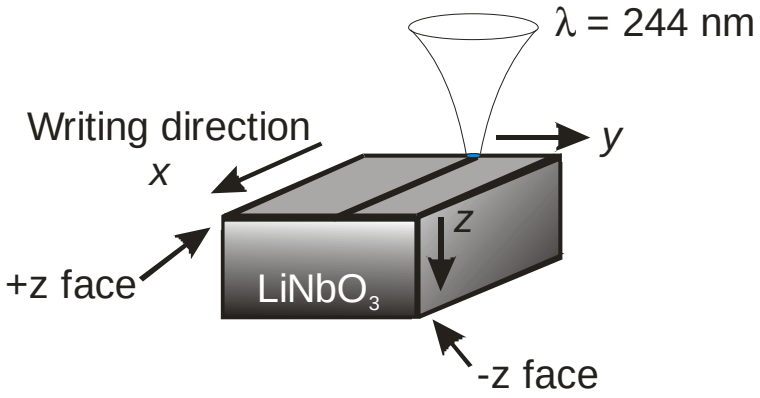

Figure 4.2: UV Direct writing of channel waveguides at λ = 244 nm on *z*-cut lithium niobate.

The set up was used to write channel waveguides principally on *z*-cut crystals, in the *x*-direction, as shown in fig. 4.2. The spot size was adjusted by moving the translation stages in the *z* direction, away from the focussing lens L3, and effectively defocusing the beam; the velocity was adjusted by moving the stages in the + and –*x* directions at velocities in the range 10 – 800 mm/min.

4.3 Single Mode Waveguides at λ = 633 nm

Single-mode waveguides were written into single-crystal 0.5 mm thick +*z*-cut $LiNbO_3$ 3" diameter wafers manufactured by Crystal Technology[1] with two beam radii: 1.75 and 3.25 μm, the laser power range was 20 - 120 mW and the beam velocity ranged from 50 to 800 mm/min. Characterisation was performed by butt-coupling optical fibre to a polished end-face and illuminating with λ = 633 nm light and the intensity profile was recorded with a CCD camera and the waveguide output power via a silicon detector.

TM only polarised light was observed on +*z* cut crystal implying an increase in the extraordinary refractive index, n_e. Propagation losses measured for 10 identically written waveguides range from ~ 0.7 to ~ 2.0 dB/cm [24] and this variation was due to several factors, principally, polishing imperfections in the end face of the crystal. Several of these guides were also exposed to high

[1] Crystal Technology Inc., 1040 East Meadow Circle, Palo Alto, CA 94303-4230. USA.

intensity visible light causing photorefractive damage. There was also a mismatch between the radius of the waveguide (3.25 μm) and the radius of the fibre (4.5 μm) used, reducing the optimal coupling achievable. The change in refractive index was deduced via numerical aperture measurements to be ~ 6 x 10^{-4} using the method outlined in section 4.4.5.

An important result of this fabrication method was the confirmation that the writing process had little affect on the crystal structure at low intensities. A single-mode fibre was butt-coupled to the waveguide and the λ = 633 nm output was monitored with a silicon detector over 35 minutes to measure any output decay. The output power degraded exponentially with time, showing that the waveguide was suffering from photorefractive damage as shown in fig. 4.3. The lifetime (time to reduce to 37% I_0) under visible irradiation is ~ 62 minutes, however, the observation of photorefractive damage indicates the crystal was still electro-optic.

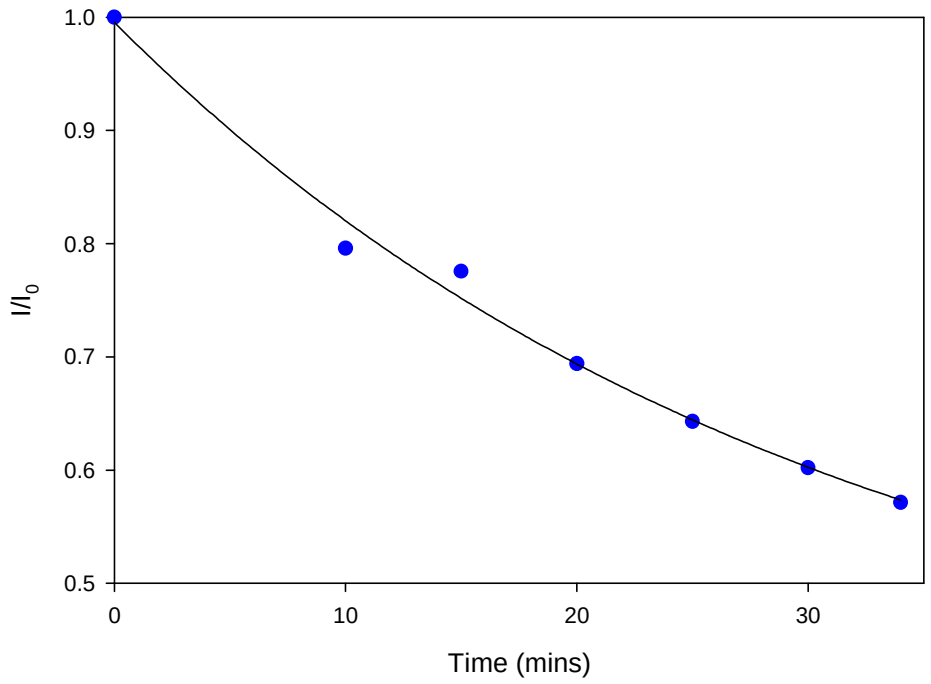

Figure 4.3: Effect of photorefractive damage on UV written +z cut $LiNbO_3$ channel waveguides illuminated with λ = 633 nm and fitted with an exponential decay, indicating a lifetime of ~ 62 minutes.

The photorefractive effect is common to all lithium niobate waveguides, although the proton exchange method as mentioned in chapter 3 is more resistant than others, so this was an expected result. As direct writing has been shown to produce promising waveguides at λ = 244 nm, efforts moved to designing waveguides for use at longer wavelengths unaffected by the photorefractive effect.

4.4 Single Mode Waveguides at λ = 1549 nm

The direct write method outlined above has been applied to fabricate waveguides for operation at λ = 1549 nm, for use in the third telecoms window. A second, lower power *FreD* laser was used for these experiments, which although still operated at λ = 244 nm and used the same set up as fig. 4.1, the output power was reduced to a maximum of 55 mW incident on the sample and the smallest beam radius possible was 4 μm. All congruent lithium niobate samples in this chapter were obtained from Crystal Technology and waveguides were fabricated from 0.5 mm thick 3" diameter congruent single-crystal wafers with a stoichiometry of 48.4 mol% Li_2O.

4.4.1 Physical Characteristics

The incident power on the sample surface ranged from 5 mW to a maximum of 55 mW. Visual inspection via an optical microscope showed surface damage for powers above 30 mW; fig. 4.4 is an example of surface damage of a waveguide written at maximum incident power (55 mW). Variation of beam velocity from 10 mm/min to 200 mm/min resulted in little observable change in optical damage over the entire range.

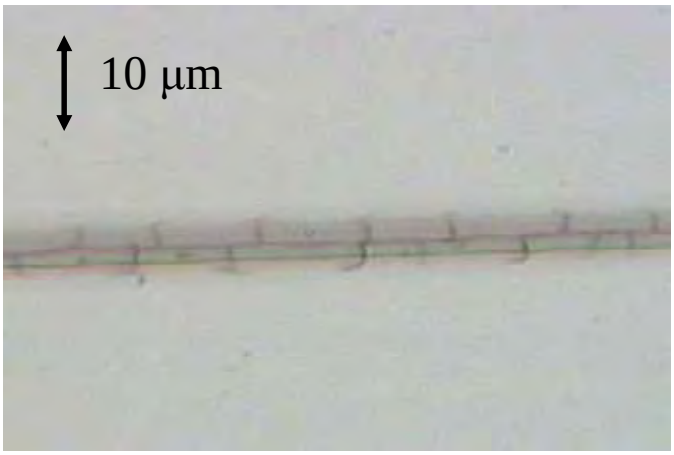

Figure 4.4: Optical microscope image of surface damage of single UV written channel waveguide written at a writing power of 55 mW, beam velocity of 50 mm/min and spot radius of 4 μm on +z congruent lithium niobate.

Micro-Raman spectroscopy can identify if a material is amorphous or crystalline via presence of peaks in the spectrograph and these peaks give information about phonon modes in the crystal but this is outside the scope of this chapter – Raman data is used here to show UV irradiated areas undergo small changes in structure compared to unexposed areas. Experiments[2] have shown that low intensity irradiated regions are still crystalline and crystal quality has not been greatly affected by the writing process for writing powers below the melting point and retains its crystallinity above the writing power needed for surface melting P_m.

Fig 4.5 illustrates the Raman spectra taken at a wavelength of λ = 633 nm of the congruent lithium niobate substrate, obtained as a reference, and a UV written channel waveguide written at a writing power 1.2 P_m and shows that the UV irradiated region still shows a high degree of order in the crystal, similar to the spectrum of the non-irradiated substrate region. The decrease in intensity is estimated to be due to the fact the UV irradiated surface region had been subjected to a small degree of amorphisation due to surface melting.

[2] Undertaken in collaboration with Dr. Jeff Scott, Optoelectronics Research Centre, University of Southampton & myself.

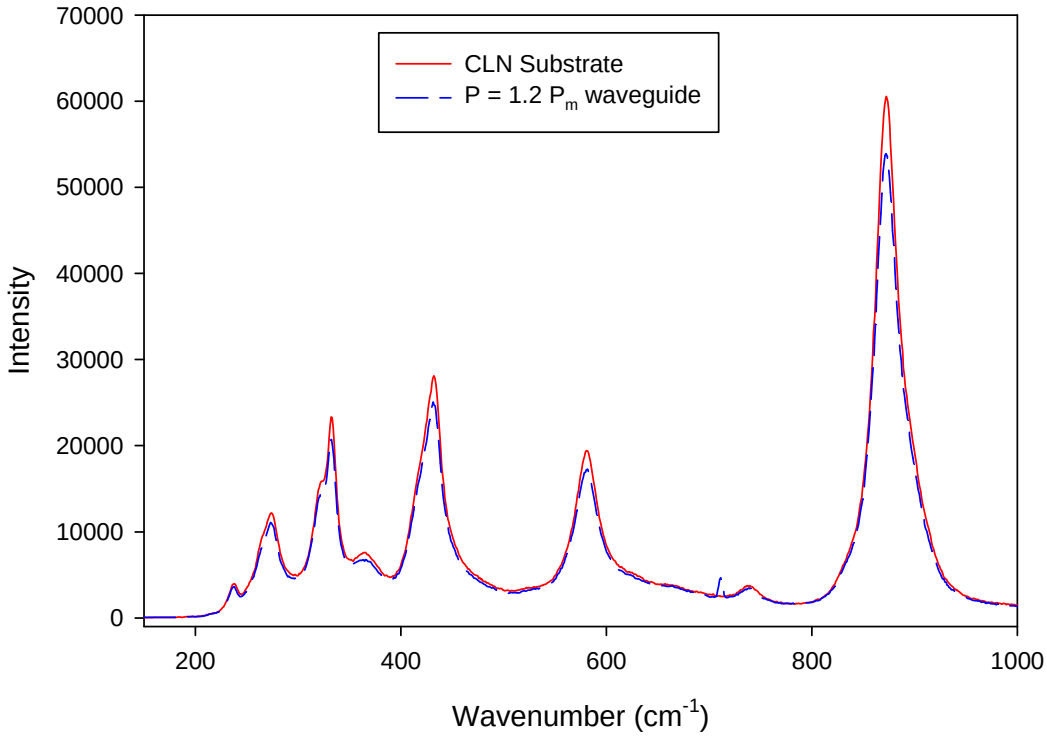

Figure 4.5: Raman spectra of congruent lithium niobate substrate and UV written channel waveguide written at a writing power 1.2 P_m, beam velocity 50 mm/min and spot radius 3 µm.

4.4.2 Optical Characteristics

By varying the incident writing power on the *z*-cut crystal, the change in waveguide quality was apparent. Initial experiments concentrated on the effect of waveguide formation by adjusting the incident writing power. The writing power ranged from 5 to 55 mW (the maximum power available) and a constant beam velocity of 50 mm/min with a spot radius of 4 µm was used. Both *x* and *y* cut samples of congruent lithium niobate were also investigated in an attempt to fabricate channel waveguides but no change in refractive index has been observed on these crystal axes under any conditions as summarised in table 4.1.

Crystal Cut	Face	Index Change	Mode
Z	+	Yes	TM
	-	Yes	TM
Y	+	No	--
	N/A	--	--
X	+	No	--
	N/A	--	--

Table 4.1: Waveguide fabrication conditions in congruent $LiNbO_3$ for three different crystal cuts and faces. The abbreviation (N/A) indicates face unavailable for experiment due to unpolished surface.

Writing powers below the 30 mW melting threshold on the +*z* face crystal resulted in very small changes in refractive index ($\Delta n \sim 10^{-4}$) and hence a diffuse mode profile; below 20 mW, an extremely weak index change was observed ($\Delta n < 10^{-5}$). From 20 to 30 mW a slight increase was observed guiding a weak waveguide mode. Fig. 4.6 shows briefly the difference in waveguide modes over the entire writing power range against the expected refractive index change and power vs. index is expanded in section 4.4.4.

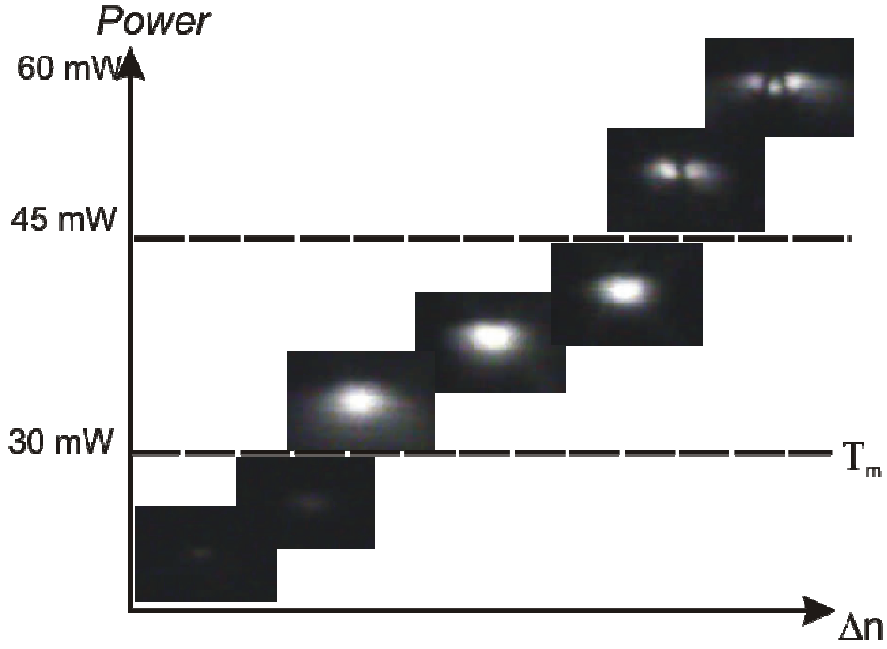

Figure 4.6: UV writing power conditions for waveguides in congruent $LiNbO_3$ characterised at λ = 1549 nm for a spot radius of 4 μm and beam velocity 50 mm/min.

Above an optical power of 30 mW, surface damage occurred and this formed a stronger waveguide that had a longer lifetime. If the optical power was higher than 50 mW, the index increase was substantial enough to form a double mode waveguide; these observations suggest surface melting was a requirement for optimal single mode UV written guides. Waveguides written on –*z* face crystals also imply surface melting is an important condition for favourable devices.

4.4.3 TE/TM

The most common waveguide fabrication method in lithium niobate, proton exchange (PE), produces polarisation specific waveguides and this polarisation dependence was tested for the UV writing technique. A fibre-coupled laser at λ = 1549 nm was fusion-spliced to a 3 dB coupler which was also fusion-spliced to a polarisation controller. Two computer controlled dual-channel power meters were used to monitor the waveguide output and the laser output simultaneously. The polarisation sensitivity of the waveguide was tested via a polarisation rotator on the 3 dB fibre coupler output, butt-coupled to the waveguide input and the waveguide output logged as depicted in fig. 4.7. The polarisation controller was adjusted to maximum output without the waveguide and the extinction ratio between the two polarisations, TE and TM, is given via Eq. 4.1.

$$r_e = 10\log\left(\frac{P_{TM}}{P_{TE}}\right) \tag{4.1}$$

The average input power to the waveguide had a 30 dB extinction ratio between TM and TE polarisation for ten identical waveguides. Figure 4.8 indicated the polarisation specificity of waveguides written on *z*-cut lithium niobate. The waveguide extinction ratio was ~ 20 dB and waveguides effectively demonstrated TM guiding only with a slight residual TE mode, possibly due to stress effects.

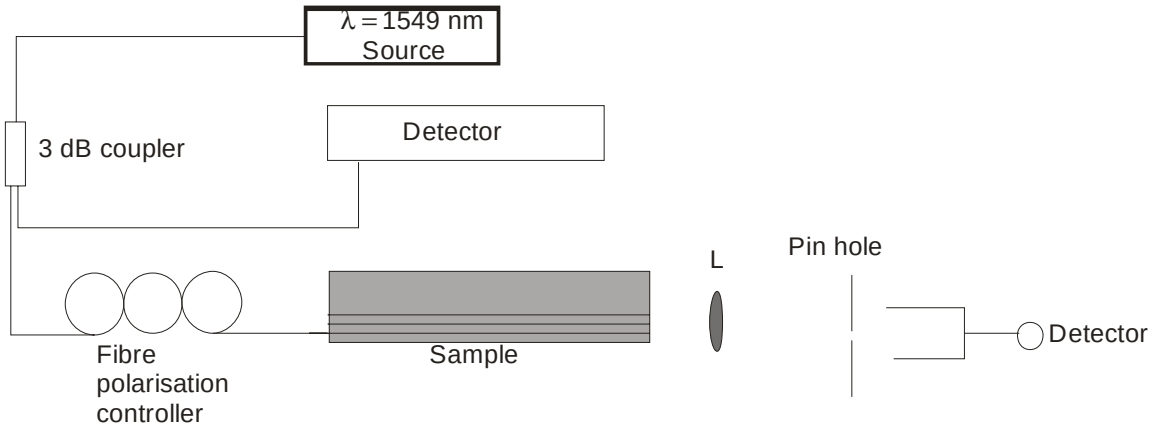

Figure 4.7: Polarisation measurement setup for waveguides on *z*-cut $LiNbO_3$.

TM TE

Figure 4.8: Mode profiles of TM and TE polarisation for a waveguide written at 45 mW, with a beam velocity of 50 mm/min and spot radius 4 μm on +*z* congruent lithium niobate.

4.4.4 Mode profiles

The profile of the waveguide output face was imaged onto a Vidicon IR camera via a microscope objective (x 10). The scale was calibrated with a graticule placed at the same focus and confirmed with ablation wells written onto the substrate. The full width half maximum (FWHM) and $1/e^2$ points of the intensity were calculated via a simple program in *Matlab* software. Mode profiles for waveguides written on +*z* and –*z* face congruent lithium niobate are given in figures 4.10 and 4.11. The mode profiles are characterised with two directions; the direction across the waveguide is denoted as the *y-direction* and the depth of the waveguide is denoted as the *z-direction* as in fig 4.9. Graticule measurements were accurate to ± 0.5 μm and mode profiles were supplemented with the standard deviation of at least ten waveguides for each writing power to identify the variance; this was repeated throughout all mode profile measurements in chapter 4 and 5.

Experiments in chapters 4 and 5 concentrated on single mode waveguides as they are most desirable for photonic applications.

Figure 4.9: Nomenclature of mode profiles used in this thesis with the z direction specifying the crystal depth and y direction the spatial direction equivalent to across the beam. The white dashed line is the crystal surface.

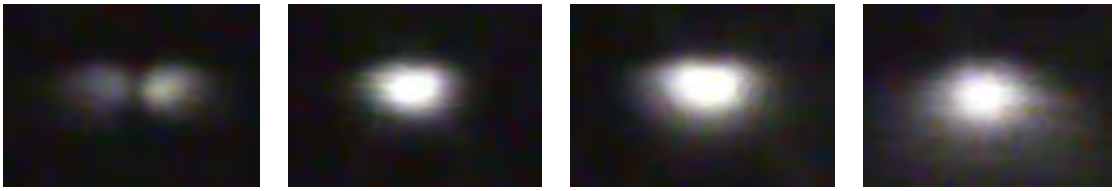

50 mW 45 mW 40 mW 35 mW

Figure 4.10: Mode profiles with variation of writing power for congruent +z $LiNbO_3$ waveguides written at 50 mm/min and a spot radius of 4 µm.

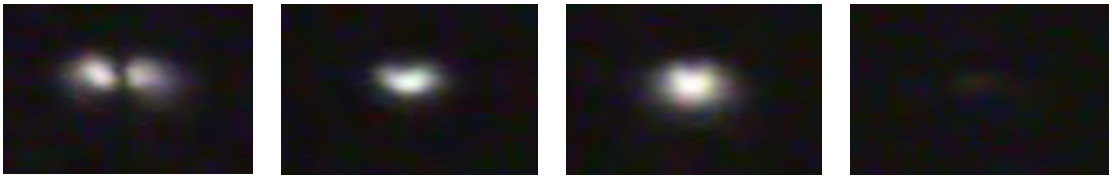

50 mW 45 mW 40 mW 35 mW

Figure 4.11: Mode profiles with variation of writing power for congruent -z $LiNbO_3$ waveguides written at 50 mm/min and a spot radius of 4 µm.

The mode profile sizes implied a greater mode confinement with increased writing power generally. Comparing the +z and –z face single mode profiles in figure 4.12, there was a greater difference in mode size in the *y* direction than in the *z* direction indicating waveguides on both faces were restricted by the shallow optical penetration depth of the incident laser. Figure 4.13 displays the relationship of increased confinement of the optical mode with increased writing power.

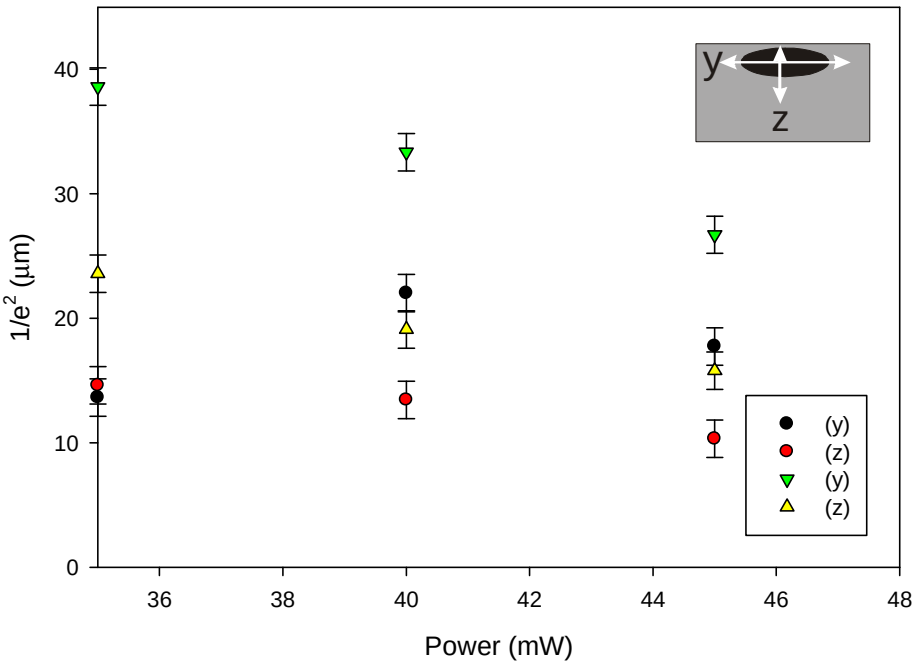

Figure 4.12: A graph to show the comparison of $1/e^2$ single mode sizes between waveguides written on the +z (triangles) and -z (circles) faces of congruent lithium niobate written at various writing powers, beam velocity 50 mm/min and spot radius 4 µm.

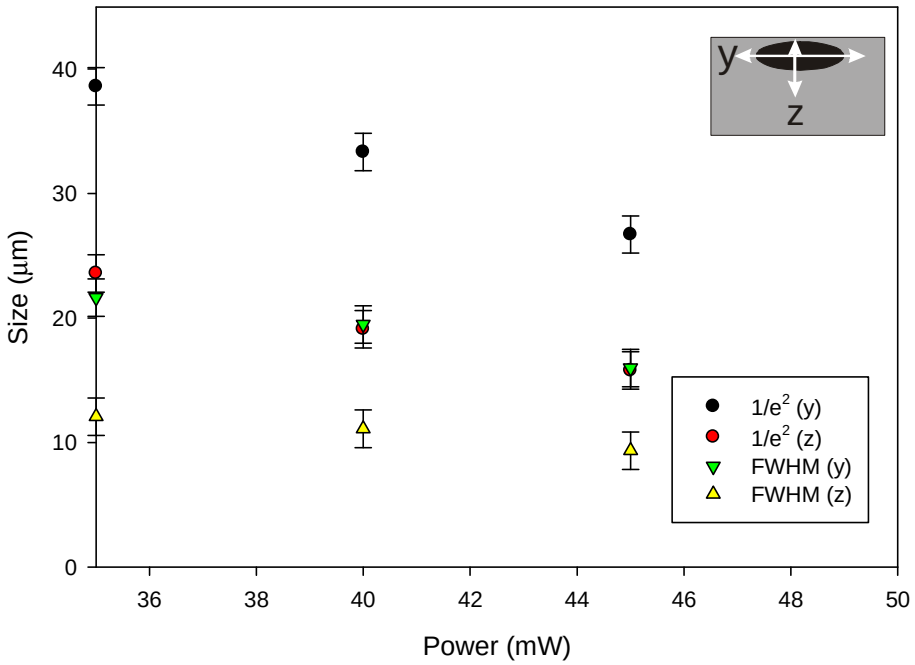

Figure 4.13: A graph showing FWHM & $1/e^2$ values of waveguides written on the +z face of congruent lithium niobate written at various writing powers, beam velocity 50 mm/min and spot radius 4 µm.

The requirement of melting has implications for the crystalline nature of the surface as it will affect the composition of the material possibly making it polycrystalline and will have a detrimental effect on the waveguiding properties by increasing propagation losses via surface scattering.

4.4.5 Numerical aperture

To measure the numerical aperture and deduce the refractive index change, methods such as prism coupling are used for planar waveguides. Prism coupling [25] was attempted but found to be too difficult due to limitations with channel waveguides of such small widths (~ 5 μm). Using the mode profile measurement obtained earlier, the numerical aperture was recorded by moving both the objective and camera to defocus the mode and recording the defocused mode size.

The numerical aperture can be calculated once the angle θ is found between the axis and edge of the defocused mode with the following equation:

$$NA = \sin\theta \tag{4.2}$$

The extraordinary refractive index at λ = 1549 nm is calculated to be 2.13 [26]. From this, the refractive index difference can also be calculated via:

$$NA = \sqrt{n_{guide}^2 - n_{substrate}^2} \tag{4.3}$$

The *NA* and Δn measurement directions are given in the same *y* and *z* directions used in the mode profile diagrams. Numerical aperture (*NA*) and subsequent refractive index difference (Δn) measurements are given in table 4.2 for UV written waveguides written at various writing powers for a beam velocity of 50 mm/min and spot size 4 μm. Measurement errors, including standard deviation, of ten waveguides are a maximum of ± 0.005 for the numerical aperture and this correspond to $\Delta n \pm 2 \times 10^{-4}$. As the mode size decreases with increasing writing

power, we saw better mode confinement and hence a larger refractive index change.

Refractive index changes from UV written waveguides compared with typical Ti:$LiNbO_3$ in-diffused single mode channel waveguides ($\Delta n \sim 10^{-3}$) are around an order of magnitude smaller so did not offer any improvement over current fabrication methods.

NA	**35 mW**	**40 mW**	**45 mW**
(*z*)	0.014	0.029	0.042
(*y*)	0.048	0.057	0.061
Δn	**30 mW**	**35 mW**	**45 mW**
(*z*)	4.6×10^{-5}	2.0×10^{-4}	4.1×10^{-4}
(*y*)	5.5×10^{-4}	7.6×10^{-4}	8.6×10^{-4}

Table 4.2: Numerical aperture and *Δn* measurements for +z congruent $LiNbO_3$ UV written waveguides at various writing powers for the *y* and *z* directions with beam velocity 50 mm/min and spot radius 4 μm.

4.4.6 Propagation Losses

There are several common techniques to measure losses in planar waveguides; cut-back and Fabry-Perot [27] being the most popular. Cut-back is the standard method for measuring propagation losses in optical fibres and was attempted for UV written channel waveguides [28]. Although successful, it is a destructive method and the limited availability of the stoichiometric, doped and lithium tantalate samples tested in chapter 5 meant it was unsuitable. The Fabry-Perot method was unsuccessfully attempted as the lack of an accurate temperature controller or variable wavelength source meant results were not reproducible.

A more appropriate loss measurement, developed by Barai [29], has been used for waveguides written for λ = 1549 nm operation and Fig. 4.14 illustrates the setup used for the propagation loss measurements. A λ = 1549 nm fibre-coupled laser was spliced to 2 x 2 3 dB fibre coupler 1; one coupler output (C) was connected to a Newport dual-channel fibre input power meter (power meter 1) and the second

output was butt-coupled to the waveguide input (A). For the second identical coupler 2, fusion-spliced at one end to the laser, one output was butt-coupled to the waveguide output (B) and the second was also connected to power meter 1 (D). The remaining two coupler outputs (F) and (E) were connected to a second power meter (2).

For the initial stage of the measurement, the laser output P_0 from coupler 1 (A) was measured before butt-coupled to the waveguide and the waveguide output optimised via measurement at coupler 2 output (E). The output of the laser was monitored with the second coupler 1 output (C).

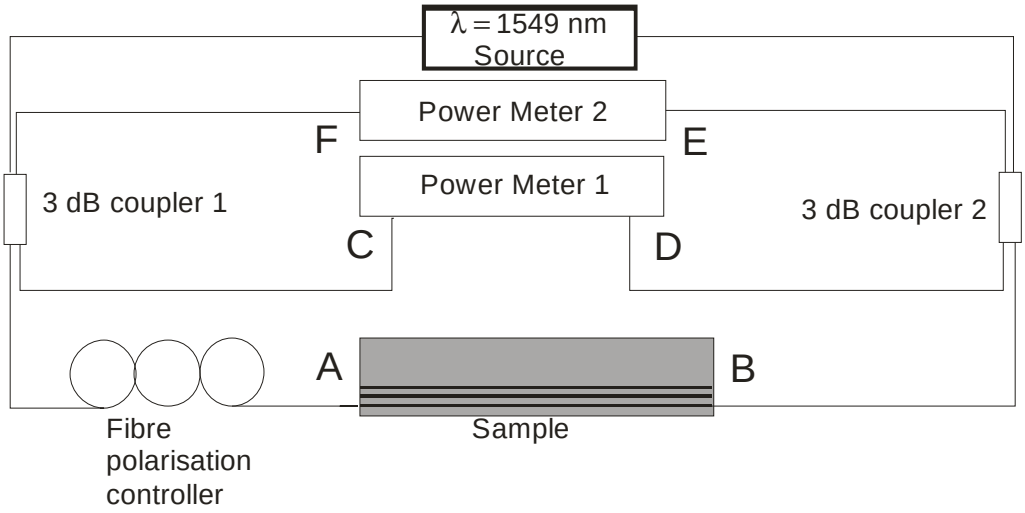

Figure 4.14: Propagation loss measurement setup with two 3 dB couplers.

Secondly, the laser input from coupler 1 was switched off with the laser input from coupler 2 switched on and coupler 2 was butt-coupled to the waveguide at point (B) and adjusted so that the output power from coupler 1 at point (E) was equal to the output power from coupler 2 at point (F). This step was to ensure the coupling coefficients from waveguide to fibre were equal. Switching off the laser input from coupler 2 and returning to a single laser input through coupler 1 only, the output power at (E) can be defined as:

$$P_E = \frac{P_0}{4} R_{fib}^2 R_{wg}^2 C_{fib-wg} C_{wg-fib} \cdot \exp(\alpha L) \qquad (4.4)$$

The coefficients in Eq. 4.4 are: the reflection coefficient at the fibre R_{fib}, reflection coefficient at the waveguide R_{wg}, coupling coefficient from fibre to waveguide $C_{fib\text{-}wg}$, coupling coefficient $C_{wg\text{-}fib}$, the loss coefficient α and the length L. The output power at point (F) is also measured:

$$P_F = \frac{P_0}{4} R_{fib}^2 R_{wg}^2 C_{fib-wg} C_{wg-fib} F_{wg} \cdot \exp(2\alpha L) \tag{4.5}$$

The coefficient F_{wg} is the Fresnel coefficient from the back reflected light. From Eqs. 4.4 and 4.5 the loss, independent of coupling conditions, could then be calculated by:

$$\alpha = \frac{1}{L} \ln\left(\frac{1}{F_{wg}} \frac{P_F}{P_E} \right) \tag{4.6}$$

To ensure a reliable measurement, the power meters were computer controlled via *Labview* software for automatic measurements over time to obtain an average power and the technique repeated again using an input from coupler 2 to minimise uncertainties. The important bonus of this method is it eliminates the greatest uncertainties, the coupling coefficients and leaves just the powers, waveguide length and waveguide Fresnel coefficient which all can be measured accurately. The total uncertainty in the loss measurement is ± 0.05 dB/cm plus the standard deviation of the propagation loss for ten identically written waveguides; this allows an estimate of the repeatability of the measurement by showing the distribution of measurement for identical waveguides. As with the measurement of mode profiles, this uncertainty is repeated in this chapter and chapter 5.

Propagation losses vs. writing power are shown in figure 4.15 and demonstrate that waveguides written on the +*z* face exhibited lower propagation losses than on the –*z* face. The loss on the +*z* face dropped slightly with an increase in writing powers with a decrease of 0.6 dB/cm from 35 – 45 mW with waveguides written at 45 mW exhibiting optimal guiding conditions. The propagation losses were high compared to other fabrication methods and both +*z* and –*z* face waveguides

exhibited losses greater than the generally accepted loss performance figure of < 1 dB/cm that is common for titanium in-diffused and proton exchanges waveguides.

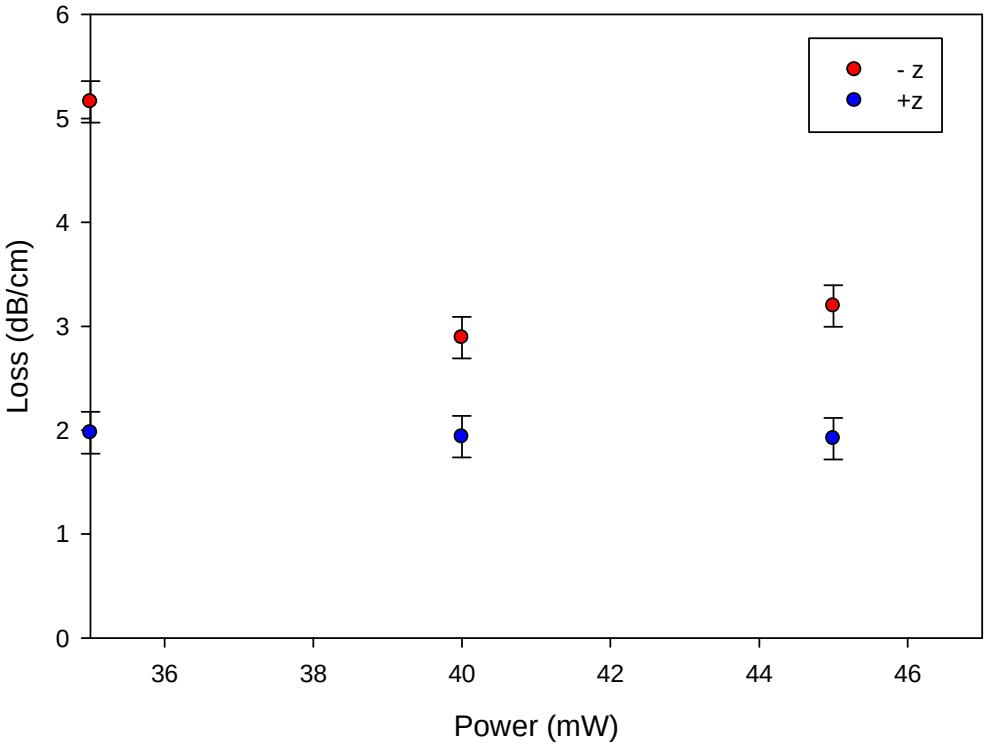

Figure 4.15: Comparison of waveguide propagation loss vs. direct UV writing power for +z and -z congruent lithium niobate with a beam velocity of 50 mm/min and spot radius 4 µm.

4.4.7 Waveguide Stability

From the original work by Mailis, UV written channel waveguides in lithium niobate were previously thought to be permanent but, after further investigation, were found to degrade over time. Lifetimes were measured by monitoring the output of the waveguide via a 3 dB coupler to a detector. The lifetime of the mode profile at an illuminating wavelength λ = 1549 nm and input power of 0.5 mW of a single waveguide written at the previously determined optimum power of 45 mW, 50 mm/min velocity and a spot radius of 4 µm is shown in figure 4.16. The formula used is Eq. 4.7 where τ is the decay constant and indicates the time until $I = 0.37\ I_0$.

$$I = I_0 \exp\left(-\frac{t}{\tau}\right) \qquad (4.7)$$

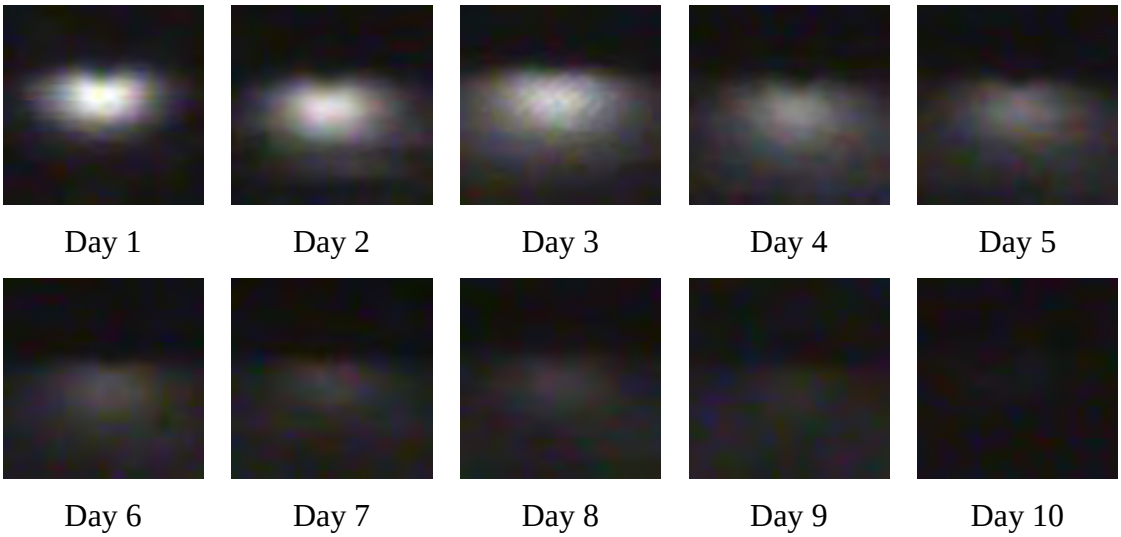

Figure 4.16: Mode profile of +*z* congruent lithium niobate waveguide, written at 45 mW and 50 mm/min and 4 μm spot radius, over 10 days.

There was a gradual decay of output power over 10 days with the mean lifetime 4.5 days as shown in fig. 4.17. Both +*z* and –*z* faces were tested; waveguides on the +*z* face did not degrade as quickly as on the –*z* face; for a waveguide written with identical writing parameters on the –*z* face, the waveguide was observed to decay to zero output power in under 24 hours.

The profile dimensions of the written guide are given in fig 4.18. An increase in *y* and *z* directions, indicating less mode confinement, was also seen as the waveguide decayed - observable in the diffuse mode profiles. The decay in the *z* direction was quicker than the *y* direction, with the mode size doubling in FWHM over 8 days, while the *y* direction plateaus over the same time period. The decay of intensity at longer wavelength suggested the index change was temporary and there may be a charge mechanism that began relaxation after the beam has passed.

This quick rate of decay implied that the use of lithium niobate for UV written waveguides was limited unless a method of stabilising the decay of Δn is found.

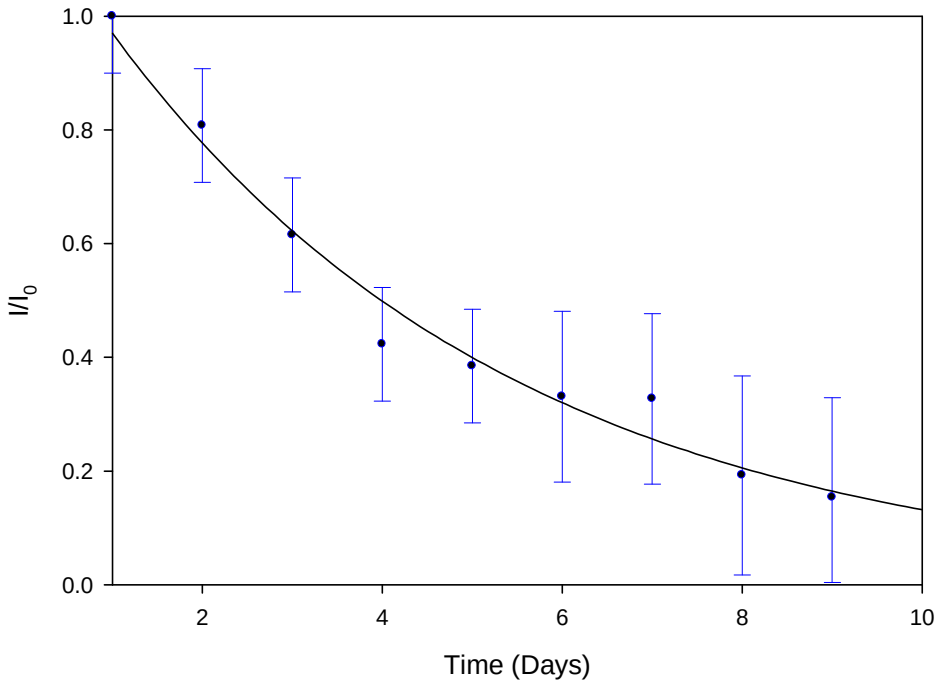

Figure 4.17: A graph to show power output/input ratio normalised to the initial output/input after writing to demonstrate lifetime of waveguide written at 45 mW on +z congruent lithium niobate with velocity 50 mm/min and spot radius 4 µm.

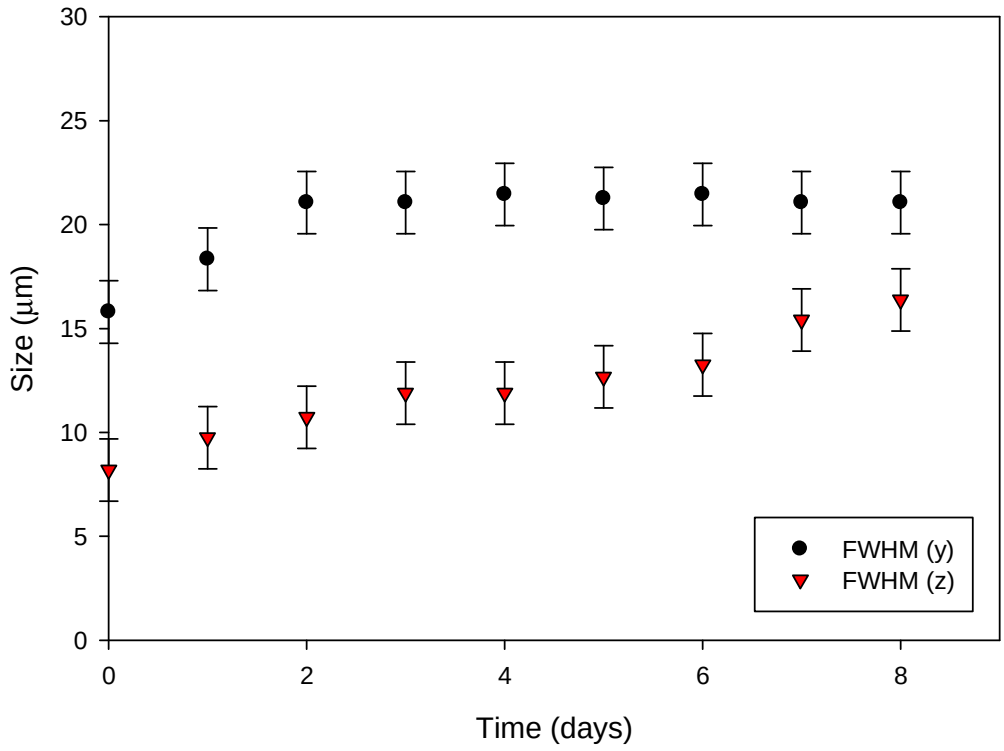

Figure 4.18: A graph to show FWHM measurements vs. lifetime of channel waveguide written at 45 mW, beam velocity 50 mm/min and spot radius 4 µm on +z congruent lithium niobate.

4.4.8 Variation of Writing Velocity

The writing velocity was tested over a range from 10 – 800 mm/min; above 200 mm/min, a wobble appeared in the written guides due to instability in the translation stages which would increase the propagation loss. Figure 4.19 illustrates the $1/e^2$ size of mode profiles vs. writing velocity for –*z* face waveguides, characterised 5 hours after writing, and shows the velocity had little effect on the characteristics of the waveguides.

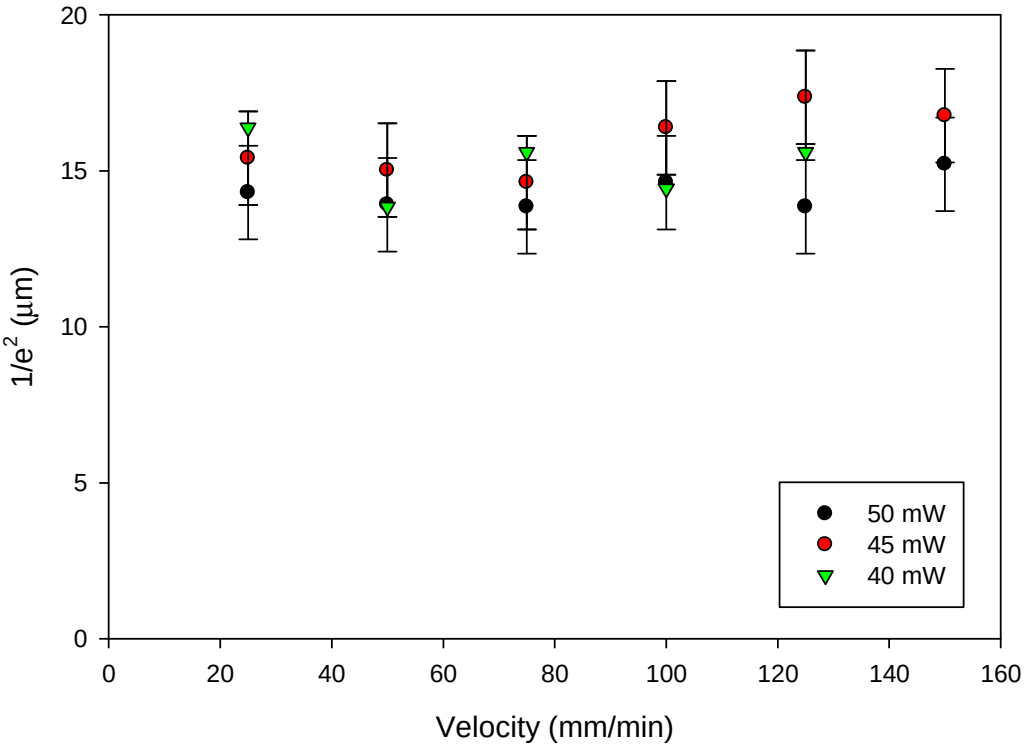

Figure 4.19: Graph of $1/e^2$ mode field depth (*z* direction) vs. writing velocity for waveguides on -*z* congruent lithium niobate written with various writing beam powers and spot radius 4 µm.

Figure 4.20 displays the propagation loss vs. writing velocity for the same –*z* sample – waveguides written at 45 and 50 mW had similar losses over the velocity range while at a lower writing power of 40 mW, the waveguide performance was more sensitive to the velocity. Similar observations of the negligible effects of writing velocity were made with waveguides written on the

+z face. The writing velocity had a much smaller effect on the optical characteristics of the written waveguides compared to the writing power.

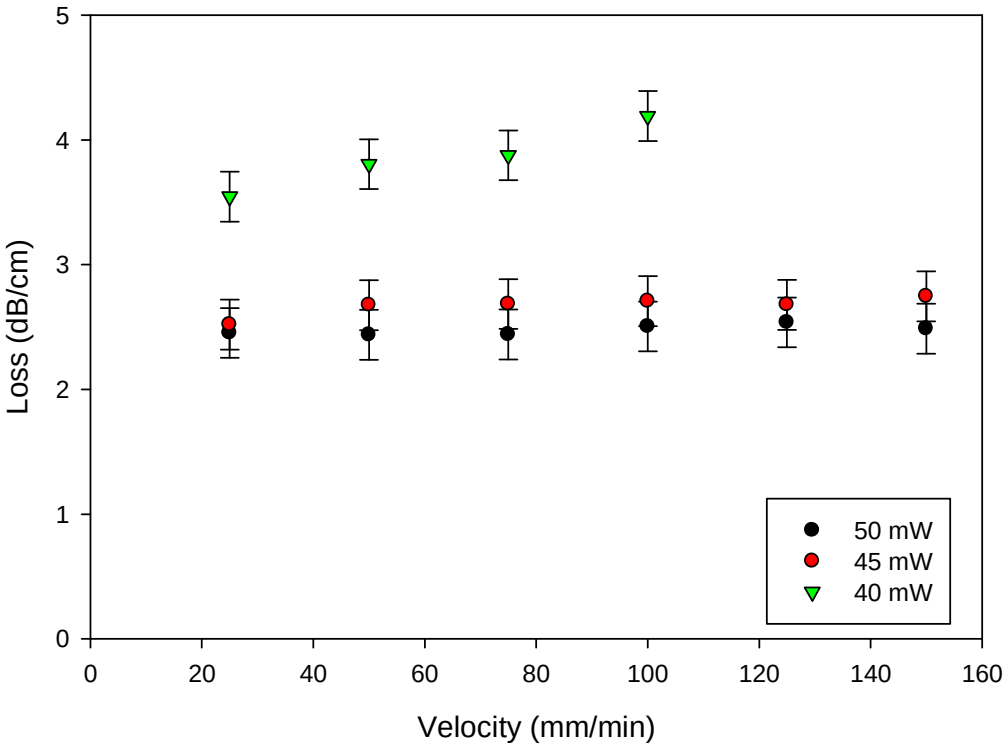

Figure 4.20: UV written propagation losses vs. writing velocity for -z congruent lithium niobate written at various writing powers and spot radius 4 µm.

4.4.9 Variation of the Waveguide Width

The diameter of the incident writing beam was adjusted by defocusing the final lens (L3) in the writing set up. Standard Gaussian beam propagation equations were used to calculate the amount of movement needed for the lens and these were checked against the size of the melted channels. The minimum beam radius, the beam waist, was 4 µm and the maximum beam size obtained by defocusing the lens was a beam radius of 8 µm.

Propagation losses vs. beam radius are shown in figure 4.21 – apart form an initial dip, increasing the beam size increases the propagation loss. Guides written at lower writing powers were more sensitive to the change in beam radius – this is

due to the intensity rapidly reducing exponentially with the radius becoming larger. Although there was a dip in the propagation losses at 40 and 45 mW and therefore greater input intensity throughput, these were offset by the increase in decay rate due to the increased beam size.

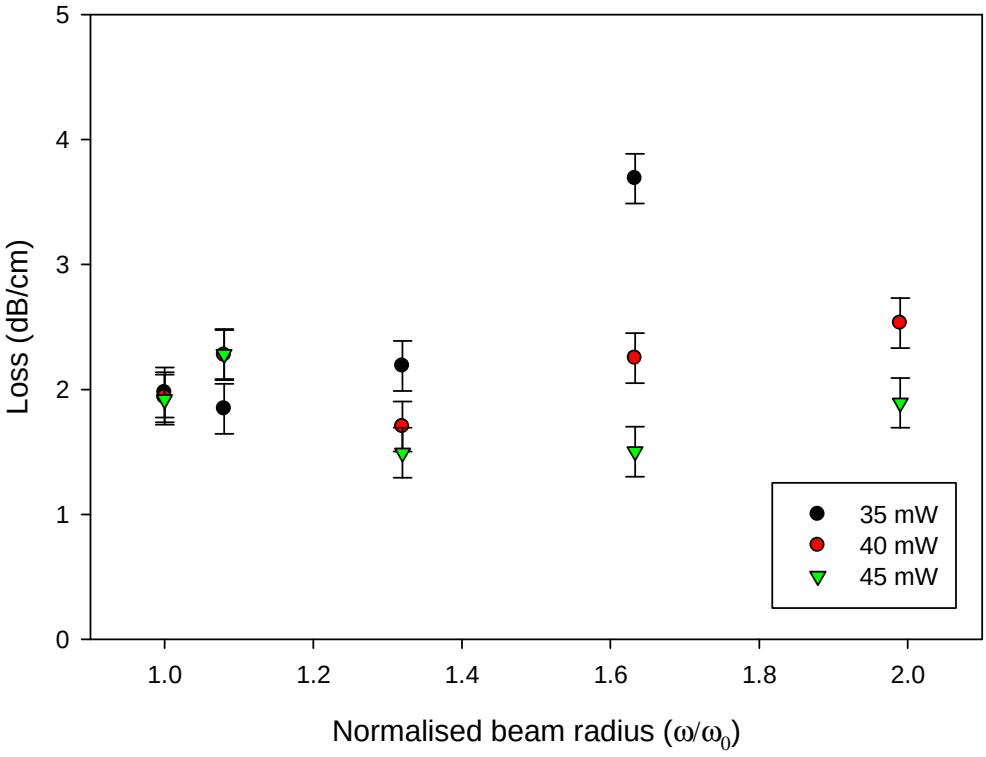

Figure 4.21: Graph of UV written propagation loss vs. normalised beam radius (ω_0 = 4 µm) for +z congruent lithium niobate written at a beam power of 45 mW and velocity 50 mm/min.

The complete set of beam profiles for +*z* and –*z* waveguides in lithium niobate are given in figure 4.22. As can be seen, the beam radius and power could be adjusted to tailor the waveguide for specific purposes – a waveguide could be fabricated for a specific size with small adjustments in writing power and focus.

The mode profile sizes with increased writing beam radius for waveguides written on +*z* and –*z* face crystals are shown in fig. 4.23 for guides written at 45 mW and 50 mm/min. As expected, the $1/e^2$ size expanded with increased beam radius. Due to the greater decay rate and decreased index change with writing off focus, the optimal beam size was the incident beam at focus and minimum waist.

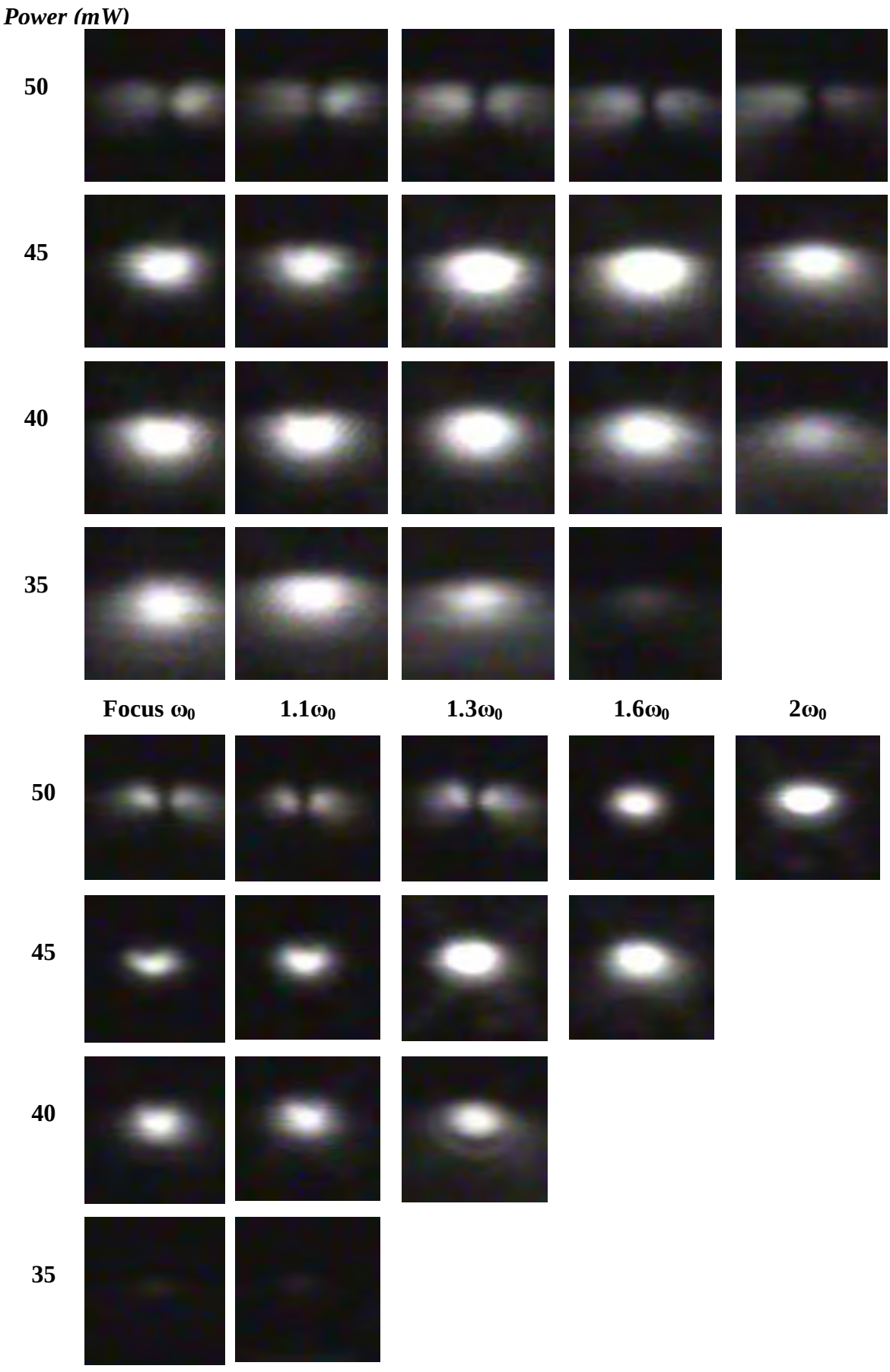

Figure 4.22: Power (mW) vs. beam radius for +*z* (above) and -*z* (below) $LiNbO_3$.

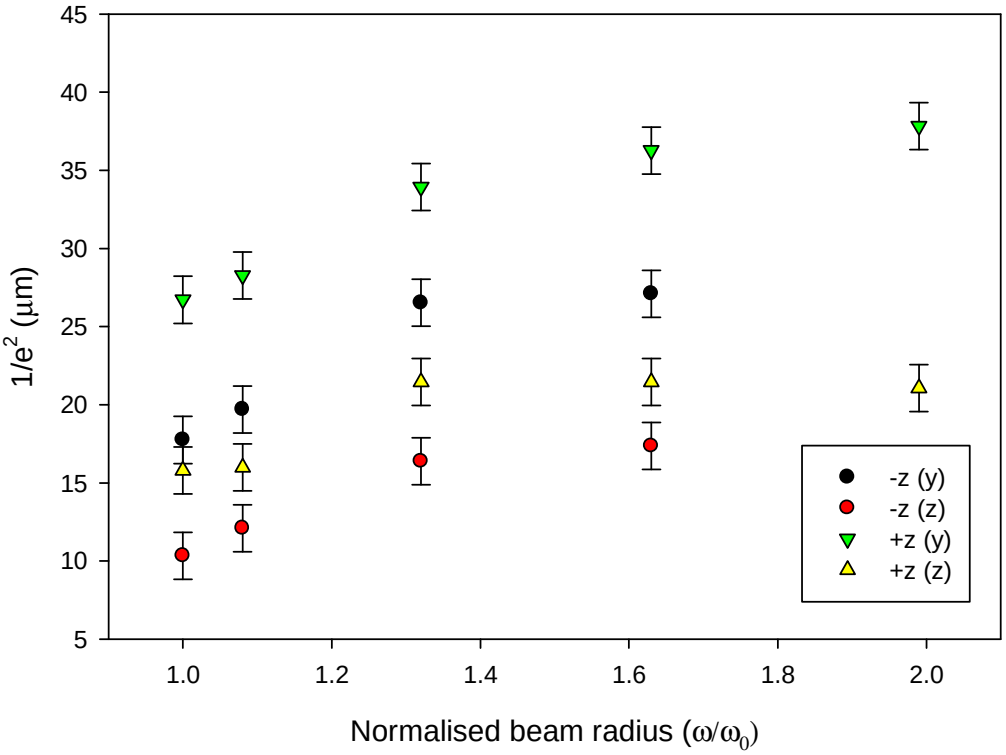

Figure 4.23: Graph of 1/e2 mode size vs. beam radius for +z (triangles) and -z (circles) congruent lithium niobate, written at power 45 mW and velocity 50 mm/min.

4.4.10 Multiple Passes

In addition to single pass writing across the substrate, multiple passes (in the *+x* and *-x* writing directions) were written to see if an improvement in waveguide characteristics appeared due to increased exposure of the writing beam. Waveguides were written on a +z congruent sample at 45 mW and at a speed of 50 mm/min with a single pass of the beam in the *+x* direction; this was followed by waveguides written with 2, 4, 6, 8 and 10 passes moving back and forward along the *x* axis. All guides were written with the same power and velocity and beam profiles at λ = 1549 nm are shown in fig. 4.24.

Immediately noticeable by the beam profiles, was an increase in the number of passes increased the size of the profile but also decreased the mode intensity of the guide. The mode sizes are shown via FWHM and 1/e2 size measurements in fig 4.25.

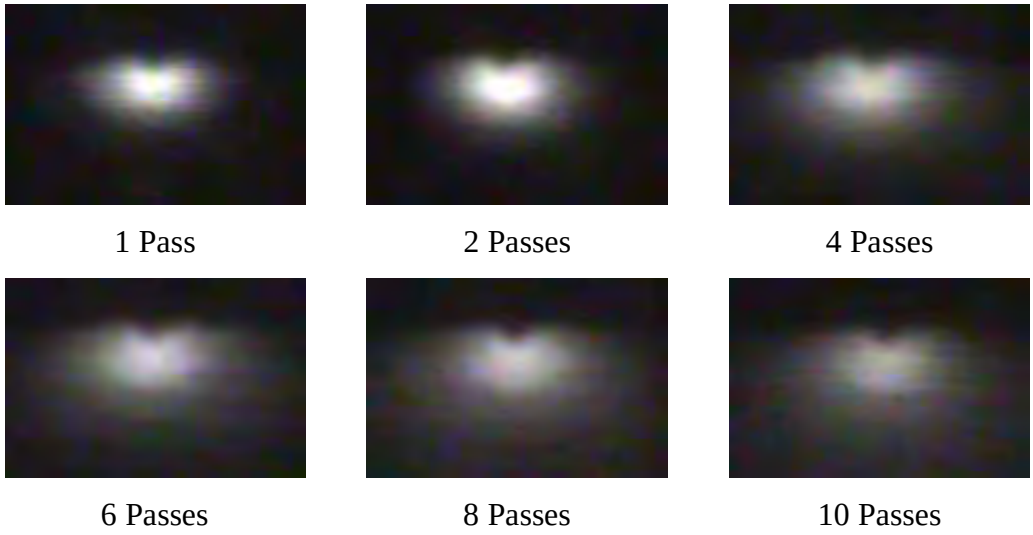

Figure 4.24: Beam profiles of multi-pass written +z waveguides starting with 1, 2, 4, 6, 8 and 10 passes at 45 mW, velocity 50 mm/min and spot radius 4 µm.

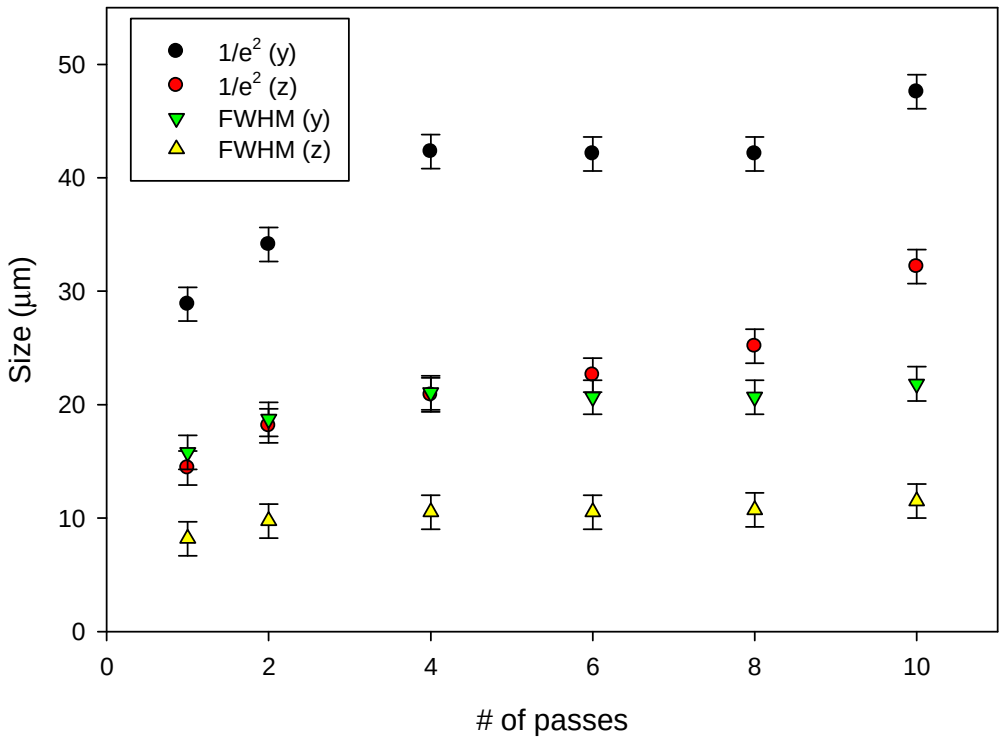

Figure 4.25: Graph of FWHM (triangles) and $1/e^2$ (circles) mode sizes for multi-pass waveguides written in +z congruent lithium niobate at 45 mW, 50 mm/min and spot radius 4µm.

A lifetime study of the multi-pass channel guides, characterised at λ = 1549 nm with an input power of 0.5 mW, is shown in figure 4.26. It indicated that a single-

pass written guide lasted longer than a waveguide with 10 passes, which had a lifetime that was significantly shorter.

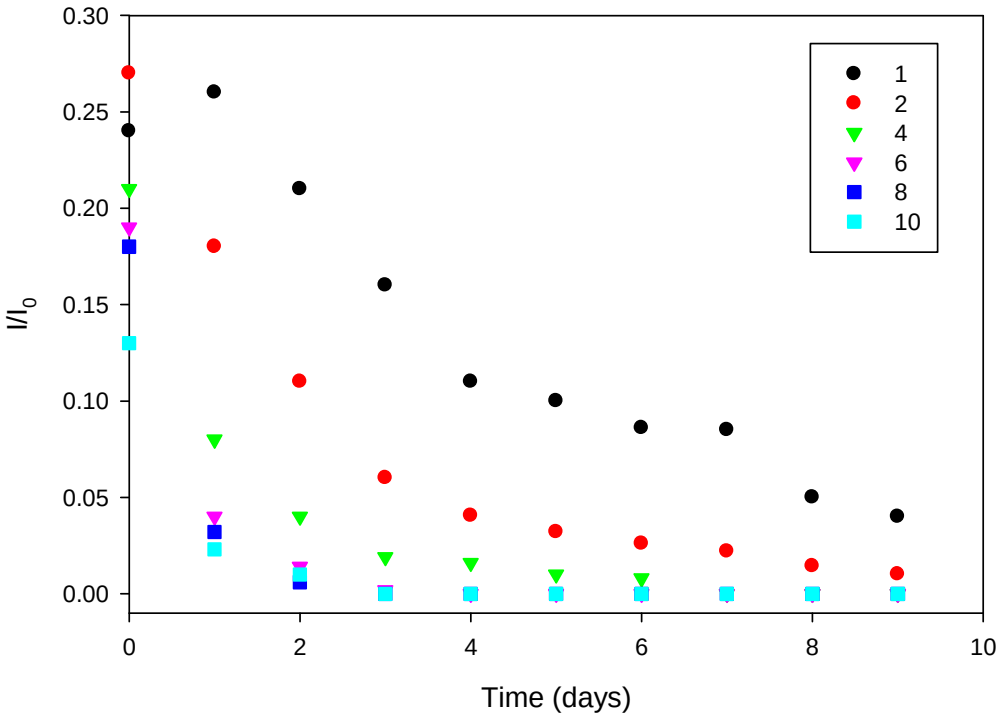

Figure 4.26: Lifetimes of multi-pass waveguides on +z congruent lithium niobate at 45 mW.

Decaying exponential fits were applied to the lifetime data and produced the following decay constants in table 4.3.

# of passes	Decay time, τ (days)
1	3.72
2	2.84
4	1.52
6	0.67
8	0.59
10	0.78

Table 4.3: Decay time vs. number of passes for UV written channel waveguides on +z congruent lithium niobate at 45 mW, velocity 50 mm/min and spot radius 4 µm.

The greater number of passes, the quicker the number of days the channel waveguide intensity took to decay to 37% of its original value.

	NA		***Δn* (10^{-4})**	
Day	**(*y*)**	**(*z*)**	**(*y*)**	**(*z*)**
1	0.039	0.035	3.6	3.0
2	0.030	0.022	2.2	1.1
3	0.034	0.022	2.6	1.2
4	0.031	0.021	2.3	1.1
5	0.032	0.02	2.5	0.89
6	0.026	0.016	1.6	0.63
7	0.016	-	0.6	-

Table 4.4: Numerical aperture and *Δn* measurements for +z congruent $LiNbO_3$ UV written waveguides for the *y* and *z* directions.

The *NA* and *Δn* measurements in table 4.4 show a common decrease in optical confinement over time indicating the waveguides were decaying. The rate of decay at a wavelength λ = 1549 nm again suggests that UV writing was a temporary phenomena that, after writing, underwent a relaxation effect over several days. As the rate of decay accelerated with an increase of the number of passes, the beam exposure and therefore heat was increased indicating that if charge was responsible for the index change it was being driven either deeper or further into the crystal, lowering the potential at the surface and creating a less significant index change.

A quick experiment to test the thermal performance of written guides was then attempted. One +z face sample with waveguides written at powers of 20 – 50 mW, a velocity of 50 mm/min and spot size 4 μm, was annealed at 200°C for 18 hours and the second identical sample was annealed at 100°C for 18 hours. Both samples did not show any residual guiding after annealing for any written waveguides. Similar waveguides written on a –*z* face sample were thermally less stable than on the +z face; with a sample heated to temperatures of ~ 70°C, waveguides on the –z face disappeared after 30 minutes.

4.5 S –Bends

Further to straight waveguides, s-bends were fabricated in congruent lithium niobate to demonstrate the application of UV writing to more advanced structures. S-bends, or sometimes called offset waveguides, are used to connect unaligned elements and are a basic structure used in devices like power splitters, directional couplers and Mach-Zender interferometers. An outline of the s-bend shape is shown in fig 4.27.

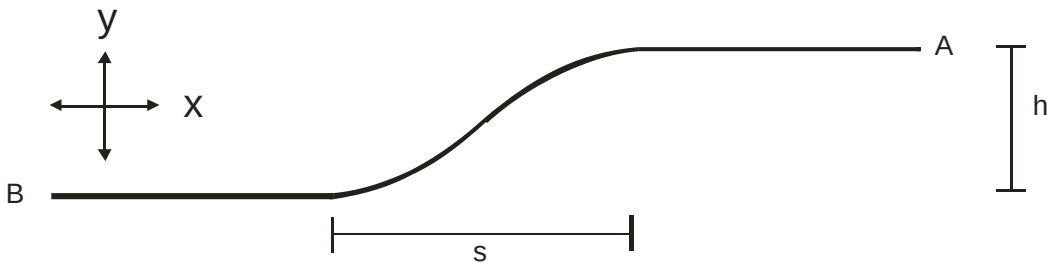

Figure 4.27: S-bend with nomenclature of variables.

There are three main expressions to describe the curve of the guide away from the input: a straight line, sine curve and cosine curve. The expression for the straight waveguide is:

$$\Delta y = \frac{h}{l} x \tag{4.8}$$

The sine bend is described by:

$$\Delta y = \frac{h}{l} x - \frac{h}{2\pi} \sin\left(\frac{2\pi x}{l}\right) \tag{4.9}$$

Finally, the cosine bend is:

$$\Delta y = \frac{1}{2} h \left[1 - \frac{\cos(\pi x)}{s}\right] \tag{4.10}$$

Where *h* is the offset, *l* the length of the curve and *s* is the bend length of the cosine bend. A graph is shown in fig 4.28 to demonstrate the differences between these expressions. The cosine curve was chosen over the sine curve as it demonstrated the least curvature and hence least loss. The straight line would incur significant losses at both abrupt junctions from straight waveguide to inclined waveguide.

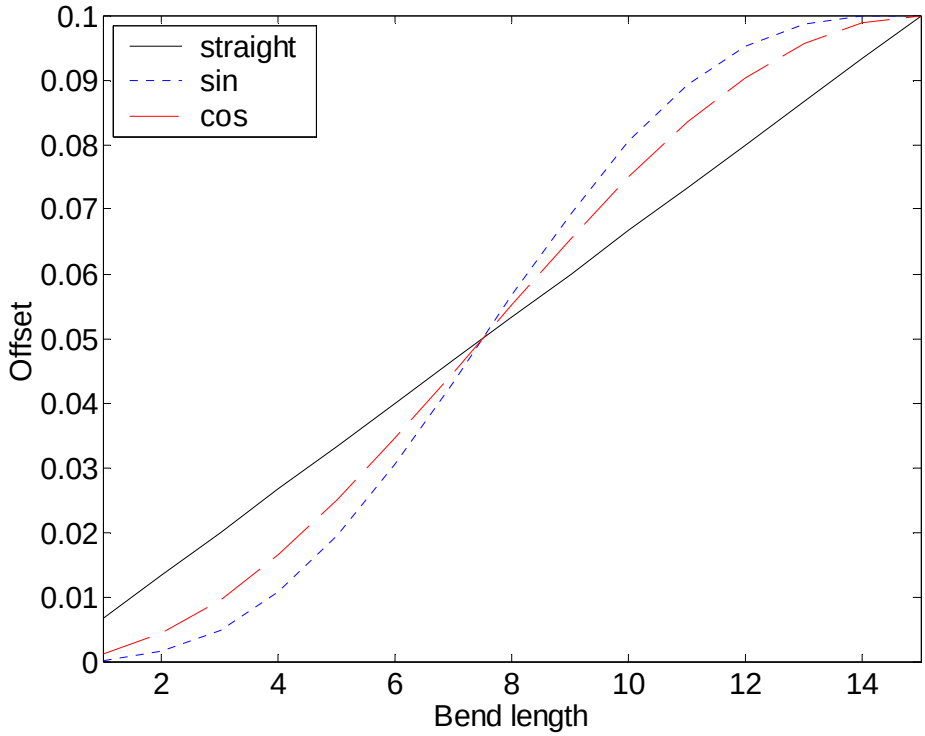

Figure 4.28: Types of s-bends calculated with arbitrary values from Eqs. 4.8- 4.10.

4.5.1 Variation of Bend Length

The initial investigation focussed on changing the bend length *s* of the s-bend with a constant offset *h* of 100 µm. The power of the incident beam was 40 mW, the spot radius 4 µm and the velocity 50 mm/min. The bend loss was calculated from Eq. 4.11.

$$BendLoss(dB) = 10Log\left(\frac{P_{INPUT}}{P_{OUTPUT}}\right) \qquad (4.11)$$

The loss was expected to increase with smaller bend length and as can be observed from figure 4.29, the bend loss increased exponentially if the bend length was smaller than 6 mm. The standard deviation of bend loss increased considerably with a tight bend radius.

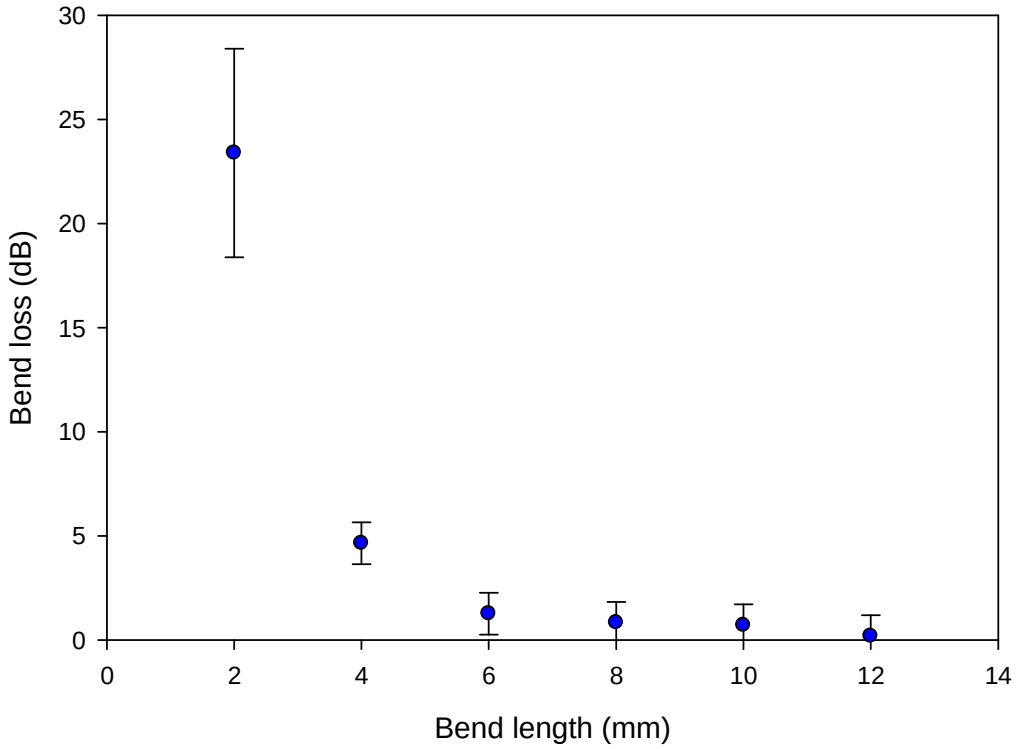

Figure 4.29: UV written bend loss vs. bend length for s-bend written at 40 mW, velocity 50 mm/min and spot radius 4 µm on +z congruent lithium niobate.

4.5.2 Variation of Bend Offset

The next step was to investigate the increase in offset *h* with a bend length of 13 mm using the above parameters for the beam size, power and velocity. As can be seen in figure 4.30, the bend loss significantly increased when the size of the bend offset increased past 200µm.

S-bends of different offsets and lengths have been fabricated and it was possible to produce structures with a large enough index change and low enough bend losses for functional devices.

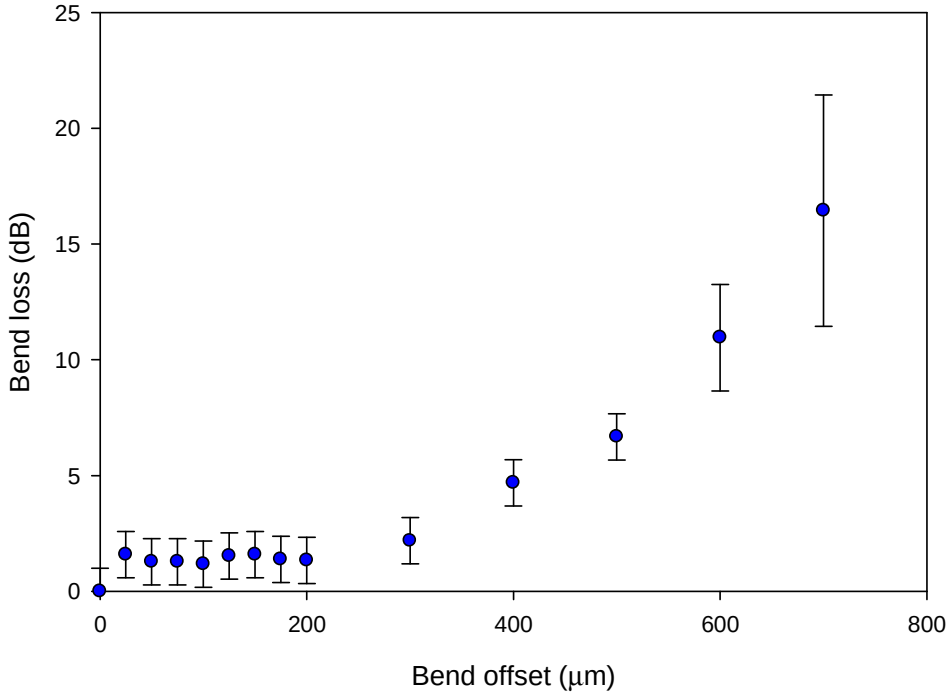

Figure 4.30: UV written bend loss vs. offset size for s-bend written at 40 mW, velocity 50 mm/min and spot radius 4 μm on +z congruent lithium niobate.

4.6 Y- Junctions

Y-junctions are commonly used as power splitters, extra pumping arms for waveguide lasers and as part of more complex devices such as integrated Mach-Zender interferometers. Y-junctions were fabricated in +z face congruent lithium niobate at a writing power of 40 mW and velocity of 50 mm/min. The junction was written by starting at the output of arm 1, tracing the cosine bend to the input of the input then tracing back to the output of arm 2.

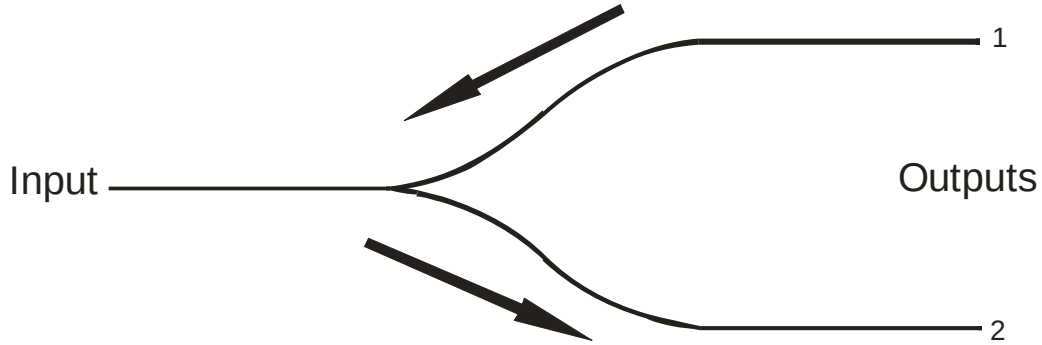

Figure 4.31: Y-junction structure with output arms 1, 2 and input. The arrows dictate the direction of writing beam.

4.6.1 Variation of Arm Separation

The first experiment was to vary the size of the arm offset from a straight waveguide to a maximum of 300 µm distance separation from each arm. Due the high loss incurred with increased offset as seen with the s-bends, the maximum offset was set to 150 µm. Fig. 4.32 illustrates the modes profiles of a selection of offsets.

Straight waveguide

Junction with 100 µm separation

Junction with 150 µm separation

Figure 4.32: Mode profiles of straight waveguide vs. y-junctions of 100 and 150 µm arm separation for writing power of 40 mW, beam velocity of 50 mm/min and spot radius 4 µm on +z congruent lithium niobate.

The immediate observation was a loss of mode intensity in the arm profiles and fig. 4.33 compares the arm separation vs. $1/e^2$ mode profile for y-junctions written at 40 mW. The figure shows a gradual increase in size of the waveguide as the arm separation increased. There was a difference in the sizes of the guides from each arm – this was probably due to the asymmetrical writing technique. As was common with the writing technique, the depth of the waveguides (z) is considerably smaller than the width (y). It is possible to produce working y-junctions with this technique but the writing process needs to be optimised for 50:50 splitters.

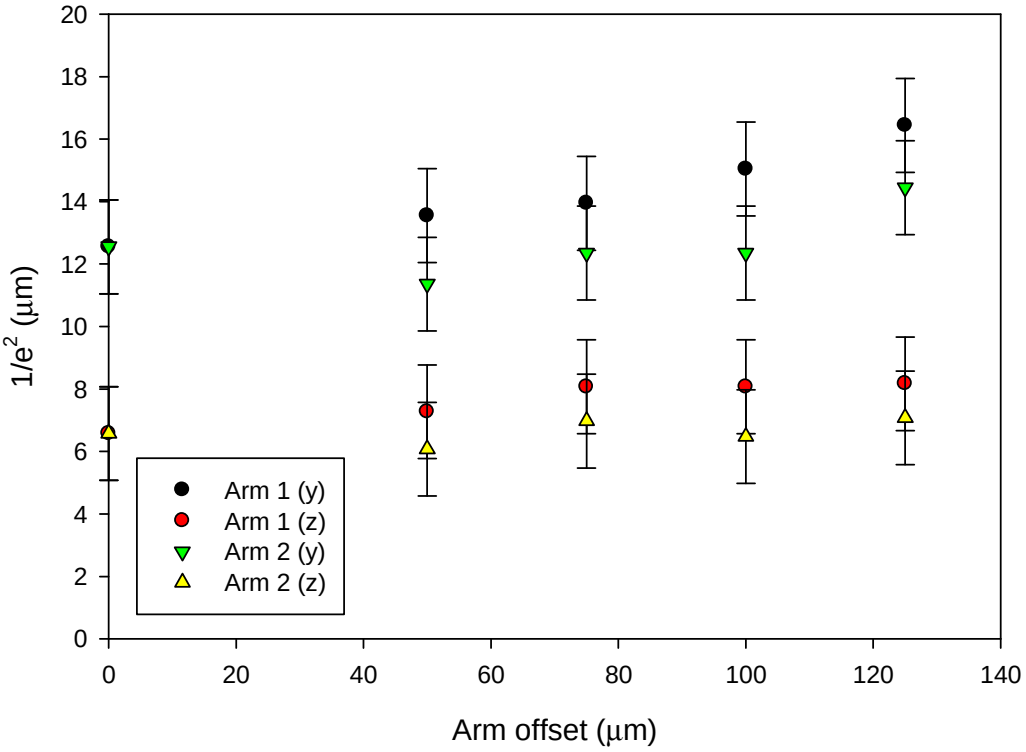

Figure 4.33: Graph of $1/e^2$ mode size of waveguide vs. arm offset for y-junction for a writing power of 40 mW, beam velocity of 50 mm/min and spot radius 4 µm on +z congruent lithium niobate.

4.7 UV Induced Index Changes in $LiNbO_3$

The mechanism behind waveguide formation from λ = 244 nm direct UV writing in congruent lithium niobate is not completely understood. Nevertheless, there are strong indicators that point to a plausible explanation. It is believed that the mechanism behind the UV writing process is thermally driven, indeed the temperature increase and profile from an incident cw Gaussian beam is well known [30] and will be examined in detail in chapter 7. Lithium ion movement is the key to this process – from chapter 3 we know that in the early days of optical waveguide fabrication in lithium niobate, lithium out-diffusion was used to fabricate guides but in some methods such as Ti-indiffusion it seen as a hindrance to low loss waveguides. For optical waveguides it was found that those which had the lowest propagation loss and the longest lifetime required surface melting during the writing process and these waveguides had surfaces considerably above

the melting temperature, T_m ~1526 K. Lithium will have a thermal diffusivity increase of several magnitudes when the crystal becomes amorphous and hence there will be a greater movement/out-diffusion of lithium in this region.

During early experiments to investigate properties of $LiNbO_3$ crystals with different stoichiometries, an increase in the extraordinary refractive index only with a decrease in Li_2O concentration was observed [31], this was also seen in $LiTaO_3$ [32]. It was also observed that by heating samples to 1100ºC for several hours, an out-diffusion of Li_2O occurs at the surface which causes an increase in the extraordinary refractive index, forming a waveguide [33]. The waveguides formed had unaffected electro-optic properties and modulators were fabricated [34]. This out-diffusion effect has been fully characterized by Carruthers [35]. A separate cause of lower index refractive index layers has been shown to be due to hydroxyl ions [36].

A suggestion for the main cause of guiding in UV written samples is an out-diffusion and concurrent sideway diffusion of lithium ions, induced by the incident optical power heating the surface, forming the guiding region. The waveguides fabricated also show a similar increase in extraordinary refractive index only and the crystal is still electro-optic. Samples were sent to Loughborough Surface Analysis[3] for secondary ion mass spectroscopy (SIMS) analysis to identify if any lithium ion concentration change occurred in irradiated samples. This technique should be able to quantify the concentration of Li ions on the surface due to the writing process.

Figs. 4.34 and 4.35 show the same single waveguide (written at 30 mW, velocity 50 mm/min and spot radius 4 μm) that has undergone SIMS analysis. Fig. 4.34 shows the contrast of lithium ions and fig 4.35 the concentration of niobium ions; the measurement of actual ion concentration was too difficult with the combination of such a small area, a small change in ion concentration and the small mass of lithium ions. They were able though to show that an ion movement does occur hence the change in contrast from black of lower concentration to

[3] Loughborough Surface Analysis Ltd., Holywell Park, Ashby Road, Loughborough, Leicestershire. LE11 3WS. UK.

white of higher concentration indicating a lithium ion deficiency in the waveguide. A similar deficiency is seen with niobium but as niobium is a much larger ion, the contrast is smaller.

Other studies of UV machining on lithium niobate with far higher incident intensities have been able to confirm that incident UV exposure causes an out-diffusion of lithium ions [37, 38] and a reduction of niobium ions due to ablation.

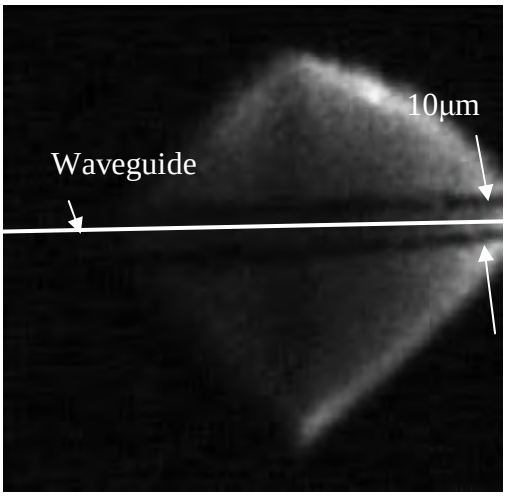

Figure 4.34: Li ion contrast with black area along waveguide denoting a lithium deficient region.

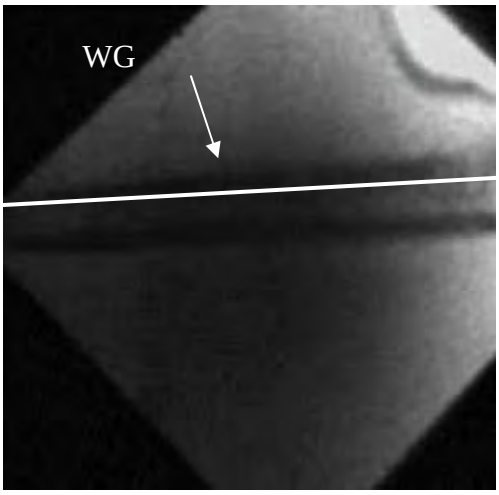

Figure 4.35: Nb ion contrast with black area along waveguide denoting niobium deficient region.

Aside from this material picture, a change in lithium concentration has a subsequent effect on the refractive index of lithium niobate as reported by Schlarb [26]. Fig. 4.36 illustrates how the change in lithium concentration will affect the extraordinary refractive index. From this analysis, the concentration of Li_2O for congruent $LiNbO_3$ is ~ 48.4 mol% and for an increase in n_e of ~9 x 10^{-4} at λ = 1549 nm from section 4.4.5, a concentration change of 0.3 mol% Li_2O is predicted. Numerical aperture measurements, taken at λ = 633 nm on a +*z* face sample show an index change of 6 x 10^{-4} from results in section 4.3 estimate an index change corresponding to a possible difference of 0.1 mol% in lithium concentration. The graph shows that even small changes in lithium concentration are enough to produce an index difference large enough to form a waveguide. These concentration changes are challenging to measure but nevertheless, lithium

out-diffusion and possible sideways diffusion presents a viable mechanism for waveguide formation due to UV writing.

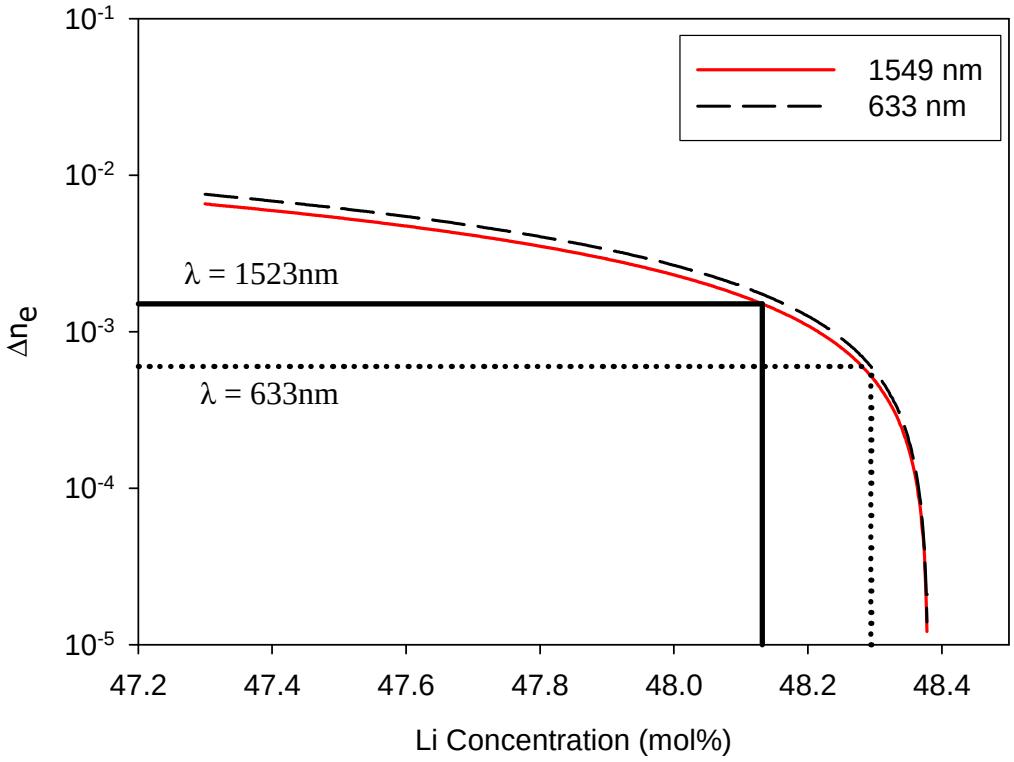

Figure 4.36: Lithium ion concentration change vs. change in n_e for congruent lithium niobate as predicted by Schlarb [26].

There are several points to make that suggest lithium out-diffusion may not be the sole effect occurring at the crystal surface and assisting waveguide formation. The decay of the output intensity over several days coupled with the fact that low temperature annealing dissipates the waveguide suggests a related mechanism is responsible for this decay. Further to the lithium out-diffusion, there is lithium ion diffusion in the crystal from the high temperature due to the incident writing beam at the surface to regions of lower temperature. This temperature gradient drives lithium ions from their sites in the irradiated region to lithium vacancy sites in the cooler areas forming an index difference. After writing, there is a charge imbalance and the ions begin to migrate back to their original positions and hence the index difference is reduce and cannot support an optical mode. This back-migration can be accelerated by high temperature annealing.

4.8 Possible Domain Formation

While investigating the optical waveguides, samples were etched to examine if possible domain formation occurred under writing conditions. Samples were etched in 48 mol% hydrofluoric acid (HF) for 10 minutes at room temperature and inspected under a scanning electron microscope (SEM). HF etching is a quick method to identify domain structures as *–z* face faces etch preferentially at a rate of ~ 0.8 μm/h compared with little evidence of etching of *+z* faces [39]. Initially, surface structures were present indicating the possibility of domains as shown in fig. 4.37. This was not conclusive proof as it was assumed that these structures were polycrystalline after melting which would affect the etching process. Recent collaboration with a group in Bonn which specialises in piezo-force microscopy (PFM) allowed us to back up this assertion of the existence of surface domains via cw UV writing by comparison with electric field poled periodically poled lithium niobate.

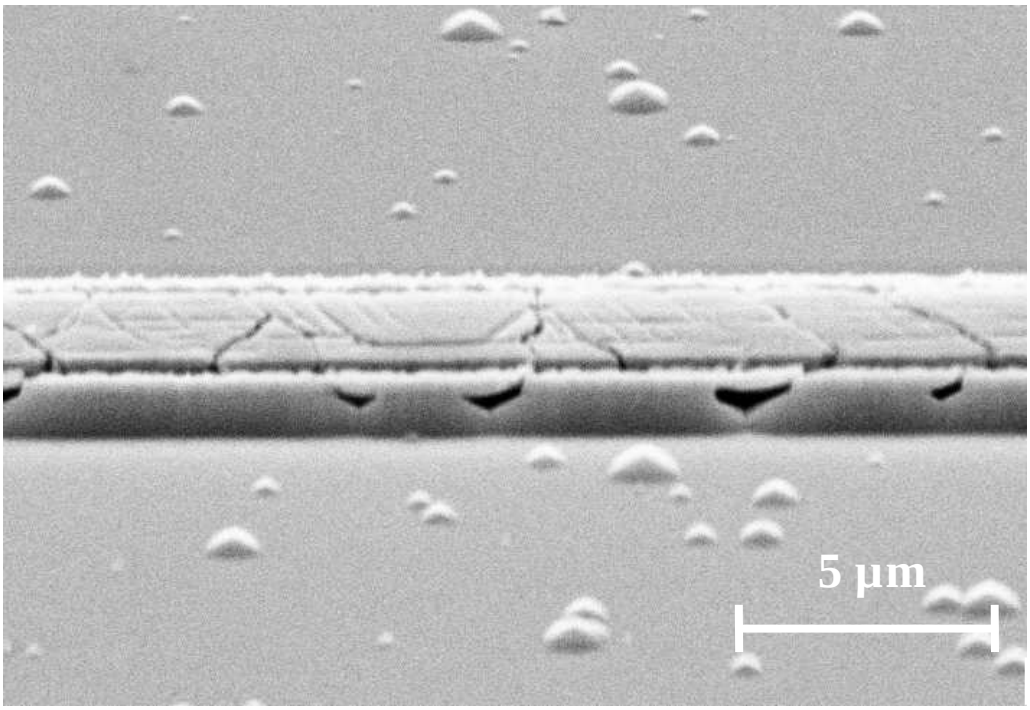

Figure 4.37: HF etched channel waveguide written with cw λ = 244 nm on -*z* congruent lithium niobate at a power of 50 mW, velocity of 50 mm/min and spot radius 4 μm.

Fig. 4.38 is a PFM contrast image of a +*z* face congruent lithium niobate sample irradiated with 30 mW and 20 mW powers with a velocity of 50 mm/min and beam radius of 4 µm. The contrast identifies differently orientated domains - the white areas indicate the spontaneous polarization direction is out of the page as with virgin +*z* single crystal $LiNbO_3$. Fig 4.38 shows two lines written: one below (20 mW) and one above (30 mW) the melting point of lithium niobate and from the figure, surface modification from the melting was visible on the 30 mW line.

Domain formation was not restricted to the +*z* face and domains are also seen on the –*z* face via separate exposures. An interesting point to note is that the size of the +*z* domain lines are around a quarter of the size of the incident writing beam which would seem to indicate a threshold intensity is needed for domain formation.

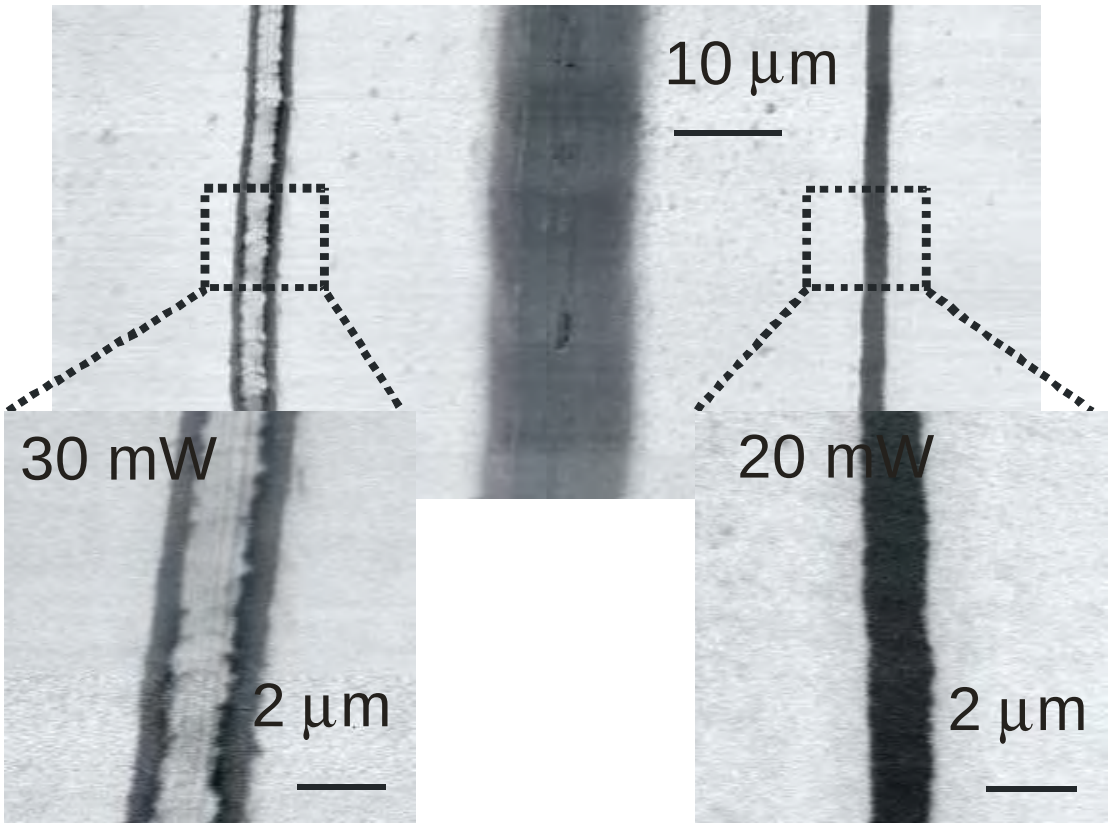

Figure 4.38: PFM study of topology and surface charge on two waveguides UV written on +*z* congruent lithium niobate at powers of 30 and 20 mW, a velocity of 50 mm/min and spot size of 4 µm.

Domain formation observed on –*z* face samples is illustrated in fig 4.39; three waveguides are shown (from left to right) written with writing powers of 25, 30 and 35 mW and written with the same velocity and spot size as those in fig. 4.38, and below these is a higher contrast picture of the 30 mW waveguide. The surface damage from the writing beam is visible along the waveguide writing axis and disrupts domain formation. As domain formation is seen with UV writing - this further complicates what is taking place in the UV exposed region and immediately below it. Two possible explanations of the inversion of the spontaneous field are due to the pyroelectric effect, from the applied laser source, or piezoelectric effect, due to the subsequent material expansion from the source.

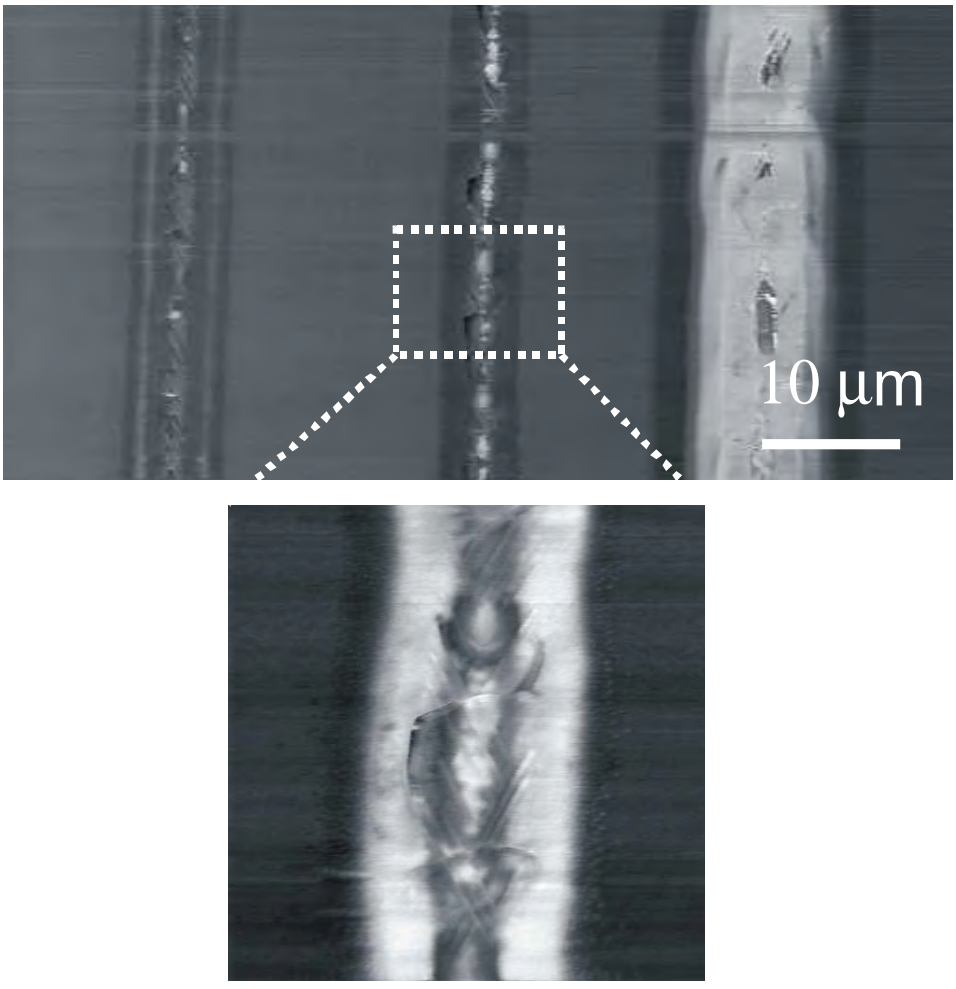

Figure 4.39: PFM study of domain formation on -*z* face congruent lithium niobate with magnified picture of waveguide written at 30 mW.

Domain inversion via heat treatment is well known [40-43] but usually require constant high temperatures for time periods of the order of hours, clearly the

exposure time from the writing beam is orders of magnitudes smaller than this and Chapter 7 will investigate the possibility that thermal distributions produced during UV heating and subsequent electric fields are responsible for this domain formation.

4.9 Congruent Lithium Niobate Summary

A study of direct UV writing parameters for the formation of channel waveguides in congruent lithium niobate on the surface of samples of different crystal cuts (*x*, *y* and *z*) have been evaluated. From these experiments I have shown that *z*-cut samples showed light confinement only and +*z* face samples the lowest propagation loss and largest Δn increase of *z*-cut lithium niobate. The waveguides on the +*z* face exhibited transmission of TM modes only indicating an increase in the extraordinary refractive index while waveguides on the *x* and *y* face samples did not show any light confinement as noted in table 4.1.

Waveguides show a minimum propagation loss of ~ 2 dB/cm and a maximum Δn of ~ 8×10^{-4}. A major drawback of these guides is the maximum mean decay time is ~ 4.5 days. This is obviously inadequate for any serious use as a device or as an alternative to current waveguide fabrication techniques in lithium niobate. Further devices such as splitters and y-junctions were possible but again, are subject to the decay process of the waveguide. The limited time scale of the index change does offer the possibility of uses for short term optical memory storage.

An unexpected effect of the writing process is the inversion of surface domains via the writing process and this result allows the possibility of tailoring domains and to significantly simplify the fabrication of quasi-phase matching devices.

4.10 References

1. Hill, K.O. and G. Meltz, *Fiber Bragg grating technology fundamentals and overview*. Lightwave Technology, Journal of, 1997. **15**(8): p. 1263-1276.

2. Davis, K.M., K. Miura, N. Sugimoto, and K. Hirao, *Writing waveguides in glass with a femtosecond laser.* Opt. Lett., 1996. **21**(21): p. 1729.

3. Contardi, C., E.R. Taylor, and A. Fu, *Study of UV-written channels in lead silicate glasses.* Journal of Non-Crystalline Solids, 2001. **291**(1-2): p. 113-120.

4. Bookey, H.T., R.R. Thomson, N.D. Psaila, A.K. Kar, N. Chiodo, R. Osellame, and G. Cerullo, *Femtosecond Laser Inscription of Low Insertion Loss Waveguides in <formula> <tex>Z</tex></formula>-Cut Lithium Niobate.* Photonics Technology Letters, IEEE, 2007. **19**(12): p. 892-894.

5. Hill, K.O., Y. Fujii, D.C. Johnson, and B.S. Kawasaki, *Photosensitivity in optical fiber waveguides: Application to reflection filter fabrication.* Applied Physics Letters, 1978. **32**(10): p. 647-649.

6. Duval, Y., R. Kashyap, and S. Fleming, *Correlation between ultraviolet-induced refractive index change and photoluminescence in Ge-doped fiber.* Applied Physics Letters, 1992. **61**(24): p. 2955-2957.

7. Meltz, G., W.W. Morey, and W.H. Glenn, *Formation of Bragg gratings in optical fibers by a transverse holographic method.* Opt. Lett., 1989. **14**(15): p. 823.

8. Mizrahi, V., P.J. Lemaire, T. Erdogan, W.A. Reed, J. DiGiovanni, and R.M. Atkins, *Ultraviolet laser fabrication of ultrastrong optical fiber gratings and of germania-doped channel waveguides.* Applied Physics Letters, 1993. **63**(13): p. 1727-1729.

9. Svalgaard, M., C.V. Poulsen, A. Bjarklev, and O. Poulsen, *Direct UV writing of buried singlemode channel waveguides in GE-doped silica films.* Electronic Letters, 1994. **30**(17): p. 1401-1403.

10. Lemaire, P.J., R.M. Atkins, V. Mizrahi, and W.A. Reed, *High pressure H_2 loading as a technique for achieving ultrahigh UV photosensitivity and thermal sensitivity in GeO_2 doped optical fibres.* Electronic Letters, 1993. **29**(13): p. 1191-1193.

11. Svalgaard, M. and M. Kristensen, *Directly UV written silica-on-silicon planar waveguides with low loss.* Electronics Letters, 1997. **33**(10): p. 861-863.

12. Svalgaard, M., *Direct writing of planar waveguide power splitters and directional couplers using a focused ultraviolet laser beam.* Electronics Letters, 1997. **33**(20): p. 1694-1695.

13. Svalgaard, M., K. Faetch, and L.-U.Anderson, *Variable Optical Attenuator Fabricated by Direct UV Writing.* Journal of Lightwave Technology, 2003. **21**(9): p. 2097-2103.

14. Guilhot, D.A., G.D. Emmerson, C.B.E. Gawith, S.P. Watts, D.P. Shepherd, R.B. Williams, and P.G.R. Smith, *Single-mode direct-ultraviolet-written channel waveguide laser in neodymium-doped silica on silicon.* Optics Letters, 2004. **29**(9): p. 947-949.

15. Emmerson, G.D., S.P. Watts, C.B.E. Gawith, V. Albanis, M. Ibsen, R.B. Williams, and P.G.R. Smith, *Fabrication of directly UV-written channel waveguides with simultaneously defined integral Bragg gratings.* Electronics Letters, 2002. **38**(24): p. 1531-1532.

16. Contardi, C., E.R. Taylor, and A. Fu, *Study of UV-written channels in lead silicate glasses.* Journal of Non-Crystalline Solids, 2001. **291**: p. 113-120.

17. Mairaj, A., P. Hua, H.N. Rutt, and D.W. Hewak, *Fabrication and Characterization of Continuous Wave Direct UV (λ=244nm) Written Channel Waveguides in Chalcogenide (Ga:La:S) Glass.* Journal of Lightwave Technology, 2002. **20**(8): p. 1578-1584.

18. Mairaj, A., A.M. Chardon, D.P. Shepherd, and D.W. Hewak, *Laser Performance and Spectroscopic Analysis of Optically Written Channel Waveguides in Neodymium-Doped Gallium Lanthanum Sulphide Glass.* IEEE Journal of Selected Topics in Quantum Electronics, 2002. **8**(6): p. 1381-1388.

19. Boulard, B., L. Brilland, and H. Poignant, *UV writing of channel waveguides in erbium doped fluoride glass thin films.* Electronic Letters, 1998. **34**(3): p. 267-268.

20. Koo, J.-S., R.B. Williams, C.B.E. Gawith, S.P. Watts, G.D. Emmerson, V. Albanis, P.G.R. Smith, and M.C. Grossel, *UV written waveguide devices using crosslinkable PMMA-based copolymers.* Electronics Letters, 2003. **39**(4): p. 394-395.

21. Mailis, S., C. Riziotis, P.G.R. Smith, J.G. Scott, and R.W. Eason, *Continuous wave ultraviolet radiation induced frustration of etching in lithium niobate single crystals.* Applied Surface Science, 2003. **206**(1-4): p. 46-52.

22. Mamedov, A.M., *Optical properties (VUV region) of $LiNbO_3$.* Optical Spectroscopy (USSR), 1984. **56**(6): p. 645-648.

23. Salgueiro, J.R., J.F. Roman, and V. Moreno, *Accurate interferometric system to perform the substrate focusing and alignment in laser writing processes.* Journal of Modern Optics, 1997. **44**(6): p. 1065-1072.

24. Mailis, S., C. Riziotis, I.T. Wellington, P.G.R. Smith, C.B.E. Gawith, and R.W. Eason, *Direct ultraviolet writing of channel waveguides in*

congruent lithium niobate single crystals. Optics Letters, 2003. **28**(16): p. 1433-1435.

25. Ulrich, R. and R. Torge, *Measurement of Thin Film Parameters with a Prism Coupler.* Applied Optics, 1973. **12**(12): p. 2901-2908.

26. Schlarb, U. and K. Betzier, *Refractive indices of lithium niobate as a function of wavelength and composition.* Journal of Applied Physics, 1993. **73**(7): p. 3472-3476.

27. Feuchter, T. and C. Thirstrup, *High Precision Planar Waveguide Propagation Loss Measurement Technique Using a Fabry-Perot Cavity.* IEEE Photonics Technology Letters, 1994. **6**(10): p. 1244-1247.

28. Wellington, I., S. Mailis, C.B.E. Gawith, G.J. Daniell, P.G.R. Smith, and R.W. Eason, *UV direct writing of low loss waveguides at 1.5υm in single crystal $LiNbO_3$,* in *Conference on Lasers and Electro-Optics (CLEO).* 2004: San Francisco.

29. Barai, S., A. Selvarajan, T. Srinivas, T. Madhan, and R. Fazludeen. *A novel technique to measure propagation loss of optical waveguides.* in *Electron Devices for Microwave and Optoelectronic Applications, 2003. EDMO 2003. The 11th IEEE International Symposium on.* 2003.

30. Muir, A.C., G.J. Daniell, C.P. Please, I.T. Wellington, S. Mailis, and R.W. Eason, *Modelling the formation of optical waveguides produced in $LiNbO_3$ by laser induced thermal diffusion of lithium ions.* Applied Physics A: Materials Science & Processing, 2006. **83**: p. 389-396.

31. Carruthers, J.R., G.E. Peterson, M. Grasso, and P.M. Bridenbaugh, *Nonstoichiometry and Crystal Growth of Lithium Niobate.* Journal of Applied Physics, 1971. **42**(5): p. 1846-1851.

32. Barns, R.L. and J.R. Carruthers, *Lithium Tantalate Single Crystal Stoichiometry.* Journal of Applied Crystallography, 1970. **3**: p. 395-399.

33. Kaminow, I.P. and J.R. Carruthers, *Optical waveguiding layers in $LiNbO_3$ and $LiTaO_3$.* Applied Physics Letters, 1973. **22**(7): p. 326-328.

34. Kaminow, I.P., V. Ramaswarmy, R.V. Schmidt, and E.H. Turner, *Lithium niobate ridge waveguide modulator.* Applied Physics Letters, 1974. **24**(12): p. 622-624.

35. Carruthers, J.R., I.P. Kaminow, and L.W. Stulz, *Diffusion Kinetics and Optical Waveguiding Properties of Outdiffused Layers in Lithium Niobate and Lithium Tantalate.* Applied Optics, 1974. **13**(10): p. 2333-2342.

36. Koide, A., H. Shimizu, and T. Saito, *Main Cause of Surface Waveguides Formed under $LiNbO_3$ Crystal Surface during Thermal Treatment.* Japanese Journal of Applied Physics, 1997. **36**(Part 1, No. 1A): p. 239-242.

37. Christensen, F.K. and M. Mullenborn, *Sub-band-gap laser micromachining of lithium niobate.* Applied Physics Letters, 1995. **66**(21): p. 2772-2773.

38. Christensen, F.K. and M. Mullenborn. *Improved laser processing of lithium niobate*. in *Ultrasonics Symposium, 1994. Proceedings., 1994 IEEE*. 1994.

39. Sones, C.L., S. Mailis, W.S. Brocklesby, R.W. Eason, and J.R. Owen, *Differential etch rates in z-cut $LiNbO_3$ for variable HF/HNO_3 concentrations.* Journal of Materials Chemistry, 2002. **12**(2): p. 292-298.

40. Nakamura, K., H. Ando, and H. Shimizu, *Ferroelectric domain inversion caused in $LiNbO_3$ plates by heat treatment.* Applied Physics Letters, 1987. **50**(20): p. 1413-1414.

41. Ahlfeldt, H., *Single-domain layers formed in heat-treated $LiTaO_3$.* Applied Physics Letters, 1994. **64**(24): p. 3213-3215.

42. Zhi-Yong Zhang, Y.-Y.Z.S.-N.Z.N.-B.M., *Domain inversion by Li_2O out-diffusion or proton exchange followed by heat treatment in $LiTaO_3$ and $LiNbO_3$.* Physica Status Solidi (a), 1996. **153**(1): p. 275-279.

43. Kugel, V.D. and G. Rosenman, *Polarization reversal in $LiNbO_3$ crystals under asymmetric diffusion conditions.* Applied Physics Letters, 1994. **65**(19): p. 2398-2400.

Chapter 5

UV Direct Writing in Stoichiometric $LiNbO_3$, Doped $LiNbO_3$ and $LiTaO_3$

This chapter covers the extension of the UV direct writing technique in lithium niobate to include fabrication of waveguides in stoichiometric lithium niobate, various forms of doped lithium niobate and lithium tantalate. Dopants were chosen to reduce lithium ion vacancies in congruent lithium niobate crystals according to their various doping concentrations and hence to provide verification of the lithium out-diffusion waveguiding mechanism. UV writing was also expanded to include channel waveguide fabrication on previously titanium-indiffused planar waveguides. As lithium tantalate is an isomorph of lithium niobate, waveguides were fabricated in lithium tantalate and compared with lithium niobate.

5.1 Introduction

The use of congruent lithium niobate for fabrication of UV written waveguides has been demonstrated in the previous chapter although waveguide performance suffers from output decay in a timescale of the order of days. The mechanism behind the index change is thought to be a combination of lithium out diffusion from surface heating and temporary sideways lithium diffusion, responsible for the lifetime decay. Various dopants and lithium compositions are used in this chapter to examine if this timescale can be extended and if the dopants can reveal more information about the waveguiding mechanism. Stoichiometric lithium niobate has been tested in section 5.2 with direct comparison to congruent lithium niobate.

Section 5.3 describes the results of waveguides fabricated in several doped congruent lithium niobate crystals. Dopants have been chosen for their various properties; some dopants such as iron enhance optical effects and can increase the photosensitivity of the material while others such as magnesium and zinc can suppress the photorefractive effect. Active-ion doped lithium niobate was used to confirm if the technique could be used to fabricate waveguide lasers and other active complex devices. Waveguides in neodymium and erbium doped lithium niobate were fabricated but had a high propagation loss and were found to be too difficult to lase.

A planar titanium in-diffused single mode lithium niobate sample with UV written channel waveguides was characterised and compared to congruent lithium niobate in section 5.4. UV written waveguides were also fabricated in lithium tantalate which has a similar structure and properties to lithium niobate; waveguide characterisation results and some properties are described in section 5.5. Section 5.6 discusses a basis for the waveguide formation mechanism and evidence from current experiments and the literature are considered.

5.2 Stoichiometric $LiNbO_3$

Waveguides were fabricated from 3" *z*-cut stoichiometric lithium niobate from Oxide Corporation[4]. The stoichiometry of the crystal sample is 49.9 mol% Li_2O estimated from T_c measurements [1]. The absorption edge is shifted further into the UV beginning at λ ~ 305 nm compared to congruent lithium niobate at λ ~ 325 nm as shown in fig. 5.1.

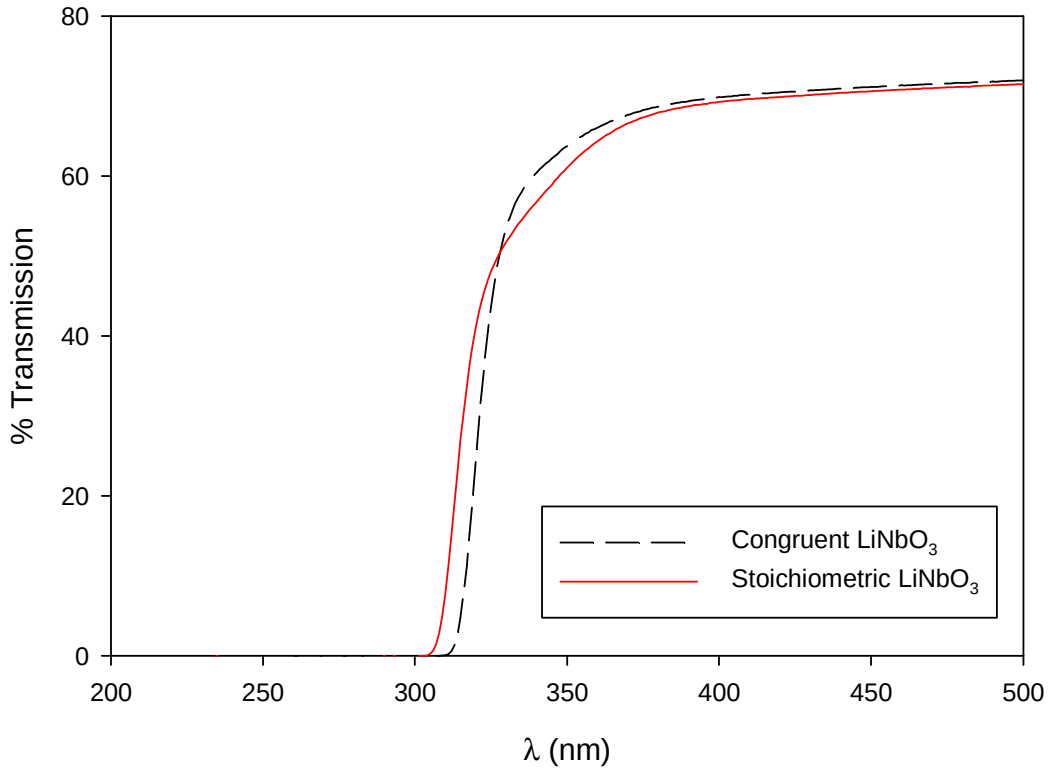

Figure 5.1: Stoichiometric vs. congruent $LiNbO_3$ transmission curve.

The stoichiometric $LiNbO_3$ samples used here have a greater concentration of lithium ions and thus reduced vacancies and defect sites in the crystal, therefore there is little scope for movement of lithium ions in the matrix and weaker waveguides are expected. Advantages for waveguide fabrication in stoichiometric lithium niobate include reduced photorefractive effect [2] and lower coercive field in periodically-poled waveguide devices [3].

[4] Oxide Corporation, 1747-1 Makihara, Mukawa, Hokuto, Yamanashi 408-0302 Japan.

Similar fabrication conditions as used for congruent lithium niobate were used to produce the waveguides as described in the previous chapter. Fig. 5.2 illustrates the mode profiles vs. writing power of waveguide written on +*z* face stoichiometric lithium niobate (SLN) for a beam velocity of 50 mm/min and a spot radius of 4 μm.

50 mW 45 mW 40 mW

Figure 5.2: Stoichiometric $LiNbO_3$ waveguides written on +*z* face written at velocity 50 mm/min and spot radius 4 μm.

An obvious difference between +*z* cut stoichiometric samples and +*z* cut congruent $LiNbO_3$ is the single-mode output at 50 mW compared to the double-mode output of for a similar power. As with congruent lithium niobate, the modes guided were TM polarised only over the range of writing powers tested but below a writing power of 40mW, no mode was formed even with surface melting observable at 35 mW. No modes propagated on the –*z* face across the entire writing power range. Figure 5.3 compares congruent LN mode profile dimensions to stoichiometric $LiNbO_3$ profiles. The SLN mode profiles are more diffuse than CLN, especially for the *y*- direction.

Waveguide lifetimes were reduced related the congruent samples; the maximum lifetime for a +*z* face SLN waveguide was approximately 3 days, just under a third of the maximum lifetime for a +*z* CLN waveguide. The propagation losses of +*z* SLN were greater than +*z* cut written congruent lithium niobate but less than –*z* cut written congruent lithium niobate for equivalent writing powers as shown in fig. 5.4. The minimum propagation loss of stoichiometric $LiNbO_3$ was ~ 2.2 dB/cm for a writing power of 45 mW.

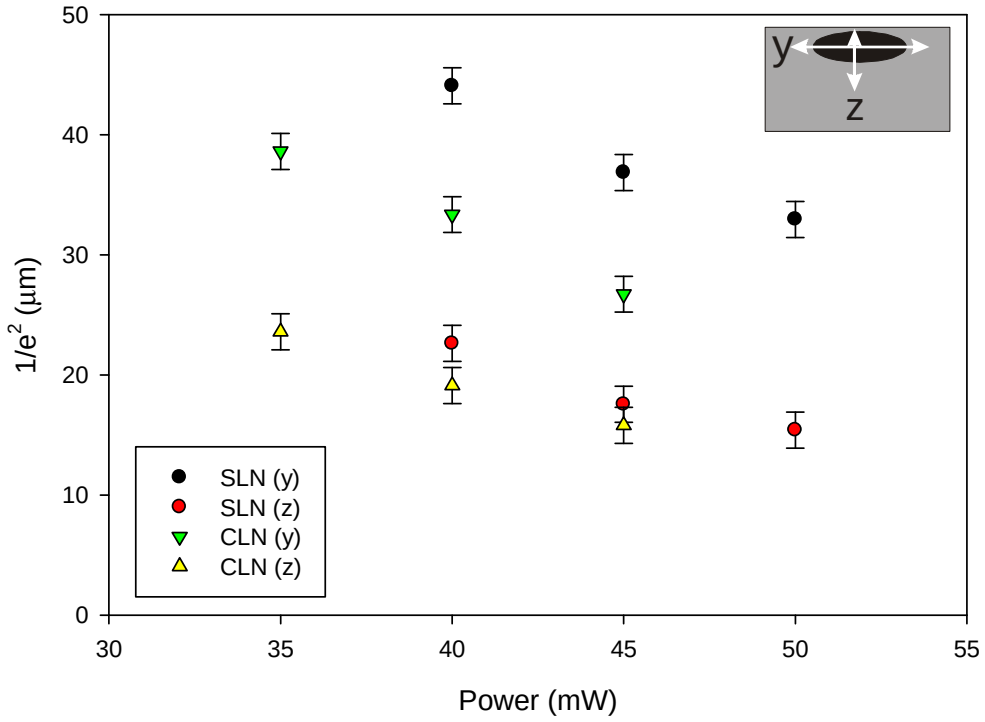

Figure 5.3: Comparison of $1/e^2$ mode size vs. writing power for +z face stoichiometric $LiNbO_3$ and congruent $LiNbO_3$ written at 50 mm/min and a spot radius of 4 µm.

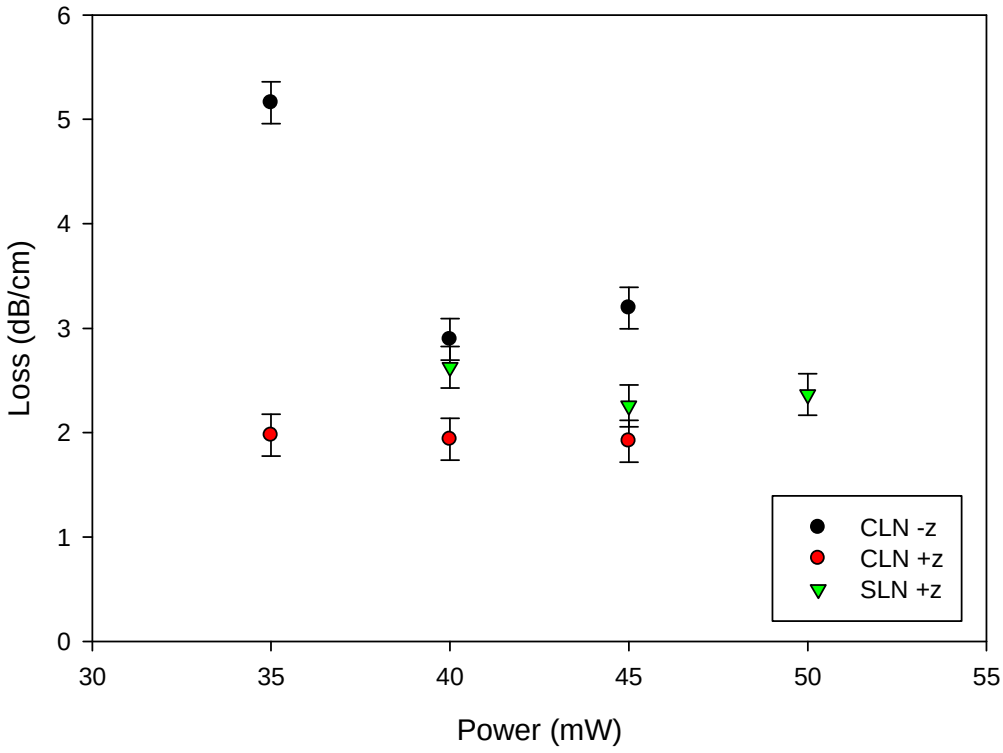

Figure 5.4: Comparison of UV written propagation loss vs. writing power for +z cut stoichiometric $LiNbO_3$ and +z and –z cut congruent $LiNbO_3$ crystals written at velocity 50 mm/min and spot radius 4 µm.

The numerical aperture and Δn measurements for various writing powers, a beam velocity of 50 mm/min and spot radius 4 μm, are illustrated in table 5.1. The substrate extraordinary refractive index, n_e, at λ = 1550 nm was calculated to be 2.13 [4].

There was a maximum of *NA* and Δn also at 45 mW in the *z*-direction; at 50 mW the power was high enough to form a cavity which inhibits the mode propagation of the waveguide as observable in fig. 5.2 and can be seen from the dip in *NA*. This indicates that melting and possible evaporation had occurred in the top layer of the waveguide. There may be an efficiency trade-off between surface melting, providing the large thermal gradients needed for charge movement, and the restriction of mode shape due to the melted channel.

NA	**40 mW**	**45 mW**	**50 mW**
(*y*)	0.034	0.035	0.036
(*z*)	0.030	0.035	0.029
Δn	**40 mW**	**45 mW**	**50 mW**
(*y*)	2.6×10^{-4}	2.9×10^{-4}	3.0×10^{-4}
(*z*)	2.0×10^{-4}	2.9×10^{-4}	2.0×10^{-4}

Table 5.1: *NA* and Δn vs. writing power for stoichiometric $LiNbO_3$ in the *y* and *z* directions [4] written at velocity 50 mm/min and spot radius 4 μm.

The optimum writing parameters for stoichiometric lithium niobate, defined by a combination of lowest propagation loss and largest Δn, was a writing power of 45 mW, spot radius 4 μm at focus and as seen in chapter 4 and beam velocity 50 mm/min. The value of propagation loss at a writing power of 45 mW was higher than in congruent lithium niobate and the index difference Δn at 45 mW was lower than congruent lithium niobate indicating that the increase in lithium content of the crystal has had a unfavourable effect on waveguide formation. The lithium out-diffusion at the surface may be greater for stoichiometric samples compared to congruent samples due to the increased lithium content but was not measureable for such small compositional

differences. The increased propagation loss and shorter lifetime of the stoichiometric sample is believed to be caused by the decrease in lithium ion vacancies in the crystal from which sideways movement of lithium away from the heated zone occurs.

5.3 Waveguides in Doped $LiNbO_3$

5.3.1 Introduction

A large variety of doped single crystal $LiNbO_3$ samples are available commercially offering a variety of different applications depending on the dopant. There are some distinct differences in the absorption spectrum of doped $LiNbO_3$ compared to congruent, undoped $LiNbO_3$ as shown in fig. 5.5.

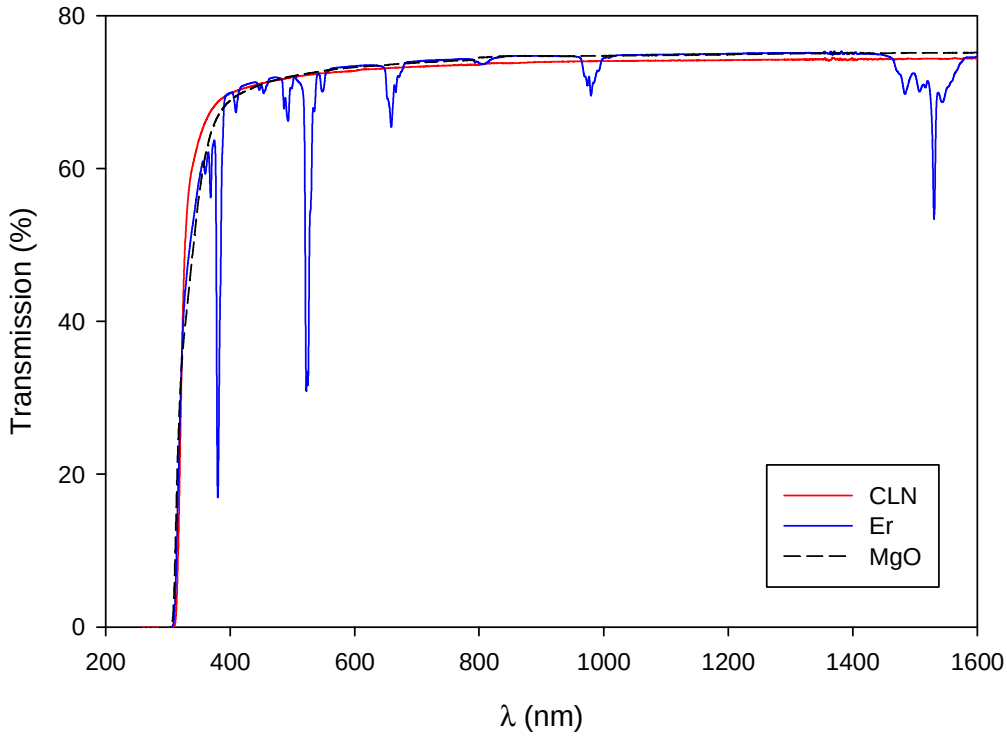

Figure 5.5: Transmission spectra for undoped congruent $LiNbO_3$, MgO- and Er- doped $LiNbO_3$.

Erbium doped samples have several absorption wavelengths seen in fig 5.5 that are exploited for stimulated emission at λ = 1550 nm via pumping at λ = 980 or 1480 nm [5]. Magnesium doped lithium niobate is discussed in the next section.

5.3.2 MgO:$LiNbO_3$

Doping the crystal with magnesium oxide increases the resistance of the crystal to optical damage from the photorefractive effect in the visible part of the spectrum. Doping of over 4.5 mol% of MgO in a crystal allows an increase of light intensity by a hundred times the level which optical damage occurs in undoped crystals [6] and was due to an increase of several orders of magnitude of the photoconductivity [7] and becomes useful if the material is used, for example, in frequency doubling experiments with high intensity visible light. The increased optical damage resistance is due to magnesium ions filling lithium host sites and reduce lithium ion vacancies in the crystal [8, 9] and at a threshold doping level where these vacancies are filled, the magnesium ions begin to replace niobium ions in the lattice [10]. In view of the fact that highly doped MgO lithium niobate has little lithium vacancies to fill, UV written channel waveguides were fabricated to test if waveguides could be formed with the lithium movement mechanism.

Two sets of waveguides, designed to operate at λ = 1523 nm and λ = 633 nm, were written into +*z* face, 1 mm thick, MgO:$LiNbO_3$ doped above the optical damage threshold level at 6 mol% from Crystal Technology[5]. The beam power was varied while the beam radius and velocity were kept constant, similar to experiments performed in chapter 4. On visual inspection, surface damage was observed for waveguides written with powers of 50 and 55 mW - 20 mW higher than for undoped congruent lithium niobate. For all MgO-doped written waveguides, there was no observed optical mode propagation either for TM or TE modes - this was expected due to the lack of lithium vacancies for the mobile lithium ions to diffuse to and hence form a region of increased refractive index.

5.3.3 Zn:$LiNbO_3$

Zinc is used in addition to magnesium to reduce the photorefractive effect in $LiNbO_3$, increasing the optical damage resistance [11]. Zinc-doped samples were manufactured

[5] Crystal Technology Inc., 1040 East Meadow Circle, Palo Alto, CA 94303-4230. USA.

by Crystal Technology and following the same conditions as used previously, mode profiles are given in figures 5.6 and 5.7. The lower doped zinc (1 mol%) sample offered greater light confinement than the higher doped (4 mol%) sample as is evident from figs. 5.6 and 5.7.

Doping above the optical damage threshold doping condition of ~ 6-7 mol% Zn:$LiNbO_3$, considerably improves optical performance at high light intensities [12] but this should have a noticeably detrimental effect on UV written waveguide characteristics, similar to the magnesium-doped samples as the zinc ions first fill lithium vacancies then lithium sites in the lattice [13].

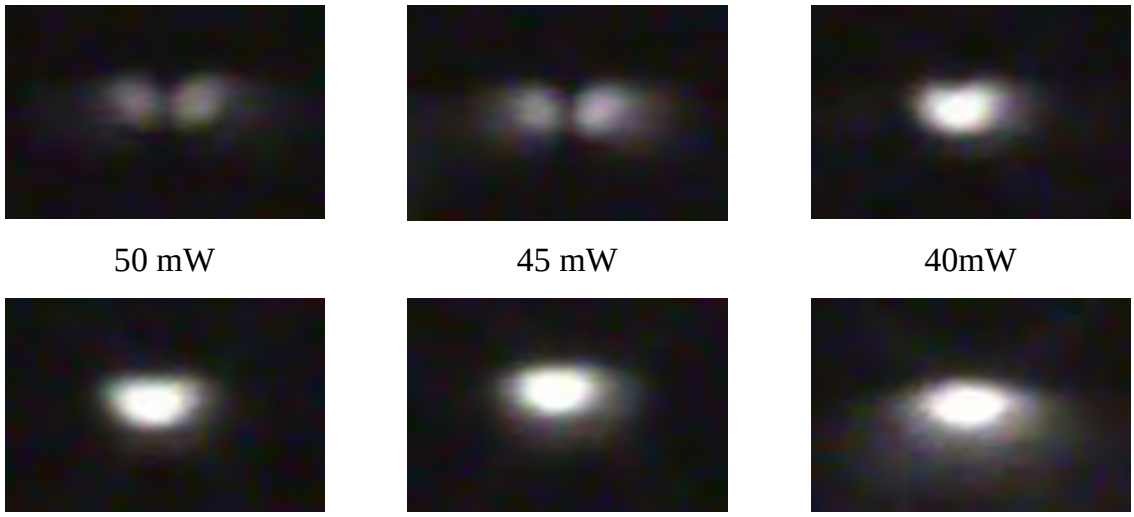

Figure 5.6: 1 mol% Zn:$LiNbO_3$ samples; mode profiles vs. writing power for channels written at 50 mm/min and spot size of 4 μm.

Propagation losses are displayed in fig. 5.8 – the 1 mol% Zn:$LiNbO_3$ sample has similar scale losses to undoped congruent lithium niobate at ~2 dB/cm; the more heavily doped sample had a minimum loss at ~2.9 dB/cm written at 40 mW. Given the high value of the doping threshold, the zinc concentration in the 1 mol% Zn-doped sample is low enough to have little effect on the propagation loss. As the zinc concentration is increased towards the threshold concentration the loss increases.

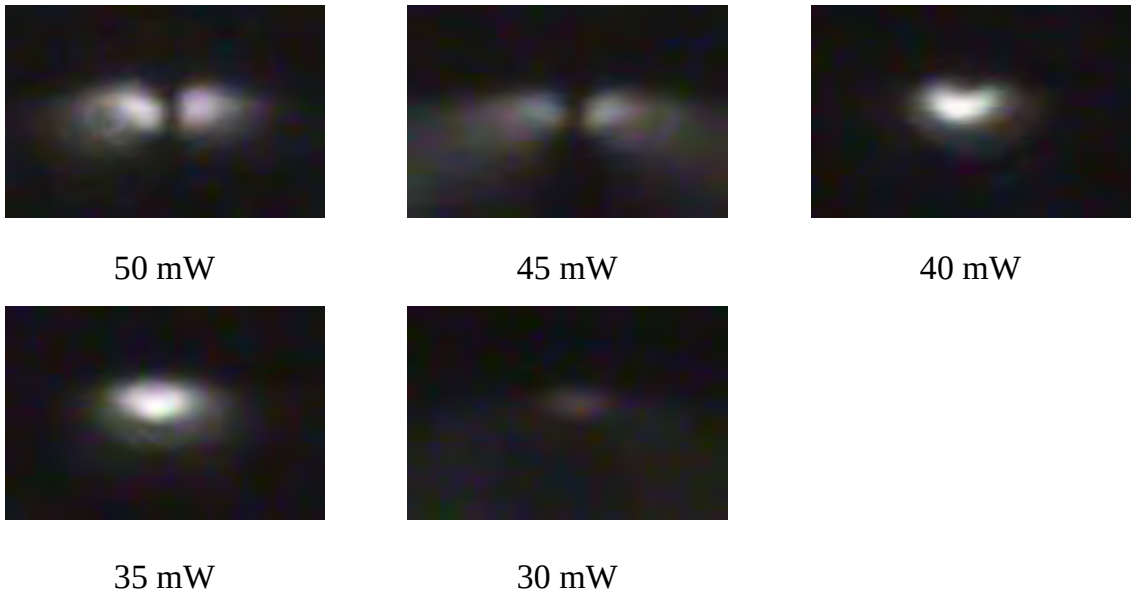

Figure 5.7: 4 mol% Zn:$LiNbO_3$ samples; mode profiles vs. writing power for samples written at 50 mm/min and spot size of 4 µm.

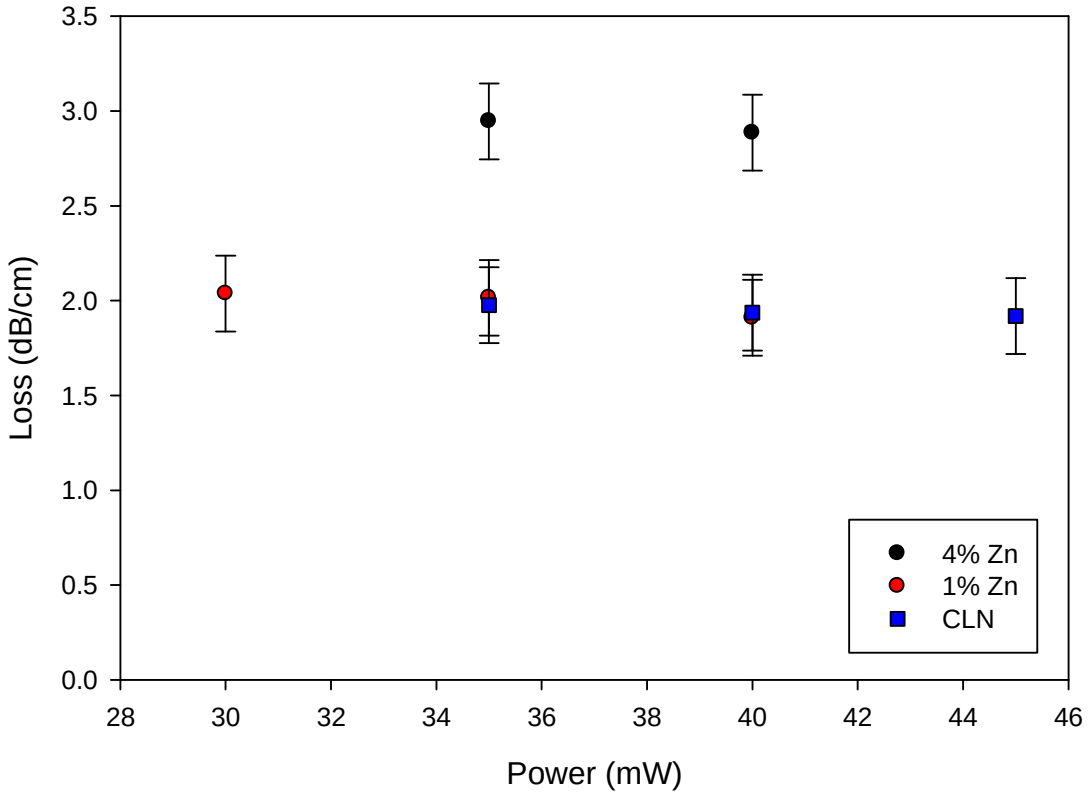

Figure 5.8: Propagation losses vs. writing power for 1 mol% Zn:$LiNbO_3$, 4 mol% Zn:$LiNbO_3$ and congruent undoped $LiNbO_3$ (CLN) written at velocity 50 mm/min and spot radius 4 µm.

The relationship between writing power and mode size is displayed in figure 5.9. Mode confinement improved with higher writing power in a similar manner to congruent lithium niobate with smaller mode sizes in the *z* direction than in the *y* direction. Congruent lithium niobate mode profiles were larger than both zinc-doped samples.

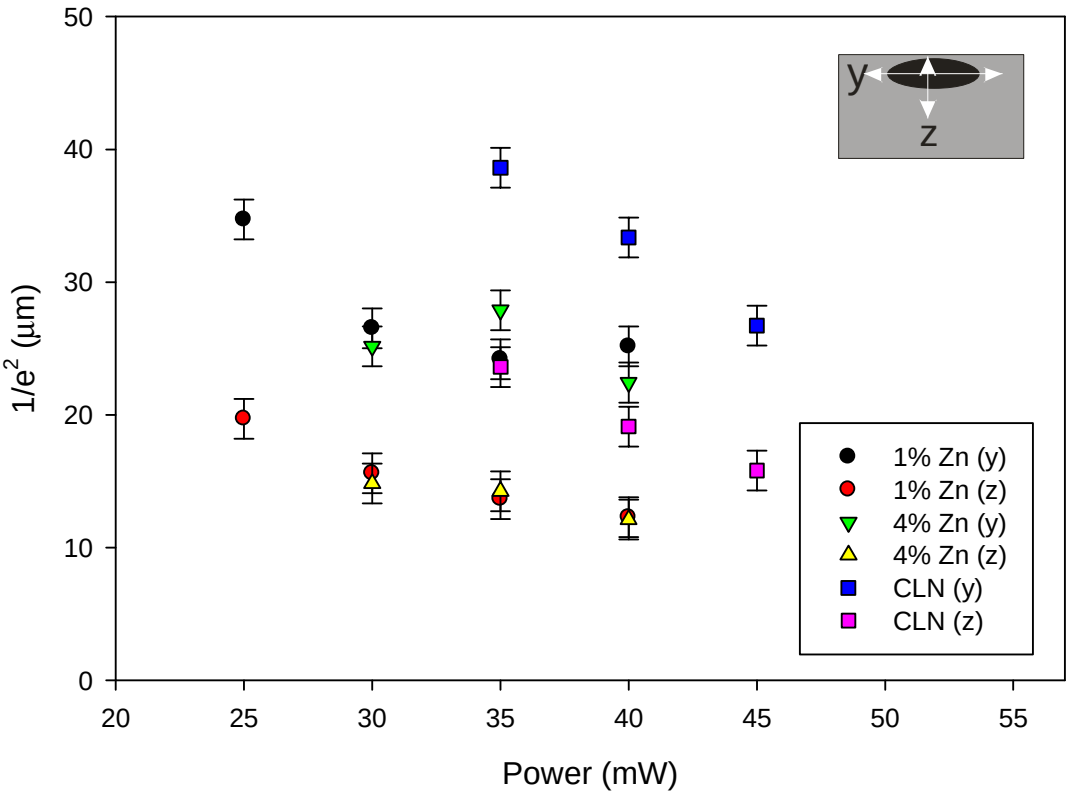

Figure 5.9: $1/e^2$ mode size vs. writing power comparison of 1mol% Zn:$LiNbO_3$, 4 mol% Zn:$LiNbO_3$ and undoped congruent $LiNbO_3$ written at velocity 50 mm/min and spot radius 4 µm.

The numerical aperture and Δn measurements vs. writing power for the 1 mol% Zn doped samples are shown in table 5.2 and the 4 mol% Zn doped sample measurements are given in table 5.3. The index differences were low compared with the iron-doped and congruent samples but this was expected due to the decreased lithium vacancies in the crystal, which is similar to magnesium-doped lithium niobate [14]. The increased doping of 4 mol% Zn led to decreased numerical apertures and index differences compared to the lower doped samples.

NA	**25 mW**	**30 mW**	**35 mW**	**40 mW**
(*y*)	0.021	0.022	0.030	0.023
(*z*)	0.033	0.049	0.047	0.051
Δn	**25 mW**	**30 mW**	**35 mW**	**40 mW**
(*y*)	1.0×10^{-4}	1.1×10^{-4}	2.0×10^{-4}	1.2×10^{-4}
(*z*)	2.5×10^{-4}	5.5×10^{-4}	5.0×10^{-4}	5.9×10^{-4}

Table 5.2: *NA* and *Δn* measurements vs. writing power for 1 mol% Zn doped $LiNbO_3$ with n_e substrate = 2.2109 [15] written at velocity 50 mm/min and spot radius 4 µm.

NA	**35mW**	**40mW**
(*y*)	0.044	0.049
(*z*)	0.017	0.025
Δn	**35mW**	**40mW**
(*y*)	6.7×10^{-5}	1.4×10^{-4}
(*z*)	4.3×10^{-4}	5.5×10^{-4}

Table 5.3: *NA* and *Δn* measurements vs. writing power for 4 mol% Zn doped $LiNbO_3$ with n_e substrate = 2.2113 [15] written at velocity 50 mm/min and spot radius 4 µm.

A small increase in *NA* and *Δn* is observable in the *z*-direction with writing power whilst again we see a trade-off of power vs. mode size in the *y*-direction. The lifetime mode profiles for 1 mol% Zn:$LiNbO_3$ are given in fig. 5.10 and for 4 mol% Zn:$LiNbO_3$ in fig. 5.11. After 6 days, there is an extremely weak mode profile for both zinc-doped samples, again less satisfactory than for congruent lithium niobate but underlining the fact that due to the decreased lithium vacancy concentration from the addition of zinc, weaker channel waveguides are produced.

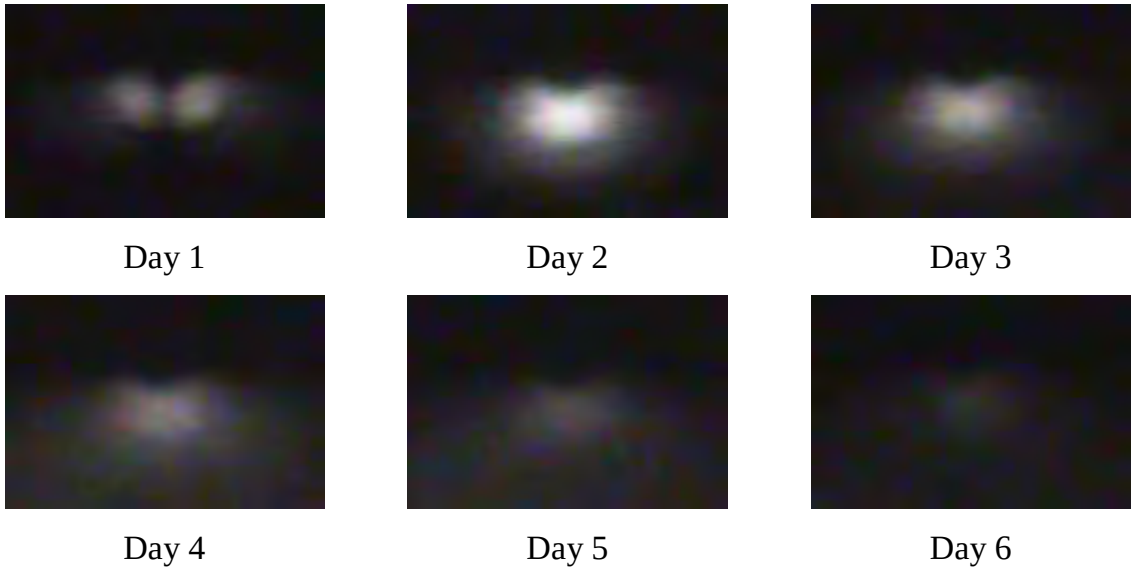

Figure 5.10: 1 mol% Zn:$LiNbO_3$ mode profile over lifetime written at writing power 45 mW, velocity 50 mm/min and spot radius 4 µm.

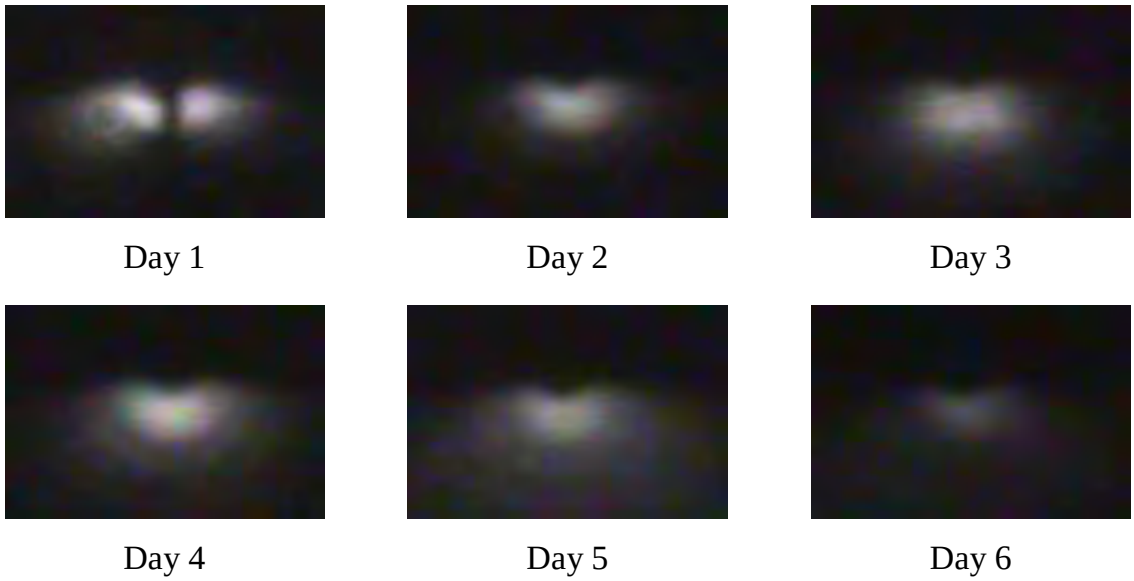

Figure 5.11: 4 mol% Zn:$LiNbO_3$ mode profile over lifetime written at writing power 45 mW, velocity 50 mm/min and spot radius 4 µm.

5.3.4 Fe:$LiNbO_3$

Iron-doped lithium niobate is used mainly for photorefractive applications such as holographic recording [16] as it is doped specifically to increase photorefractive

susceptibility. Chen first analysed refractive index changes in lithium niobate after illumination with a cw λ = 488 nm Ar ion laser [17] and Peithmann measured index changes of ~ 10^{-4} in Fe:$LiNbO_3$ due to pyroelectric fields after illumination of crystals with cw λ = 514 nm [18]. Iron-doped $LiNbO_3$ samples were tested in contrast to the MgO:$LiNbO_3$ and Zn:$LiNbO_3$ samples, as the iron ion (in common with most transitional metals) occupies lithium sites via substitution preferentially [19, 20].

Samples were obtained from Crystal Technology in two different compositions: 0.01 and 0.1 mol% Fe_2O_3. The increase in mol% doping increases the amount of charge migration in the material and the transmission curves of the two doped samples, 0.01 mol% and the highly doped 0.1 mol% Fe:$LiNbO_3$ are shown in fig. 5.12.

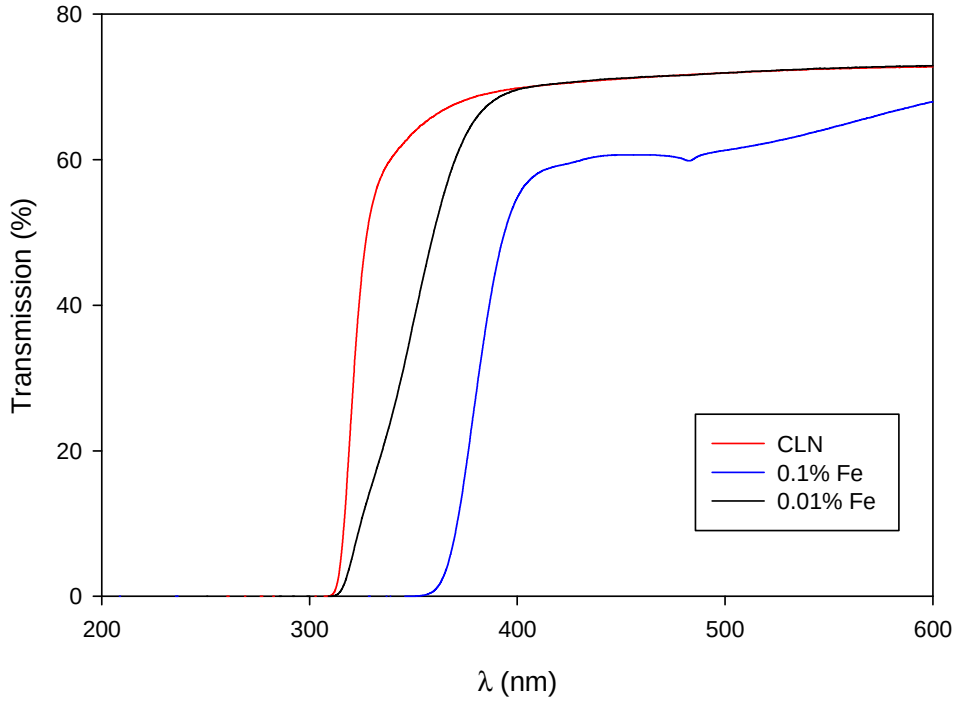

Figure 5.12: Transmission curve of 0.01 mol% and 0.1 mol% Fe-doped lithium niobate and undoped congruent lithium niobate.

The $1/e^2$ mode profile sizes vs. writing power illustrated in figs.5.13/5.14 show quite different profiles to congruent $LiNbO_3$ with an increased refractive index difference causing stronger confinement as seen with writing powers of 45 and 50 mW, the formation of multimode waveguides was also restricted by the surface melting as seen

with CLN. The highly doped 0.1 mol% sample did not show much more improvement over the 0.01 mol% doped samples, signifying a low optimum threshold doping level.

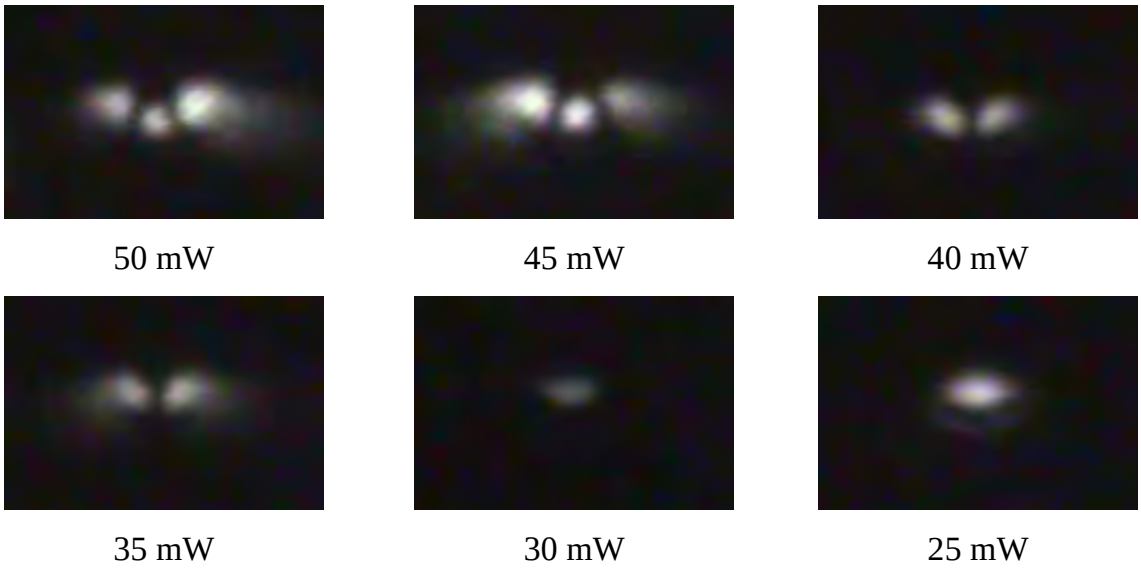

Figure 5.13: 0.01 mol% Fe:$LiNbO_3$ mode size vs. writing power written at velocity 50 mm/min and spot radius 4 µm.

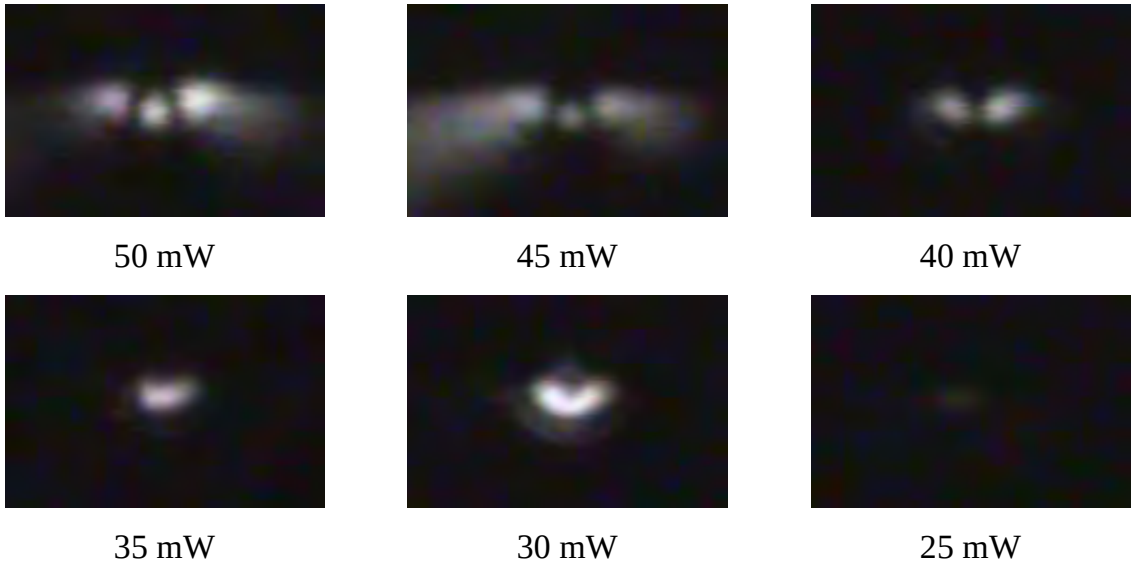

Figure 5.14: 0.1 mol% Fe:$LiNbO_3$ mode size vs. writing power written at velocity 50 mm/min and spot radius 4 µm.

Both doped samples demonstrated stronger confinement and smaller $1/e^2$ mode sizes compared with undoped congruent lithium niobate, as predicted by an increased index

difference, shown in fig 5.15. Propagation losses were higher however than in undoped congruent $LiNbO_3$ – single mode waveguide losses for both iron-doped samples and CLN are listed in table 5.4.

Writing Power (mW)	**Loss (dB/cm)**		
	0.01 mol% Fe	**0.1 mol% Fe**	**CLN**
30	3.65	3.78	
35		2.86	1.93

Table 5.4: Propagation losses vs. writing power for 0.01 mol% Fe:$LiNbO_3$, 0.1mol% Fe:$LiNbO_3$ and undoped congruent $LiNbO_3$ written at velocity 50 mm/min and spot radius 4 µm

The numerical aperture and Δn measurements for 0.1% doped Fe:$LiNbO_3$ in the *y*- and *z*-directions are given in table 5.5.

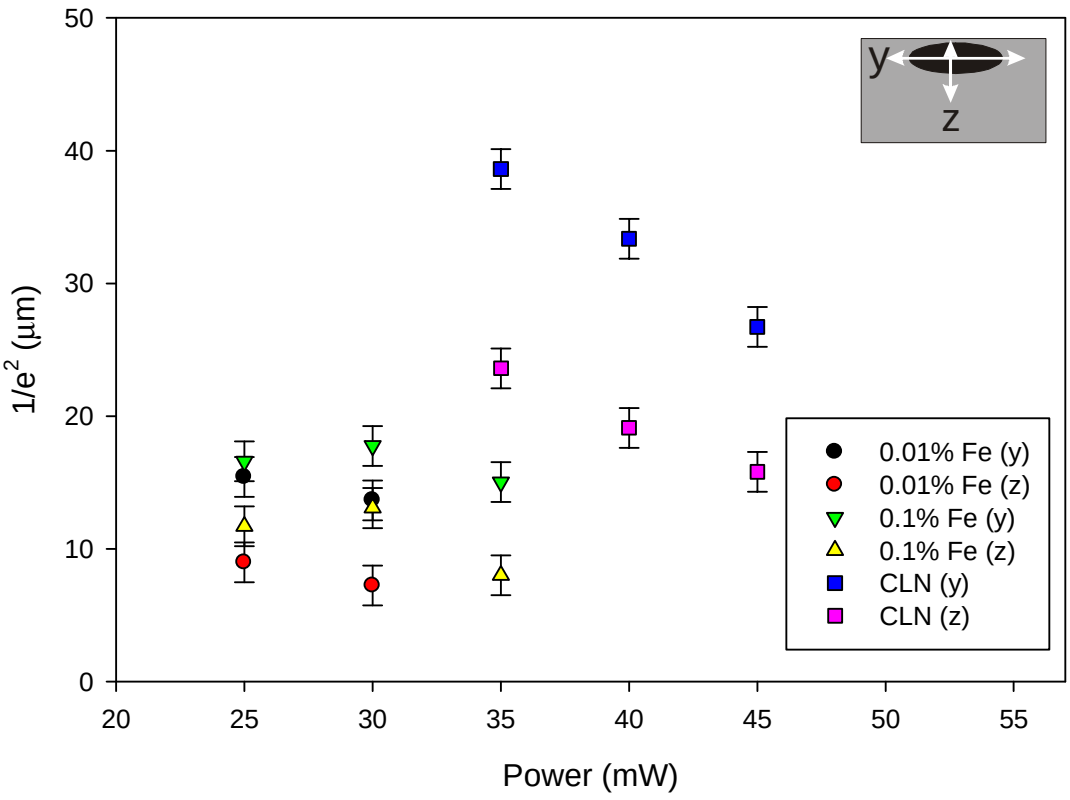

Figure 5.15: $1/e^2$ mode size vs. writing power comparison of 0.01% Fe:$LiNbO_3$, 0.1% Fe:$LiNbO_3$ and undoped congruent $LiNbO_3$ written at velocity 50 mm/min and spot radius 4 µm.

Waveguides in 0.01% doped Fe:$LiNbO_3$ were too weak for numerical aperture measurements to be performed but 0.1 mol% doped samples exhibited the largest single mode Δn observed, at ~ 1.3 x 10^{-3} in the *z* direction for a writing power of 35 mW.

The lifetime profiles of these guides are given in figures 5.16 and 5.17.

NA	**30mW**	**35mW**
(*y*)	0.033	0.038
(*z*)	0.056	0.075
Δn	**30mW**	**35mW**
(*y*)	2.6 x 10^{-4}	3.4 x 10^{-4}
(*z*)	7.3 x 10^{-4}	1.3 x 10^{-3}

Table 5.5: Numerical aperture and Δn measurements for 0.1% doped Fe:$LiNbO_3$ UV written waveguides at writing powers of 30 and 35 mW, velocity 50 mm/min and spot radius 4 µm.

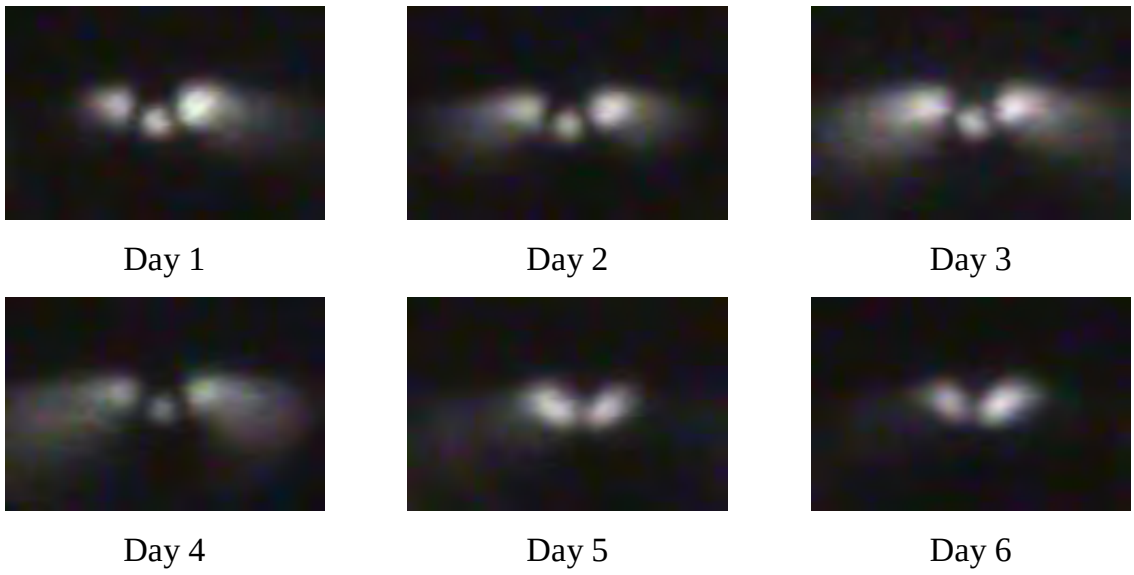

Figure 5.16: 0.01 mol% Fe:$LiNbO_3$ mode profiles vs. lifetime for waveguide written at 45 mW, beam velocity 50 mm/min and spot radius 4 µm.

Compared to the congruent $LiNbO_3$, the lifetime was considerably shorter for the 0.1 mol% doped sample and effectiveness as a waveguide was limited for the highly doped Fe:$LiNbO_3$. The 0.01 mol% Fe-doped sample conversely indicated mode degradation

over a longer timescale with a multimode output still after 6 days which repeats the suggestion of a low threshold doping level. Doping with small amounts of iron may extend the lifetime of waveguides to some extent but has to be weighed up with increased propagation loss.

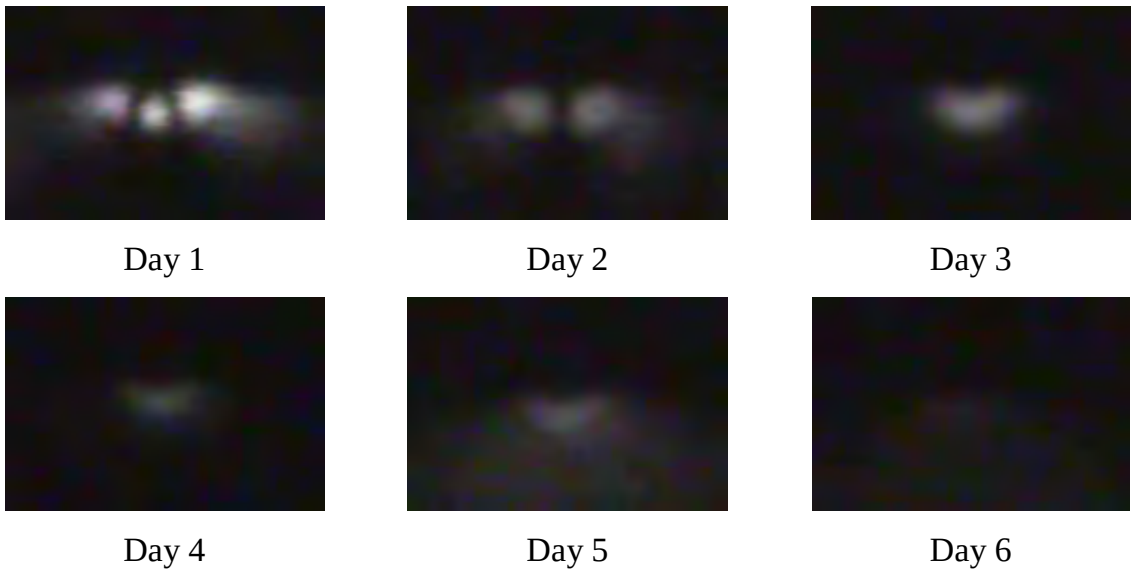

Figure 5.17: 0.1 mol% Fe:$LiNbO_3$ mode profile vs. lifetime for waveguide written at 45 mW, beam velocity 50 mm/min and spot radius 4 µm.

5.3.5 Er:$LiNbO_3$ & Nd:$LiNbO_3$

Doping the crystal with active ions, such as erbium or neodymium, allows the operation of laser waveguide devices. We have written channel waveguides into the +*z* face, 0.5 mm thick, neodymium-doped $LiNbO_3$ (1 mol%) obtained from Impex[6]. Channel waveguides were successfully fabricated in erbium-doped substrates and, although had higher propagation losses and lower numerical apertures than congruent lithium niobate with the same writing conditions, an attempt was made to make the sample lase. A tuneable Ti:sapphire laser was used as a pumping laser and the cavity created by attaching thin film mirrors to the waveguide end-faces. The attempt to get the neodymium-doped sample was unsuccessful as the substrate could be made to lase but

[6] Impex High-Tech GmbH., Hovesaarstr. 6, D-484432 Rheine. Germany.

the waveguides could not; for this reason, channel waveguides written on a +*z* face, 0.5 mm thick, 2 mol% erbium-doped lithium niobate sample to lase was not evaluate.

5.4 Titanium in-diffused $LiNbO_3$

In-diffused +*z* and –*z* face congruent lithium niobate samples were fabricated with a 100 nm thick titanium layer at $T \sim 1050°C$ in a dry O_2 atmosphere for 10 hours to give a planar waveguide device[7]. Channel waveguides were then UV written using similar parameters as used before on the Ti:in-diffused surface to establish if UV writing could simplify the current fabrication process involving photolithography. UV written waveguides have been fabricated previously in proton exchanged samples [21] and increased the index change of the planar waveguide, forming a channel on the surface with the channel waveguide lifetime unaffected after several months.

As with UV written congruent lithium niobate, TM polarisation only waveguides were present on both the +*z* and –*z* faces. Immediately obvious from observation of the mode profile was the depth of the UV written waveguides was restricted to the depth of the previously in-diffused titanium layer as shown in fig. 5. 18.

Planar +*z* $Ti:LiNbO_3$ UV written +*z* $Ti:LiNbO_3$

Figure 5.18: Comparison of planar $Ti:LiNbO_3$ waveguide vs. $Ti:LiNbO_3$ UV written channel waveguide written on +*z* face lithium niobate at velocity 50 mm/min and spot radius 4 µm. Both samples were in-diffused with a 100 nm thick Ti layer at 1050°C for ten hours in a dry O_2 atmosphere.

[7] Fabricated by Tleyane Sono, Optoelectronics Research Centre, University of Southampton, UK.

The power needed to write waveguides in Ti:$LiNbO_3$ was considerably less than undoped congruent $LiNbO_3$. Indeed, using powers ranging from 20 – 50 mW produced multi-mode waveguides when initially analysed after writing. After 24 hours, only the waveguides written at 20 mW had become single mode.

Numerical aperture and subsequent Δn measurements for waveguides, written at a writing power of 20 mW and velocity 50 mm/min, the day of writing and four days after writing are listed in table 5.6. The optical confinement due to the titanium in-diffused layer resulted in a higher numerical aperture than possible with congruent lithium niobate at ~ 0.1. This was consistent with other Ti:$LiNbO_3$ waveguides. After 4 days, the UV written waveguide in the *y*-direction had degraded significantly whereas the Ti:$LiNbO_3$ planar waveguide was mostly unaffected.

NA	**Day 1**	**Day 4**
(z)	0.096	0.098
(y)	0.035	0.007
Δn	**Day 1**	**Day 4**
(z)	2.1×10^{-3}	2.2×10^{-3}
(y)	2.8×10^{-4}	4.8×10^{-5}

Table 5.6: Numerical aperture and Δn results for UV written waveguides on titanium in-diffused lithium niobate written at a writing power of 20 mW, velocity 50 mm/min and spot radius 4 µm.

The use of UV writing on Ti:$LiNbO_3$ planar waveguides enables fabrication of channel waveguides on the substrate surface but the lifetime of the channel waveguide considerably degrades in the *y*-direction after several days.

5.4 Waveguides in $LiTaO_3$

5.4.1 Introduction

Fabrication of UV written waveguides in congruent lithium tantalate ($LiTaO_3$) was performed with identical conditions to waveguides in lithium niobate. Samples were cut and end-face polished before writing. The samples were single-crystal 0.5 mm thick +z-face $LiTaO_3$ 2" diameter wafers manufactured by Yamaju Ceramics[8]. Several properties of $LiTaO_3$ are outlined in table 5.7.

Lithium tantalate has a similar physical structure as lithium niobate and is preferred to lithium niobate for applications such as high power frequency conversion due to it's higher optical damage threshold [22]. Lithium tantalate is a positive uniaxial birefringent crystal and has an absorption edge in the ultraviolet but, shifted deeper into the ultraviolet region and is also optically opaque at λ = 244 nm as illustrated in fig. 5.19.

Property	Value
Density	7460 kg m^{-3}
Crystal Structure	3m
Melting Point	1923 K
Optical Transmission	0.45 - 5.0 µm
Curie Temperature	907 K
Specific Heat Capacity	676 J kg^{-1} K^{-1}
Refractive indices at λ = 633 nm	n_e= 2.180
	n_o= 2.176

Table 5.7: Some properties of $LiTaO_3$.

[8] Yamaju Ceramics Co., Ltd. Via Roditi International Corp. Ltd., Carrington House, 130 Regent St., London. W1B 5SE. UK.

Initial viewing of the written waveguides revealed light guidance in the *x*- and *y*-propagating directions for TM modes only, as seen in congruent +*z*-face $LiNbO_3$ and no guidance on the –*z* face. Waveguides written with a beam radius of 3 µm exhibited surface damage for beam powers above 40 mW and mode profiles of written waveguides are shown in figure 5.20. A difference to lithium niobate was the ability to propagate a strong optical mode below 30 mW. Fig. 5.21 illustrates the mode profile size ($1/e^2$) vs. writing power and compares lithium tantalate with lithium niobate.

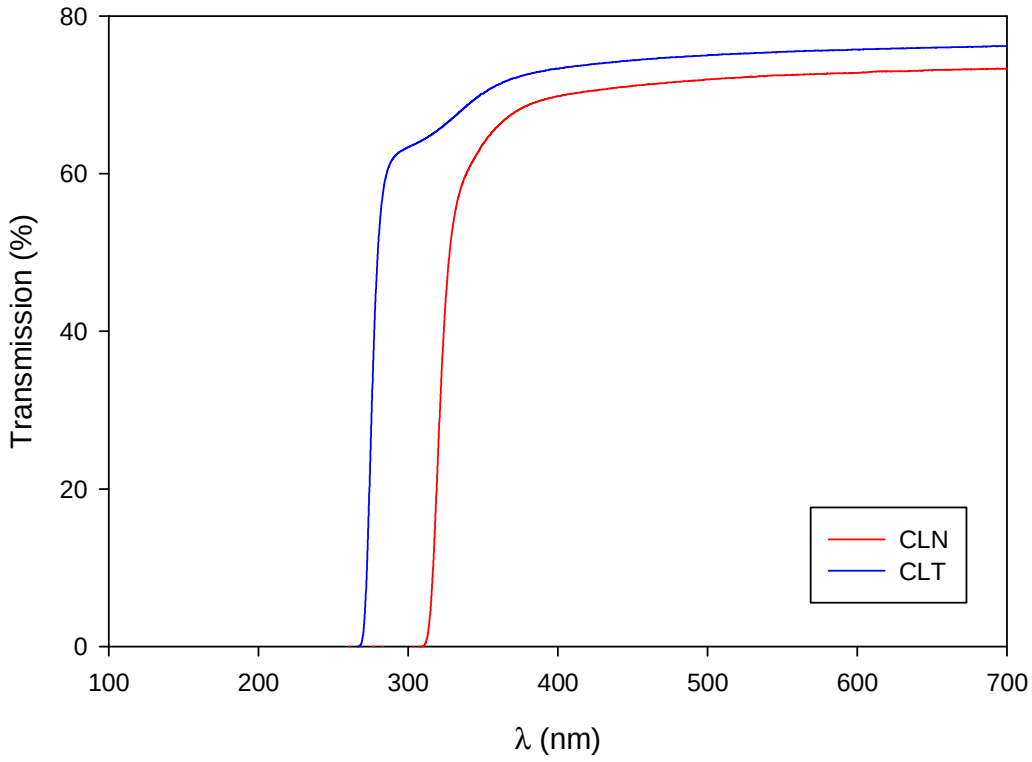

Figure 5.19: Transmission spectrum for congruent $LiTaO_3$ and $LiNbO_3$.

As seen from figure 5.21, the mode profiles for lithium tantalate were smaller than lithium niobate and had a smaller degree of change as the writing power increases.

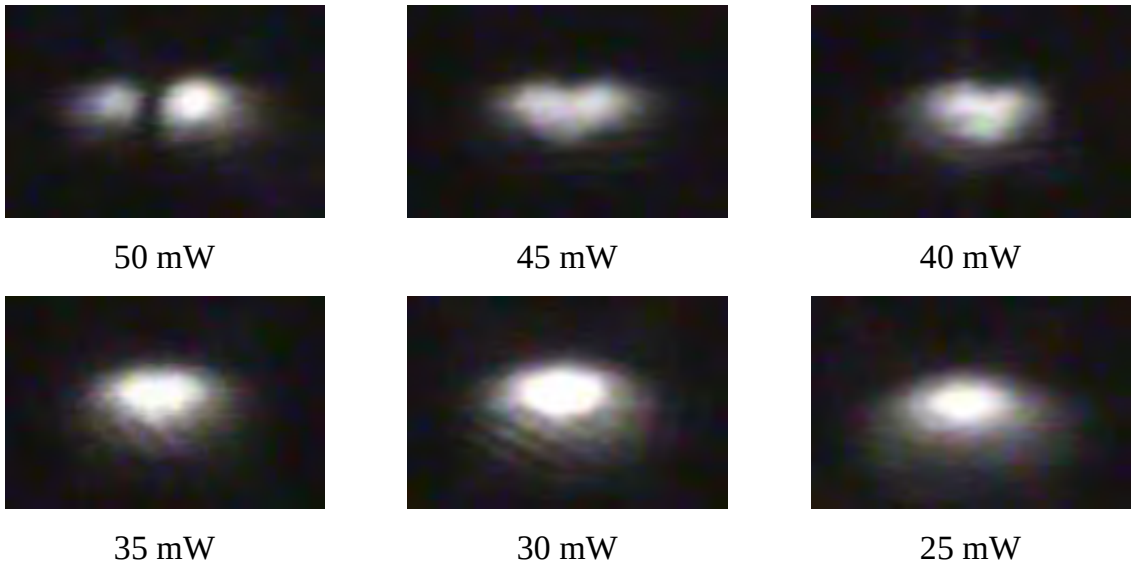

Figure 5.20: Mode profiles vs. writing power for waveguides written in +z lithium tantalate written at velocity 50 mm/min and spot radius 4 µm.

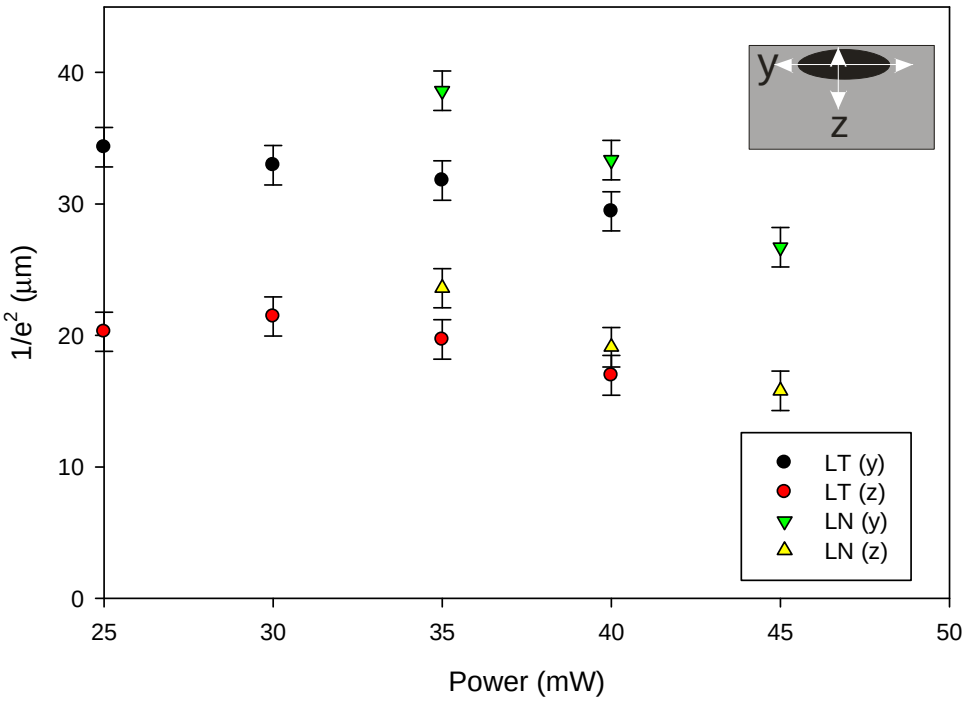

Figure 5.21: Comparison of $1/e^2$ mode sizes vs. writing power for $LiTaO_3$ and $LiNbO_3$ written at velocity 50 mm/min and spot radius 4 µm.

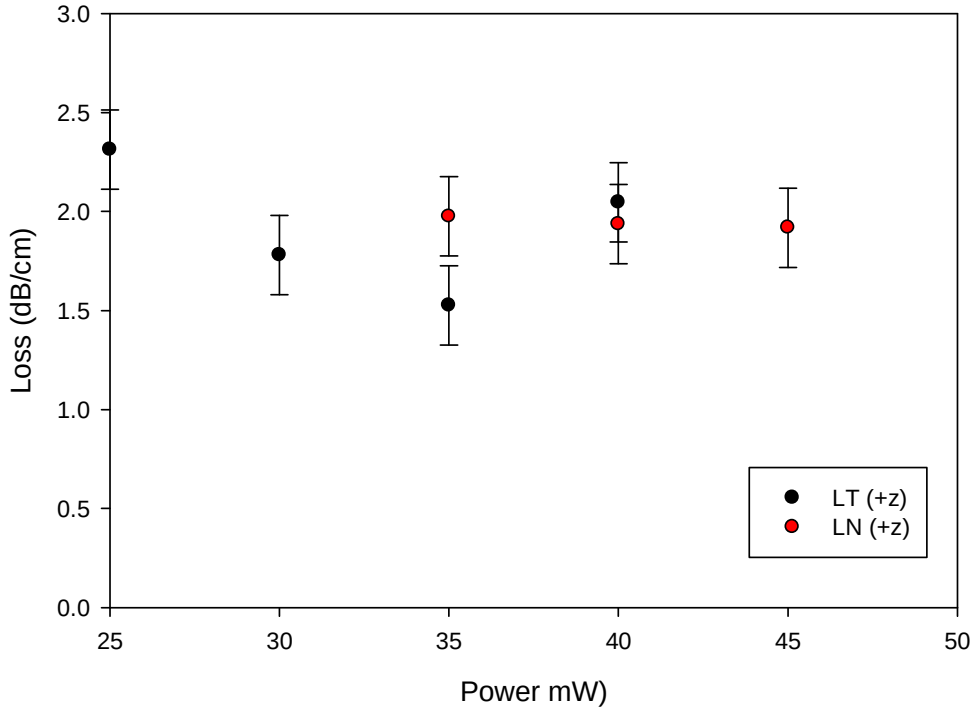

Figure 5.22: Comparison of loss vs. writing power for +*z* face $LiTaO_3$ and $LiNbO_3$ written at velocity 50 mm/min and spot radius 4 µm.

Losses measured in comparison with congruent lithium niobate are shown in fig. 5.22. Although the losses were smaller than lithium niobate, the lifetime of the waveguides was extremely short and considerable decay of the output power occurred within 4 hours.

NA	**25 mW**	**30 mW**	**35 mW**	**40 mW**
(*y*)	0.015	0.020	0.027	0.030
(*z*)	0.026	0.025	0.024	0.032
Δn	**25 mW**	**30 mW**	**35 mW**	**40 mW**
(*y*)	5.2×10^{-5}	9.3×10^{-5}	1.8×10^{-4}	2.1×10^{-4}
(*z*)	1.6×10^{-4}	1.4×10^{-4}	1.3×10^{-4}	2.4×10^{-4}

Table 5.8: Numerical aperture and *Δn* results for UV written waveguides on congruent $LiTaO_3$ written at velocity 50 mm/min and spot radius 4 µm.

The numerical aperture and Δn of the UV written waveguides vs. writing power are shown in table 5.8. As the writing power increased, the confinement of the mode in the *z*-direction increased but decreased in the *y*-direction – this was consistent with the high writing power causing surface damage and constricting the mode profile.

Lithium tantalate is less effective as a waveguide medium than lithium niobate as demonstrated by a lower Δn and lifetime and this is assumed to be due to the bonding structure of the crystal compared to lithium niobate; the higher melting temperature indicates stronger covalent bonding between the constituent ions and this reduces the amount of mobile lithium ions in the crystal.

5.5 Lithium Diffusion Mechanism

The additional evidence in this chapter of UV written waveguides in doped lithium niobate indicates that the mechanism can be interpreted via a surface out-diffusion and sideways lithium ion movement in the crystal. Stoichiometric lithium niobate, with increased lithium ion content and reduced intrinsic defects, supports weaker waveguide modes than congruent lithium niobate and this is attributed to a reduction in sideways movement of lithium ions due to decreased vacancy sites.

The lack of waveguide formation in magnesium-doped $LiNbO_3$ and weak optical modes produced in zinc-doped $LiNbO_3$ can also be explained by the concentration of the dopant ions and their occupancy of lithium ion vacancies. The magnesium-doped sample was doped above the optical damage threshold and this point has been inferred as the level where the dopant ion has filled lithium ion vacancies and begins to replace niobium ions on their sites; as the mobile lithium ions from the UV exposure has insufficient movement available via the vacancy sites, a region of increased index cannot be formed and thus no mode is propagated. A comparable effect occurs in the zinc-doped samples except the threshold doping level is greater and both samples tested were doped below this level therefore lithium vacancies were still available for lithium ion movement.

Although the observance of double mode waveguides in iron-doped lithium niobate compared to single mode waveguides in undoped lithium niobate suggests a greater index difference for the same writing conditions, the lifetime is shorter and propagation losses higher. Doping $LiNbO_3$ with iron ions has the substitution of iron ions for lithium ions at the lithium octahedral sites; this substitution drives lithium ions into other positions such as vacancy sites and therefore reduces the sites available for mobile lithium ions.

5.6 Conclusion

UV written waveguides have been fabricated in a variety of different doped lithium niobate samples and in lithium tantalate. While waveguide fabrication is indeed possible in these samples, the propagation losses and mode confinement of the different materials are inferior to waveguides in congruent lithium niobate. Results from doped lithium niobate strengthen the hypothesis that out-diffusion and sideways diffusion of lithium ions is the possible mechanism for waveguide formation in congruent and doped lithium niobate. While out-diffusion occurs at the surface in all samples as implied by SIMS analysis, the sideways lithium diffusion is reduced by doping the substrate; this reduces the lithium ions site vacancies and hence the available free sites for itinerant lithium ions to diffuse to and so the index difference Δn is reduced as seen experimentally. Waveguide formation was also shown to be possible in lithium tantalate.

5.7 References

1. Wohlecke, M., G. Corradi, and K. Betzler, *Optical methods to characterise the composition and homogeneity of lithium niobate single crystals.* Applied Physics B: Lasers and Optics, 1996. **63**(4): p. 323-330.

2. Jermann, F., M. Simon, and E. Kratzig, *Photorefractive properties of congruent and stoichiometric lithium niobate at high light intensities.* J. Opt. Soc. Am. B, 1995. **12**(11): p. 2066.

3. Chen, Y.L., J.J. Xu, X.Z. Zhang, Y.F. Kong, X.J. Chen, and G.Y. Zhang, *Ferroelectric domain inversion in near-stoichiometric lithium niobate for high efficiency blue light generation.* Applied Physics A: Materials Science & Processing, 2002. **74**(2): p. 187-190.

4. Schlarb, U. and K. Betzler, *Refractive indices of lithium niobate as a function of temperature, wavelength, and composition: A generalized fit.* Physical Review B, 1993. **48**(21): p. 15613.

5. Brinkmann, R., W. Sohler, and H. Suche, *Continuous-wave Er-diffused $LiNbO_3$ waveguide laser.* Electronic Letters, 1993. **27**: p. 415.

6. Bryan, D.A., R. Gerson, and H.E. Tomaschke, *Increased optical damage resistance in lithium niobate.* Applied Physics Letters, 1984. **44**(9): p. 847-849.

7. Gerson, R., J.F. Kirchhoff, L.E. Halliburton, and D.A. Bryan, *Photoconductivity parameters in lithium niobate.* Journal of Applied Physics, 1986. **60**(10): p. 3553-3557.

8. Donnerberg, H., *Comments on the Defect Chemistry of Magnesium-Doped Lithium Niobate ($LiNbO_3$).* Journal of Solid State Chemistry, 1996. **123**(2): p. 208-214.

9. Xue, D., K. Betzler, and H. Hesse, *Induced Li-site vacancies and non-linear optical behavior of doped lithium niobate crystals.* Optical Materials, 2001. **16**(3): p. 381-387.

10. Sweeney, K.L., L.E. Halliburton, D.A. Bryan, R.R. Rice, R. Gerson, and H.E. Tomaschke, *Threshold effect in Mg-doped lithium niobate.* Applied Physics Letters, 1984. **45**(7): p. 805-807.

11. Volk, T.R., V.I. Pryalkin, and N.M. Rubinina, *Optical-damage-resistant $LiNbO_3$:Zn crystal.* Optics Letters, 1990. **15**(18): p. 996-998.

12. Suhara, T., T. Fujieda, M. Fujumura, and H. Nishihara, *Fabrication of Zn:$LiNbO_3$ Waveguides by Diffusing ZnO in Low-Pressure Atmosphere.* Japanese Journal of Applied Physics, 2000. **39 Part 2**(8B): p. L864-L865.

13. He, X. and D. Xue, *Doping mechanism of optical-damage-resistant ions in lithium niobate crystals.* Optics Communications, 2006. **265**(2): p. 537-541.

14. Zhang, Y., Y.H. Xu, M.H. Li, and Y.Q. Zhao, *Growth and properties of Zn doped lithium niobate crystal.* Journal of Crystal Growth, 2001. **233**(3): p. 537-540.

15. Schlarb, U., M. Wohlecke, B. Gather, A. Reichert, K. Betzler, T. Volk, and N. Rubinina, *Refractive indices of Zn-doped lithium niobate.* Optical Materials, 1995. **4**(6): p. 791-795.

16. Frejlich, J., I. de Oliveira, L. Arizmendi, and M. Carrascosa, *Fixed holograms in iron-doped lithium niobate: simultaneous self-stabilized recording and compensation.* Apl. Opt., 2007. **46**(2): p. 227-233.

17. Chen, F.S., *Optically Induced Change of Refractive Indices in $LiNbO_3$ and $LiTaO_3$.* Journal of Applied Physics, 1969. **40**(8): p. 3389-3396.

18. Peithmann, K., A. Wiebrock, K. Buse, and E. Krätzig, *Low-spatial-frequency refractive-index changes in iron-doped lithium niobate crystals upon illumination*

with a focused continuous-wave laser beam. J. Opt. Soc. Am. B, 2000. **17**(4): p. 586-592.

19. Rebouta, L., P.J.M. Smulders, D.O. Boerma, F. Agulló-Lopez, M.F. da Silva, and J.C. Soares, *Ion-beam channeling yields of host and impurity atoms in $LiNbO_3$: Computer simulations.* Physical Review B, 1993. **48**(6): p. 3600.

20. Rebouta, L., M.F.d. Silva, J.C. Soares, M. Hage-Ali, J.P. Stoquert, P. Siffert, G. Sanz, J.A. a, Di, E. guez, Agull, L., and F. pez, *Lattice Site of Iron in $LiNbO_3(Fe^{3+})$ by the PIXE/Channelling Technique.* EPL (Europhysics Letters), 1991. **14**(6): p. 557-561.

21. Gallo, K., C.B.E. Gawith, I.T. Wellington, S. Mailis, R.W. Eason, P.G.R. Smith, D.J. Richardson, and S.M. Kostritskii, *Ultraviolet writing of channel waveguides in proton-exchanged $LiNbO_3$.* Journal of Applied Physics, 2007. **101**(1): p. 014110-3.

22. Matsumoto, S., E.J. Lim, H.M. Hertz, and M.M. Fejer, *Quasiphase-matched second harmonic generation of blue light in electrically periodically-poled lithium tantalate waveguides.* Electronics Letters, 1991. **27**(22): p. 2040-2042.

23. Muir, A.C., G.J. Daniell, C.P. Please, I.T. Wellington, S. Mailis, and R.W. Eason, *Modelling the formation of optical waveguides produced in $LiNbO_3$ by laser induced thermal diffusion of lithium ions.* Applied Physics A: Materials Science & Processing, 2006. **83**: p. 389-396.

Chapter 6

UV Pulsed Direct Writing in $LiNbO_3$

Experiments using a λ = 266 nm pulsed laser have revealed domain formation on the surface of lithium niobate. The use of a phasemask during UV writing has allowed fabrication of ordered domain structures. Results are presented showing a degree of control of the formation of such domain distributions. An explanation of the mechanism is proposed which involves surface ablation combined with a Nb anti-site model.

6.1 Introduction

Fabrication of periodically inverted domain patterns in ferroelectric materials such as lithium niobate and lithium tantalate has been widely researched for the realization of applications such as quasi-phase-matched (QPM) non-linear devices and electro-optic Bragg deflectors.

While several techniques such as Li_2O out-diffusion [1], proton-exchange followed by heat treatment [2], Ti-indiffusion [3], scanning force microscopy [4], e-beam [5, 6] and electric field poling [7] have been successfully used for domain inversion in lithium niobate crystals over the past few years, even the most routinely used technique of electric-field-induced domain inversion (E-field poling) becomes problematic when periodicities of a few microns and below are required for first-order QPM non-linear processes for the generation of blue or near ultraviolet light.

To overcome the limitations associated with E-field poling, the technique of light-assisted E-field poling (LAP) which takes advantage of the ultraviolet light-induced transient change in the coercive field of the illuminated ferroelectric material has been developed during the past few years for lithium tantalate [8, 9] and lithium niobate [10-12] crystals. Similar LAP experiments that use high intensity visible laser light, which has the effect of reducing the coercive field through a light-induced space charge field, have recently demonstrated directly written domain structures of ~2 μm width in undoped lithium niobate [8] and ~2 μm overall size in doped lithium niobate samples [9].

To improve on LAP the goal of removing the applied electric field technique to pole the crystal would greatly simplify the method of fabricating PPLN. Previously, domain formation was observed when *-z* face iron-doped lithium niobate was illuminated with 532 nm light while simultaneously being etched with 48% HF acid [15, 16]. Surface domains only appeared with the presence of acid and light and these were at specific intensities; high intensities caused frustration of etching while very low intensities cause no surface modifications. In between these intensities, self-organised patterns were observed.

An even simpler method for surface domain inversion has been investigated recently. This method exploits the interaction of intense ultraviolet laser light with ferroelectric lithium niobate to fabricate inverted ferroelectric domains of sub-micron width and few micron separation [17, 18]. The resulting all optically poled (AOP) ferroelectric domains in this case nucleate randomly within the irradiated laser spot and propagate along the principal crystal symmetry directions. Of course, for any practical application it is necessary to have control over the nucleation and propagation of the ferroelectric domains using such a method. It is shown in this chapter that it is indeed possible to impose a degree of control in the alignment of these UV induced surface domains by illuminating with a spatially modulated UV laser beam i.e. using a phasemask.

This chapter outlines investigations to show that it is possible to obtain ordered and aligned surface domains via a periodic intensity pattern produced with a phase mask. Section 6.2 summarises the apparatus and method used to achieve this domain formation and section 6.3 elaborates on the characterization of the laser-modified crystals; the domain nature was investigated via hydrofluoric acid etching of the UV exposed surface and then analysed with a scanning electron microscope (SEM). Section 6.4 proposes an explanation of the mechanism behind AOP and the chapter is concluded in section 6.5.

6.2 Experimental Procedure

Undoped congruent lithium niobate crystal samples were cut from 500 μm thick wafers obtained from Crystal Technology optically polished *z*-faces. Two different pulsed UV laser sources were used to investigate the wavelength sensitivity of the effect. The first laser was a frequency-quadrupled Nd:YVO_4 operating at $\lambda = 266$ nm with up to ~5 mJ pulses of ~10 ns duration. The second laser system was a frequency-doubled dye laser (Continuum Powerlite 8000) pumped by a frequency doubled Q-switched Nd:YAG laser. The dye laser system was tuneable from 289 nm to 329 nm, producing 0.5-1.5 mJ pulses of ~7 ns duration. Although this degree of tuneability was in principle an advantage that enabled exposure around the UV absorption edge of $LiNbO_3$, the laser

output proved to have a highly inhomogeneous beam profile with undesirable local intensity variations. For this reason an aperture was used in an attempt to select an acceptably uniform area of the beam.

Two different phase-masks, both with a period of 726 nm, were used for the UV laser exposures, optimized for λ = 266 nm and λ = 298 nm respectively. The experimental results and subsequent analysis suggested that the effect was essentially insensitive to the UV wavelength used (298 nm and 266 nm), however due to the poor beam quality of the dye laser beam (298 nm), it is the 266 nm results that are mainly discussed here.

Two different cuts of lithium niobate were tested, *z*- and *y*-cut. Domain formation was confirmed on the *z*-cut samples but on the *y*-cut samples the phase mask did not produced ordered domain formation. For the *z*-cut samples, the phase mask was carefully aligned so that the grating lines would be parallel to one of the *y*-axes of the lithium niobate crystal, thereby ensuring preferential *y*-axis illumination and hence an increase in the probability for the optically induced ferroelectric inversion to occur along this particular axis.

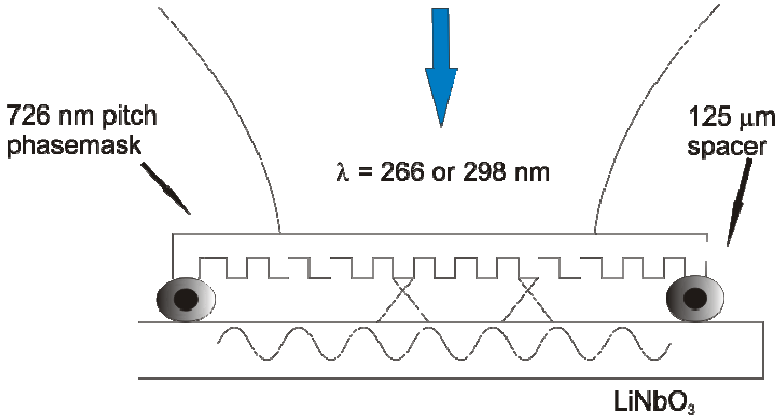

Figure 6.1: Phasemask assembly

The phase mask was separated from the sample by two spacers consisting of two sections of standard telecom optical fibres having a diameter of 125 µm as shown in fig 6.1. After illumination, the UV exposed sample surface was etched for 20 minutes in 48% hydrofluoric acid (HF) and inspected with optical and scanning electron

microscopy (SEM). Single and multi-pulse (up to 10 pulses) exposures at 266 nm, over a wide range of fluences (between 5 and 200 mJ/cm^2), were performed on crystal samples and compared with samples exposed under the same conditions but without the phase-mask.

6.3 Results and Discussion

6.3.1 Z-cut exposures

Initial experiments were conducted to establish the single pulse ablation threshold for the +*z* face of lithium niobate samples at both laser wavelengths. It is important to note at this point that AOP occurs near the ablation threshold. The single pulse ablation thresholds for 266 nm and 298 nm light were established experimentally to be between 95 - 105 mJ/cm^2. However, these figures are subject to some degree of uncertainty due to the intrinsic spatial non-uniformity and temporal (pulse to pulse) fluctuation of the dye laser. Experiments in the literature with longer UV wavelengths have revealed considerably higher ablation thresholds due to large changes in absorption coefficients over a few nm - Rodenas reported a threshold of 850 J/cm^2 at 355 nm [10] and Eyett a threshold of 900 mJ/cm^2 at 308 nm [11]. The high fluences at these wavelengths are due to the longer optical penetration depths as $LiNbO_3$ is optically transparent at $\lambda >$ ~300 nm. This small shift of wavelength is useful for a fabrication technique as it allows low fluence, inexpensive diode-pumped solid state lasers to be used instead of bulky excimer gas lasers.

Areas of the samples were irradiated through the phase-mask at fluences significantly below the ablation threshold showed no evidence of domain formation. There exists, however, a narrow range of fluences (~ 90 - 150 mJ/cm^2) between which domain formation parallel to the phase-mask lines is possible with some limited degree of ablative damage. Considerably above the ablation threshold for a single pulse, weak domain formation was also observed, but it was accompanied by pronounced trenches from the attendant ablation grating. Nevertheless, it is rather easy to distinguish between the laser damage pattern as subsequently revealed by the chemical etching and

the ferroelectric pattern because etched ferroelectric domains are deeper and sharper than the ablated trenches.

The effect of UV illumination without the use of a phase mask is shown in figure 6.2[9]. Here an SEM scan of the irradiated surface after HF acid etching is presented showing the random nucleation and propagation of photo-induced domains along the three equivalent symmetry directions of the crystal. This effect has been extensively discussed before in references [12, 13].

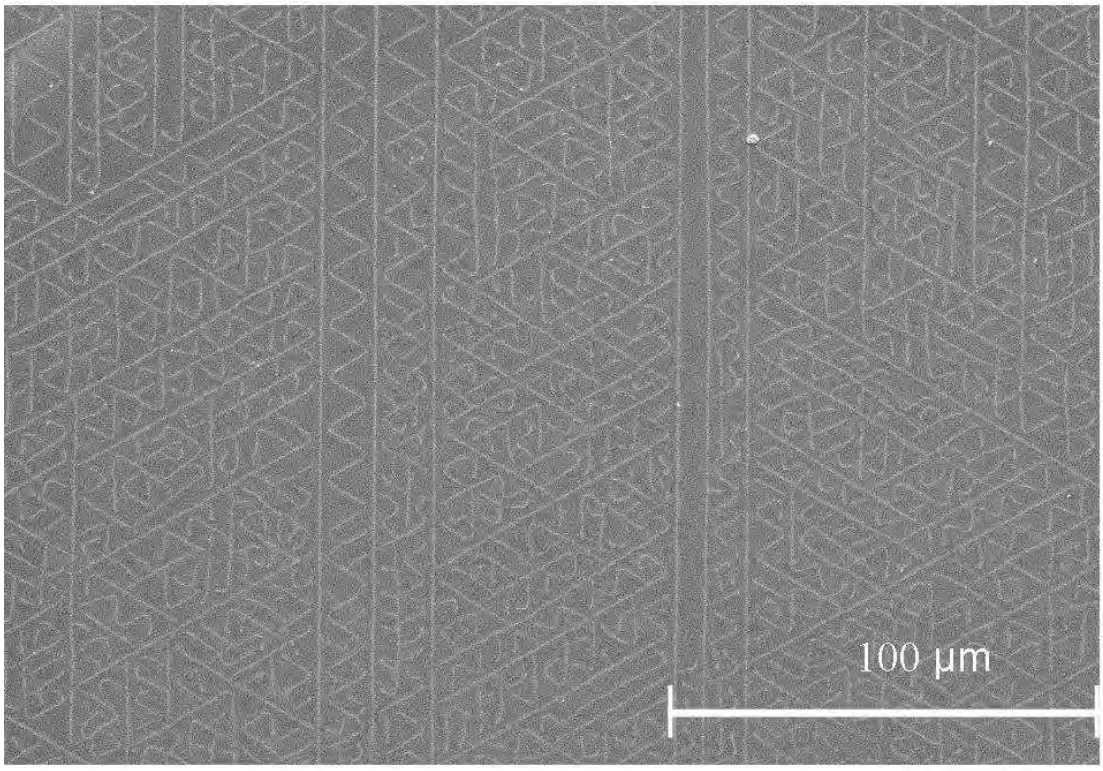

Figure 6.2: SEM micrograph of the etched +*z* face following illumination with a non-spatially-modulated beam. The exposure was performed with the frequency-quadrupled YAG laser at λ = 266 nm, with fluence 140 mJ/cm^2 (above the threshold for ablation).

The observed structures have been proven to be domains via several methods; the first uses the very common technique of HF acid etching to reveal the domain nature of the irradiated structures. The second method uses scanning force microscopy in piezo-response mode and shows these domains are consistent with bulk poled samples [14,

[9] Micrograph obtained from Dr. C. Valdivia as part of experiments in ref 17.

15]. The third technique employed focussed ion beam (FIB) milling to show the domain depth is consistent with other surface poled structures [12]. The classical triangular shape of observed domain structures are synonymous with other domain studies.

Figure 6.3 shows an SEM image of the crystal surface that has been irradiated using a phase mask. The difference between figs. 6.2 and 6.3 is readily apparent. Figure 6.3 shows that the majority of the photo-induced domains are aligned along a specific symmetry direction (vertical in the figure), dictated by the orientation of the phase mask which was arranged to coincide with one of the crystal symmetry axes as shown in the inset direction indicator (top right). This was expected as the AOP domains nucleate only in the presence of optical intensities at or around the damage threshold and propagate along the symmetry directions.

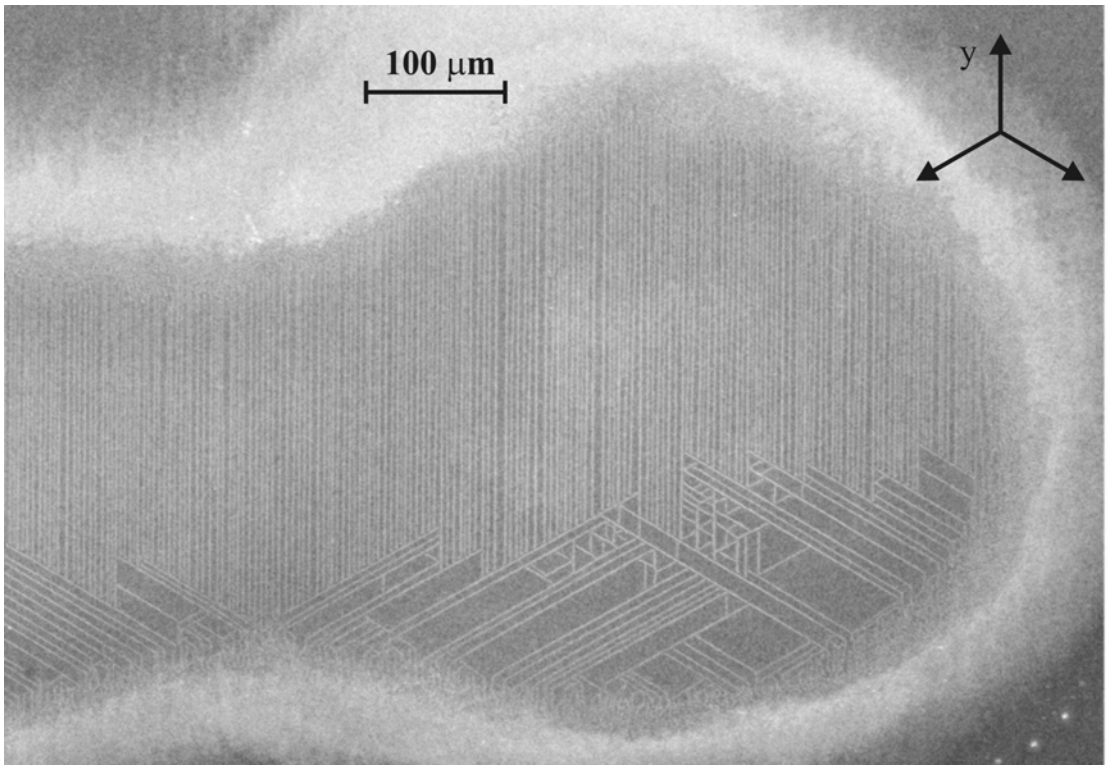

Figure 6.3: SEM micrograph of the etched +*z* face following illumination via a phase mask. The three symmetrical *y*-axes are indicated on the top right of the figure. The exposure was also performed with the frequency-quadrupled YAG laser at λ = 266 nm, with the fluence 105 mJ/cm^2 (above the threshold for ablation).

Further studies have also indicated that surface damage is always present when domain formation occurs. In this experiment there is light only along a specific symmetry directions where the AOP domains are encouraged to nucleate and propagate resulting in the direction preference observed.

However, careful investigation of this domain formation shows that the effect is more complex than initially thought. The SEM image presented in Figure 6.4 shows a magnified section of figure 6.3. Although the domain lines formed are parallel to the phase mask lines, it is clear that the periodicity imposed by the phase mask (Λ = 0.726 μm) has not been faithfully reproduced in the resultant domain spacing. While measured domain widths are in the range from 200 - 700 nm, the distance between them varies between ~3 μm and ~7.5 μm; this behaviour appears to underlie all such AOP experiments performed.

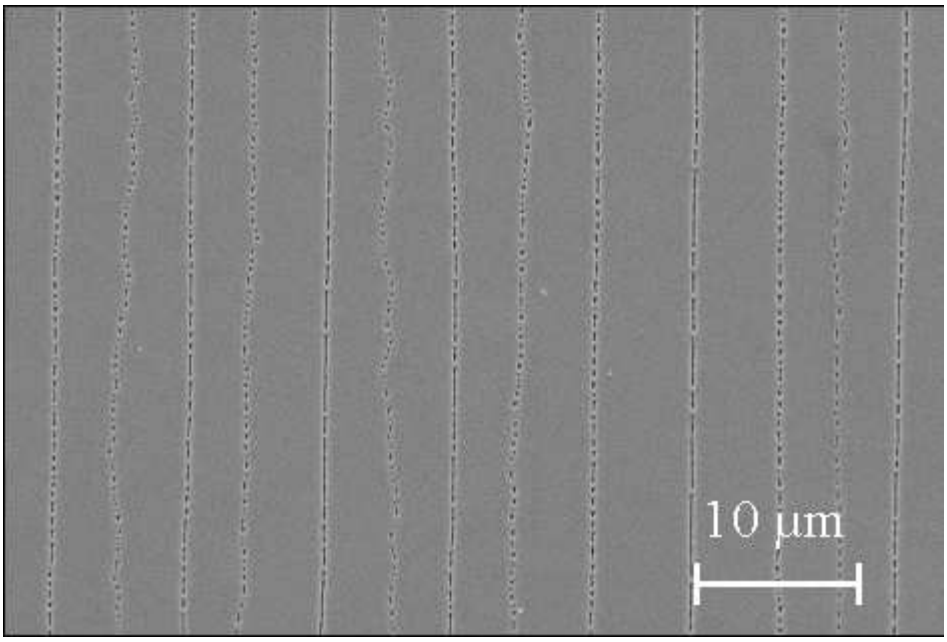

Figure 6.4: SEM close-up of aligned discrete domain patterned region within the central area of a sample exposed via a phase mask at a laser fluence ~100 mJ/cm^2.

The imposition of a spatially extended light pattern with sub-micron periodicity, such as from the phase mask, appears to be opposed by the physical mechanism responsible for AOP. The behaviour observed in fig. 6.4 is suggestive of an electrostatic mechanism, as the photo-generated surface charge, likely to occur at the highly UV absorbing surface, will result in electrostatic repulsion and re-organisation (e.g.

clustering around surface defects) which imposes a characteristic electrostatic interaction length that overrides the imposed periodicity of the intensity pattern as the material is unable to both nucleate and subsequently sustain such closely packed domain distributions via a strictly AOP process only. Another interesting observation can be made in figure 6.4 that also suggests electrostatic interaction between individual domains, namely that the domain lines produced are not continuous, but consist of irregular sections along the *y*-axis direction.

Of interest is the difference between apparently straight domain patterning at approximate values of 10Λ, and irregular domain lines that develop between them, as can also be seen in figure 6.4. This observation indicates that the initial conditions such as the sequence of nucleation and propagation of the domains are important. One possible explanation for the formation of the irregular domain lines between the straight lines could be that they were developed under the electrostatic influence of the previously formed straight lines.

Further investigation of the surface topography suggests that local intensity level variations significantly affect the AOP domain formation. Since there are variations of the local intensity across the laser spot (e.g. from the centre to the edge) different parts of the illuminated surface showed different stages of nucleation and propagation of the photo-induced domains as a function of intensity.

Figure 6.5 shows a spot exposed to a 266 nm single pulse of 150 mJ/cm^2 fluence with three snapshots from a) the top edge, b) the centre of the spot and c) the bottom edge of the spot. The fluence of the incident laser pulse is high enough to form an ablation grating but, due to the low magnitude of the fluence at the edges, the initial conditions of domain nucleation with small domain dots are observable; as we move closer to the centre where the intensity of the spot is at maximum the domains become ordered along the phasemask and form lines. An interesting observation is at low spatial intensities of the incident pulse, the domain dots are smaller and more closely packed than the domain lines at high intensities. There is also no dominant *y*-axis growth preference at low intensities.

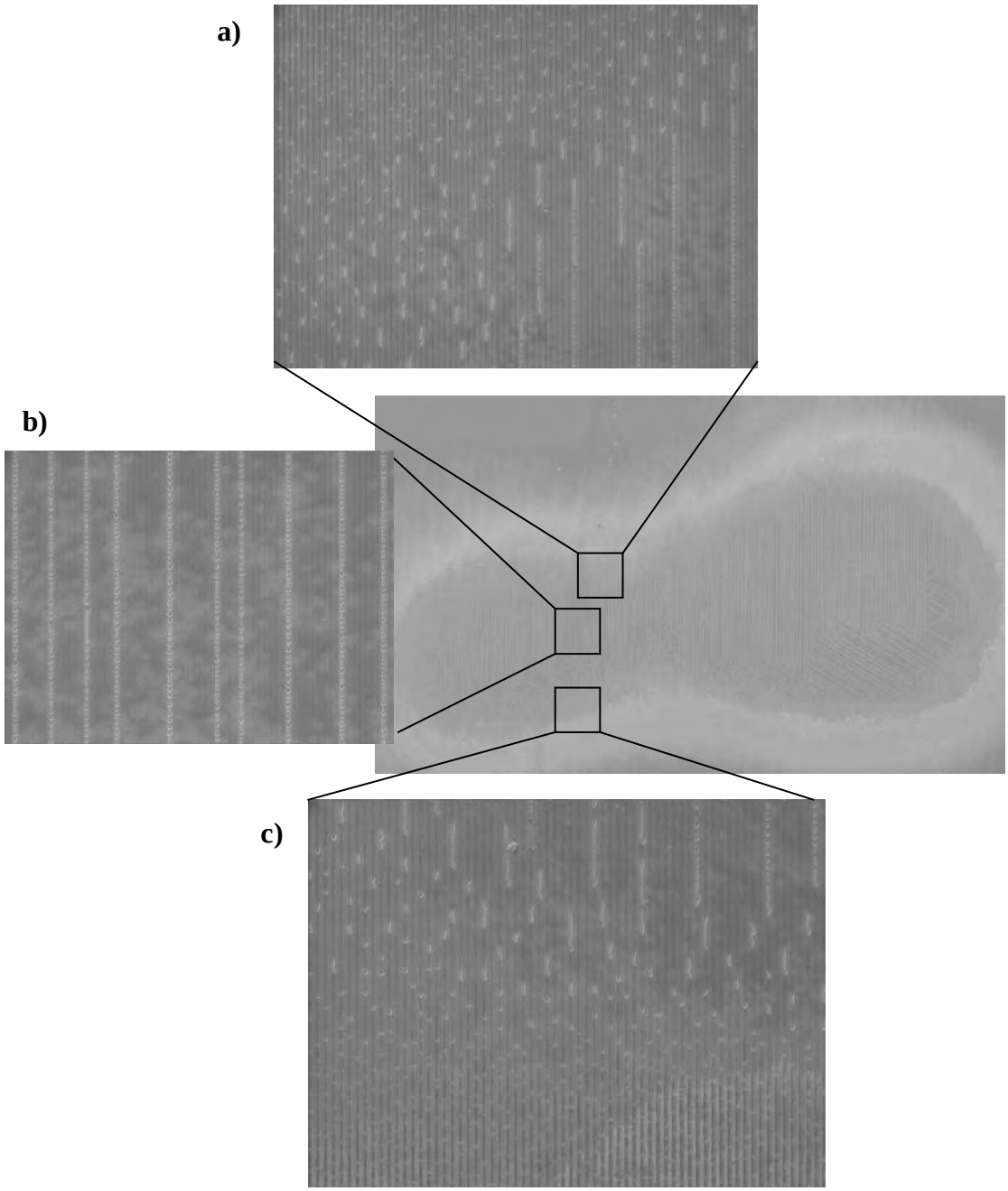

Figure 6.5: Spot illuminated on +z $LiNbO_3$ with single pulse at 150 mJ/cm^2 at edges a) and c) and centre b).

Figure 6.6 is a magnified version of fig 6.5c. It becomes immediately clear after observing this SEM image that nucleation, and occasional limited subsequent propagation of domains, occurs only at positions of maximum light intensity. For this specific local exposure condition, simultaneous nucleation of sub-micron domains was obtained which are located in close proximity, even on adjacent phase mask intensity maxima. The dots are all similar in size and are closer to each other in a direction perpendicular to the phasemask lines than along the phasemask lines.

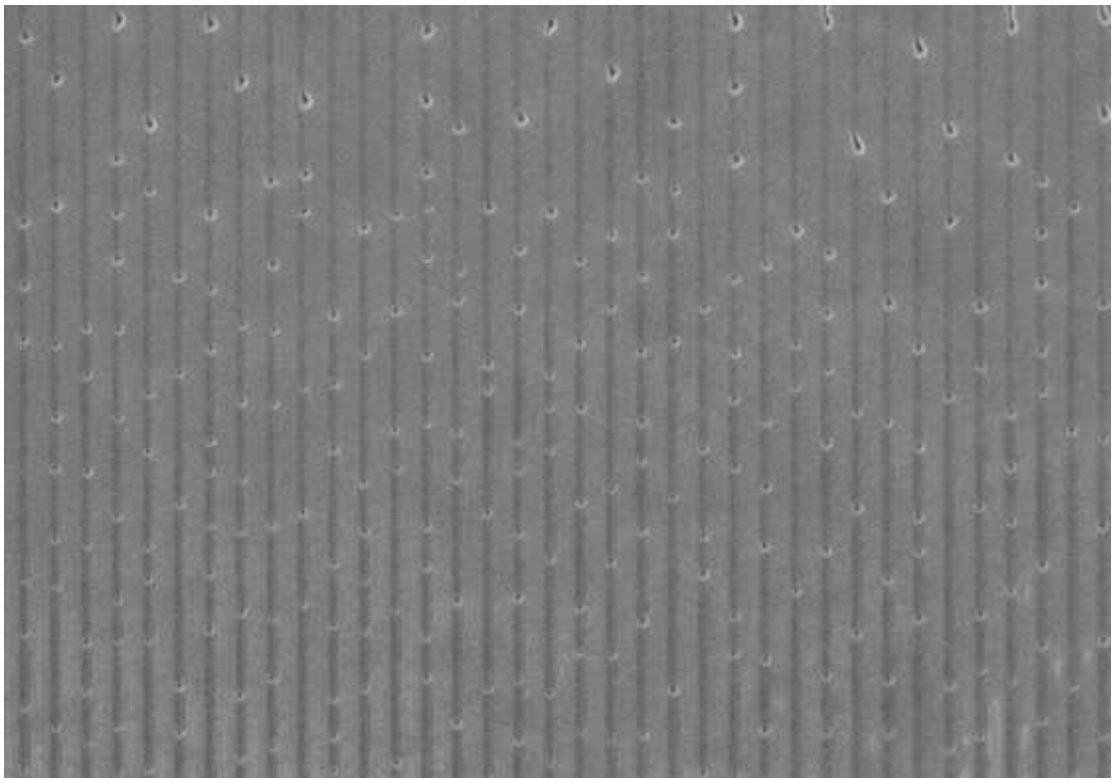

Figure 6.6: Magnified SEM micrograph of fig 6.4c illustrating domain dots from regions of low pulse intensity.

Figure 6.7 shows another magnified part of the etched surface corresponding to the edge of an irradiated area exposed through a phase mask, and therefore experienced a slightly lower fluence. The area was illuminated with two pulses at $\lambda = 298$ nm at a fluence of ~160 mJ/cm^2. An area where both nucleation and growth (propagation) occur can also be observed in the same figure (bottom right), however these expanded domains are spaced further apart, resembling the situation shown in figure 6.3 where the domain lines maintain a critical distance of 3.6 - 7.2 μm.

To confirm if misaligned micro-domains either introduced during crystal fabrication or from scratches in handling were responsible for domain nucleation, samples were re-poled prior to exposure either once before exposure or up to 4 times to ensure a uniformly poled area. Exposures revealed very little difference in samples re-poled and virgin samples from Crystal Technology.

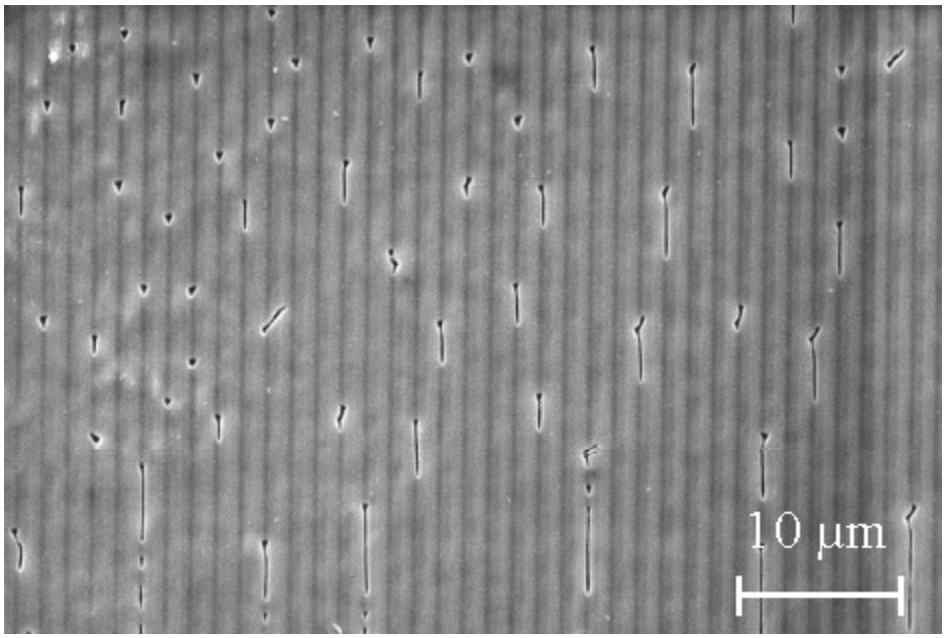

Figure 6.7: SEM micrograph taken at the edge of the phase mask irradiated area. The varying intensity profile across the laser beam allows investigation of the effect of local intensity variation on the AOP domain development.

6.3.2 Effect of Sample Rotation

In a different experiment the phase-mask was rotated so that the grating lines were at an angle of approximately 22° with respect to the crystallographic *y*-axis of the exposed sample. The purpose of this experiment was to conclude whether the crystal symmetry prevails over the spatial modulation of the optical intensity pattern, in other words to show whether arbitrarily aligned domain patterns can be produced. In this experiment a single 266 nm pulse of fluence ~150 mJ/cm^2 was applied to generate a clearly visible ablation grating which was used to identify the rotation angle.

Investigation of the surface topography after etching showed that it is not possible to override the symmetry directions of the crystal. As in all previous cases the AOP domains nucleate on the maxima of the optical intensity but they cannot be encouraged to propagate along an arbitary direction imposed by the optical intensity distribution unless this direction coincides with one of the *y*-axes of symmetry. Figure 6.8 shows a detailed SEM scan of the HF-etched surface where the ablation grating is clearly visible and the *y*-axis directions are indicated in the inset diagram (top left).

Investigation of figure 6.8 confirms the earlier statement that sub-micron (~300 nm) AOP domains are located on the maxima of the optical intensity pattern but they can only propagate along the *y*-directions which in this case is not possible due to the absence of light in the "dark" fringes of the illuminating optical intensity pattern produced by the phase mask.

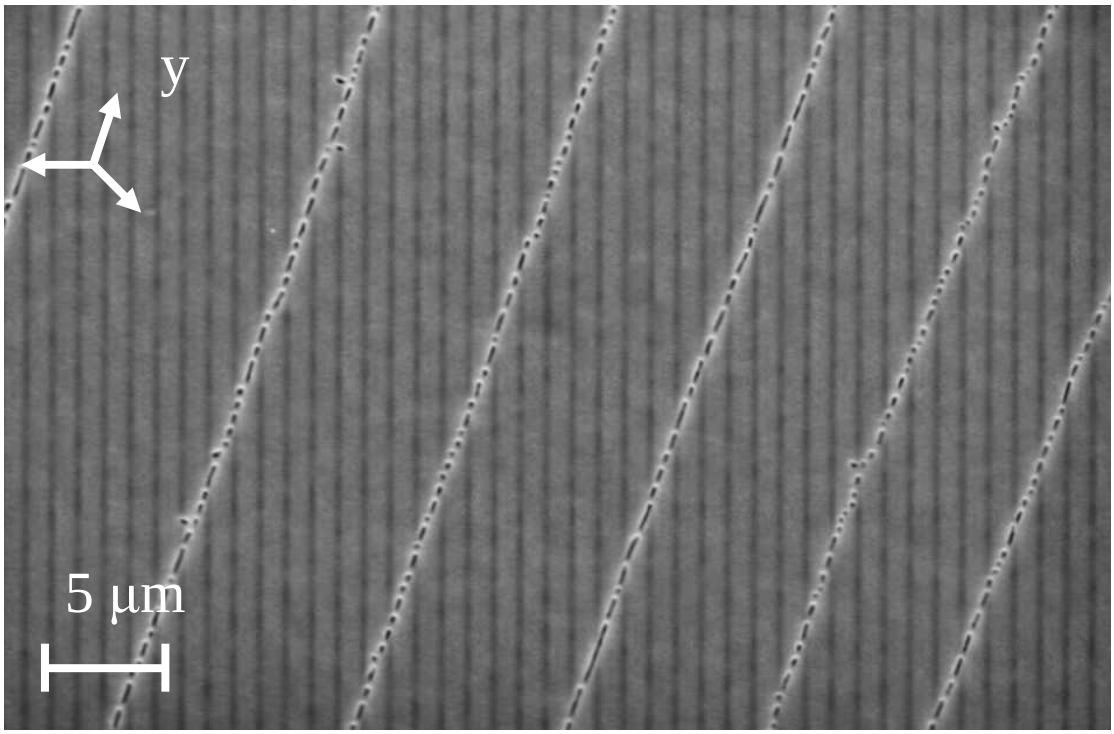

Figure 6.8: SEM micrograph of the +*z* face illuminated through a phase mask which has been misaligned with respect to a *y*-axis by ~22°. The three "*y*" directions are indicated on the top left of the figure.

However, it is interesting to note that individual adjacent domains are aligned along these three *y*-directions of the crystal at a fixed period imposed by the intensity pattern. Hence it is possible to have close dense packing of periodic domains along the "*y*" symmetry directions, for example, by 2D periodic illumination.

6.3.3 Elevated Temperature Exposures

The effect of temperature on the formation of AOP domains was also investigated by a simple experiment. The crystal/phase mask assembly was placed on a hot plate, and exposures were performed at different temperatures ranging from room temperature to 200°C. No qualitative difference was observed at temperatures below 100°C, however as the temperature increased, it was observed that the domain density is significantly reduced and domain lines tend to develop even further apart than in the room temperature case. The major difference is that the domain lines no longer consist of individual sections but form continuous lines. Figure 6.9 shows an SEM micrograph of continuous domain lines as a result of irradiation at a temperature of 154°C.

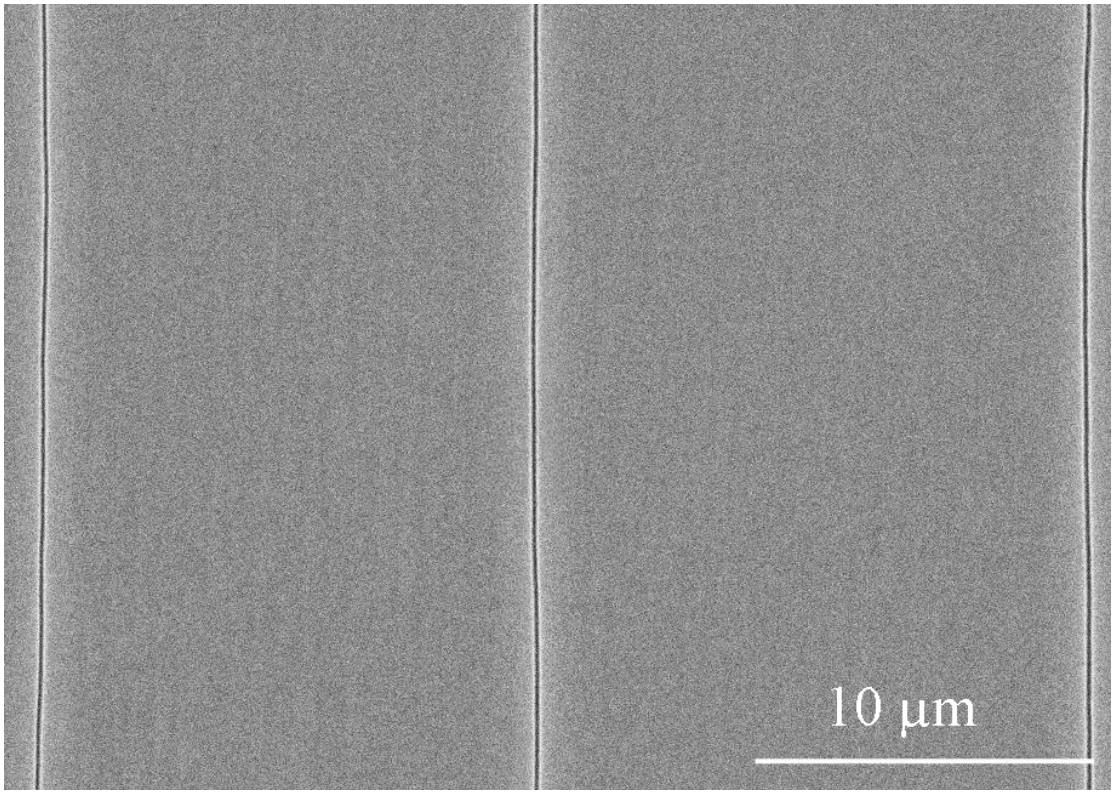

Figure 6.9: SEM micrograph of +*z* face illuminated through a phase mask with single 266 nm pulse (~110 mJ/cm^2) at a sample temperature of 190°C.

6.3.4 Exposures on Other Samples

Exposures performed on –*z* face samples revealed a very different situation to the +*z* face. Sones [13] had previously exposed–*z* face congruent lithium niobate with λ = 248 nm light from an excimer using a phasemask and demonstrated that no domains were formed. Repeating this with 266 nm and 297.5 nm light it was also seen that no ordered structures were formed on the –*z* face as shown in fig. 6.10.

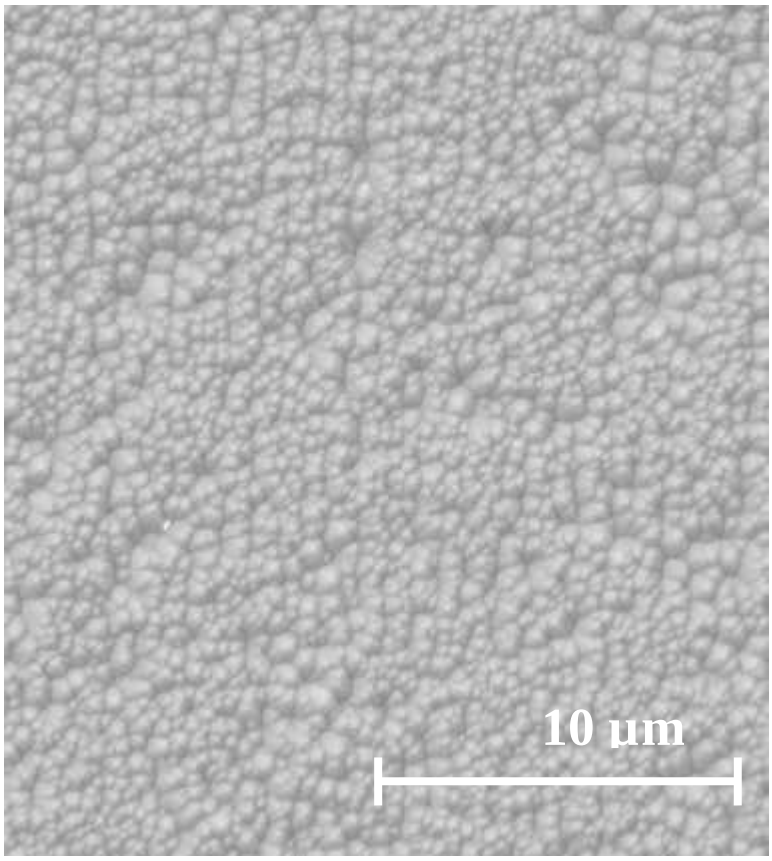

Figure 6.10: Minus *z* face sample exposed to single λ = 266nm pulse through a phasemask at 120 mJ/cm^2.

Similar experiments were performed with *y*-cut lithium niobate and there was a significant difference observed in topology compared to *z*-cut samples. Figure 6.11 shows an etched sample that had been exposed with 10 pulses at 500 mJ/cm^2. This is a very high fluence compared to the *z*-cut crystal – below 450 mJ/cm^2 no surface structures were visible under SEM analysis.

Magnesium doped lithium niobate samples from Moltech[10] were used to repeat the previous experiments and compare with congruent lithium niobate. Using 266 nm light, a range of fluences from 0 to 200 mJ/cm^2 was tested with a 0.726 μm phasemask aligned along the *y*-axis. No observation of surface ablation was present once the phasemask was removed and after a twenty minute etch in HF acid, no observable surface modification appeared under SEM examination.

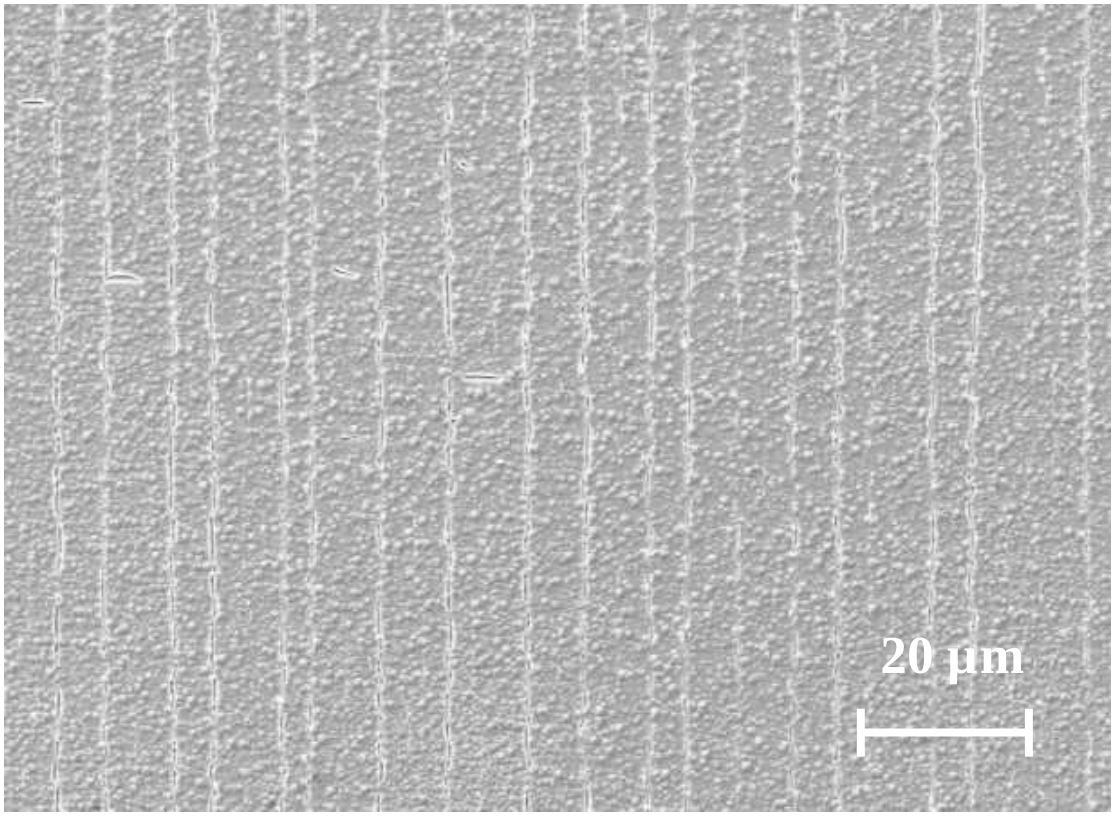

Figure 6.11: *Y*-cut $LiNbO_3$ exposed at 298 nm at a fluence of 500 mJ/cm^2 with 10 pulses

6.3.5 Analysis and Discussion

As noted previously, all optical ferroelectric domain reversal on +*z* $LiNbO_3$ occurs only at the maxima of the laser intensity distribution as produced by the phase-mask. However, the separation between adjacent domains, although always a multiple of the phase mask period, is variable. A systematic study of the domain separation along the *x*-axis was performed on samples fabricated using a range of laser fluences (~100 –

[10] Moletech Technology GmbH., Rudower Chaussee 29-31 (OWZ), 12489 Berlin, Germany.

~150 mJ/cm^2). This study revealed that the distribution of domain separation does not depend on the laser energy fluence. The observed separation distributions have shown a maximum of 10% deviation from the average domain separation across this range of fluences, with little difference between single or double-pulse exposures.

Initially, a Fourier Transform analysis similar to that performed in [16] where the SEM image was transformed and the frequency components analysed to resolve an average separation distance. As there was no observed single repeating separation distance in common, statistics were then used to explain the domain formation.

Due to the ordered nature of the separation distances, spot were examined and the separation distances measured with respect to the phasemask period. The average of domain separation distribution over different samples is shown in the histogram of figure 6.12. This histogram indicates that 88% of the measured domain separation widths lie between the range of 4 - 8 Λ, (2.88 μm- 5.76 μm).

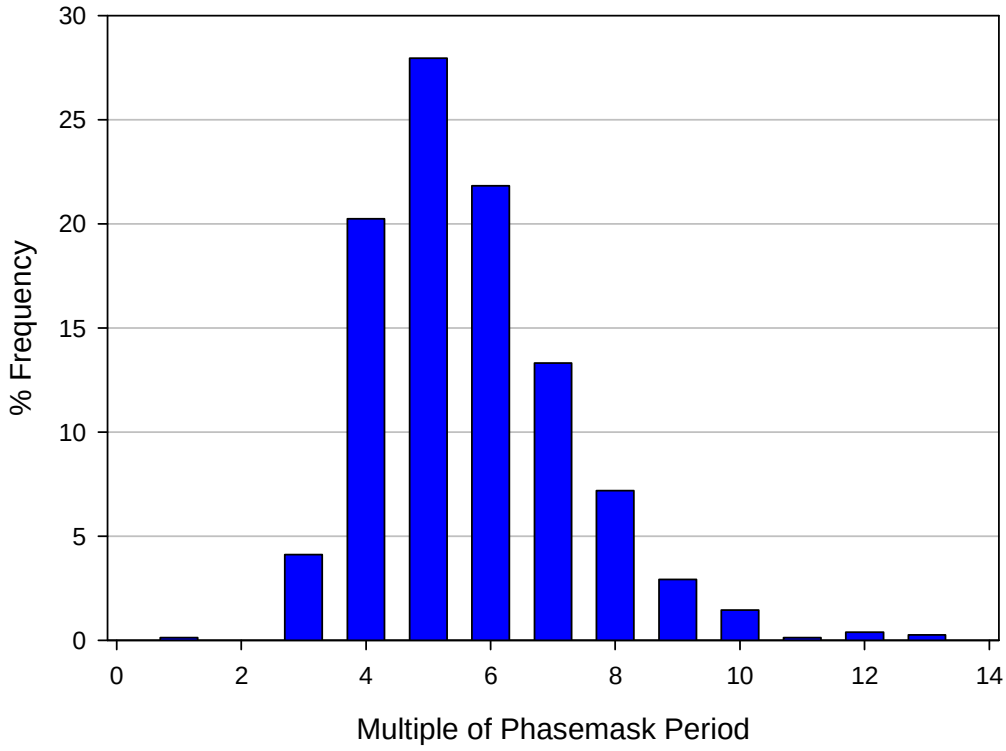

Figure 6.12: Histogram showing the occurrence probability of different domain separation widths (normalized to the period of the phase mask). The data shown here are the average of measurements performed on samples produced with a range of laser fluences (~100 mJ/cm^2 - ~150 mJ/cm^2).

Significantly, as shown in the histogram there are very few domain separation widths under 3Λ (2.16 μm), underlining the hypothesis of a minimum domain separation. Fig 6.13 a) details the average phase mask period vs. fluence for single and double pulse spot exposures on +*z* face $LiNbO_3$. While each spot has a range of periods, the average period appears to be almost independent of fluence, indicating that domain formation relies only on the onset of ablation. Figure 6.13 b) and c) compares single and double pulse exposures for two fluences b) 105 mJ/cm^2 and c) 140 mJ/cm^2. This illustrates there is a similar % frequency period profile of the phase mask at the same fluence when the number of incident pulses is increased. Experiments suggest domain formation is irrespective of the number of pulses with the current laser repetition rate of 20 Hz.

6.4 Mechanism of Poling

The confirmation of the presence of domains due to the interaction of UV light with the surface of lithium niobate – even with a single pulse - makes the mechanism behind domain formation very interesting.

All the experimental results so far have not been able to provide a conclusive physical interpretation of the effect. Nevertheless there are numerous indications suggesting that the AOP process originates from charge imbalance which is the result of the removal of surface charge compensating crystal layers via ablation.

It is well known that heat treatments lead to domain inversion in congruent lithium niobate [17] tantalate [18] and titanium diffused lithium niobate [19, 20]. These treatments have used temperatures of ~300 - 1100°C for several hours, even days. Nakamura [17] has reported a domain inversion of ~ 40 μm depth after heating at a temperature of 500°C for several hours. The mechanism behind UV all-optical poling is believed to be due to a thermally induced process. The major difference between this process and the previous heat treatments is the timescale, which will be discussed later.

a)

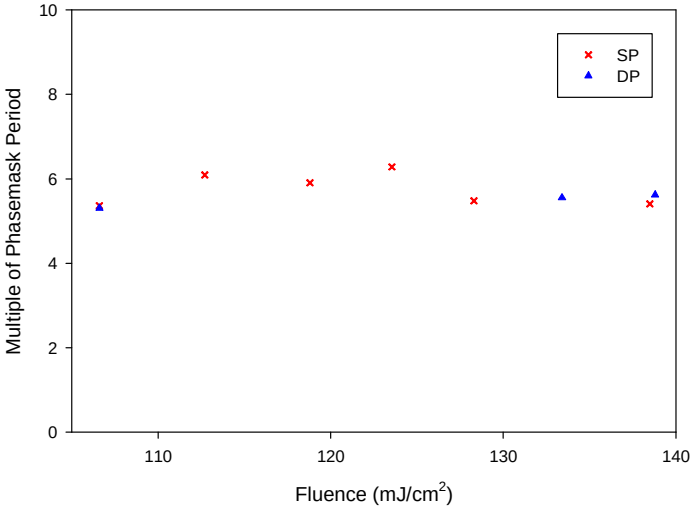

b)

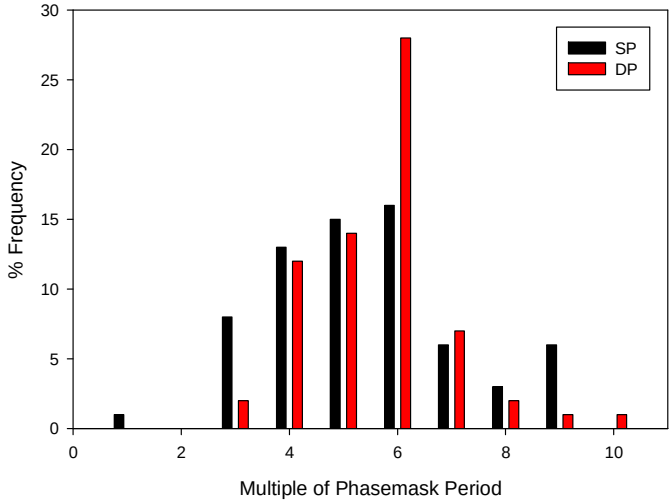

c)

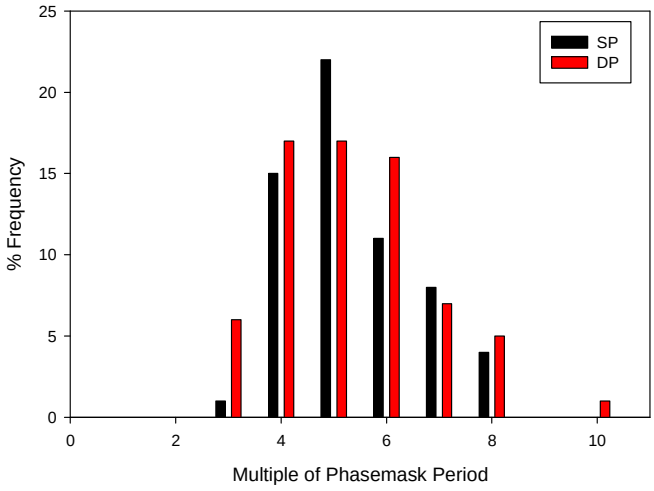

Figure 6.13: Mean PM period vs. fluence for single and double pulse exposures on +z $LiNbO_3$. Single pulse (SP) vs. double pulse (DP) exposures vs. phase mask period for fluences b) 105 mJ/cm^2 and c) 140 mJ/cm^2.

There are two important processes involved in all optical poling: surface heating and subsequent ablation. Although domain inversion occurs here after a single 10 ns pulse, the gradient of the temperature difference is the important factor in ion migration according to Muir [21].

Ablation is key to the domain formation on the +z face – without ablation, no macroscopic domains are observed. Domains are also only observed in the incident spot and there is no propagation outside the illuminated region. The presence of ablation indicates the surface of the sample has been heated to high temperature and there has been an expulsion of material from the surface. The heat penetration depth of lithium niobate is ~ 0.1 μm with a pulse duration of 10 ns [22]; this is very shallow but it is enough to eject material from the surface.

The subsequent surface of the sample after the mass ejection then becomes charged as described in figure 6.14. As the temperature in the ablated zone is still high, and lithium being such a light ion, the thermal diffusivity [23] and ion conductivity [24] are orders of magnitude higher than at room temperature when the crystal becomes amorphous so out-diffusion of lithium is also very possible. This plus the ablation adds to the deficiency of lithium in the heated area. In comparison, there is little movement of Nb ions due to their much larger atomic weight [25].

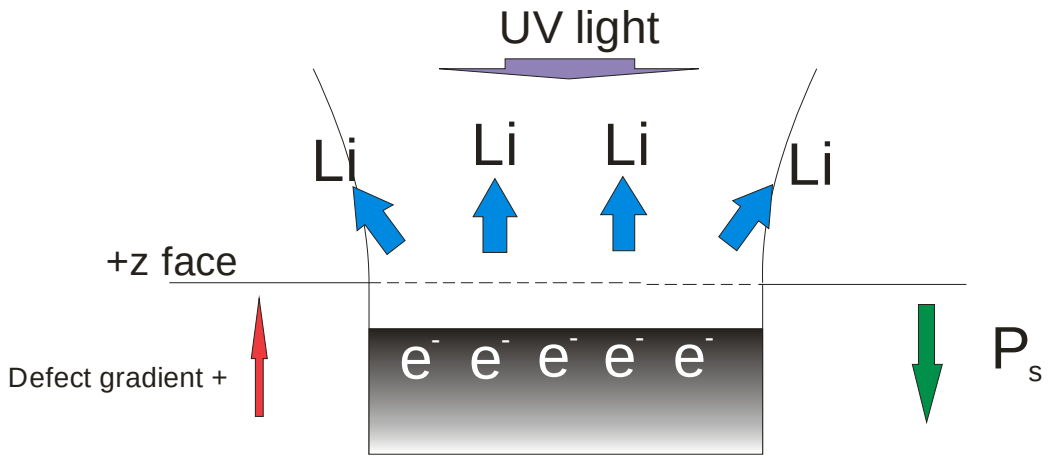

Figure 6.14: Description of all optical poling mechanism

Huang [26] has indicated that the Nb anti-site model, where out-diffusion of Li will cause a slight increase the Nb concentration and the electron density in the heated region, will lead to a domain reversal on the +*z* face only which is consistent with observations of all optical poling.

Out-diffusion of lithium from the surface allows a high concentration of electrons to form near the surface – the concentration diffuses into the bulk forming a defect concentration gradient. The electric field, in the direction of the crystal centre to the +*z* surface, caused by the electron diffusion leads to domain inversion. No domains are formed on the –*z* face due to the direction of the defect concentration gradient being aligned opposite to the +*z* face. If we combine the presence of ablative effects with this defect model, it will increase the magnitude of this concentration.

Heating the crystal to temperatures of 200°C decreases the amount of domain formation on the crystal surface. This can be explained by the decrease in the concentration gradient. Magnesium doped lithium niobate has less excess charge in the crystal and hence a smaller gradient was also formed, reducing the likelihood of domain inversion.

The nucleation process of the domains as illustrated in figs 6.5 and 6.6 appears to commence at random points in the crystal and these could be either nano-domains in the crystal or point defects arising from imperfections formed during crystal growth. Ohnishi points to stress induced polarization change of micro-domains on the surface as responsible for domain nucleation [27]. The previously reported heat treatment induced domain reversal on an 'hours' timescale however all optical poling occurs in the ns timescale – the size of the domains may reflect this smaller timescale with domain widths on the nm scale.

Other charge effects such as the piezoelectric and pyroelectric effects which occur upon absorption of an intense UV pulse and subsequent rapid temperature rise may also contribute to the formation of AOP domains. The high intensity of an incident pulse, causing ablation and subsequent ejection of material, would cause a rapid

change in the temperature profile; the temperature would induce a thermal strain in the irradiated area and be at its peak strength at the surface where nucleation occurs and these effects are discussed further in chapter 7.

6.5 Summary

Ordered alignment of AOP domains has been achieved by spatially modulated UV laser radiation using a phase mask. The pulsed UV laser-induced domains nucleate on the maxima of optical intensity and are encouraged to grow along a specific "*y*" direction of the crystal specified by the aligned orientation of a periodic optical intensity pattern. However, full replication of the periodic optical pattern was not achieved probably due to electrostatic repulsion between adjacent domains which limits the minimum distance between them to ~2 μm. This minimum distance has been observed to be independent of the illumination conditions and represents a fundamental restriction imposed by the material itself for the fabrication of short period domain structures with this optical poling method.

Furthermore, for experiments performed at room temperature the ordered domain lines consist of discrete smaller domains, while at higher temperatures domain lines are continuous but tend to grow even further apart from each other. Experimental results suggest that although long domain lines cannot grow in close proximity due to electrostatic limitations, it may be possible to achieve denser packing of individual domains (domains which have just nucleated but not expanded) by illuminating with a 2D periodic intensity pattern. Experimental evidence suggests that once ablation occurs, domain formation is approximately independent of fluence and number of pulses.

A phenomenological model that involves ablation combined with a Nb antisite model is discussed to explain how the formation of surface domains occurs under such extreme conditions. The investigation is an important first step towards successful manipulation and control of AOP ferroelectric domains in congruent lithium niobate. Further studies are needed to attain full control over domain formation and period.

6.6 References

1. Kazuhisa, Y., M. Kiminori, T. Kunihiko, S. Yoichi, and T. Tetsuo, *Characteristics of periodically domain-inverted $LiNbO_3$ and $LiTaO_3$ waveguides for second harmonic generation.* Journal of Applied Physics, 1991. **70**(4): p. 1947-1951.

2. Nakamura, K. and H. Shimizu, *Ferroelectric inversion layers formed by heat treatment of proton-exchanged $LiTaO_3$.* Applied Physics Letters, 1990. **56**(16): p. 1535-1536.

3. Shintaro, M., *Ferroelectric domain inversion in Ti-diffused $LiNbO_3$ optical waveguide.* Journal of Applied Physics, 1979. **50**(7): p. 4599-4603.

4. Terabe, K., M. Nakamura, S. Takekawa, K. Kitamura, S. Higuchi, Y. Gotoh, and Y. Cho, *Microscale to nanoscale ferroelectric domain and surface engineering of a near-stoichiometric $LiNbO_3$ crystal.* Applied Physics Letters, 2003. **82**(3): p. 433-435.

5. Yamada, M. and K. Kishima, *Fabrication of periodically reversed domain structure for SHG in $LiNbO_3$ by direct electron beam lithography at room temperature.* Electronic Letters, 1991. **27**(10): p. 828-829.

6. Ito, H., C. Takyu, and H. Inaba, *Fabrication of periodic domain grating in $LiNbO_3$ by electron beam writing for application of nonlinear optical processes.* Electronics Letters, 1991. **27**(14): p. 1221-1222.

7. Yamada, M., N. Nada, M. Saitoh, and K. Watanabe, *First-order quasi-phase matched $LiNbO_3$ waveguide periodically poled by applying an external field for efficient blue second-harmonic generation.* Applied Physics Letters, 1993. **62**(5): p. 435-436.

8. Dierolf, V. and C. Sandmann, *Direct-write method for domain inversion patterns in $LiNbO_3$.* Applied Physics Letters, 2004. **84**(20): p. 3987-3989.

9. Sones, C.L., M.C. Wengler, C.E. Valdivia, S. Mailis, R.W. Eason, and K. Buse, *Light-induced order-of-magnitude decrease in the electric field for domain nucleation in MgO-doped lithium niobate crystals.* Applied Physics Letters, 2005. **86**(21): p. 212901-3.

10. Ródenas, A., D. Jaque, C. Molpeceres, S. Lauzurica, J.L. Ocaña, G.A. Torchia, and F. Agulló-Rueda, *Ultraviolet nanosecond laser-assisted micro-modifications in lithium niobate monitored by Nd^{3+} luminescence.* Applied Physics A: Materials Science & Processing, 2007. **87**(1): p. 87-90.

11. Eyett, M. and D. Bauerle, *Influence of the beam spot size on ablation rates in pulsed-laser processing.* Applied Physics Letters, 1987. **51**(24): p. 2054-2055.

12. Valdivia, C.E., C.L. Sones, J.G. Scott, S. Mailis, R.W. Eason, D.A. Scrymgeour, V. Gopalan, T. Jungk, E. Soergel, and I. Clark, *Nanoscale surface domain formation on the +z face of lithium niobate by pulsed ultraviolet laser illumination.* Applied Physics Letters, 2005. **86**(2): p. 022906-3.

13. Sones, C.L., C.E. Valdivia, J.G. Scott, S. Mailis, R.W. Eason, D.A. Scrymgeour, V. Gopalan, T. Jungk, and E. Soergel, *Ultraviolet laser-induced sub-micron periodic domain formation in congruent undoped lithium niobate crystals.* Applied Physics B: Lasers and Optics, 2005. **80**(3): p. 341-344.

14. Gruverman, A., O. Auciello, and H. Tokumoto, *Imaging and Control of Domain Structures in Ferroelectric Thin Films Via Scanning Force Microscopy.* Annual Review of Materials Science, 1998. **28**(1): p. 101-123.

15. Luthi, R., H. Haefke, K.P. Meyer, E. Meyer, L. Howald, and H.J. Guntherodt, *Surface and domain structures of ferroelectric crystals studied with scanning force microscopy.* Journal of Applied Physics, 1993. **74**(12): p. 7461-7471.

16. Scott, J.G., A.J. Boyland, S. Mailis, C. Grivas, O. Wagner, S. Lagoutte, and R.W. Eason, *Self-ordered sub-micron structures in Fe-doped $LiNbO_3$ formed by light-induced frustration of etching.* Applied Surface Science, 2004. **230**(1-4): p. 138-150.

17. Nakamura, K., H. Ando, and H. Shimizu, *Ferroelectric domain inversion caused in $LiNbO_3$ plates by heat treatment.* Applied Physics Letters, 1987. **50**(20): p. 1413-1414.

18. Ahlfeldt, H., *Single-domain layers formed in heat-treated $LiTaO_3$.* Applied Physics Letters, 1994. **64**(24): p. 3213-3215.

19. Miyazawa, S., *Ferroelectric domain inversion in Ti-diffused $LiNbO_3$ optical waveguide.* Journal of Applied Physics, 1979. **50**(7): p. 4599-4603.

20. Peuzin, J.C., *Comment on ``Domain inversion effects in Ti-$LiNbO_3$ integrated optical devices" [Appl. Phys. Lett. **46**, 933 (1985)]*. Applied Physics Letters, 1986. **48**(16): p. 1104-1104.

21. Muir, A.C., G.J. Daniell, C.P. Please, I.T. Wellington, S. Mailis, and R.W. Eason, *Modelling the formation of optical waveguides produced in $LiNbO_3$ by laser induced thermal diffusion of lithium ions.* Applied Physics A: Materials Science & Processing, 2006. **83**: p. 389-396.

22. Lu, Q., S.S. Mao, X. Mao, and R.E. Russo, *Delayed phase explosion during high-power nanosecond laser ablation of silicon.* Applied Physics Letters, 2002. **80**(17): p. 3072-3074.

23. Kaminow, I.P. and J.R. Carruthers, *Optical waveguiding layers in $LiNbO_3$ and $LiTaO_3$.* Applied Physics Letters, 1973. **22**(7): p. 326-328.

24. Glass, A.M., K. Nassau, and T.J. Negran, *Ionic conductivity of quenched alkali niobate and tantalate glasses.* Journal of Applied Physics, 1978. **49**(9): p. 4808-4811.

25. Born, E., J. Hornsteiner, T. Metzger, and E. Riha, *Diffusion of Niobium in Congruent Lithium Niobate.* physica status solidi (a), 2000. **177**(2): p. 393-400.

26. Huang, L. and N.A.F. Jaeger, *Discussion of domain inversion in $LiNbO_3$.* Applied Physics Letters, 1994. **65**(14): p. 1763-1765.

27. Ohnishi, N. and T. Iizuka, *Etching study of microdomains in $LiNbO_3$ single crystals.* Journal of Applied Physics, 1975. **46**(3): p. 1063-1067.

Chapter 7

Temperature Modelling of UV Heating of $LiNbO_3$

This chapter discusses temperature distributions due to heating of lithium niobate via nanosecond pulsed and cw laser sources. Simple stress and pyroelectric models are considered to determine the effect of temperature on the crystal properties and if domain formation and waveguide formation are possible via these effects.

7.1 Introduction

The widespread use of mathematical modelling in laser materials' processing to predict temperature gradients allows the confirmation of heat diffusion theories to fit experimental results and from this, to apply them to novel materials and processes. Most laser processes are based on energy absorption via a locally heated spot. The temperature increase due to the incident laser spot is determined by the laser power, spot radius and the substrate material parameters. There are two major techniques for temperature modelling – analytical and numerical. Both methods were used to simulate the laser heating as seen experimentally. Initially, an analytical model was computed but is quite restrictive so a numerical model using the finite difference method was judged to be most preferable.

Lax [1] first calculated the temperature rise due to a stationary laser beam, followed by Cline and Anthony [2] who interpreted analytically the heat diffusion equation with a moving Gaussian heat source. They demonstrated the relationships between spot size, beam power and beam velocity with temperature profiles and cooling rates. Later models expanded this and performed similar calculations to investigate elliptical beams [3, 4] and melt depths [5]. Analytical models were later produced to include temperature-dependent absorption and reflection coefficients via the Kirchhoff transform [6] and the temperature-dependent thermal conductivity [7]. Early Raman studies have shown that there is reasonable agreement between the temperature modelling of Lax and experimental work in silicon [8].

As computer processing power improved, numerical models [9, 10] using the finite-element or finite-difference methods [11, 12] allowed the use of more complicated simulations which included radiative heat transfer, multi-layered substrates [13] and non-linear variables found through experimental analysis such as heat capacity and thermal diffusivity [14] – concepts difficult to include in analytical models as this needs refining via iteration.

Section 7.2 outlines the finite difference method used to model the temperature distribution from an applied heat source in the form of a laser beam incident on a plane sample of lithium niobate. By means of varying parameters such as beam power or radius, we are able to predict maximum temperatures at the beam centre and the temperature distributions as we move away from the beam.

Section 7.3 concentrates on temperature distributions produced using a moving cw heat source as used in chapters 4 and 5. Utilising the temperature distributions, it is possible to estimate the thermal stress due to local heating – this is important as the composition of the material will change when melting occurs. Above a point known as the elastic limit, the strain induced in the crystal is permanent and non-reversable and this will affect the optical properties of the crystal.

UV writing had been observed to induce domain reversal in waveguides written in chapter 4 on congruent lithium niobate with a cw beam and while the waveguiding mechanism is believed to be via lithium out- and sideways diffusion, the cause of domain reversal is less clear. Two main methods of domain reversal are identified in chapter 4 as thermal stress and the pyroelectric effect; the first is via induced strain in crystal from the local heating of the laser and an estimate of the magnitude of this stress is modelled with the temperature distribution. The second probable cause of domain reversal is via the pyroelectric effect - the heat induced electric field is also derived from the temperature distribution. These models will aim to clarify the underlying cause of domain reversal in congruent lithium niobate.

Section 7.4 focuses on pulsed heating of lithium niobate via a pulsed UV source as in chapter 6. Section 7.5 and 7.6 sums up the limitations of the models and concludes the chapter.

7.2 Definition of Numerical Model

The physical description of the waveguide writing process is defined using a semi-infinite medium as described in figure 7.1. The UV exposure is on the *x*-*y* plane, (i.e. the *z* face) with *x* being the propagation direction of the incident beam along the surface, *y* the transverse direction across the guide and the depth direction is denoted as *z*.

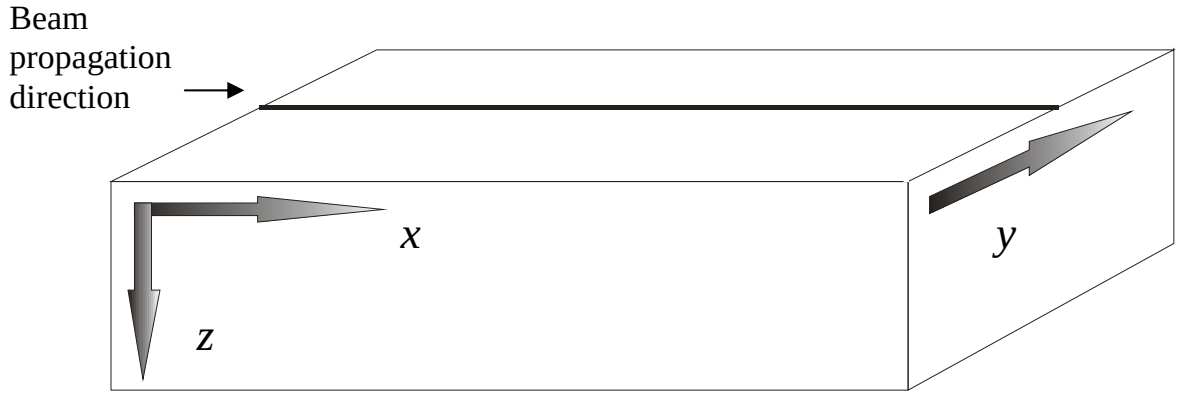

Figure 7.1: UV writing model parameters.

The heat equation (Eq. 7.1) is the basis for a numerical model reproduced using the finite difference method. The non-steady one-dimensional heat equation is given by:

$$\rho \cdot C_v \frac{\partial T(x,t)}{\partial t} - k\nabla^2 T = S(x,t) \tag{7.1}$$

The first term on the left hand side is the rate of temperature change over time (with ρ being the density and C_v the specific heat capacity at constant volume), the second term is the heat conduction term (with k being the thermal conductivity) and the term on the right hand side is the heat source function – in this case the intensity profile.

Differential equations are solved via summation and the first order partial differential equations can be represented as:

$$\frac{\partial T}{\partial t} \sim \frac{T^{g} - T^{g-1}}{\Delta t} \tag{7.2}$$

The superscript g denotes the temporal step while subscript values such as i and j denote spatial steps. Second order differentials contained in the conduction term are represented as:

$$\frac{\partial^2 T}{\partial x^2} \sim \frac{T_{i-1} + 2T_i - T_{i+1}}{\Delta x^2} \tag{7.3}$$

The 1D heat equation in differential notation is then given by:

$$\rho C_V \left(\frac{T_i^{g} - T_i^{g-1}}{\Delta t} \right) = k \left(\frac{T_{i-1}^{g} + 2T_i^{g} - T_{i+1}^{g}}{\Delta x^2} \right) + S_i^{g} \tag{7.4}$$

This can be easily expanded to 3 spatial dimensions and one temporal dimension as given in Eq. 7.5.

$$\rho C_V \frac{\partial T}{\partial t} = k \frac{\partial^2 T}{\partial x^2} + k \frac{\partial^2 T}{\partial y^2} + k \frac{\partial^2 T}{\partial z^2} + S(x, y, z, t) \tag{7.5}$$

The model is based on a seven point x, y & z grid of spacing Δx, Δy and Δz. The five point grid nomenclature in 2D for the x and y- dimensions is shown in fig. 7.2 with the z-dimension omitted for clarity.

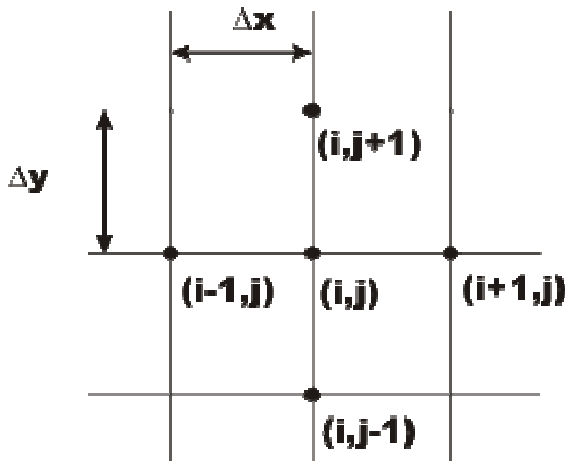

Figure 7.2: 2D finite difference grid for *x* and *y*- dimensions.

Once we have the model parameters, this non-steady state heat equation is then solved via an iterative process for each point in the grid with an appropriate heat source term. An initial guess of the temperature is made at each grid point then the source term is calculated to evaluate the heat equation at that node. To achieve the correct temperature, convergence is checked via the successive over-relaxation (SOR) method [15]. The equation for SOR in 2 spatial dimensions and one time dimension is given in Eq. 7.6.

$$T(i,j,g+1)=\left\{\begin{array}{l}\dfrac{\omega}{4}(T(i-1,j,g+1)+T(i+1,j,g)\\+T(i,j-1,g+1)+T(i,j+1,g))\\+(1-\omega)T(i,j,g)\end{array}\right\} \tag{7.6}$$

The relaxation factor ω is found from testing to be $1 < \omega < 2$ for over-relaxation and for a grid of 30 points, optimal at $\omega = 1.3$.

Phase changes are difficult to model because of a discontinuity at the phase change boundary so the temperature change is converted to an energy change via the enthalpy method [16]. This allows phase changes to be included if we assume that

the enthalpy change is constant at the point of the phase change. The enthalpy is given as a sum of sensible heat h and latent heat ΔH [17]:

$$H = h + \Delta H \tag{7.7}$$

The sensible heat is a type of thermal potential energy and the latent heat (or enthalpy of transformation) is the amount of energy released or absorbed during a phase change. It is endothermic when we change form solid to liquid and exothermic in the reverse direction. We now use the heat equation as an enthalpy equation:

$$\rho\left(\frac{\partial h}{\partial t} + \frac{\partial \Delta H}{\partial t}\right) = k\frac{\partial^2 H}{\partial x^2} + k\frac{\partial^2 H}{\partial y^2} + k\frac{\partial^2 H}{\partial z^2} + S(x, y, z, t) \tag{7.8}$$

Where the sensible heat h and latent heat ΔH are:

$$\begin{aligned} h &= \int_0^T C_v dT \\ \Delta H &= \rho x_m L \end{aligned} \tag{7.9}$$

Where x_m is the mass fraction and L is the latent heat of fusion which is the energy required to change the material's phase without increasing the temperature. During the heating process, once the melting temperature is met, the formation of a melt zone called the 'mushy' zone[11] is formed as shown in fig. 7.3. The mushy zone is made up of a fraction of solid and liquid phases and this is represented by x_m, the mass fraction. The mass fraction is calculated by iteration. An advantage of the enthalpy method is this can be calculated at each time step and so the melt front movement can be modelled without explicitly tracking the melt front. Above the melting temperature, the substrate properties are assumed to be liquid. The mass fraction is described by:

[11] Historically this zone is called mushy due to the first use of the enthalpy method with ice/water phase change.

$$x_m = \begin{cases} 0 & T < T_m \\ \dfrac{T - T_m + \Delta T}{2\Delta T} & T - \varepsilon < T < T + \varepsilon \\ 1 & T > T_m \end{cases} \qquad (7.10)$$

The factor ε is included to simulate the compound nature of the material – if the material was pure, melting would occur exactly at T_m. For example, 304 stainless steel has an ε factor of ~ 30 K .

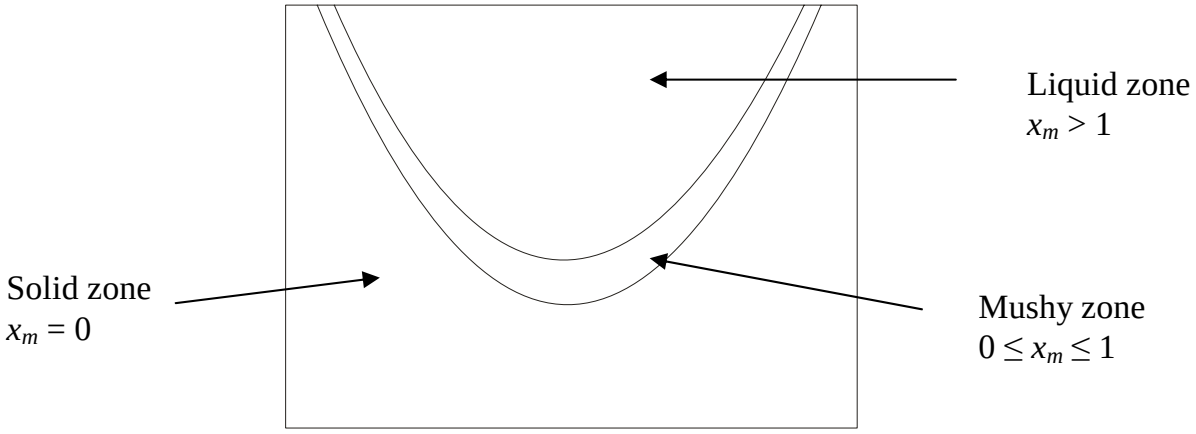

Figure 7.3: Melt zone including 'mushy' zone

The mushy zone parameters are in table 7.1. The parameters of the liquid zone compared to the solid zone are shown in table 7.2.

Parameter	Value
Melting temperature, T_m	1526 K
Latent heat of fusion, L_m	4.56 x 10^5 J kg^{-1}
Impurity factor, ε	10 K
Ambient temperature, T_a	300 K

Table 7.1: Melting parameters for $LiNbO_3$ [18]

Parameter	Solid	Liquid
Density (kg m^{-3}), ρ	4648	3670
Thermal conductivity ($Wm^{-1}K$), k	3.09	4.09
Specific heat capacity (J kg m^{-3}), C_v	1023	1023

Table 7.2: $LiNbO_3$ solid and liquid properties [18].

The initial boundary conditions are as follows:

$$T_{initial} = 300\,\mathrm{K}$$
$$T_{\infty} = 300\,\mathrm{K} \tag{7.11}$$

The initial conditions state the temperature before irradiation, $T_{initial}$, and at a large distance away, $T_{\infty,}$ from the beam becomes the ambient temperature. At the melt front, the boundary condition is:

$$k_s \frac{\partial T}{\partial z} - k_l \frac{\partial T}{\partial z} = \rho H_m \frac{\partial x_m}{\partial t}$$
$$T(x_m) = T_m \tag{7.12}$$

The subscripts *s* and *l* refer to the solid and liquid phases respectively. These conditions state that at the melt front boundary, the temperature is at the melting point.

Several assumptions have been made in this model:

1) Gaussian shaped beam incident perpendicular to surface.
2) Temperature independent material properties.
3) Cavity effects are not considered.

The computer algorithm flowchart is presented in fig. 7.4.

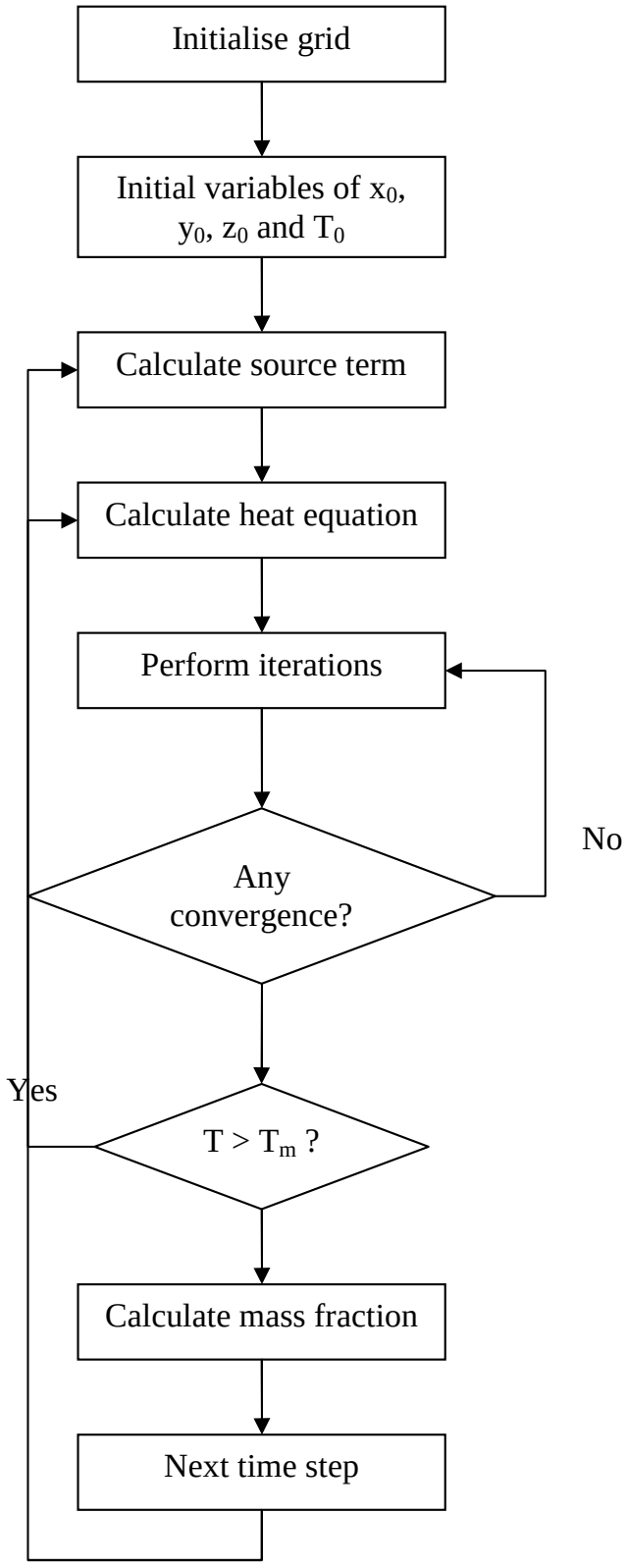

Figure 7.4: Flowchart for numerical scheme

7.2 UV cw Heating

Numerical modelling is introduced to simulate the processes of laser heating with a continuous source with the more complex aspects of phase changes such as melting and radiative effects which are difficult to add into an analytical model. The temperature profiles and depths of the melted region with varied parameters are investigated to discern the effect of UV laser heating with a cw beam.

The size of the beam is small enough to make the addition of radiative effects on the surface negligible; simulations run including radiative losses show this decrease is of the order of ~10^{-6} K. Convective effects are also not considered here due to the small beam size and the relatively small temperature differences between the melt and solid. The extra simulation parameters needed for cw laser heating are given in table 7.3. The optical absorption depth for lithium niobate at 244 nm is estimated to be ~ *15* nm [19].

Parameter	Value
Beam power. P	0 – 100 mW
Beam radius, ω	1.5 – 6 μm
Beam velocity, v	0 – 200 mm min^{-1}
Absorption co-efficient, α	15 nm
Wavelength, λ	244 nm
Reflection co-efficient, R	0.36

Table 7.3: cw laser heating simulation parameters, the reflection and absorption coefficients are from [19].

The one-dimensional heat equation is modified to take into account the moving source function (moving in the *x*-direction only):

$$\rho C_v \frac{\partial T}{\partial t} = k \frac{\partial^2 T}{\partial \xi^2} - v \frac{\partial T}{\partial \xi} + S(\xi, t) \qquad (7.13)$$

The co-ordinate transform $\xi = x - vt$ allows us to consider the beam movement in the time and *x* axes.

7.2.1 Beam Power

A range of incident powers was applied to discern the effect of melting on the temperature profile. Once melting begins, a sharp increase in the temperature past the latent heat contribution occurs at a writing power of 40 mW as observable in fig. 7.5. The interface between solid and liquid at the melting point, T_m begins to expand, once past the melting point of 30 mW, and increases in depth with applied writing power as shown in fig. 7.6. The time taken for the onset of melting changes with applied power, at the maximum power, 50 mW and velocity 50 mm/min, the time taken to reach melting is ~ 3 μs.

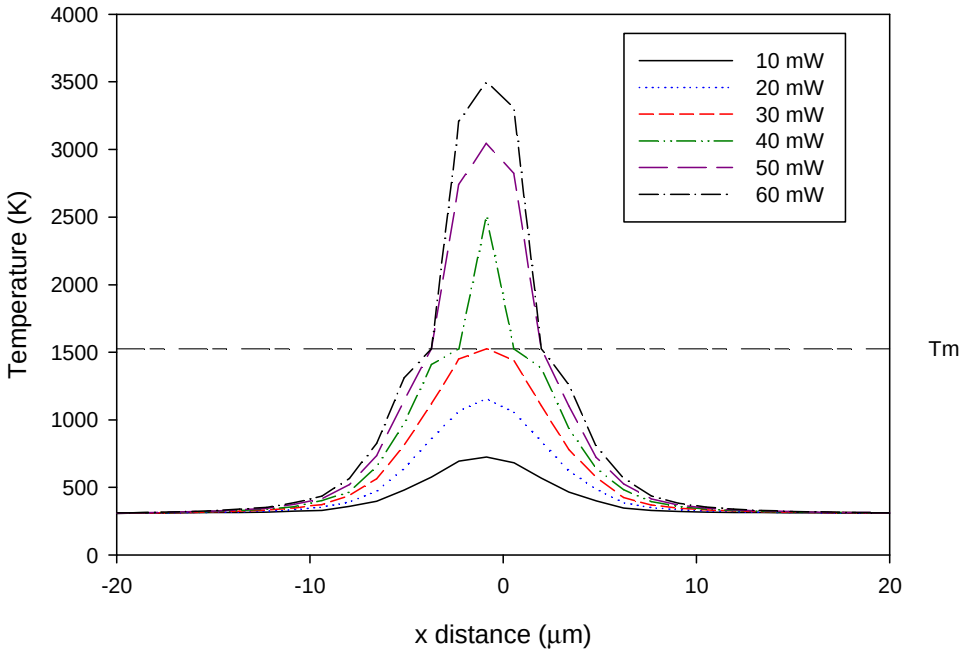

Figure 7.5: *x*- direction across the beam vs. temperature profile for various writing powers at a velocity of 50 mm/min and beam radius of 4 μm. The melting point is T_m.

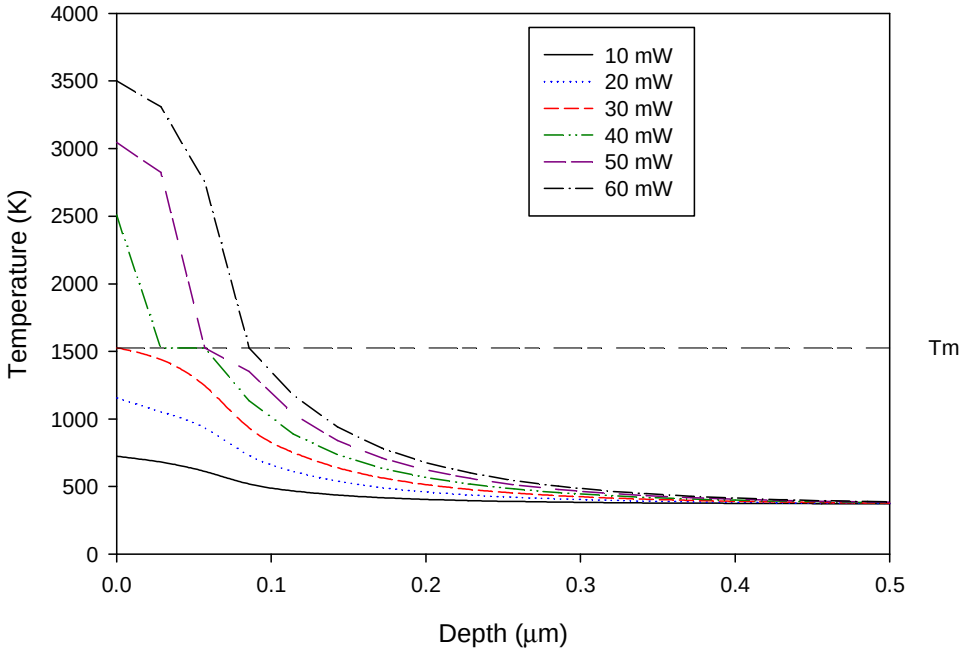

Figure 7.6: Temperature profile vs. depth for various writing powers at a velocity of 50 mm/min and beam radius of 4 µm. The melting point is T_m.

7.2.2 Beam Velocity

The velocities used experimentally were limited to a maximum of 200 mm/min due to an instability in the translation stage movement. The effect of velocity on the waveguide formation is limited; Chen [20] calculated a minimum velocity required for a change in peak temperature and for lithium niobate this is ~ 0.25 m/s – far outside the experimentally possible values. This was confirmed by the model, so velocity effects are not considered any further.

7.2.3 Temperature Related Effects

The thermal distribution from the rapid heating will affect the electric field in the crystal in several ways; firstly, strain from the rapid heating will cause thermal expansion and induce a piezoelectric effect. Secondly, a pyroelectric current which

increases the available charge on the surface – this will affect the charge field in the crystal.

7.2.3.1 Crystal Stress

Strain is the physical quantity that causes stress in the crystal; there are two types of strain in the crystal, axial (or plane) and shear strain. Axial strain occurs in directions normal to the crystallographic axes e.g. the *x*, *y* and *z* directions. Shear strain occurs as a combination of strains between axes e.g. *xz*, *xy* and *yz* directions. When a crystal is heated, the stress on the crystal is assumed in this section to from the strain due to thermal expansion only. Eq. 7.14 describes the thermal strain tensor in the three crystallographic directions, including shear strain.

$$\varepsilon_{therm} = -\alpha \begin{bmatrix} x \\ y \\ z \\ xy \\ xz \\ yz \end{bmatrix} \Delta T \tag{7.14}$$

The stress is thus induced via Hooke's law with the constant *E* being Young's or the elastic modulus for lithium niobate and is direction dependent in Eq. 7.15.

$$\sigma = E\beta(T)\Delta T \tag{7.15}$$

The value of Young's modulus in the *z*-direction at T = 300 K is listed in table 7.4.

Direction	Young's Modulus (GPa)	Thermal Expansion, β (K^{-1})
z (E_{33})	170	5.2 x 10^{-6}

Table 7.4: Parameters used in stress model at T ~ 300 K [21].

The thermal expansion coefficients are also directional and temperature dependent with fig. 7.7 illustrating the *x* axis coefficient undergoing an inflexion with an increase in temperature while the *z* axis coefficient increases gradually with temperature.

For simplicity, an isotropic crystal is modelled in the direction of greatest interest, the *z* direction, so the thermal stress is only considered from the surface into the crystal to a depth of 1 μm as modelled previously for temperature distributions and assumed to have no shear strains. The equation for thermal stress in the *z* direction is [22, 23] is given in Eq. 7.16.

$$\sigma_z = \frac{E\beta(T)(T - T_0)}{3(1-\upsilon)} \tag{7.16}$$

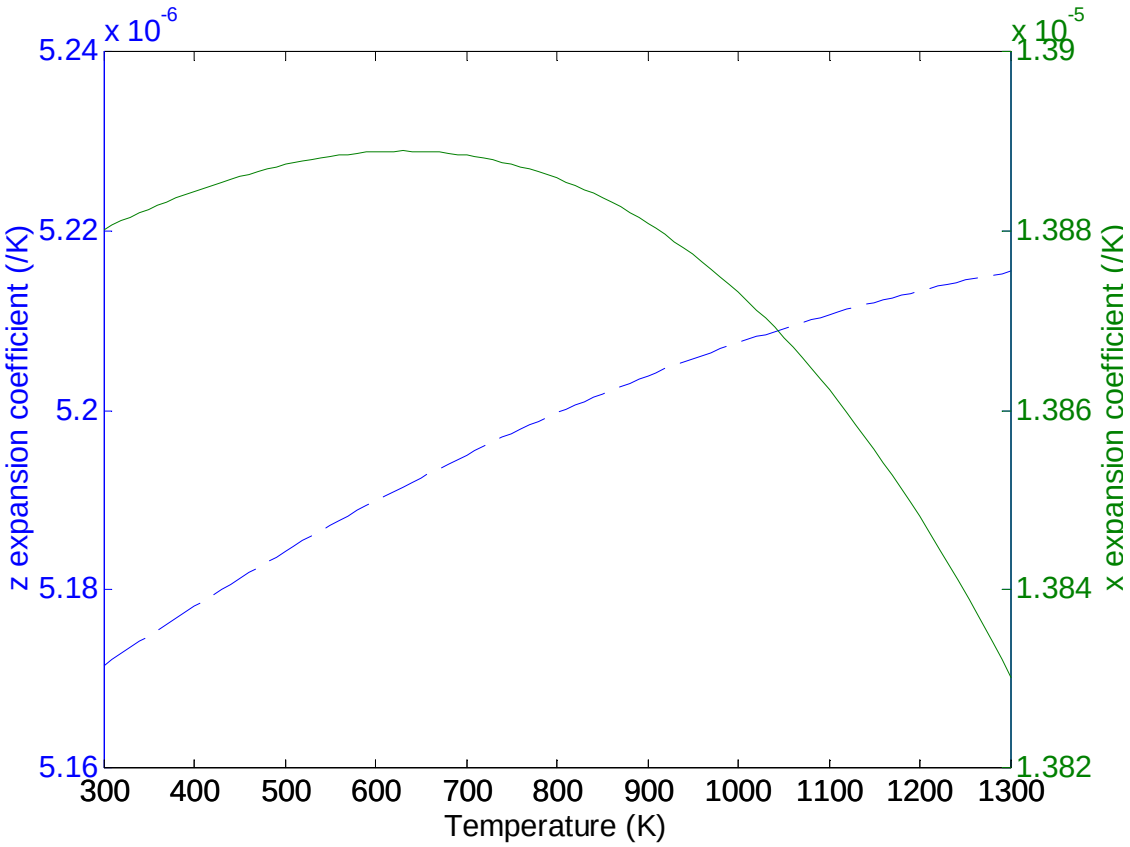

Figure 7.7: Temperature dependent thermal expansion coefficients for lithium niobate in the *z* (blue) and *x* (green) directions [21].

The term υ is the Poisson ratio and describes the ration of the extension strain divide by the axial strain and is taken to be 0.17 [22]. The thermal axial stress from a UV written channel waveguide written with various cw writing powers with a beam velocity of 50 mm/min and a beam radius of 4 μm on a crystal is given in fig. 7.8.

Miyazaki [24] specifies a figure of 10 MPa above which thermal shock will increase the risk of cracking in the crystal significantly but this is specific across a wafer – the stress due to the heat in this case will be confined close to the beam size. The yield strength for *z* cut lithium niobate, the point at which the crystal deformation becomes permanent and irreversible, has been described by Brannon [25] as 2.5 GPa and the thermal stress in the crystal for a channel written at the maximum writing power of 55 mW is 0.98 GPa so does not reach this point and we can assume it is still an elastic material.

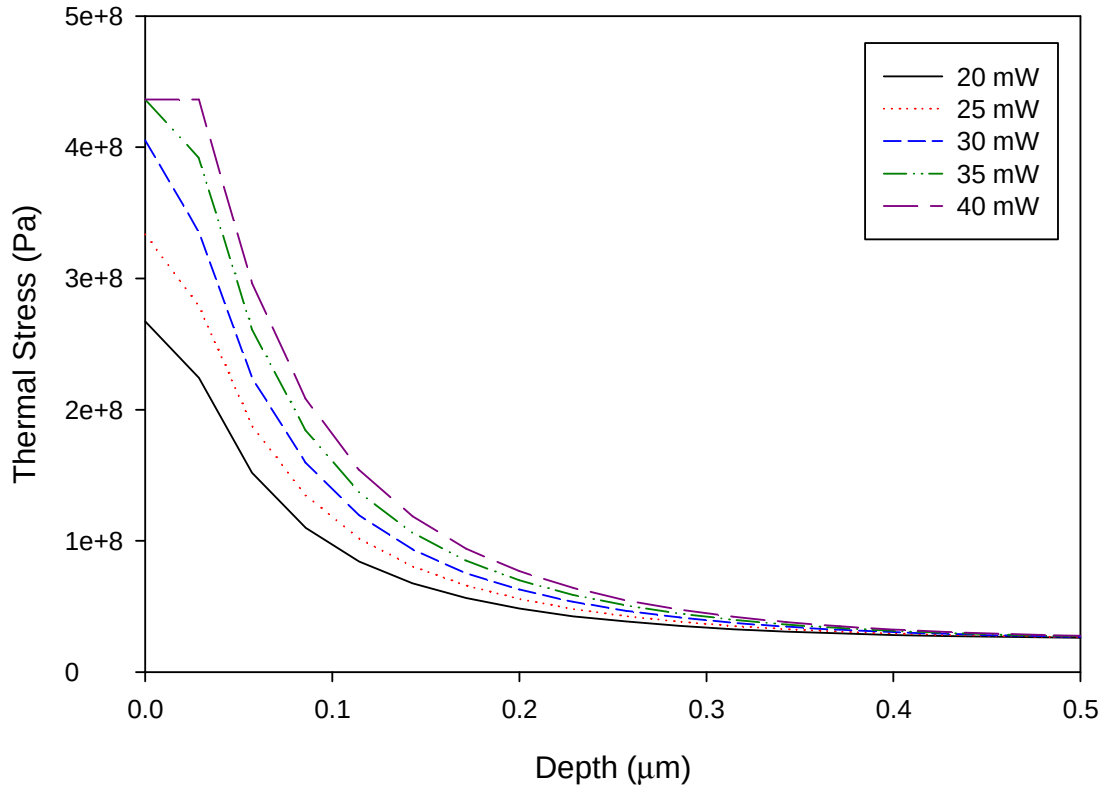

Figure 7.8: Thermal stress distribution into the crystal depth vs. writing powers for channel waveguides written at 50 mm/min and beam radius 4 μm.

Ohnishi inverted ferroelectric domains by applying mechanical stress of 250 GPa via a diamond scribe [26] This value was large enough to exceed the spontaneous polarisation at room temperature 0.7 C m^{-2}. Even at high temperatures where the spontaneous polarisation decreases with temperature, thermal stress alone is not suspected to be larger enough to explain domain formation of cw written waveguides on the crystal.

7.2.3.2 Pyroelectric Field

The polarisation due to a pyroelectric field produced from the heating in the *z*-dimension can be estimated via Eq. 7.17:

$$P = \begin{bmatrix} 0 \\ 0 \\ \lambda_p \end{bmatrix} \Delta T \tag{7.17}$$

The pyroelectric co-efficient at room temperature is λ_p = -4 x 10^{-5} C K^{-1} m^{-2}. The dielectric displacement ***D*** and the polarisation ***P*** of the crystal can be given as:

$$\begin{aligned} D &= \varepsilon_0 E + P \\ P &= P_s + \varepsilon_0 \chi E \end{aligned} \tag{7.18}$$

If we choose P_s to be parallel to the *z*-direction and include the dielectric constant $\varepsilon = (1+\chi)$ and as we are not applying an external electric field, the pyroelectric field can be estimated by [27]:

$$E_{pyro} = \frac{\lambda_p(T)}{\varepsilon(T)\varepsilon_0} \Delta T \tag{7.19}$$

Both the dielectric constant and the pyroelectric coefficient are temperature dependent and will vary as high temperatures are present in the analysis, especially as the dielectric constant begins to increase quickly above 500 K. The dielectric constant follows the relationship [28] in Eq. 7.20. Data on the pyroelectric coefficient above 500 K is scarce so a linear temperature dependence (Eq. 7.21) is assumed from the value for λ_p at room temperature above to zero at the Curie temperature.

$$\varepsilon(T) = 8x10^{-10}T^4 - 1x10^{-6}T^3 + 7x10^{-4}T^2 - 1.2x10^{-1}T + 34.74 \tag{7.20}$$

$$\lambda_p(T) = 3.28x10^{-8}T - 4x10^{-5} \tag{7.21}$$

Fig. 7.9 illustrates the field strength due to waveguide writing on congruent lithium niobate with a cw λ = 244 nm laser with an incident optical power of 20 mW.

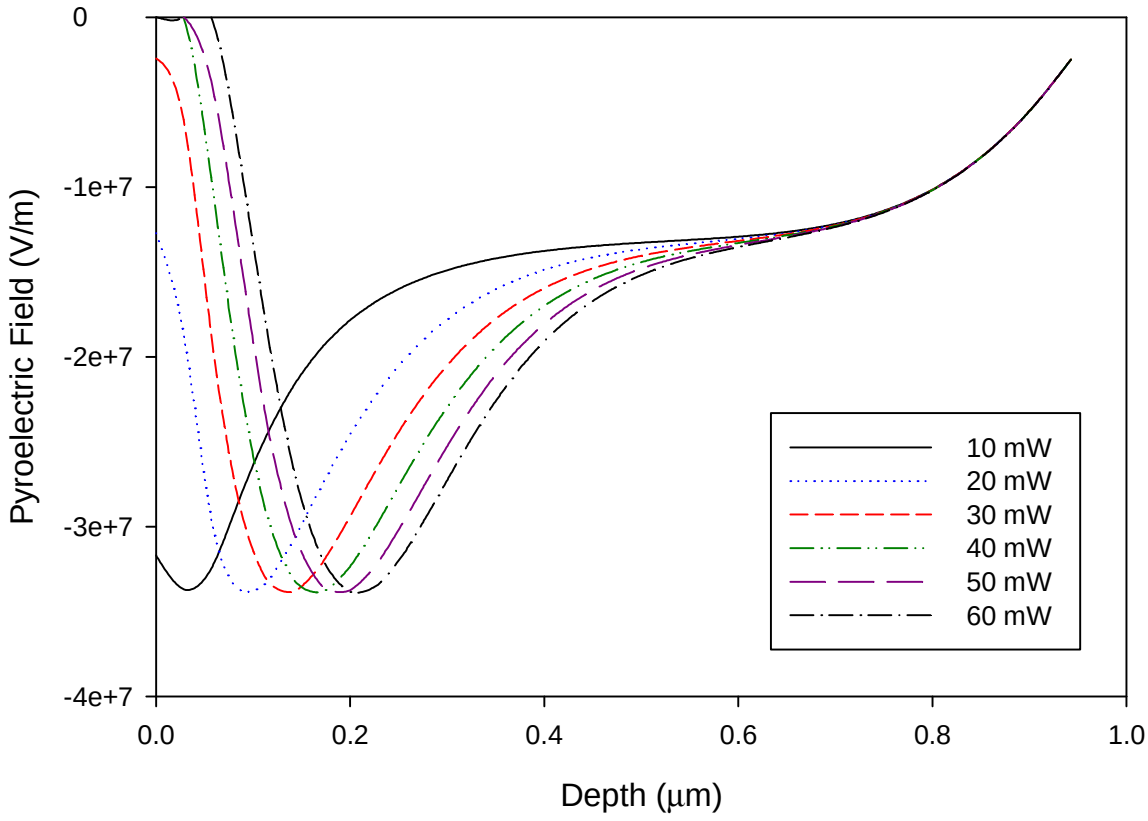

Figure 7.9: Pyroelectric field due to channel waveguide writing at 20 mW at λ = 244 nm on lithium niobate.

The field strength is high – even a temperature increase of 1 K has been calculated to cause a field strength of ~ 10^6 V/m [29] but the distribution in fig. 7.9 is restricted by the large increase in dielectric constant at high temperatures and the loss of pyroelectricity past the Curie point. The maximum field is 3.37 x 10^7 V/m which occurs at ~ 600 K independent of writing power once the temperature is reached. At these high temperatures the field needed for domain reversal is low and it appears possible for the pyroelectric field to indeed pole the crystal.

7.3 UV Pulsed Heating

To simulate the temperature distribution and melt characteristics of the pulsed heating we simulate the application of a stationary pulsed source and compare with experimental work. Variables such as number of pulses, temporal separation of pulses and the cooling rate are investigated in this section.

Lithium niobate has an extremely small absorption depth for a source of λ = 266 nm and this, coupled with nanosecond pulse duration, ensures ablation will occur soon after the onset of melting. UV pulsed lasers have the advantage of limiting the heat transfer from the area know as the heat affected zone (HAZ) which is dependent on the pulse duration and the material parameters. The smaller the absorption depth, the less material will be ejected from the HAZ. This HAZ is an area which we are particularly interested in as surface domains are formed in this zone. As a rough guide, the thermal penetration depth is given by [30]:

$$x_{th} = 0.969\left[(k\tau)^{1/2}\right] \tag{7.22}$$

For a diffusivity of k = 2.5 x 10^{-5} m^2 s^{-1} and a pulse length of τ ~ 10 ns, the thermal penetration depth is ~ 0.5 µm. As the optical absorption depth is an unknown quantity at this wavelength is it tailored to adjust the process to fit experimental

observations and is assumed to be similar to the λ = 244 nm value, 15 nm. This value is orders of magnitude smaller than the thermal penetration depth from Eq. 7.22.

The source term describes the heat input of the model and is defined as laser heating via a Gaussian shaped pulsed source; this includes a temporal term:

$$S(x,y,z,t) = \frac{Q}{\tau} e^{-\left(\frac{t}{\tau}\right)^2} \tag{7.23}$$

Where τ is the pulse duration and Q the incident fluence. The extra model parameters needed in the pulsed scenario are given in table 7.5.

Parameter	Value
Pulse duration, t_p	10 ns
Repetition Rate, τ	20 Hz
Fluence, F	10 – 200 mJ cm^{-2}
Wavelength, λ	266 nm
Absorption co-efficient, α	15 nm [19]
Vapour temperature, T_b	3500 K
Heat transfer co-efficient, h_c	~0.01 W K^{-1}

Table 7.5: Pulsed laser heating model parameters [18].

An extra boundary condition is added due to the size of beam radius; a convective loss term is added to the surface. If the beam radius was much smaller, this term would be minimal.

$$k\frac{\partial T}{\partial z}\Big|_{surface} = S(r,z,t) - h_c\left(T - T_a\right) \tag{7.24}$$

This term is added with the onset of melting where additional heat dissipation occurs from the melt surface. While we add this term, convection effects in the melt zone

have been neglected due to the very short time for melting to occur and solidify again, and we reasonably assume a solid surface exists by the time the next pulse is incident.

An additional caveat is included with pulsed melting due to the ablation process and that is the vapour temperature - data for this is extremely limited and so 3500 K is assumed. This term is included to simulate the evaporation of the material at high incident peak powers. Most of the energy is transferred to kinetic energy once this temperature is reached and so it acts as a limiter to higher temperatures.

7.3.1 Fluence effects

Investigating the ablation threshold for a single pulse on lithium niobate with comparison to observed experiments, the temperature distributions for various fluences are given in figure 7.10. The melting temperature T_m ~ 1526 K is marked on the graph to highlight the obvious change of phase to the temperature profile. It can be seen that the effect of surface melting considerably changes the shape of the material cooling behaviour.

The experimentally observed ablation threshold for a single pulse is ~ 95 mJ/cm^2, and this is close to the numerical threshold with the difference being due to the constant thermal conductivity assumed independence of temperature. Below the threshold level, the temperature follows the usual heat profile; above this threshold, there is a period of ~ 1 ns for melting to occur then the profile continues to rise with liquid heating before cooling with decreased laser intensity until solidification and then solid cooling.

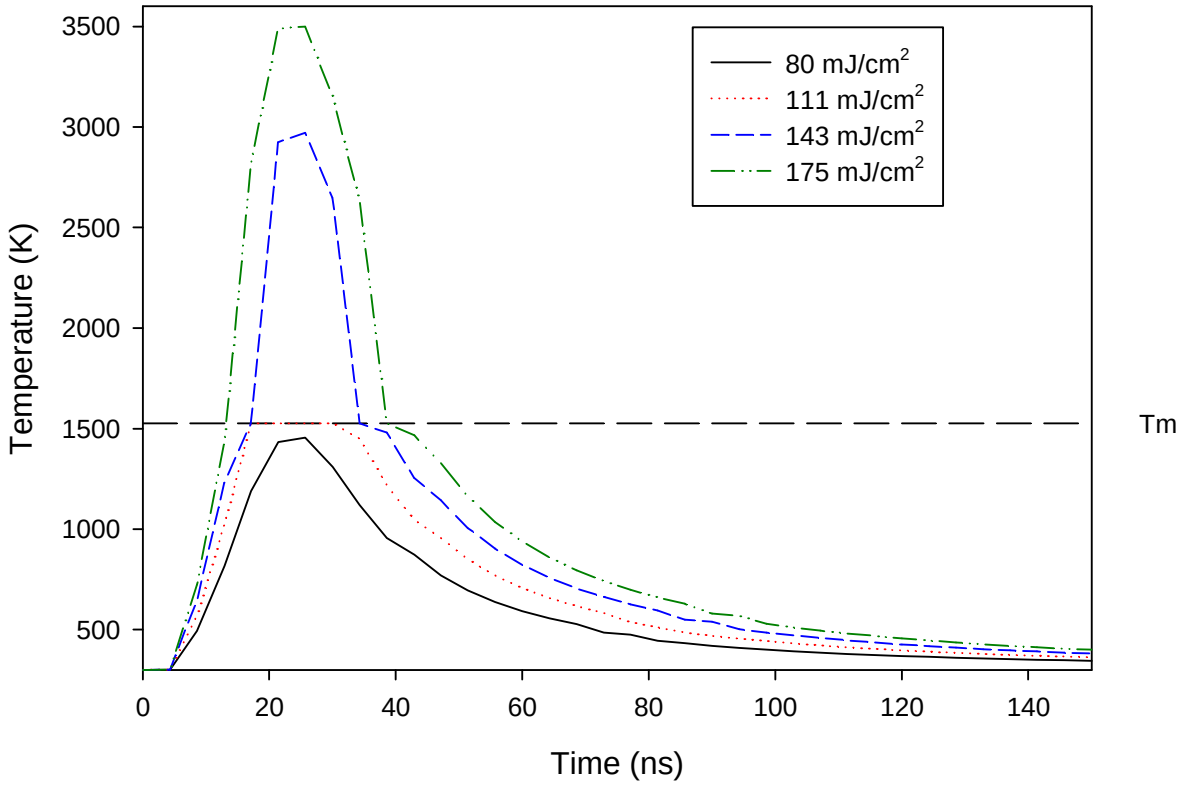

Figure 7.10: Temperature distribution vs. time for range of fluences at $LiNbO_3$ surface.

Fluence values greater than 200 mJ/cm^2 reach the assumed vaporisation temperature indicating that ejection of material from the surface occurs as seen by visual inspection of the spot under SEM. Other studies have shown that the cavity shape formed is dictated by reaching this temperature – the liquid and solid/liquid mushy zones are small compared to the cavity shape [31].

Figures 7.11 and 7.12 show the temperature profiles of lithium niobate irradiated with various fluences. The thermal distribution is limited to ~ 0.5 μm in depth across the applied fluence and ~ 2ω across the distribution width. The melt zone can be seen to expand as expected with increase fluence. The melt zone will be investigated later in the chapter.

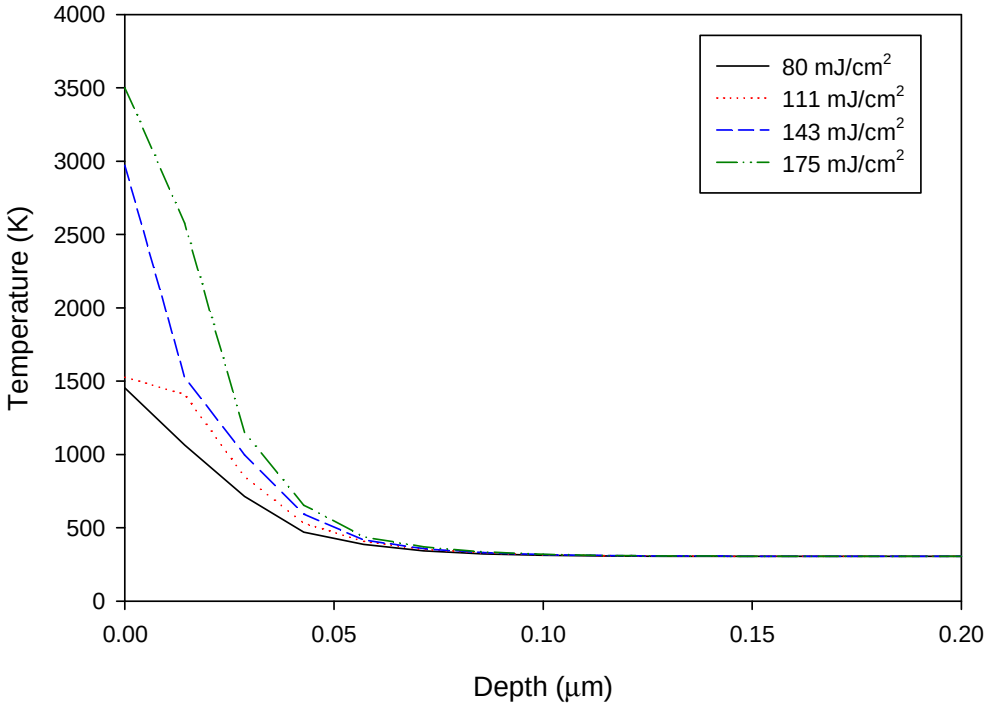

Figure 7.11: Temperature profile vs. depth for pulsed heating of lithium niobate.

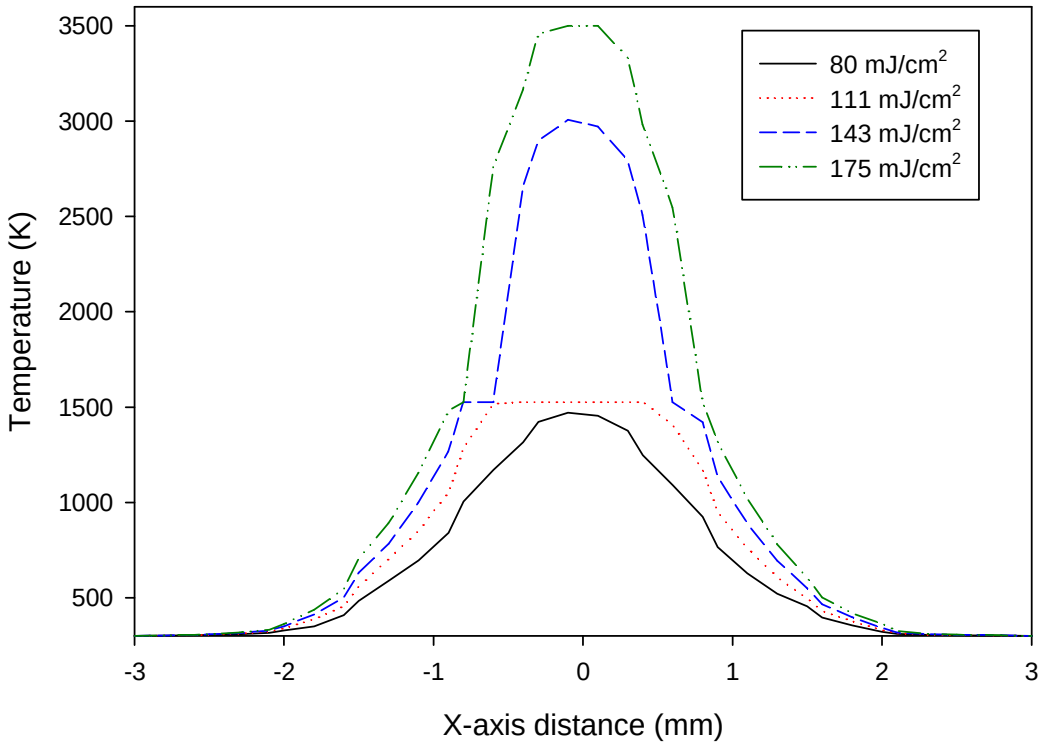

Figure 7.12: Temperature distribution vs. *x*-axis distance for pulsed heating of lithium niobate.

7.3.2 Multi-pulse regime

If the number of pulses is increased, with the long cooling times compared to the pulse duration length, the maximum temperature can increase quickly with each pulse. The temperature increase is related to the separation of the pulses and increases with decreasing separation.

The pulse separation time needed to increase the surface temperature is extremely short; in fact it is too short for us the replicate experimentally – the shortest repetition rate possible with our laser was 20 Hz so a minimum of 50 ms between pulse peaks. According to the simulation, at the maximum fluence, the pulse separation has a negligible effect on increasing the surface temperature after 0.15 μs, effectively acting as a separate, initial pulse with no interaction with the previous pulse. Below this significant separation time, we see the peak surface temperature increase with each pulse – the temperature distribution also expands in the radial distance as well.

7.3.3 Melt depth vs. fluence

The melt depth and melt width during the pulse are presented in fig. 7.13. The pulse maximum occurs at 15 ns and the melt zone expands and contracts before and after this point. The melt depth is limited to a maximum value of ~30 nm at a maximum fluence of 191 mJ/cm^2. This greatly restricts the heat zones from the incident laser fluence.

The melt pool size versus fluence is illustrated in fig. 7.14. The pool width and depth are limited by the beam size and the optical absorption length. With a large fluence, the depth is still restricted to ~ 30 nm and the melt width to the beam radius of ~ 1 mm.

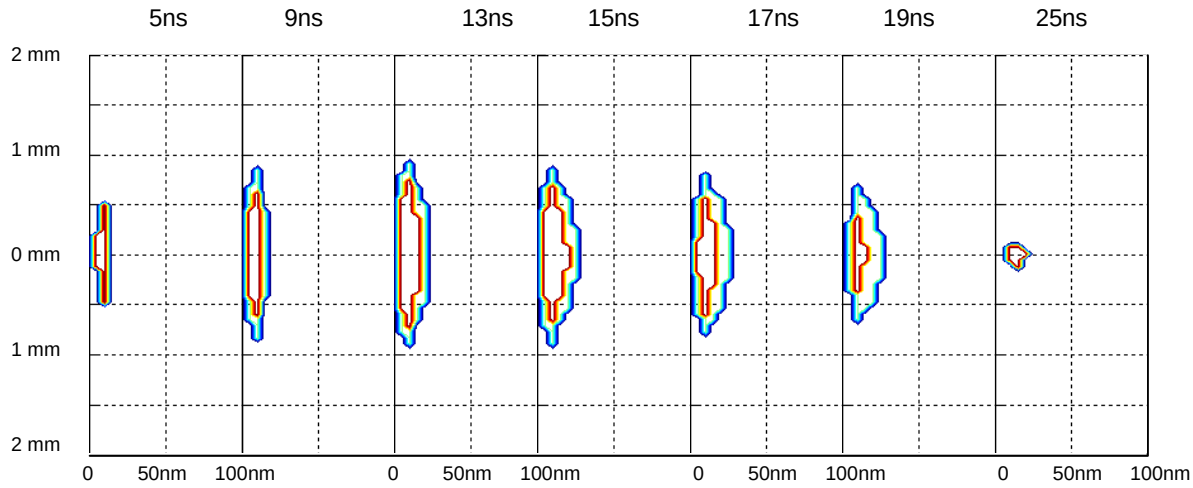

Figure 7.13: Melt pool size vs. time during heating pulse.

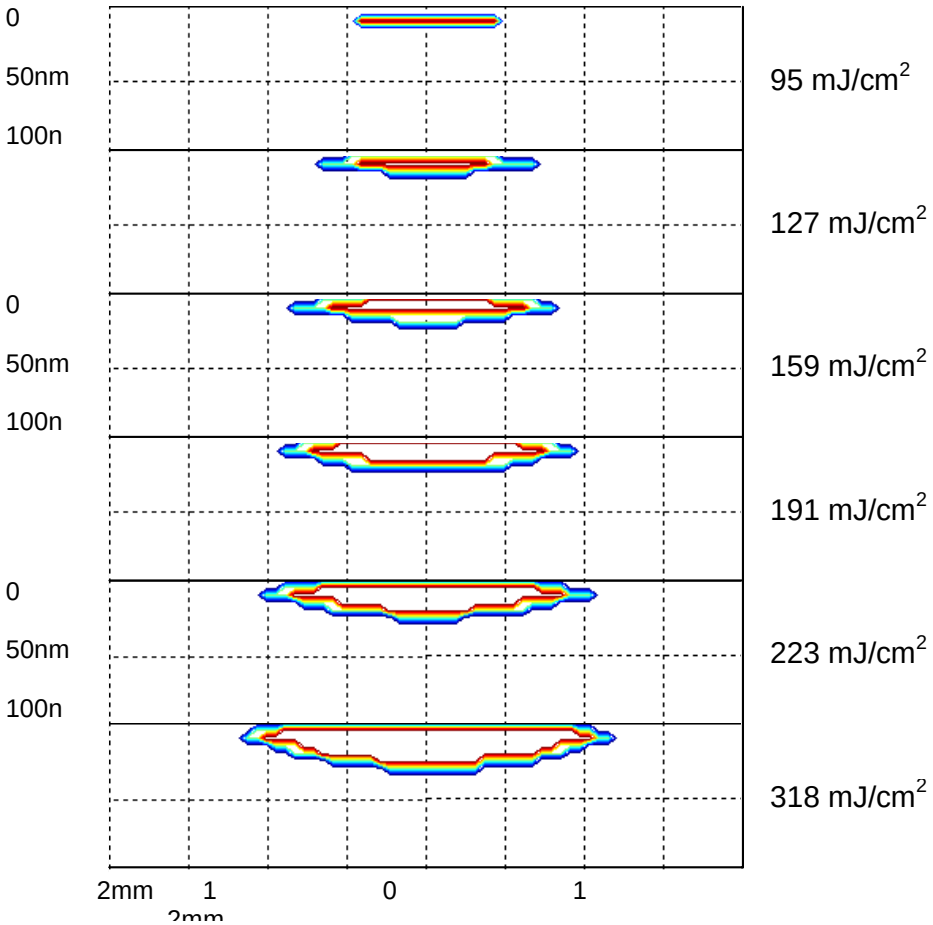

Figure 7.14: Melt pool size vs. fluence 3 ns after pulse

7.3.4 Temp increase vs. fluence

If we increase the ambient temperature as done experimentally via a hotplate, we find the onset of melting occurs at lower fluences as expected. Fig. 7.15 illustrates the fluence required for melting versus initial temperature. The increase in ambient temperature allows a linear decrease in applied fluence. Although important in the formation of surface domains experimentally, the ambient temperature just lowers the melting threshold but has no major effect on the final temperature distribution.

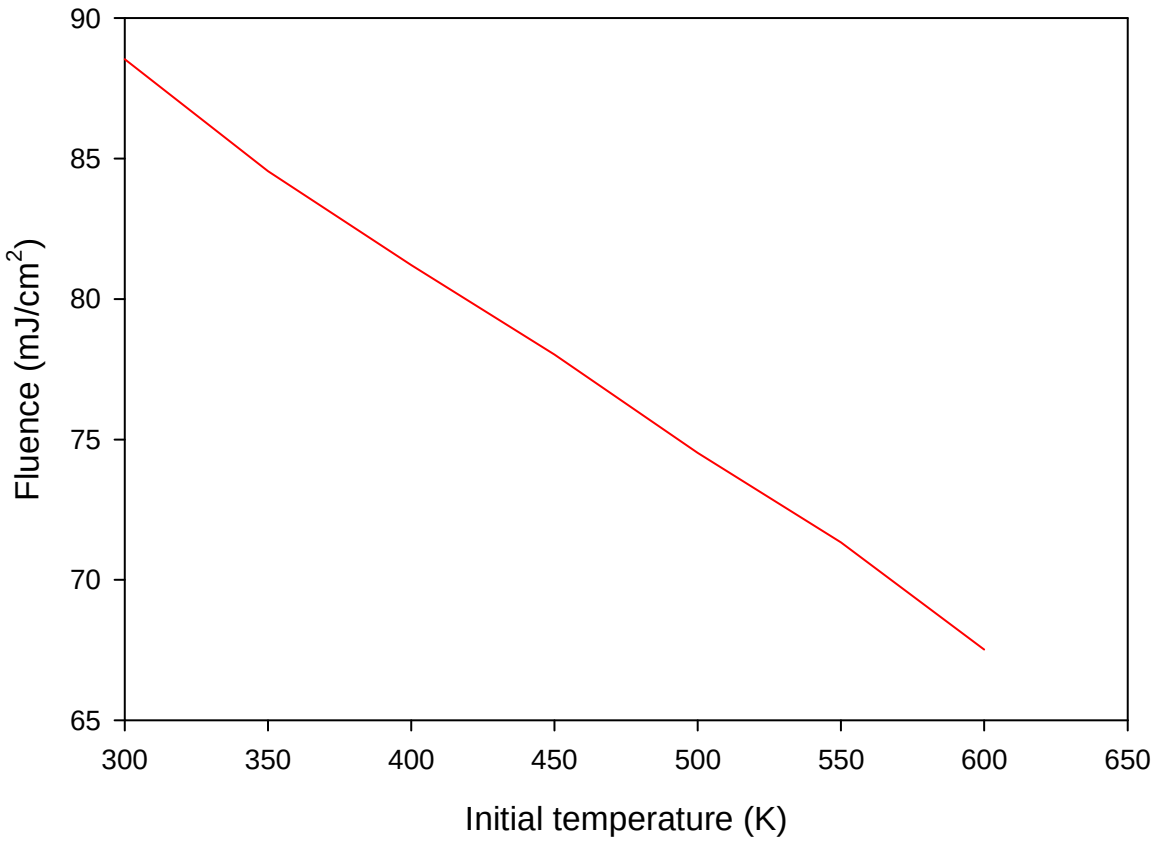

Figure 7.15: Fluence vs. initial temperature

7.3.5 Stress and Pyroelectric Field

The axial stress as modelled previously for cw irradiation has also been applied to the pulsed heating condition. The stress from a single 2.5 mJ/cm^2 pulse vs. time is given in fig. 7.16. As expected with similar high temperatures to the cw case, the peak axial thermal stress in the *z* direction reaches ~ 1.1 GPa at the pulse intensity peak and the field extends ~ 200 nm into the crystal.

The pyroelectric field verses time in the *z* direction is illustrated in fig. 7.17. Again, due to the magnitude of the temperature profile and the temperature dependent coefficients, the field has a similar magnitude to the cw case.

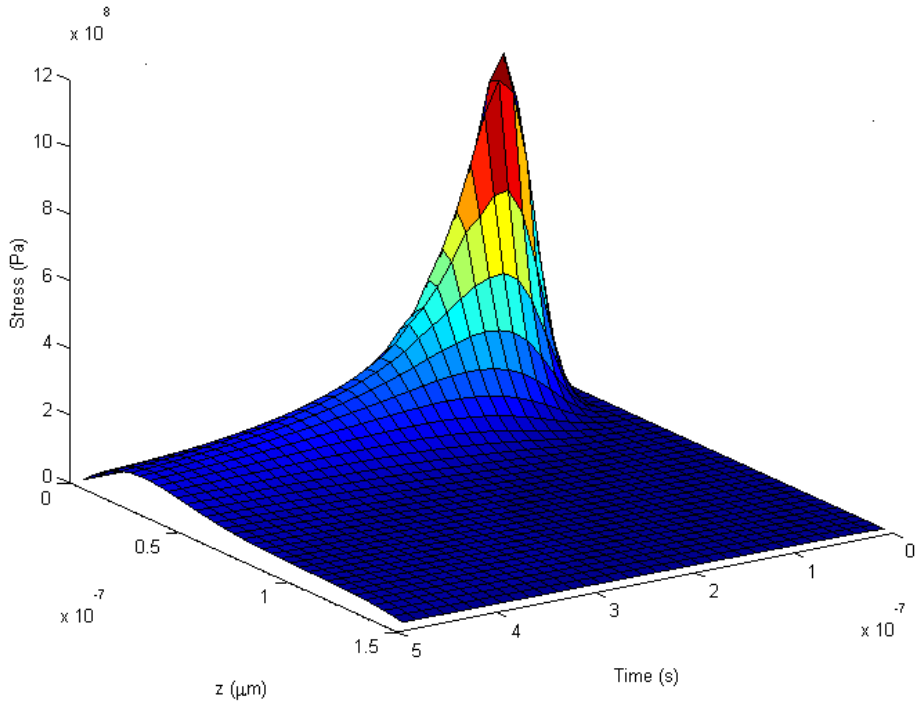

Figure 7.16: Axial stress in the *z* direction (depth) vs. time for a single 2.5 mJ/cm^2 pulse.

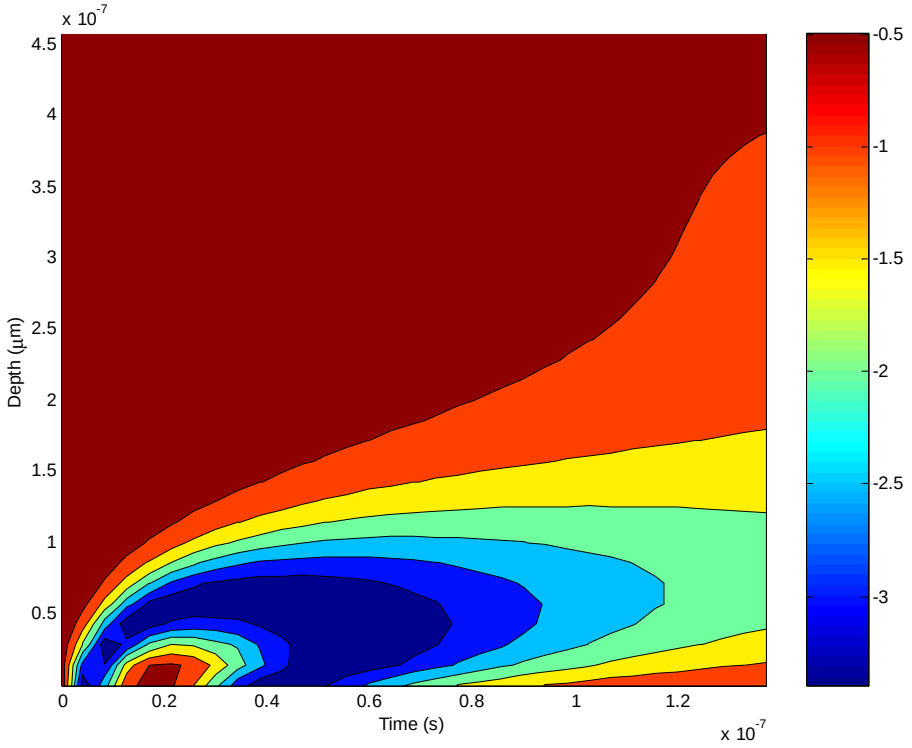

Figure 7.17: Pyroelectric field vs. time for a single 2.5 mJ/cm^2 pulse exposure. The scale is x 10^7 V/m.

While both pulsed and cw heating have the large pyroelectric field that is estimated to be able pole the crystal, the models are simple and do not take into account all possible variables. One condition that has not been examined is the time scale needed for the field to pole the crystal permanently although the field may be of the right order of magnitude, the timescales are considerably shorter than conventional E-field poling. Gopalan estimates a switching time of ~ 30 ms for congruent lithium niobate [32] but this may be reduced due to the highly inhomogeneous heating from the incident laser radiation.

7.4 Numerical Model Future Work

These models can be expanded in many ways, principally:

Applying temperature-dependent material parameters such as the thermal conductivity, reflection co-efficient, density, absorption co-efficient and specific heat capacity will allow a more realistic simulation. The addition of convective and radiative effects in the melt zone can give insight into the movement and concentration of species in the melt, also allowing the understanding of beam effects on the melt zone. Parameters such as the liquid velocity, viscosity and volume expansion of the liquid can be included.

For greater accuracy, an adaptive grid such as an exponential grid centred on the spot peak intensity and greater spacing far away from the spot would ideally concentrate computing effort on the spot of interest and neglect areas far away from the beam where little occurs.

A useful addition to he stress and pyroelectric models would be an investigation into the timescales needed for poling and followed up with experimental verification.

7.5 Conclusion

The modelling of heating lithium niobate via a cw and pulsed UV laser source provides an estimate of conditions of the surface of the material which can be used to explain the effect of surface domain formation under both conditions and waveguide formation in the cw case.

The cw case agrees with experimental conditions with the onset of surface melting occurring after 30 mW and an expansion of the liquid depth to a maximum of 100 nm at 50 mW. The heat penetration depth is ~ 5 times the melt depth and ~ 30 times the optical penetration depth. Due to temperature dependent material coefficients, the pyroelectric field reaches a maximum value at ~ 600 K of ~ 3 x 10^{7} V/m. At this high temperature, this field strength may be enough to pole the crystal. The simple

axial stress analysis shows the thermal stress via Hooke's law is not enough to reverse the domain with the modelled stress values several orders of magnitude too small to those required experimentally as observed by Ohnishi [26]. This points to the pyroelectric field as the probably cause of surface domain formation via UV writing in lithium niobate.

In the pulsed case, the temperature distribution above the ambient temperature also reaches a maximum of ~ 0.5 μm into the crystal, several orders of magnitude higher than the estimated optical absorption depth and expands to a maximum of ~ 2ω across the material surface. The application of more than one pulse has no effect on the temperature distribution if the pulse separation is above ~ 0.15 μs and crystal heating reduces the melting threshold fluence linearly.

The melt zone is restricted by the beam and material parameters – the melt zone depth with this small temporal exposure time is limited to ~ 30 nm and the melt zone width expands to the full beam radius at maximum applied fluence. This amorphous melt zone has considerably different material parameters to the solid crystal parameters. Charge transportation and electron mobility are increased by many orders of magnitude in this zone – domain formation is observed to occur across the beam radius but we can hypothesise that the domain nucleation is formed in this melt zone in the top 30 nm layer of the material. The depth of domains has been observed to be ~ 2 μm; without the melt zone this may be significantly reduced. As with the cw UV writing, the pyroelectric field is also believed to be the cause of the surface domain reversal.

7.6 References

1. Lax, M., *Temperature rise induced by a laser beam.* Journal of Applied Physics, 1977. **48**(9): p. 3919-3924.

2. Cline, H.E. and T.R. Anthony, *Heat treating and melting material with a scanning laser or electron beam.* Journal of Applied Physics, 1977. **48**(9): p. 3895-3900.

3. Moody, J.E. and R.H. Hendel, *Temperature profiles induced by a scanning cw laser beam.* Journal of Applied Physics, 1982. **53**(6): p. 4364-4371.

4. Nissim, Y.I., A. Lietoila, R.B. Gold, and J.F. Gibbons, *Temperature distributions produced in semiconductors by a scanning elliptical or circular cw laser beam.* Journal of Applied Physics, 1980. **51**(1): p. 274-279.

5. Xie, J. and A. Kar, *Mathematical modeling of melting during laser materials processing.* Journal of Applied Physics, 1996. **81**(7): p. 3015-3022.

6. Liarokapis, E. and Y.S. Raptis, *Temperature rise induced by a cw laser beam revisited.* Journal of Applied Physics, 1985. **57**(12): p. 5123-5126.

7. Lax, M., *Temperature rise induced by a laser beam II: The nonlinear case.* Applied Physics Letters, 1978. **33**(8): p. 786-788.

8. Lo, H.W. and A. Compaan, *Raman measurements of temperature during cw laser heating of silicon.* Journal of Applied Physics, 1979. **51**(3): p. 1565-1568.

9. Mazumder, J. and W.M. Steen, *Heat transfer model for cw laser material processing.* Journal of Applied Physics, 1980. **51**(2): p. 941-947.

10. Rantala, T.T. and J. Levoska, *A numerical simulation method for the laser-induced temperature distribution.* Journal of Applied Physics, 1989. **65**(12): p. 4475-4479.

11. Shih, T.-M., *Numerical Heat Transfer*. Series in Computational Methods in Mechanics and Thermal Sciences, ed. W.J. Minkowycz and E.M. Sparrow. 1984, London: Hemisphere Publishing Corporation.

12. Patankar, S.V., *Numerical Heat Transfer and Fluid Flow*. Series in Computational Methods in Mechanical and Thermal Sciences, ed. W.J. Minkowycz and E.M. Sparrow. 1980, London: Hemisphere Publishing Corporation.

13. Calder, I.D. and R. Sue, *Modeling of cw laser annealing of multilayer structures.* Journal of Applied Physics, 1982. **53**(11): p. 7545-7550.

14. Lu, Y.-F., *Heat flow in substrates induced by a scanning laser beam.* Journal of Applied Physics, 1992. **71**(8): p. 3701-3712.

15. Nogotov, E.F., *Applications of Numerical Heat Transfer*. Series in Thermal and Fluids Engineering, ed. B.M. Berkovsky. 1978, London: Hemisphere Publishing Corporation.

16. Voller, V.R., *Implicit Finite--difference Solutions of the Enthalpy Formulation of Stefan Problems.* IMA J Numer Anal, 1985. **5**(2): p. 201-214.

17. Alexiades, V. and A.D. Solomon, *Mathematical Modeling of Melting and Freezing Processes*. 1993, London: Hemisphere Publishing Corporation.

18. Tsukada, T., M. Hozawa, and N. Imaishi, *Global Analysis of Heat Transfer In CZ Crystal Growth of Oxide.* Journal of Chemical Engineering of Japan, 1994. **27**(1): p. 25-31.

19. Mamedov, A.M., *Optical properties (VUV region) of $LiNbO_3$.* Optical Spectroscopy (USSR), 1984. **56**(6): p. 645-648.

20. Chen, I. and S. Lee, *Transient temperature profiles in solids heated with scanning laser.* Journal of Applied Physics, 1983. **54**(2): p. 1062-1066.

21. Wong, K.K., ed. *Properties of Lithium Niobate*. EMIS Datareviews Series. 2002, INSPEC: London.

22. Pendergrass, L.L., *Ferroelectric microdomain reversal at room temperature in lithium niobate.* Journal of Applied Physics, 1987. **62**(1): p. 231-236.

23. Zhang, C., I.A. Salama, N.R. Quick, and A. Kar, *One-dimensional transient analysis of volumetric heating for laser drilling.* Journal of Applied Physics, 2006. **99**(11): p. 113530-10.

24. Miyazaki, N., A. Hattori, and H. Uchida, *Thermal shock cracking of lithium niobate single crystal.* Journal of Materials Science: Materials in Electronics, 1997. **8**(3): p. 133-138.

25. Brannon, P.J., R.W. Morris, and J.R. Asay, *Shock-induced luminescence from Z-cut lithium niobate.* Journal of Applied Physics, 1985. **57**(5): p. 1676-1679.

26. Ohnishi, N. and T. Iizuka, *Etching study of microdomains in $LiNbO_3$ single crystals.* Journal of Applied Physics, 1975. **46**(3): p. 1063-1067.

27. Buse, K. and K.H. Ringhofer, *Pyroelectric drive for light-induced charge transport in the photorefractive process.* Applied Physics A: Materials Science & Processing, 1993. **57**(2): p. 161-165.

28. Rauber, A., *Chemistry and physics of lithium niobate*, in *Current Topics in Materials Science*, E. Kaldis, Editor. 1978, North-Holland Publishing Company. p. 481-601.

29. Bravina, S.L., A.N. Morozovska, N.V. Morozovsky, and Y.A. Skryshevsky, *Low-Temperature Pyroelectric Phenomena in Lithium Niobate Single Crystals.* Ferroelectrics, 2004. **298**(1): p. 31 - 42.

30. Lu, Q., S.S. Mao, X. Mao, and R.E. Russo, *Delayed phase explosion during high-power nanosecond laser ablation of silicon.* Applied Physics Letters, 2002. **80**(17): p. 3072-3074.

31. Bin-Mansoor, S. and B.S. Yilbas, *Laser Pulse Heating of Steel Surface: Consideration of Phase-Change Process.* Numerical Heat Transfer, Part A: Applications, 2006. **50**(8): p. 787 - 807.

32. Gopalan, V., T.E. Mitchell, and K.E. Sicakfus, *Switching kinetics of 180 degree domains in congruent $LiNbO_3$ and $LiTaO_3$ crystals.* Solid State Communications, 1998. **109**(2): p. 111-117.

Chapter 8

Conclusion

Channel waveguide fabrication by UV direct writing at λ = 244 nm in lithium niobate and lithium tantalate was demonstrated and analysed in this thesis. Waveguides written in congruent lithium niobate were only present in *z*-cut samples with no light propagation on *x* or *y*-cut samples tested. Optical modes propagated in *z*-cut samples guided the TM polarisation only, suggesting an increase in the extra-ordinary refractive index (n_e). Comparing waveguides produced on the +*z* and –*z* faces, the +*z* face channels exhibited lower propagation losses at ~ 2dB/cm and an index difference Δn ~ 8 x 10^{-4}. A significant characteristic of UV written guides is the decay rate of the optical mode which had a maximum mean lifetime of ~ 4.5 days. More complex waveguides such as s-bends and splitters were also fabricated and although had large propagation and bend losses, the structures were realised. A mechanism behind the waveguide formation was suggested to

be a permanent lithium out-diffusion from the surface melting, and sideways lithium diffusion underneath the illuminated region.

Stoichiometric and doped lithium niobate samples were investigated to confirm this hypothesis of lithium movement and examine if the waveguide lifetime could be extended via different dopants. Stoichiometric lithium niobate with magnesium and zinc doped congruent lithium niobate samples, with an increased resistance to the photorefractive effect, demonstrated lower index differences and higher propagation losses than undoped congruent lithium niobate. Iron doped lithium niobate, which increases the photorefractive susceptibility of the crystal, displayed higher index changes for low iron doped samples but propagation losses remained high. The iron-doped waveguide lifetime implied an extended timescale compared to undoped congruent lithium niobate.

All optical poling is an interesting feature of cw UV writing with domains line of width ~ 2 μm identified via PFM studies. This presents the opportunity to write domain gratings of small periods once optimised and eliminating the need for photolithography in the fabrication process. Further studies are needed to examine whether these surface domains can be propagated deeper into the crystal.

All optical poling via pulsed UV exposure at λ = 266 nm has established that domains can be ordered along crystallographic directions in regions of spatially periodic intensity. Domain formation has been shown to occur once ablation is present and displays a minimum separation distance between domains of ~ 2 μm. This technique cannot replicate the accuracy of domain formation at small periods yet but further experiments to improve domain formation control will make this method feasible.

8.1 Suggestions for Future Work

8.1.1 UV Written Waveguides

The technique of UV direct-write to produce waveguides in lithium niobate in this thesis has demonstrated the ease of waveguide fabrication in contrast to other current fabrication methods but, due to the instability of the waveguide over time is unsuitable for long term applications. Currently, a possible application which may suit this method is short term holographic storage. To extend the lifetime of the waveguides, two potential techniques remain to be explored; the first, using the application of an external electric field and the second, writing while at an elevated temperature.

The application of an external electric field while writing with λ = 257 nm light incident on MgO-doped lithium tantalate has recently been show to prolong the charge re-compensation mechanism [1]. This technique may allow an extended 'locking' of lithium ions away from the irradiated region but further experiments to investigate if the lithium movement can be fixed to provide longer waveguide lifetimes are necessary.

The second technique of direct writing while at elevated temperatures also attempts to 'lock-in' charge and has been used successfully in fixing holograms written at temperatures of over 100°C in both titanium-doped and iron-doped lithium niobate [2, 3]. While the lithium ions in UV written waveguides are much larger than the electrons and holes responsible in the fixed holograms, the increased temperature may allow further drift away from the irradiated region and delay the waveguide decay.

8.1.2 UV Written Ferroelectric Domains

There is considerable potential for cw UV written domains due to the speed and ease of fabrication. A full investigation of UV exposure versus domain size and depth is needed

to produce optimal fabrication conditions. Further work will include confirmation of the UV writing technique by fabricating periodic domains for quasi-phase matching, perhaps via a phasemask, which would verify the domain nature by its ability to produce second harmonic frequencies.

To extend work on pulsed UV domain formation, an expansion of writing conditions is needed to fully understand the process. This can be partly achieved by the use of different UV wavelengths and phasemask periods to investigate the most limiting factor of the fabrication process, the minimum interaction length, which constrains the practicality of this technique. The depth of the domain formation is limited to ~2 microns and the application of an external field during writing may also push these domains deeper into the crystal for use in high power frequency conversion.

8.2 References

1. Juvalta, F., B. Koziarska-Glinka, M. Jazbinsek, G. Montemezzani, K. Kitamura, and P. Günter, *Deep UV light induced, fast reconfigurable and fixed waveguides in Mg doped $LiTaO_3$.* Opt. Express, 2006. **14**(18): p. 8278-8289.

2. Becker, R.A., *"Thermal fixing" of Ti-indiffused $LiNbO_3$ channel waveguides for reduced photorefractive susceptibility*. Applied Physics Letters, 1984. **45**(2): p. 121-123.

3. An, X., D. Psaltis, and G.W. Burr, *Thermal Fixing of 10,000 Holograms in $LiNbO_3$:Fe.* Applied Optics, 1999. **38**(2): p. 386-393.

Appendix A

List of Publications

Journal Papers

1) Wellington, I.T., C.E. Valdivia, T.J. Sono, C.L. Sones, S. Mailis, and R.W. Eason, *Ordered nano-scale domains in lithium niobate single crystals via phase-mask assisted all-optical poling.* Applied Surface Science, 2007. **253**(9): p. 4215-4219.

2) Mailis, S., C. Riziotis, I.T. Wellington, P.G.R. Smith, C.B.E. Gawith, and R.W. Eason, *Direct ultraviolet writing of channel waveguides in congruent lithium niobate single crystals.* Optics Letters, 2003. **28**(16): p. 1433-1435.

3) Muir, A.C., G.J. Daniell, C.P. Please, I.T. Wellington, S. Mailis, and R.W. Eason, *Modelling the formation of optical waveguides produced in $LiNbO_3$ by laser induced thermal diffusion of lithium ions.* Applied Physics A: Materials Science & Processing, 2006. **83**: p. 389-396.

4) Gallo, K., C.B.E. Gawith, I.T. Wellington, S. Mailis, R.W. Eason, P.G.R. Smith, D.J. Richardson, and S.M. Kostritskii, *Ultraviolet writing of channel*

waveguides in proton-exchanged $LiNbO_3$. Journal of Applied Physics, 2007. **101**(1): p. 014110-3.

Conference Papers

1) Wellington, I., S. Mailis, C.B.E. Gawith, G.J. Daniell, P.G.R. Smith, and R.W. Eason, *UV direct writing of low loss waveguides at 1.5υm in single crystal $LiNbO_3$*, in *Conference on Lasers and Electro-Optics (CLEO)*. 2004: San Francisco.

2) Jungk, T., A.Hoffman, E.Soergel, S.Mailis, A.C.Muir, I.T.Wellington, C.E.Valdivia, C.L.Sones, R.W.Eason, *UV laser-induced ferroelectric domain structures ivestigated by piezoresponse force microscopy,* in *Conference on Lasers and Electro-Optics (CLEO)*. 2007: Munich.

3) Muir, A.C., I.T.Wellington, G.J.Daniell, R.W.Eason, S.Mailis, C.P.Please, *Modelling of UV direct-write waveguides in single crystal lithium niobate,* in *Conference on Lasers and Electro-Optics (CLEO)*. 2005: Munich.

4) Mailis, S., C.Riziotis, I.T.Wellington, P.G.R.Smith, R.W.Eason, *Direct UV writing of optical waveguides in congruent undoped lithium niobate,* in *Conference on Lasers and Electro-Optics (CLEO)*. 2003: Munich.